

The background of the cover is a composite image. The top portion shows a spacecraft in orbit against a starry space background. The bottom portion shows a large, hexagonal solar panel array in orbit, with a smaller satellite nearby. The Earth's surface is visible in the background of the bottom portion.

Interface Design for On-Orbit Assembly of Space Telescopes

Andrei Hutan (4195744)

Master of Science Thesis

Interface Design for On-Orbit Assembly of Space Telescopes

MASTER OF SCIENCE THESIS

For the degree of Master of Science in Space Flight at Delft University
of Technology

Andrei Hutan (4195744)

June 15, 2022

Supervisor: dr. Jian Guo



Copyright © Department of Space Systems Engineering
All rights reserved.

Executive Summary

Space engineering has progressed through leaps and bounds from its inception up until current times, however launcher limitations have become increasingly important as it becomes more and more desirable to create bigger and heavier structures. Furthermore, since the loads experienced during launch are exceedingly high in comparison to those felt in orbit, traditional monolithic spacecraft have a much heavier and sturdier structure than would be necessary during their operational lifetimes just so they can withstand launch. Taking this into consideration, modular concepts that permit not only servicing but assembly directly on orbit have received increased interest. One of the fields of satellite design most affected by this issue is space observation, where an increase in size of the usable aperture directly translates to an increase in performance. With the launch of the James Webb Space Telescope (JWST), on December 24th 2021, the limits to which apertures can be launched without orbital assembly or manufacturing has been reached provided no new launch opportunities arise.

Whilst on-orbit assembly (OOA) of modular structures is not a new concept, enabling technologies have not been sufficiently developed to permit a large amount of demonstration missions. However, advances in robotics, sensing equipment and computational systems could be repurposed to the space sector in order to advance such concepts. One of the missing pieces in the technological development of such projects is the development of standardized interfaces capable of mechanical, electrical, digital and thermal transfer. To address this gap, this thesis aims at developing such an interface to be used for space telescopes specifically, with the in-built flexibility to allow for easily serviceable/maintainable systems that can be launched into orbit by bypassing launcher constraints, at reduced costs and scheduling limitations.

To satisfy this goal, a need analysis of space telescopes is performed, this time not based on a single point design, but instead on the basis of a whole range of reference missions, some launched, some at a conceptual level, such that future requirements for space telescopes can be synthesized for short- to long-term timeframes. These estimates serve as preliminary interface design requirements and are further refined based on existing interface performance, as well as the critical goals of reusability across multiple missions/platforms and ease of serviceability. Based on these refined interface requirements, the Modular Interface for Space Telescopes (MIST) design is created with an initial slide-in mechanism requiring a significant amount of sensors during proximity operations and assembly. Various iterations are performed to

this first design, lessening the need for sensing, as well as reducing the requirements for the robotic assembly satellite that would use this system for OOA. Further work includes addition of redundancy and lowering of risk of damage during operational lifetime through simple design changes. Following significant simulation of all interface models including a scaled down version that is comparative in size to existing interfaces (used in a performance comparison), a proof of concept (PoC) is manufactured and tested within the thesis budget.

The final iteration of the interface (MIST V2.2) not only satisfies all requirements defined during this thesis but, according to the simulation results, outperforms all existing state-of-the-art interface concepts from a mechanical point of view (from a minimum of 194.17% increase in performance for the bending moment in the Z-axis, to a 1537.61% increase under compressive loads). With respect to electrical transfer, it is capable of passing 100 V and 100 A, and has the ability to pass 1 Gbps of data. This design signifies an improvement compared to available options and, given more testing and a space demonstration, can become a worthy choice for a plethora of space observation missions or even other mission types that employ large platform-like structures (i.e. communication missions or even large solar farms). If this concept is sufficiently explored and validated through experimental work, MIST has the potential of becoming a key technology for the development of next-generation space systems that are no longer constrained by launcher limitations, and can be increased in scale up to sizes that have been previously impossible to achieve - due to the high structural performance shown in simulations. For space telescopes, this means the potential of increasing humanity's knowledge and understanding of our galaxy and universe as a whole.

Table of Contents

Acknowledgements	xiii
1 Introduction	1
2 Literature Study	7
2-1 Short Overview of On-Orbit Assembly	7
2-2 "Crawl" Stage - Early Modular Concepts	9
2-3 "Walk" Stage - On-orbit Servicing (OOS)	10
2-3-1 Orbital Express and Phoenix	17
2-4 "Jog" stage - Current State-of-the-Art	25
2-4-1 Current State-of-the-Art Interfaces	30
2-5 A different approach to modularity - Fractionated spacecraft concept	34
2-6 Value proposition and current needs of OOA	40
3 Need Analysis on Space Telescopes for OOA	45
3-1 Mission and Assembly Type	45
3-2 Top-level mission requirements	47
3-3 Modular Optics Considerations	55
3-4 Spacecraft Configuration	57
3-5 Astrodynamics	59
3-6 Attitude Determination and Control subsystem	60
3-7 Launcher Considerations	65
3-8 Thermal subsystem	67
3-9 Command and Data Handling subsystem	69
3-10 Robotic Assembler	71
3-11 Concept of operation (CONOPS)	71

4	Detailed Interface Design - Preliminary design	75
4-1	First Iteration of Interface Design	76
4-1-1	Preliminary Interface Design (MIST V0.0)	76
4-1-2	Selection of Material, Data and Electrical Connectors	80
4-2	ANSYS simulation setup	83
4-2-1	Assembled state simulation setup	83
4-2-2	Assembly simulation setup	88
4-3	ANSYS simulation results for interface V0.0	91
5	Detailed Interface Design - First Iteration	107
5-1	First Design Iteration (MIST V1.0)	107
5-2	ANSYS Simulation Results for MIST V1.0	113
6	Detailed Interface Design - Final Iterations	129
6-1	Interface Final Design (MIST V2.0-V2.2)	129
6-2	ANSYS simulation results - Natural Frequency	132
6-3	Clearance and Thermal Considerations	141
7	Experimental Setup and Results	147
7-1	Experimental Setup	147
7-2	Experimental Results	155
8	Conclusions and Future Recommendations	159
A	Appendix A - Interface Technical Drawings (Full Scale)	i
A-1	Interface V0.0	i
A-2	Interface V1.0	iv
A-3	Interface V2.0	vii
A-4	Interface V2.1	xi
A-5	Interface V2.2	xvi
B	Appendix B - Interface Technical Drawings (120x120 Scale)	xxiii
B-1	Interface V0.0	xxiii
B-2	Interface V1.0	xxvi
B-3	Interface V2.0	xxix
B-4	Interface V2.1	xxxiii
C	Appendix C - Interface Proof of Concept (PoC)	xxxix
	Bibliography	xlix
	Glossary	lix
	List of Acronyms	lix
	List of Symbols	lxi

List of Figures

2-1	Roadmap of current and future OOA technologies, courtesy of [1]	8
2-2	Modular Spacecraft System Patent May 1989, courtesy of [2]	9
2-3	Multipurpose Modular Spacecraft Architecture Patent November 1989, courtesy of [3]	10
2-4	Modular Spacecraft Architecture Patent November 1999, courtesy of [4]	10
2-5	Conceptual SUMO system block diagram, courtesy of [5]	12
2-6	Conceptual SIRE system	13
2-7	Logic structure of simulation architecture, courtesy of [6]	13
2-8	Summary of FDNA results	15
2-9	Initial (top) and final (bottom) configuration of ISAR robotic arm in stowed configuration, courtesy of [7]	17
2-10	NextSat architecture and corresponding standardized interfaces between various modules	18
2-11	Operational phases of Phoenix demonstration mission, courtesy of [8]	21
2-12	Schematic of Standard Hosted Payload Assembly (HPA), courtesy of [9]	23
2-13	Results of cost comparisons between HISAT and monolithic designs	24
2-14	Conceptual Satlet-based systems, courtesy of [9]	25
2-15	TALISMAN robotic arm ground testing	26
2-16	NINJAR ground testing, courtesy of NASA	27
2-17	DILO conceptual illustrations of different assembly stages, courtesy of NASA/Made In Space	28
2-18	ULISSES manufacturing A) nodes and B) trusses, C) mating of structural elements, and D) truss assembly	28
2-19	Dragonfly concept of operation, courtesy of NASA	29
2-20	OOAN docking schematic, courtesy of [10]	30
2-21	HISat design, courtesy of [9]	31

2-22 UDA plate CAD (left-hand side) and block diagram (right-hand side), courtesy of [11] and [9], respectively	31
2-23 SWARM standard interface CAD, courtesy of [12]	32
2-24 "iBoss" interface CAD, courtesy of [13]	32
2-25 Schematic of SIROM interface design, courtesy of [14]	33
2-26 Definition of attributes	35
3-1 Evolution of mission parameters over time	49
3-2 Mission parameter evolution with increasing power usage	50
3-3 Data rate ordered by increasing number of pixels	50
3-4 Evolution of pixel count and power consumption with increasing aperture size	51
3-5 Telescope primary aperture design separated in layers - Mirrors, supporting structure, modular platform containing operational subsystems (from top to bottom)	59
3-6 Visibility Factor (F), courtesy of [15]	68
4-1 Top view of cross-sectional geometries considered for use in vertical assembly system	77
4-2 Overview of MIST interface components (V0.0)	78
4-3 MIST V0.0 dimension notation for first order estimation	79
4-4 Assembled state simulation - fixed support constraints	84
4-5 Tensile force direction and surface application for assembled state	85
4-6 Compressive force direction and surface application for assembled state	85
4-7 Vertical Shear force direction and surface application for assembled state	86
4-8 Lateral Shear force direction and surface application for assembled state	86
4-9 Vertical Bending moment direction and surface application for assembled state	87
4-10 Lateral Bending moment direction and surface application for assembled state	87
4-11 Twist moment direction and surface application for assembled state	88
4-12 Assembly - fixed support constraints	88
4-13 Tension and compression load cases - direction and surface application for assembled state	89
4-14 Vertical and lateral shear load cases - direction and surface application for assembled state	90
4-15 All moments - direction and surface application for assembled state	90
4-16 Stress distribution under 10 kN tensile load - Assembled state MIST V0.0	91
4-17 Deformation under 10 kN tensile load - Assembled state MIST V0.0	92
4-18 Stress distribution under 10 kN compressive load - Assembled state MIST V0.0 male	92
4-19 Stress distribution under 10 kN compressive load - Assembled state MIST V0.0 female	93
4-20 Deformation under 10 kN compressive load - Assembled state MIST V0.0	93
4-21 Stress distribution under 10 kN vertical shear load - Assembled state MIST V0.0	94
4-22 Deformation under 10 kN vertical shear load - Assembled state MIST V0.0	94
4-23 Stress distribution under 10 kN lateral shear load - Assembled state MIST V0.0	95
4-24 Deformation under 10 kN lateral shear load - Assembled state MIST V0.0	96

4-25	Stress distribution under 1 kNm vertical bending moment - Assembled state MIST V0.0 male	96
4-26	Stress distribution under 1 kNm vertical bending moment - Assembled state MIST V0.0 female	97
4-27	Deformation under 1 kNm vertical bending moment - Assembled state MIST V0.0	97
4-28	Stress distribution under 1 kNm lateral bending moment - Assembled state MIST V0.0	98
4-29	Deformation under 1 kNm lateral bending moment - Assembled state MIST V0.0	98
4-30	Stress distribution under 1 kNm moment of twist - Assembled state MIST V0.0	99
4-31	Deformation under 1 kNm moment of twist - Assembled state MIST V0.0	100
5-1	Overview of MIST interface components (V1.0)	108
5-2	MIST V1.0 dimension notation	109
5-3	Visualization of structure when using cube-shaped modules	112
5-4	Stress distribution under 10 kN tensile load - Assembled state MIST V1.0	113
5-5	Deformation under 10 kN tensile load - Assembled state MIST V1.0	113
5-6	Stress distribution under 10 kN compressive load - Assembled state MIST V1.0	114
5-7	Deformation under 10 kN compressive load - Assembled state MIST V1.0	115
5-8	Stress distribution under 10 kN vertical shear load - Assembled state MIST V1.0	115
5-9	Deformation under 10 kN vertical shear load - Assembled state MIST V1.0	116
5-10	Stress distribution under 10 kN lateral shear load - Assembled state MIST V1.0 male	116
5-11	Stress distribution under 10 kN lateral shear load - Assembled state MIST V1.0 female	117
5-12	Deformation under 10 kN lateral shear load - Assembled state MIST V1.0	117
5-13	Stress distribution under 1 kNm vertical bending moment - Assembled state MIST V1.0	118
5-14	Deformation under 1 kNm vertical bending moment - Assembled state MIST V1.0	118
5-15	Stress distribution under 1 kNm lateral bending moment - Assembled state MIST V1.0	119
5-16	Deformation under 1 kNm lateral bending moment - Assembled state MIST V1.0	120
5-17	Stress distribution under 1 kNm moment of twist - Assembled state MIST V1.0 male	120
5-18	Stress distribution under 1 kNm moment of twist - Assembled state MIST V1.0 female	121
5-19	Deformation under 1 kNm moment of twist - Assembled state MIST V1.0	121
6-1	Overview of MIST interface components (V2.0)	130
6-2	Main parts modified with guide elements for MIST V2.1	131
6-3	Modified end-connector element with redundancy and tapered end	131
6-4	Male plate - deflection at f_1	132
6-5	Male plate - deflection at f_2	133
6-6	Male plate - deflection at f_3	133
6-7	Male plate - deflection at f_4	134
6-8	Male plate - deflection at f_5	134
6-9	Male plate - deflection at f_6	135

6-10 End-connector - deflection at f_1	135
6-11 End-connector - deflection at f_2	136
6-12 End-connector - deflection at f_3	136
6-13 End-connector - deflection at f_4	137
6-14 End-connector - deflection at f_5	137
6-15 End-connector - deflection at f_6	138
6-16 Male/Female module - deflection at f_1	138
6-17 Male/Female module - deflection at f_2	139
6-18 Male/Female module - deflection at f_3	139
6-19 Male/Female module - deflection at f_4	140
6-20 Male/Female module - deflection at f_5	140
6-21 Male/Female module - deflection at f_6	141
6-22 Contact dimensions notation for top of the male plate	141
6-23 Contact dimensions notation for bottom of the male plate	142
6-24 Central contact dimensions notation	142
7-1 MakerBot Replicator 3D printer used for PoC production, courtesy of [16]	148
7-2 Technical drawing of 3D printed male plate	148
7-3 Technical drawing of 3D printed female plate	149
7-4 3D Printed Components for Assembly Testing	150
7-5 Assembly Test of 3D Printed Model	150
7-6 Envisioned test setup for interface PoC	152
7-7 Plates and Assembled Central Locking Mechanism - PoC MIST V2.0	153
7-8 Example of Assembly	153
7-9 Suggested driver circuit for linear actuator	154
7-10 Inputs required for driving the linear actuator	155
7-11 Complete Experimental Setup	155
7-12 Results of data transfer testing	156
A-1 Technical drawing of MIST-01 part, Interface V0.0 (400x400 Scale)	i
A-2 Technical drawing of MIST-02 part, Interface V0.0 (400x400 Scale)	ii
A-3 Technical drawing of MIST-03 part, Interface V0.0 (400x400 Scale)	iii
A-4 Technical drawing of MIST-01 part, Interface V1.0 (400x400 Scale)	iv
A-5 Technical drawing of MIST-02 part, Interface V1.0 (400x400 Scale)	v
A-6 Technical drawing of MIST-03 part, Interface V1.0 (400x400 Scale)	vi
A-7 Technical drawing of MIST-01 part, Interface V2.0 (400x400 Scale)	vii
A-8 Technical drawing of MIST-02 part, Interface V2.0 (400x400 Scale)	viii
A-9 Technical drawing of MIST-03 part, Interface V2.0 (400x400 Scale)	ix
A-10 Technical drawing of MIST-04 part, Interface V2.0 (400x400 Scale)	x

A-11	Technical drawing of MIST-01 part, Interface V2.1 (400x400 Scale)	xi
A-12	Technical drawing of MIST-02 part, Interface V2.1 (400x400 Scale)	xii
A-13	Technical drawing of MIST-03 part, Interface V2.1 (400x400 Scale)	xiii
A-14	Technical drawing of MIST-04 part, Interface V2.1 (400x400 Scale)	xiv
A-15	Technical drawing of MIST-05 part, Interface V2.1 (400x400 Scale)	xv
A-16	Technical drawing of MIST-01 part, Interface V2.2 (400x400 Scale)	xvi
A-17	Technical drawing of MIST-02 part, Interface V2.2 (400x400 Scale)	xvii
A-18	Technical drawing of MIST-03 part, Interface V2.2 (400x400 Scale)	xviii
A-19	Technical drawing of MIST-04 part, Interface V2.2 (400x400 Scale)	xix
A-20	Technical drawing of MIST-05 part, Interface V2.2 (400x400 Scale)	xx
A-21	Technical drawing of MIST-07 part, Interface V2.2 (400x400 Scale)	xxi
A-22	Technical drawing of MIST-08 part, Interface V2.2 (400x400 Scale)	xxii
B-1	Technical drawing of MIST-01 part, Interface V0.0 (120x120 Scale)	xxiii
B-2	Technical drawing of MIST-02 part, Interface V0.0 (120x120 Scale)	xxiv
B-3	Technical drawing of MIST-03 part, Interface V0.0 (120x120 Scale)	xxv
B-4	Technical drawing of MIST-01 part, Interface V1.0 (120x120 Scale)	xxvi
B-5	Technical drawing of MIST-02 part, Interface V1.0 (120x120 Scale)	xxvii
B-6	Technical drawing of MIST-03 part, Interface V1.0 (120x120 Scale)	xxviii
B-7	Technical drawing of MIST-01 part, Interface V2.0 (120x120 Scale)	xxix
B-8	Technical drawing of MIST-02 part, Interface V2.0 (120x120 Scale)	xxx
B-9	Technical drawing of MIST-03 part, Interface V2.0 (120x120 Scale)	xxxi
B-10	Technical drawing of MIST-04 part, Interface V2.0 (120x120 Scale)	xxxii
B-11	Technical drawing of MIST-01 part, Interface V2.1 (120x120 Scale)	xxxiii
B-12	Technical drawing of MIST-02 part, Interface V2.1 (120x120 Scale)	xxxiv
B-13	Technical drawing of MIST-03 part, Interface V2.1 (120x120 Scale)	xxxv
B-14	Technical drawing of MIST-04 part, Interface V2.1 (120x120 Scale)	xxxvi
B-15	Technical drawing of MIST-05 part, Interface V2.1 (120x120 Scale)	xxxvii
C-1	Technical drawing POC: support plates (X2)	xxxix
C-2	Technical drawing POC: interface - support plate connectors (X6)	xl
C-3	Technical drawing POC: linear actuator mount (X1)	xli
C-4	Technical drawing POC: interface - male plate (X1)	xlii
C-5	Technical drawing POC: interface - female plate (X1)	xliii
C-6	Technical drawing POC: interface - central locking cylinder (x1)	xliv
C-7	Technical drawing POC: interface - central end connector (X1)	xlv
C-8	Technical drawing POC: interface- central inter-connector (X1)	xlvi
C-9	Technical drawing POC: interface - interface between end-connector and actuator head (X1)	xlvii

List of Tables

2-1	Main dimensions and performance parameters of existing SoA interfaces	33
3-1	Characteristics of reference space telescopes - Part 1	47
3-2	Characteristics of reference space telescopes - Part 2	48
3-3	Comparison between WFIRST and ATLAST w.r.t. data rate and pixel count . . .	52
3-4	Top-level requirements and interface applicability	54
3-5	Combinations of module number and corresponding size	56
3-6	Mechanical environment constraints for considered launch vehicles - Part 1	65
3-7	Mechanical environment constraints for considered launch vehicles - Part 2	66
3-8	Mechanical environment constraint envelope for considered launch vehicles	66
3-9	Limit summary of mechanical environment constraint envelope for considered launch vehicles	66
4-1	Materials considered and their mechanical properties - Part 1	80
4-2	Materials considered and their mechanical properties - Part 2	81
4-3	Part and assembly load simulation results MIST V0.0 (ANSYS) - Part 1	100
4-4	Part and assembly load simulation results MIST V0.0 (ANSYS) - Part 2	101
4-5	Percentile difference between averaged and unaveraged stress values - MIST V0.0 Part 1	101
4-6	Percentile difference between averaged and unaveraged stress values - MIST V0.0 Part 2	102
4-7	Percentile comparison between assembled state and assembly simulation - unaveraged stress results	103
4-8	Maximum load bearing capabilities of MIST V0.0	104
4-9	Part and assembly load simulation results MIST V0.0 120x120 version (ANSYS) - Part 1	104
4-10	Part and assembly load simulation results MIST V0.0 120x120 version (ANSYS) - Part 2	105
4-11	Maximum load bearing capabilities of MIST V0.0 (120x120)	106

5-1	Part and assembly load simulation results MIST V1.0 (ANSYS)	122
5-2	Percentile difference between averaged and unaveraged stress values - MIST V1.0 Part 1	123
5-3	Percentile difference between averaged and unaveraged stress values - MIST V1.0 Part 2	123
5-4	Percentile comparison between assembled state and assembly simulation - unaveraged stress results	124
5-5	Maximum load bearing capabilities of MIST V1.0	125
5-6	Part and assembly load simulation results MIST V1.0 120x120 version (ANSYS)	126
5-7	Maximum load bearing capabilities of MIST V1.0 (120x120)	127
5-8	Performance Comparison Between MIST and Existing Interfaces	127
6-1	First six natural frequencies of MIST V2.2 elements and modules using MIST V2.2	132
6-2	ISO 286-1 standard fits explained, courtesy of [17]	143
6-3	Initial and final values for dimensions requiring clearance	144
6-4	Thermal expansion of critical clearance dimensions both before and after applying clearance	145
7-1	Porteschap 26DBM20B2U-L Technical specifications	151
8-1	Dimensions and performance parameters of MIST V2.2	159
8-2	Dimensions and performance comparison between existing SoA interfaces and the down-scaled version of MIST	160
8-3	Requirements Verification Matrix - Part 1	160
8-4	Requirements Verification Matrix - Part 2	161

Acknowledgements

I would like to thank my supervisor prof. Dr. Jian Guo for the time invested as well as his assistance during the writing of this thesis. I would like to extend my thanks to my colleagues from TU Delft as well as my friends for their feedback and ideas that helped me refine my thesis approach. Of course, I would also like to show my appreciation for my flatmates who were not only supportive during the whole making of the thesis but showed their understanding during the whole work process and always backed me up when I needed the help. Furthermore, I would like to thank my parents for supporting me both financially and mentally during this whole process, always being on my side whilst also giving sound advice throughout this whole experience as well as reading and giving their opinion on the first draft of this work. Last but not least, I would like to dedicate this finished work to my late grandmother who would have taken great joy and pride in knowing her grandson finally finished his studies and has grown up quite significantly from the little boy that caused playful mischief during his childhood to the space engineer he will hopefully become in the future.

Delft, University of Technology
June 15, 2022

Andrei Hutan (4195744)

Chapter 1

Introduction

The space sector has provided unimaginable insight into the scale and inner workings of the galaxy since its inception. From space exploration to using the resources around us in a more efficient way, space missions have added a myriad of discoveries that advanced our knowledge and due to stringent requirements necessary to achieve such feats, humanity has been forced to further technological development constantly. However, progress is currently greatly limited by the launch capabilities available, both in terms of volume, as well as mass. One of the main fields in which this is an issue is space telescopes, where the current upper limit is the James Webb Space Telescope (JWST), recently launched on December 24th, 2021. In order to solve this, the development of modular concepts that enable on-orbit assembly or even on-orbit manufacturing have become necessary as a workaround to the current limits.

The aim of this thesis is to design a standardized interface for modular space telescopes that can enable assembly in orbit, with sufficient flexibility to allow usage across multiple missions, thus becoming a stepping stone in the development of the space sector. In other words: "Create an interface for modular space telescopes which can enable on-orbit assembly (OOA), such that launch constraints can be bypassed, and cost and scheduling limitations can be attenuated". This leads to the creation of the Modular Interface for Space Telescopes or MIST for short. The design requirements are based off of an analysis of a significant amount of reference missions, that have either already been launched or are at a conceptual stage due to the limitations of current launcher technologies.

The purpose of this thesis report is to document the final design of MIST, albeit still preliminary, as well as the entire process that led up to and guided it. The design allows for ease of serviceability and maintainability, thus opting to use a sliding system instead of other means that necessitated movement in the locking plane of the interface for disassembly/removal. The first step that led to this was the creation of a literature study which addressed three major topics: modular spacecraft design, on-orbit servicing, and integration of small satellites. During this process, some major gaps were identified in the literature pertaining mainly to enabling technology for OOA - the most critical of these was the creation of an interface for modular systems.

As such, based on the results of the evaluation of state-of-the-art OOA concepts and enabling technology, the main research gap identified is: modular spacecraft design for OOA using smart interfaces. Based on this, the main research question is defined as follows:

Can a flexible modular spacecraft design for OOA be created, in order to bypass launcher constraints, and offset costs and scheduling limitations?

This can further be refined into sub-questions that together lead to the answer of the main research question. The reasoning that led to these is also included below:

1. What mission types are enhanced by OOA? - This question serves to select a number of different missions that could reap the most advantages from making use of OOA. The main criteria of evaluation are if the considered mission type is subject to launcher constraints already, and if systems of a much larger scale that cannot be launched with current technology would significantly outperform existing missions. Furthermore, an important factor that need be considered is if modularity is possible for the mission type evaluated. For example, an exploration mission that uses fuel-based propulsion may be enhanced by adding more propellant, however modularizing a very large propellant tank raises some technical difficulties with regards to interfacing compared to other mission types. Since modular interfaces are still a fairly new topic of study and design, it is desirable to restrict mission types to those that do not present such issues.
2. Which mission type is most benefited by the advantages provided by OOA? - It is important to limit the scope of the design, as very different spacecraft structures will affect how the system can be broken up into modular parts. This not only affects number of modules, but interface placement, locking technology and lastly, but most importantly, the needs that drive the interface design (such as structural performance and electrical and data transfer capabilities).
3. What is the optimal choice of assembly method for the selected mission type? - Any assembly technology option will have some influence on how a modular design works. One example of this is that using self-assembly has two main consequences, the limitation in reach creates a size limit, and the fact that the assembly subsystem is attached to the main spacecraft makes it so that it cannot be reused for other missions that employ the same interface design. On the other hand, making use of a free-flyer concept makes it so that multiple systems using the same interface design can be assembled by the same spacecraft, however stricter requirements involving proximity operations need to be taken into account (for the assembler spacecraft).
4. Is homogeneous or heterogeneous modularity more advantageous for the selected case? - This choice mainly influences the interface design itself. For example, considering heterogeneous modularity may require the creation of a suite of interfaces with varying capabilities depending on placement within the spacecraft system. In this case some interfaces may require transfer of data and/or electricity, or only structural performance, depending on how the spacecraft design is framed. Although this may create a more streamlined design in some cases, the choice of using a suite of interfaces raises some issues with respect to servicing and mass production.
5. To what extent should the spacecraft be modularized? - The answer to this question affects the number of interfaces to be produced, as well as the available volume in each

module in which spacecraft sub-systems can be designed. Furthermore, the smaller the module, the more convenient it is in terms of costs for launch, as the possibility of piggy-backing becomes available.

6. What interface requirements are dictated by such a design? - This question aims at linking the top-level need analysis on the selected mission type to the technical requirements that drive the detailed interface design itself.
7. Which technologies are most suited for implementation in inter-modular transfers? (This includes thermal and mechanical loads, as well as data or even power transfers between different modules) - The choice of having or not having transfer capabilities for data, power, as well as structural and thermal loads influences the complexity of the interface design, which in turn affects the modular spacecraft design itself.
8. Can an interface satisfy the requirements imposed by the modular design? - This question is derived from the need to evaluate if current technology is sufficiently developed to create a working standardized interface that can be used for OOA.
9. What testing or simulation methods should be applied in order to qualify the interface for use in an OOA demonstrations? - The answer to this is meant to link the interface design produced in this thesis with the work necessary to qualify it for space usage. Due to the scope limitations of this work, not all phases required for raising the technological readiness level of such a concept can be achieved, however a detailed plan of the steps necessary to do so will be included in the recommendations for future work section.

In light of these questions, the following main goal is proposed:

Create a flexible inter-modular interface design for OOA by designing a modular spacecraft conceptually in a top-down manner, such that mission-specific requirements can be synthesized.

Which can further be divided into sub-goals:

- Choose OOA application such that a top-down spacecraft design can be performed
- Trade-off assembly technology options
- Based on mission type and chosen assembly method synthesize potential mission requirements
- Top-down conceptual spacecraft design
- Trade-off different designs for a conceptual modular solution
- Synthesize detailed interface requirements based on top-level mission need analysis
- Detailed interface design
- Trade-off inter-modular transfer technologies (mechanical and thermal loads, data and power)
- Create prototype based on final interface design specifications

- Choose testing methodology for qualifying interface for future OOA demonstrations
- Test prototype
- Evaluate results of testing and success of prototype
- Provide drawbacks as well as recommendations for future work

Although the above list represents a comprehensive step-by-step plan for achieving the main goal of the thesis, due to schedule and budget limitations, the scope needs to be reduced to a certain extent. With this in mind, a revised list of main goals that will be addressed in this work are:

1. Choose OOA application - this includes both mission type and assembly technology
2. Based on a top-level mission need analysis, synthesize a list of interface requirements
3. Produce an interface design that can satisfy said requirements
4. Create a prototype of the interface
5. Analyze performance of prototype

Based on this list this thesis aims at producing a successful modular interface that will potentially satisfy a few important enabling technology needs for OOA (i.e. standardized mechanical interface, power and data transfer capabilities and ease of assembly [18]). If flexible enough, this design can be adopted as a starting point for standardized interfaces for the chosen mission type as well as other missions that employ large plane-like structures, as will be further explained in Chapter 3.

This list of goals coupled with the need for better observation missions, the performance of which is directly dependent on aperture size and number of pixels of the instrument, led to the decision of using a top-level need analysis of space telescope missions as a basis for generating preliminary interface requirements. These requirements were further refined into detailed interface requirements by considering future goals for space observation, flexibility in usage across multiple missions, and comparative performance with existing modular interface designs. Using these requirements, MIST was designed and iterated for improved performance. Following extensive simulation of all the different iterations, the final one was manufactured and tested.

The thesis report is structured as follows: Chapter 2 gives a short summary of the literature study performed before the writing of this work, giving the most prominent examples of on-orbit servicing (OOS), assembly (OOA) and manufacturing (OOM), based on which the research question and sub-questions to be tackled as well as the thesis goals were identified. Subsequently, Chapter 3 handles the selection of both mission type, and assembly methodology, followed by a top-level need analysis of space telescope missions for which the interface will be designed. Using the first-order estimations of requirements resulting from the previous sections, Chapter 4 refines a list of detailed interface requirements, which are used to perform the preliminary interface design. The setup of the ANSYS simulations as well as the corresponding results are also included in this chapter. Subsequently, Chapter 5

details the design logic and choices that led to the first iteration of the interface, as well as the associated simulation results. Chapter 6 elaborates on the final iterations of the interface design, the results of vibration simulations, and clearance considerations for the final concept. This is followed by Chapter 7, where all the physical experiments performed on a manufactured interface prototype are described. Finally, Chapter 8 synthesizes the conclusion of the interface design, including main performance parameters, and defines a list of future work to be performed in order for the MIST design to be used successfully and adopted in the space industry.

Chapter 2

Literature Study

In order to refine the goal of the thesis and set some achievable standards, it is necessary to evaluate both the history of the topic at hand, as well as its evolution over time through a literature study. An overview of on-orbit assembly operations and an introduction of the Crawl-Walk-Jog-Run terminology is given in Section 2-1. A series of examples and enabling technologies are investigated for the Crawl and Walk stages in Sections 2-2 and 2-3, respectively, whilst the current state-of-the-art is considered as part of the Jog stage, discussed in Section 2-4. A different approach to modularity, namely fractionated systems, is explored in Section 2-5. Finally, the value proposition, applications of OOA and current needs will be discussed in Section 2-6.

2-1 Short Overview of On-Orbit Assembly

On-orbit assembly (OOA) is not by any means a new concept, however to this day it is still considered an area of technological innovation. In order to understand this phenomenon, one need only look at the first successful instance of this technology, the International Space Station (ISS), the very first international collaboration in the space sector. Various segments have been added or upgraded, starting from the 90s and continuing to date [19], [20]. Due to the length of this time frame, the evolution of OOA over time can be quantified to some extent, from a task mainly involving astronauts and relatively high risk space walks, to helper robots, tele-operated systems, and even autonomous operations, with varying extent of supervision. The trend that can be observed here is a minimization of risk to harm by lowering or even eliminating human involvement in such tasks. Thus, a need for systems with higher levels of autonomy is readily apparent. As a result of this fact, it is considered appropriate to limit the scope of this thesis to mechatronic systems that do not require direct human involvement. From a technological standpoint, this reduces the options for OOA to self-assembly, use of small satellite assembler units, or autonomous robotics.

When considering the applications of OOA, these can be divided into near-term and long-term. When examining the former, it is very important to note the similar problems tackled

by both OOA and on-orbit servicing (OOS), such as module replacement, upgrade operations, collision avoidance, as well as proximity operations. This fact is further reinforced by a study performed by the Aerospace Corporation [1], giving a roadmap of OOA activities, as well as their respective needs, which shows the commonality between enabling technologies for OOA and OOS, as shown in Figure 2-1.

	Phase			
	Crawl	Walk	Jog	Run
Goal	Human-in-the-loop on-orbit servicing and assembly 	Inter-vehicle on-orbit assembly (i.e., servicing) 	Intra-vehicle on-orbit assembly 	Space fleets for planetary exploration 
Demonstration examples	<ul style="list-style-type: none"> Construction and servicing of the International Space Station with more than 1000 hours of space walks Servicing of the Hubble Space Telescope 	<ul style="list-style-type: none"> On-orbit repair of malfunctioning satellites through removal and replacement of initially external systems in LEO and GEO, followed by satellite design changes to allow complete refurbishment 	<ul style="list-style-type: none"> On-orbit assembly, reconfigurability, and property function transferability with an assembly of mass-producible CubeSats and an evolving "smart" interconnect interface 	<ul style="list-style-type: none"> Reconfigurable telescope Reconfigurable moon outpost Reconfigurable Mars surface vehicle
Key capabilities	<ul style="list-style-type: none"> Basic procedures and best practices for zero-gravity construction and interface development Some standardized mechanical interfaces for docking of modules and spacecraft 	<ul style="list-style-type: none"> Short-range wireless links and networking as well as external vehicle-to-vehicle proximity communication wireless links and networking (up to a few 100 m in range) Some standardized mechanical and power interfaces 	<ul style="list-style-type: none"> Inter-component (on same vehicle) communication, short-range wireless links, and networking capabilities Widespread standardized mechanical, electrical, power, and thermal interfaces 	<ul style="list-style-type: none"> Longer-range wireless links Completely autonomous assembly
Benefits	<ul style="list-style-type: none"> Foundations for international and industry collaboration "Safe" learning environment 	<ul style="list-style-type: none"> Technology refresh Life extension Reduced costs Reduced risks 	<ul style="list-style-type: none"> Unprecedented mission flexibility Reduced spacecraft complexity Ease of entry into market Variety of spacecraft capabilities Reduced costs Reduced risks 	<ul style="list-style-type: none"> Large and modularized exploration missions built to match (inter)national budget cycles
Working groups	<ul style="list-style-type: none"> ISO (sub)committees NASA Other international space agencies 	<ul style="list-style-type: none"> CONFERS CCSDS IOAG 	<ul style="list-style-type: none"> None to date 	<ul style="list-style-type: none"> None to date

Figure 2-1: Roadmap of current and future OOA technologies, courtesy of [1]

This roadmap also gives rise to the analogy of "Crawl", "Walk", "Jog", "Run" which can be used to quantify the evolution of OOA technologies, creating a clearer definition by which working groups can be classified. Two important conclusions can be drawn from this, firstly the fact that this roadmap can serve as an initial evaluation of what level of progress has been made for OOA technology up until this point, and what possible future applications can look like. Secondly, due to the similarity in enabling technologies between assembly and servicing, one can argue that any advances in OOS preceding the same level of performance in OOA, can be used to further develop the latter, and vice-versa.

In order to have a good overview of the evolution of OOA, one must first identify the current state of the art so as to define areas of research. Considering the terminology established in Figure 2-1, it is clear that the "Crawl" and "Walk" phase contain concepts that have already been used or are gaining popularity, in the case of the latter. Whilst any concepts that can be categorized under "Jog" are the current state-of-the-art, with numerous instances of conceptual projects, but very few realizations of such. With this in mind, an overview of the literature study can be given using the aforementioned classification. Furthermore, it is considered that any concepts pertaining to the "Run" class can be excluded from the study for now, as the enabling technologies are not at the level where these should be considered.

2-2 "Crawl" Stage - Early Modular Concepts

Even before the ISS was launched, early patents for modular concepts were made, varying greatly in modularity in the short span of a couple of years. The earliest patent, published in May 1989, involves at least two, substantially identical modules to be launched using the Space Shuttle [2] and assembled through simple mechanical interfaces, as shown in Figure 2-2.

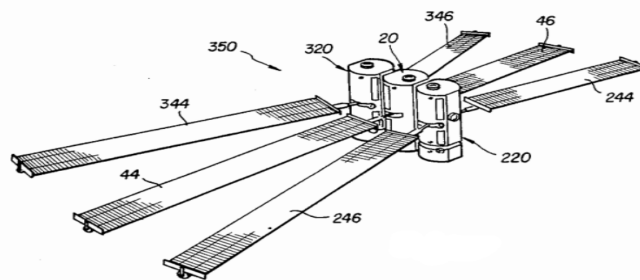


Figure 2-2: Modular Spacecraft System Patent May 1989, courtesy of [2]

A few months later, in November 1989, a patent for a multipurpose, adaptable spacecraft, with different modules designed to satisfy separate functions [3] is created. This shows a trend of increased modularity as early as the inception of such concepts. Figure 2-3 shows the proposed structure of the spacecraft. The observant reader will note that there are a relatively high number of interfacing points between the modules, and that due to the fact that each is meant to satisfy a different spacecraft function, the interfaces cannot be the same.

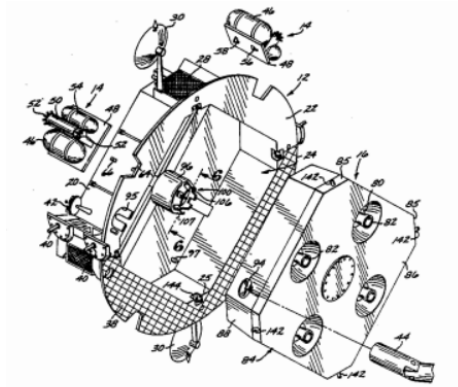


Figure 2-3: Multipurpose Modular Spacecraft Architecture Patent November 1989, courtesy of [3]

The trend of increased modularity continues after the launch of the ISS with the idea of a core structure extending radially being proposed in [4]. This concept suffers from the same problem as the previous one, with interfaces needing to be different depending on what modules need to mate with each other, however it does have the advantage of structural variety as shown in Figure 2-4 - modules can be assembled in various directions and orders, thus the overall spacecraft structure is not immediately set, as for the previous concept.

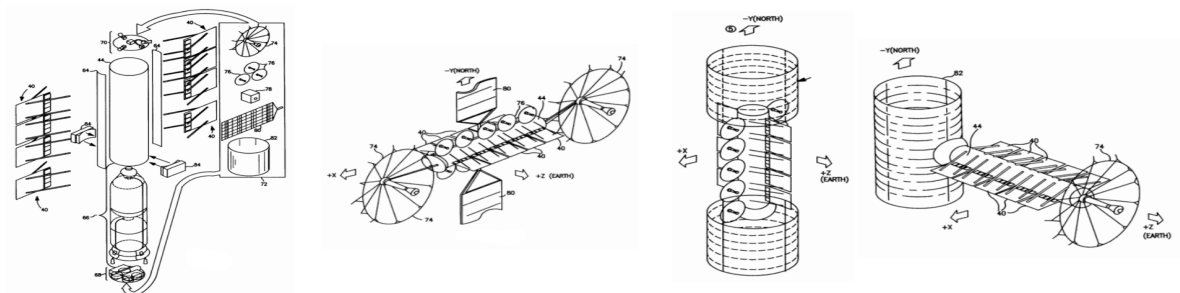


Figure 2-4: Modular Spacecraft Architecture Patent November 1999, courtesy of [4]

Unfortunately, these patents were never pursued, and the only successful instance of a "Crawl" OOA concept remains the ISS. Despite this fact, these concepts served to highlight the main challenges of servicing and assembly, so that future missions could try to contribute to enabling technologies that did not exist during these early times. With respect to OOS, the servicing missions of the Hubble Space Telescope (HST) [21] remain the only successful instances in this category. For more information on the specifics of the four servicing missions and the operations performed on the HST, the interested reader is referred to [22].

2-3 "Walk" Stage - On-orbit Servicing (OOS)

Although servicing missions for existing satellites have not been very common, the field of OOS has not stagnated in the least, constantly developing and creating demonstration missions

aimed at reducing human involvement to a minimum as well as propagating the idea of serviceable designs. In essence servicing an existing spacecraft that was in no way designed with OOS in mind is a daunting task which requires unnecessary complexity to be added to the servicing mission itself, thus a shift was necessary at the design philosophy level. One of the first studies to tackle such concepts was the Spacecraft Modular Architecture Design (SMAD) study performed by the US government [23], which identified six potential advantages granted through OOS:

- Overall reduced life cycle costs
- Increased availability payload sensors
- Extended mission lifetime
- Enhanced mission capabilities
- Enhanced flexibility and operational readiness
- Pre-launch spacecraft integration flexibility

Based on this, [23] goes on to provide a definition for serviceable spacecraft as "any spacecraft for which the benefits of on-orbit servicing outweigh the associated cost. The purpose of servicing can be to replace degraded or failed components, to upgrade existing capabilities, or add new functionality or capabilities." Based on this, four different options for servicer spacecraft were investigated which can be summarized as follows:

- The servicer permanently docks with the satellite.
- The servicer is essentially a modular spacecraft comprised of a bus module, and two payload modules carrying replacement parts. The attachment to the target spacecraft to be serviced is only temporary.
- The servicer docks temporarily and leaves nothing permanently attached to the target satellite (in other words, only refueling is possible).
- The servicer is outfitted with propellant and replacement components sufficient to service two satellites (this concept requires a longer lifetime).

By categorizing components by replaceability, in other words by how minor or major the effect of servicing the current architecture influences the mission in terms of design changes, this paper then considers a Rendezvous/Docking (R/D) Servicer concept and provides a baseline for its design [23]. Applying this mission to the initial SMAD concept showed that savings between 10.3% and 38.2% could be achieved, reinforcing the expected benefits of OOS.

In 2004 an entirely different concept is explored by the Naval Research Laboratory (NRL) called the SUMO mission (spacecraft for the universal modification of orbits) [5]. Although based on the previous work this could be qualified as a servicer corresponding to option 4, SUMO does not provide refueling services. Instead it aims at rendezvousing with the target spacecraft and, using its own highly efficient propulsive capabilities, push the target back into

its desired orbit. This not only allows for a very simple design consisting of only a payload and a propulsion module, as illustrated in Figure 2-5, but also serves as a demonstration bed for machine vision, robotics, mechanisms and autonomous control algorithms designed to rendezvous and grapple a variety of interfaces.

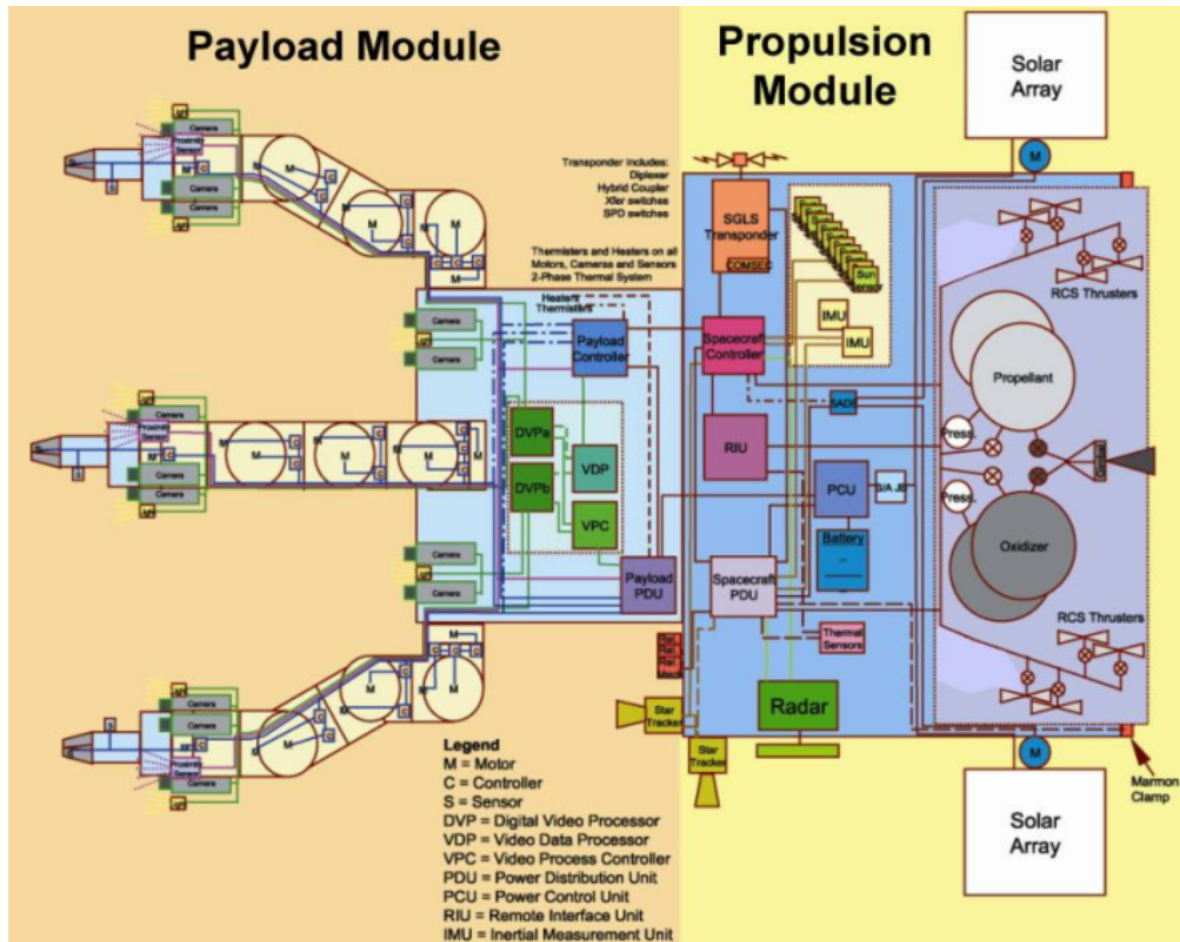


Figure 2-5: Conceptual SUMO system block diagram, courtesy of [5]

Depending on the required timeframes, this concept is expected to be able to service between 5 and 20 spacecraft before it needs refueling. For more information on ground testing and the proposed flight demonstration, the interested reader is referred to the base material.

A similar concept to SUMO is found in a US patent, namely the Satellite Inspection Recovery and Extension (SIRE) spacecraft [24]. Although it also aims at satisfying trajectory changes, or even planned re-entry or deorbit maneuvers, it aims at doing so through simpler means than the SUMO concept. As such, there are no signs of using high-end robotic arm technologies, as illustrated by Figure 2-6, courtesy of [24].

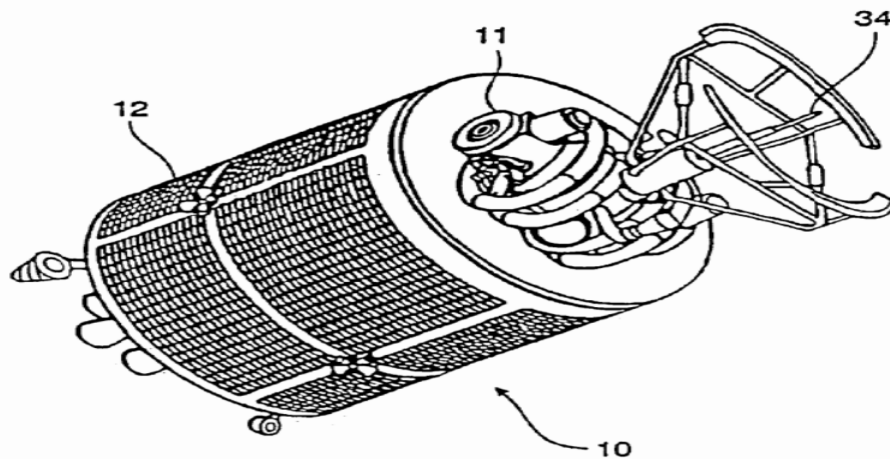


Figure 2-6: Conceptual SIRE system

In order to aid demonstration missions, real-time simulations were also developed to serve as training grounds for OOS. One such software was created by the German Aerospace Center (DLR) in 2011 [6], and consists of four different modules: the manager module which hosts the central logic of the system, the haptics module which controls the haptics device as well as covering the force computation and collision detection fronts, the physics module in charge of the rigid-body physics aspects, and the visualization module which produces high-quality renders of the interactions and results. These four modules are linked through the logical structure shown in Figure 2-7.

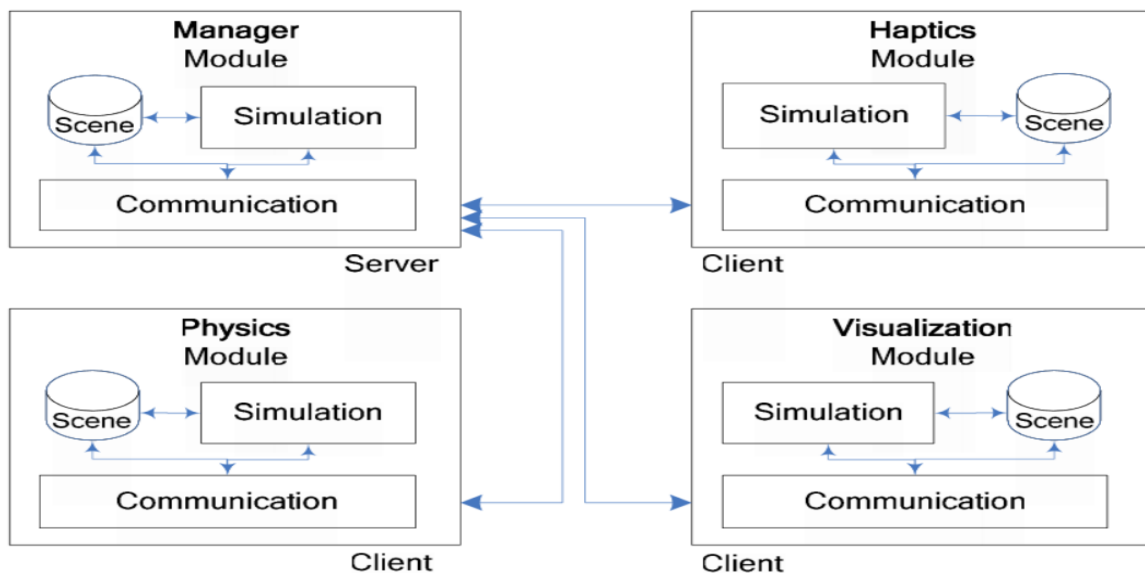


Figure 2-7: Logic structure of simulation architecture, courtesy of [6]

Five different on-orbit scenarios were considered: removing multi-layer insulation (MLI), taking measurements, loosening/tightening of screws, flicking a switch and module replacement. Out of these only the three latter scenarios were implemented at the time of writing of [6],

although it is mentioned that future work will include implementation of the other two scenarios as well as exploring alternative real-time physics engines and optimization algorithms for the haptic rendering.

Whilst simulation plays a big role in enabling and enhancing OOS capabilities, so does analysis as it reinforces the benefits of this field in a quantifiable manner, such that the usage of such technology is more desirable for all stakeholders involved. One such highly comprehensive analysis is introduced in [25], where a Functional Dependency Network Analysis (FDNA) is utilized to showcase the impact of functional dependencies between systems and subsystems in OOS scenarios. This study can be classified as spanning two different levels, a lower one and a higher one.

On the lower level, modular satellites that contain modules that are easy to replace or service are considered, spanning ten distinct missions that can be categorized as belonging to one of three types: communication, observation or experimental. The goal of this level of analysis is to gain insight into the effects of interdependencies, redundancy and various architectures. A random generator is used to create the given architectures based on probabilities suggested from current engineering practices. The inputs required for the FDNA are the topology of the network and the evolution of self-effectiveness of a given spacecraft over time. The latter simulates self-effectiveness loss, with a timestep of a single month, based on three distinct factors: aging/wearing out/losses, degradation through minor failures, and major failures/accidents/catastrophic events.

The higher level uses the results of the former to model the architecture of possible constellations of satellites and their overall operability as a function of the individual operability of each satellite. This method essentially groups all mission types considered, including the OOS elements as a System-of-Systems (SoS). Of course, some simplifying assumptions are considered:

- Servicing spacecraft are not subject to failure
- The cost analysis only accounts for the δV required in servicing target satellites
- Different stakeholders and their effects on both design and servicing are not considered
- Servicing is assumed to always be successful
- The tools described are solely used for analysis and not to guide design decisions for the production of the SoS

After defining the 10 missions used as inputs, as well as their orbits, and payload details (i.e. number of sensors, antennae or experiments), 1000 instances of quantifying the operability of individual modules as well as architectures are run. Based on these simulations, an expected value of overall operability is computed, as well as the evolution of said parameter over time. Based on how critical the desired capability of each mission is, the percentile of instances where OOS would be necessary for each mission type is computed. The way in which this is done is by assigning a servicing mission once operability decreases below 70%, using a relatively long timeframe of 100 months as mission duration. The results of the FDNA are summarized in Figure 2-8, courtesy of [25].

Servicing Architecture (number of satellites, orbit, [spare parts])	Average number of request (100 months)	Average percentage of satisfied requests	Average Δv	Average increase in expected value of the overall capability	Average increase in overall capability of the worst case
1 servicing satellite, LEO, [1 Sensor, 1 Battery, 2 Fuel Cells]	181.33	1%	8.21 km/s	0.826	9.14
1 servicing satellite, MEO, [2 Solar Arrays, 1 Power Regulator, 2 Antennas]	168.44	1.55%	9.31 km/s	1.334	0.43 (not serviced in most cases)
1 servicing satellite, GEO, [1 Solar Array, 2 Batteries, 1 Antenna, 1 Sensor]	158.46	1.87%	11.16 km/s	1.520	3.42
3 servicing satellites, LEO, [3 Fuel Cells, 1 Electronics, 1 Gyro, 3 Batteries, 1 Power Regulator, 3 Antennas, 1 Sensor]	124.41	5.59%	24.99 km/s	2.355	12.68
3 servicing satellites, MEO, [1 Solar Array, 2 Power Regulators, 3 Sensors, 1 Antenna, 2 Fuel Cells, 2 Batteries, 1 Electronics]	118.30	6.07%	26.35 km/s	2.294	13.40
3 servicing satellites, GEO, [3 Solar Arrays, 2 Batteries, 3 Fuel Cells, 2 Antennas, 3 Sensors, 2 Electronics]	124.29	5.33%	20.38 km/s	2.393	15.656
3 servicing satellites, LEO, [2 Batteries, 1 Sensor, 1 Antenna, 1 Fuel Cell], MEO, [1 Solar Array, 1 Antenna, 1 Sensor, 1 Electronics], GEO, [1 Antenna, 1 Solar Array, 1 Power Regulator, 1 Battery, 1 Fuel cell]	115.39	6.78%	27.44 km/s	2.544	13.39
6 servicing satellites, 2 LEO, [2 Sensors, 2 Fuel Cells, 1 Electronics, 1 Antenna, 1 Power Regulator, 1 Solar Array], 2 MEO, [2 Batteries, 2 Fuel Cells, 2 Electronics, 2 Power Regulators, 1 Sensor], 2 GEO, [2 Antennas, 3 Sensors, 2 Solar Arrays, 1 Power Regulator, 1 Battery, 1 Fuel Cell]	107.55	8.53%	30.63 km/s	2.68	16.087

Figure 2-8: Summary of FDNA results

In essence this analytical tool offers critical information for various applications, including but not limited to optimization of architectures, analysis and comparison of different architectures, and decision-driving metrics for design. It is also mentioned that the model can be enhanced through the addition of more interdependencies and inputs for the risk analysis, simulating the servicing satellites as prone to failure, as well as the implementation of time-variation for the interdependencies themselves. Although this would indeed improve the results, this paper still has merit in quantifying the attractiveness of using OOS options in various mission and system architecture types as is.

Moving away from simulation and analysis tools, as one would most probably expect, the most advancements in enabling technology for OOS is detected in the field of robotics, as high-end robotic arm technologies have not only been pushed forward by space engineering but all other fields which employ automation in their manufacturing process. A review of such robotic technologies aimed at enabling OOS is compiled in 2013 [26], giving a comprehensive view on each historical advancement as well as its utility. Due to space constraints all of these will not be detailed here but summarized in a few words, although the interested reader is referred to the source material for more information on this topic.

- **Shuttle Remote Manipulator System (SRMS)** - 15.2m long, 6 degree of freedom

(DOF) robotic manipulator developed by the Canadian Space Agency (CSA); used on the Space Shuttle and ISS.

- **Space Station Remote Manipulator System (SSRMS or Canadarm2)** - 17m long, 7-DOF, capable of walking around the ISS; modular design for easy maintenance and force-moment sensors for advanced robotic control
- **Robot Technology Experiment (ROTEX)** - developed by DLR to study and demonstrate robotic technologies on board the ISS.
- **Robotics Component Verification on the ISS (ROKVISS)** - designed by DLR.
- **Robonaut 1 (R1)** - designed by the National Aeronautics and Space Administration (NASA) to assist astronauts with Extra Vehicular Activities (EVA).
- **Robonaut 2 (R2)** - designed by NASA in conjunction with General Motors; upgrades include higher bandwidth, greater dexterity, larger range of motion and increased force sensing capabilities.
- **Experimental Test Satellite VII (ETS-VII)** - developed by the Japan Aerospace Exploration Agency (JAXA), included a 2m long 6-DOF robotic arm.
- **Orbital Express** - developed by the Defense Advanced Research Projects Agency (DARPA), more details in Subsection 2-3-1.
- **Front-end Robotics Enabling Near-Term Demonstration (FREND)** - a 7-DOF flight robotic arm system, currently used in the DARPA Phoenix mission, detailed in Subsection 2-3-1.
- **Demonstration for Autonomous Rendezvous Technology (DART)** - sponsored by NASA with the objective of validating hardware and software required for autonomous rendezvous and proximity operations.
- **Technology Satellites for Demonstration and Verification of Space Systems (TECSAS)** - jointly developed by DLR, CSA and the Russian Space Agency (RKA) it was discontinued due to a priority shift of the collaborating agencies.
- **Advanced Telerobotic Actuation System (ATLAS)** - consists of a dual-arm robotic manipulator system.

In addition to the systems mentioned here, this review also summarizes advances performed in the kinemo-dynamics of robotic manipulators, innovations registered in the observation and planning phase as well as the final approach phase, and techniques that enhanced flexibility and vibration suppression [26].

On the other hand, a less comprehensive review that tackles robotic technologies for OOA is performed by DLR in [8]. It is important to note that due to the significant similarities between these applications with respect to robotic technologies, most of the information provided overlaps with the previous review.

In 2017 however, a new concept for space assembly robotics is presented by the US Naval Academy (USNA) the next-generation Intelligent Space Assembly Robot (ISAR) system [27].

The idea is to expand on the existing set of robotic arms housed in a 3U CubeSat previously developed by USNA. Using a CubeSat for demonstration drastically reduces the costs required to validate this system in its intended operational environment, as well as mitigating losses in the case of failure. The system is equipped with both the RSat arm and the ISAR, in order to better quantify the difference in performance between the two. Whilst [27] gives an overview of the software employed and the simulation results for the ISAR arm, [28] delves deeper into both the design process and ground testing of said technology.

Finally, in 2018, the ISAR is further improved through the addition of a centrally mounted 3D camera, a miniaturization at the system level, as well as the implementation of a more advanced control software [7]. In addition to these, a DOF was removed (specifically the shoulder joint) due to the ability to maintain high manipulability at the end-effector level. The differences between the initial model and improved design are illustrated in Figure 2-9.

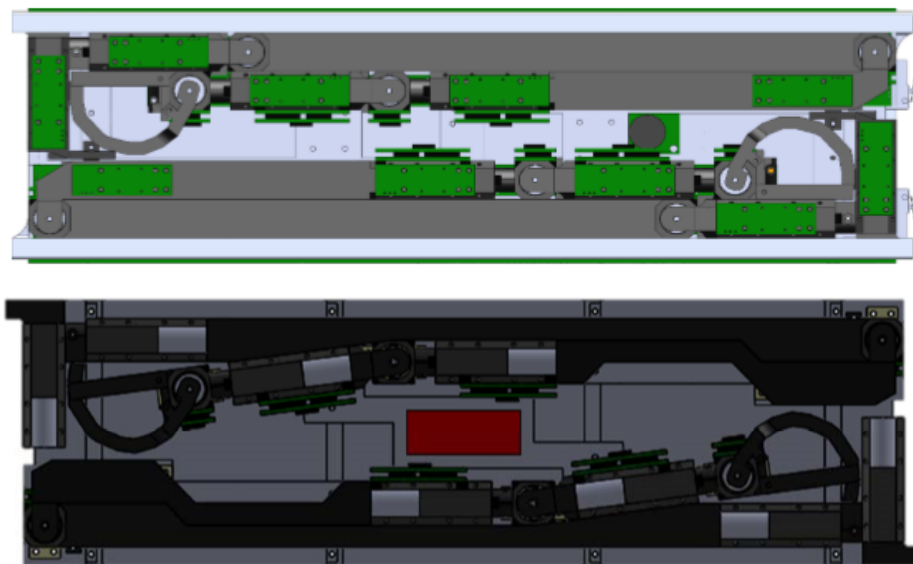


Figure 2-9: Initial (top) and final (bottom) configuration of ISAR robotic arm in stowed configuration, courtesy of [7]

Although this concludes most of the work that can be classified into the "Walk" stage, the work provided by DARPA with the Orbital Express and Phoenix project is borderline in between the two stages, as it not only enables the "Jog" stage but systems designed in these works can be repurposed for current state-of-the-art systems, as will be seen in Subsection 2-3-1.

2-3-1 Orbital Express and Phoenix

The conceptualization of the Orbital Express program by DARPA is documented in 2000 [29]. The goal of this program is to enable refuellable and upgradeable satellite constellations as well as their support architecture. The intent is to shift the paradigm from monolithic traditional spacecraft design to modular design by providing fuel and module servicing as "space commodities" in a post-2010 timeframe. The demonstration mission envisioned here consists

of two individual entities, the Autonomous Space Transporter and Robotic Orbiter (ASTRO) - a permanently orbiting servicing spacecraft - and the Next Generation Serviceable Satellite (NextSat), which is designed in a modular manner to permit ease of servicing, nonintrusive refueling and compatibility with the ASTRO spacecraft. An initial schematic of NextSat is provided in Figure 2-10, courtesy of [29].

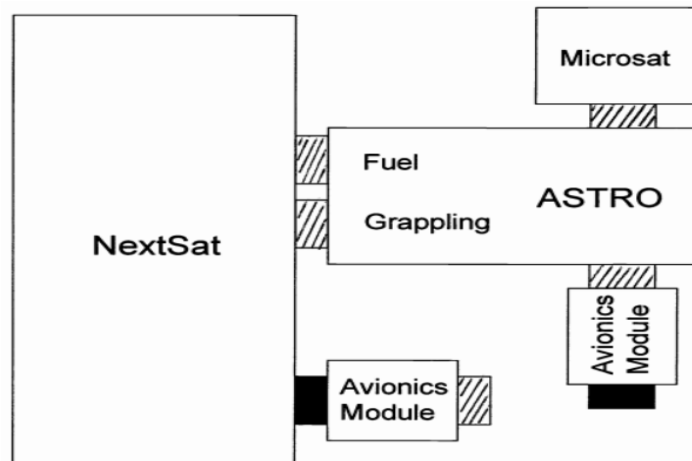


Figure 2-10: NextSat architecture and corresponding standardized interfaces between various modules

At a system level, the Orbital Express concept considers:

- Target satellite maneuverability
- Target satellite performance recovery given hardware replacement
- Target satellite performance enhancement when performing hardware upgrades
- Capability/operations, location and sizing of servicing ground control station
- Required responsiveness of OOS services
- Duration of OOS mission
- Level of autonomy desired or required of the servicing spacecraft
- OOS satellite ground control coordination with other control station or ground command centers
- Potential demand and opportunities for OOS
- Implications of OOS-imposed redesign of potentially serviceable satellites

It is also mentioned in [29] that using a built-in microsatellite hosting capability on the servicing spacecraft could widen the variety of space applications such small satellites could be used for. In 2008, a summary of the Orbital Express program is published at the SPIE

Defense and Security Symposium, detailing a mission overview as well as the results and unexpected problems said demonstration had to overcome [30]. One of the most critical mission requirements for said demonstration was the raising of Technological Readiness Level (TRL) of various technologies:

- "Non-proprietary servicing interfaces"
- "Autonomous operations and servicing software"
- "Autonomous proximity operations and Autonomous Guidance Navigation & Control (AGN&C); Autonomous capture and mating"
- "ORU transfer" (ORU refers to Orbital Replacement Unit, in other words a module used in servicing)
- "Zero gravity fluid transfer"
- "Avoidance of contamination of NextSat"
- "Advanced robotics"

The Orbital Express demonstration mission was launched on March 8, 2007, and was successful in attaining a 492 km circular orbit with an inclination of 46°, however this happened approximately 10 seconds earlier than expected. This was in no way the only unexpected event, as during initialization the SIGI space receiver on the ASTRO failed to initialize completely. This led to the choice of switching to reaction wheel control, however it was noted that the RWA (reaction wheel assembly) pitch axis was saturating. Upon investigation of this system, it was discovered that the flight software assumptions were incorrect for said axis of the reaction wheel installation and a corrected version was sent along with a new RNP matrix, state vector and time tag, which served as preparation for the SIGI GPS reinitialization. The issues did not stop there as upon GPS reinitialization it was observed that the Star Tracker attitude quaternion had a deviation of nearly 180 degrees away from what the SIGI quaternion indicated. This led to the ASTRO immediately turning away from the Sun, thus taking the Sun off both NextSat and ASTRO solar arrays, leading to a loss in communication. Although the ground team was successful in sending a command to ASTRO to switch to Free Drift mode, this ended up disabling the Antenna Manager, thus putting it in toggle mode. As a last resort, the team requested NextSat take control over the stack by disabling all fault protection and sending a command directly to NextSat telling it that it was unmated.

The following pass it was verified that NextSat was in control and slowly turning the mated couple towards the Sun and, approximately two hours later, power was restored to both spacecraft. Due to these series of unfortunate events, even more problems had arisen such as the propellant lines freezing over and the battery capacity of ASTRO being slightly compromised, however these were settled without much trouble. Once the SIGI GPS was reinitialized the vector error was solved however the SIGI was closely monitored thereafter. Further issues such as one Thermal Control System and two OEDMS (Orbital Express Demonstration Manipulator System) related anomalies were experienced but overcome successfully. Lastly a ground station transmission anomaly was also detected where the upload was 3048 blocks whereas the receiver could only permit 3045 blocks to be transmitted. This was solved by

stitching the last 4 blocks to the previously uploaded blocks and installing it once the second transmission was achieved. After all these issues, finally the Orbital Express demonstrations could start.

The first scenario considered consisted of a coupler system mating (with ASTRO approaching NextSat) and leak check, as well as a pressure-fed hydrazine propellant transfer from ASTRO to NextSat. ASTRO successfully delivered 19 pounds of hydrazine to NextSat, followed by a reverse transfer (from NextSat back to ASTRO) of 52.5 pounds. The first ORU transfer was also performed, consisting of moving the battery from ASTRO and integrating it with NextSat. This marked a historic first for battery transfer among spacecraft [30]. After multiple more fluid transfers in both directions, Scenario 0 was concluded successfully.

Scenario 1 essentially consisted of ASTRO using its robotic arm to grapple NextSat, release the separation ring band attached to it and extend said satellite to pre-berth position. In spite of a slight anomaly being discovered in the robotic arm system, this segment was also completed with success. Scenario 2 was the first unmated demonstration where ASTRO would demonstrate final approach and direct capture of NextSat from a separation distance of 10 meters. This entire scenario was performed at autonomy level 4 and following the capture, two battery transfers were demonstrated at autonomy level 3 (higher level than previous scenarios). Scenario 3 was planned to be a "Free-Flyer" capture scenario at a range of 30 meters, however during operations ASTRO experienced a failure of the primary sensor computer. As rebooting failed to fix this issue, ASTRO autonomously aborted said maneuver and began station keeping at roughly 120 meters away from NextSat. Further actions from the ground team resulted in a passively safe orbit with a separation of 6 kilometers between ASTRO and NextSat. Although this event highlighted some system limitations for the Orbital Express mission, once ASTRO successfully locked on to NextSat, it continuously tracked it with its infrared camera and laser range finder starting at a separation of slightly over 4 kilometers. Once the ground team uploaded a new scenario for ASTRO, the distance between the two spacecraft had shrunk to approximately 2 kilometers. After an approach that put ASTRO within 140 meters of its target, ancillary sensors were activated and a perfect direct capture of NextSat was achieved. Scenario 4 was supposed to involve the validation of the laser range finder at a distance of 1 kilometer, however this was already achieved hence it was dropped. For similar reasons, the fly-around objective originally pertaining to Scenario 6 was moved to Scenario 7.

The following scenario involved the ASTRO separating from NextSat to a distance of 120 meters, using solely onboard cameras and the advanced video guidance system, subsequently flying around NextSat, approaching and capturing said target. This marked another historical first time where a fly-around was performed using primarily passive sensors and without exchanging relative navigational information [30]. Furthermore, this demonstration occurred at full autonomy, requiring no supervision, approval or confirmation from the ground station. Due to the problems experienced in Scenario 3, Scenario 7 was significantly redesigned. From a planned departure to 7 kilometers followed by a return and direct capture, as well as a combined ORU and fluid transfer, the goal was changed to 4 kilometers, whilst the rest remained unchanged. Although an arm anomaly prevented immediate berthing and mating with NextSat, once this was fixed this scenario also proved to be successful. Finally Scenario 8 was essentially the Orbital Express design reference mission which included all servicing activities, Free-Flyer capture from a distance of 7 kilometers, unmated operations, as well as fluid, battery and computer transfers. This scenario spanned a total of 5 days and ended in

complete success.

The only thing left was to perform the end-of-life scenario. Although the original plan was to leave both satellites in trajectories with no possibility of re-contact which would naturally decay within 25 years, ASTRO still had approximately 88% of its original propellant left and this had to be depleted. Furthermore it was decided that there was value in further characterizing the sensors and this could be integrated in this last scenario. After transferring all fuel to NextSat, the separation between the two satellites was enlarged up until the sensors lost track of each other at a range of 400 kilometers. A return command was issued to ASTRO which successfully reacquired NextSat as a target at a range of 200 kilometers. The final decommissioning sequence was successfully uploaded on July 20th, 2007, thus concluding the Orbital Express demonstration mission. With a duration of approximately 4 months, this mission was a definitive success, achieving all demonstration scenarios proposed [30].

The results of this demonstration mission are further quantified in [31], where the focus is primarily on the robotic manipulator system, as well as its role in the Orbital Express demonstration.

Another significant project created by DARPA is the Phoenix System [8] which can be classified through two major designs - the Payload Orbital Delivery (POD) system [32], [33], which paves the way for the Satlets [9], a conceptualization of satellite cellularization. [8] provides a summary of progress on hardware prototyping and systems analysis as well as initial testing and demonstration results as of 2013. At this time, the concept of operations planned for the Phoenix demonstration mission includes ten distinct stages, as illustrated in Figure 2-11.

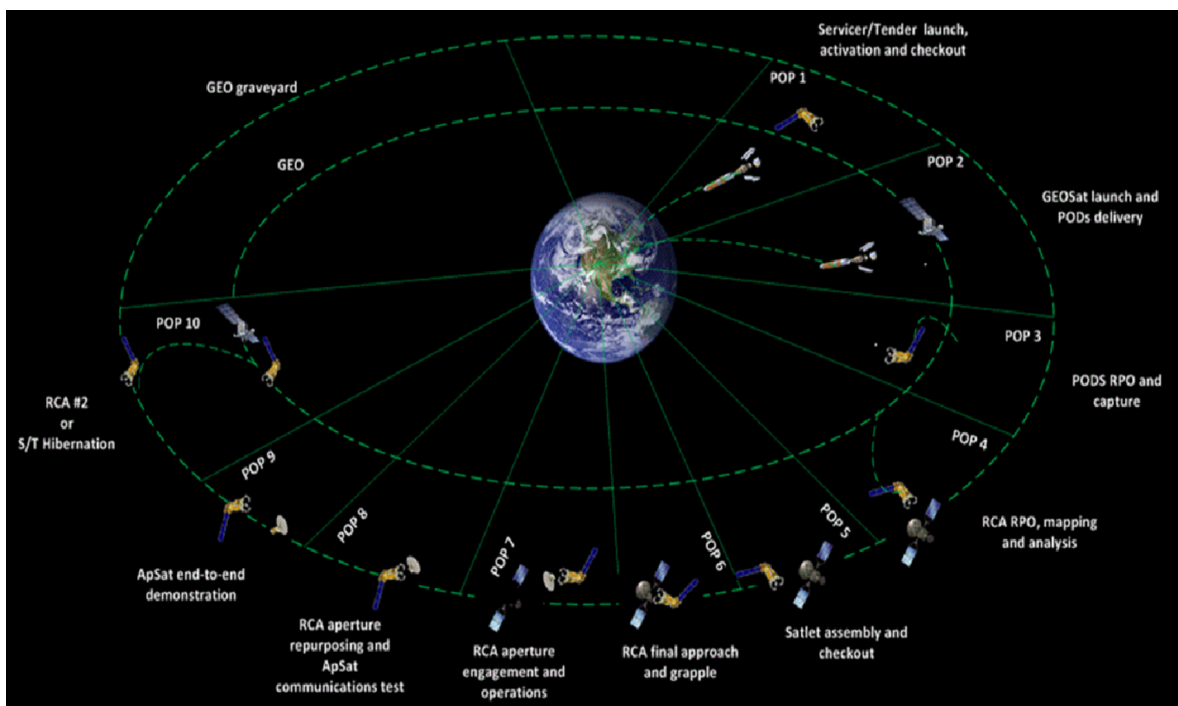


Figure 2-11: Operational phases of Phoenix demonstration mission, courtesy of [8]

The goal cited in [8] is to "develop and demonstrate technologies to cooperatively harvest

and reuse valuable components from retired, non-working satellites in Geosynchronous Earth Orbit GEO and demonstrate the ability to create new space systems at greatly reduced cost". The first step in achieving this is the design of a Servicer/Tender satellite with enough fuel and robotic dexterity to enable satellite-to-satellite operations. This includes a variety of technologies to be hosted, including but not limited to:

- A toolbelt accommodating robotic and sensing paraphernalia as well as rendezvous and proximity operations systems and associated sensing equipment
- Two FRENDD Mark 2 robotic manipulators
- A collection of tools and end-effectors for the primary robotic arms
- Next Generation Hyper-Dextrous Manipulator (NGHDM) technology used in proximity operations
- Tele-robotic capabilities and corresponding software

To ensure the continued operability for said Service/Tender to act as an on-orbit asset, the Payload Orbital Delivery system (PODs) is envisioned to essentially act as a "FedEx to space", providing the ability of bringing additional or upgraded tools, hardware or even satellites. This, however, represents the full scope of the Phoenix project, whereas the very first phase solely considers the repurposing of an aperture of a Retired Cooperative/Candidate Asset (RCA) through the use of the FRENDD robotic system. As such, more details are given with respect to ground testing of various aspects of such an endeavor such as: EMI/EMC on the robotic manipulators, POD grapple and contact dynamics, initial end effector performance, boom severing and tele-operations. At the time of writing of this paper, Phase 2, namely the building phase was planned for fall of 2013 [8].

Also published in 2013, [33] mainly considers the POD system as a whole, briefly mentioning other aspects of the Phoenix program, but focusing on the benefits and concerns such a system would raise. With respect to performance, DARPA estimates that about 15 commercial launches to GEO could be achieved per year, and considers an overall total of 66 candidate missions that could be applicable for launch using PODs. The timeframes before launch, as well as from launch to POD separation are briefly considered as well as separation from host and post-separation aspects.

Finally [33] gives an overview of envisioned POD capture operations once it has satisfied host launch and deployment as well as potential commercial operator and even manufacturer concerns that could be raised by this system, including but not limited to avoidance of complex mission profiles, minimization of propellant usage, positive avoidance of re-contact risk following separation from POD system, as well as minimization of potential insurance underwriter concerns regarding POD hosting and release. Future considerations quoted by this work can be summarized as: the usage of PODs as ESPA payloads, the design of Fuel PODs (specialized in propellant delivery), the potential use of PODs as an enabler for small satellite missions, as well as using the POD interface to augment potential future GEO hosts [33].

On the other hand, [9] aims at providing a sort of user's guide for the PODs concept, by not only comparing it with other hosted payload opportunities but also exploring planned

flight testing scenarios, alongside POD hosting opportunities and launch integration cycle. However, the most noteworthy information provided by [9] is the description of the Standard Hosted Payload Assembly (HPA) concept, illustrated in Figure 2-12.

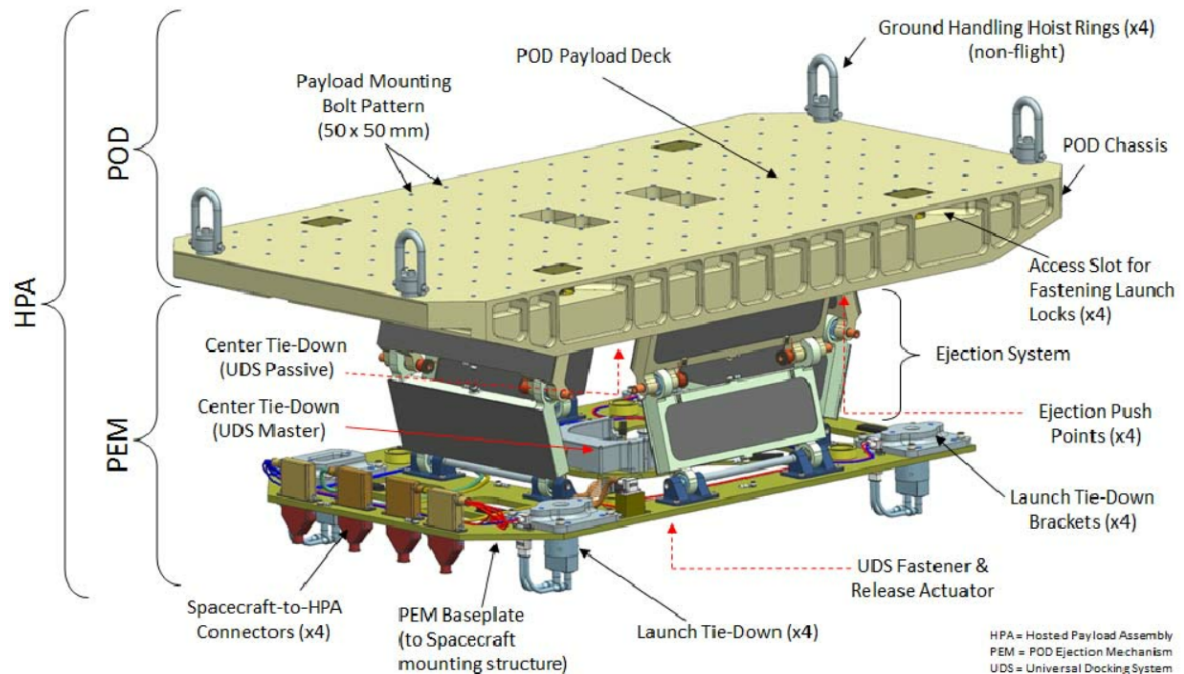


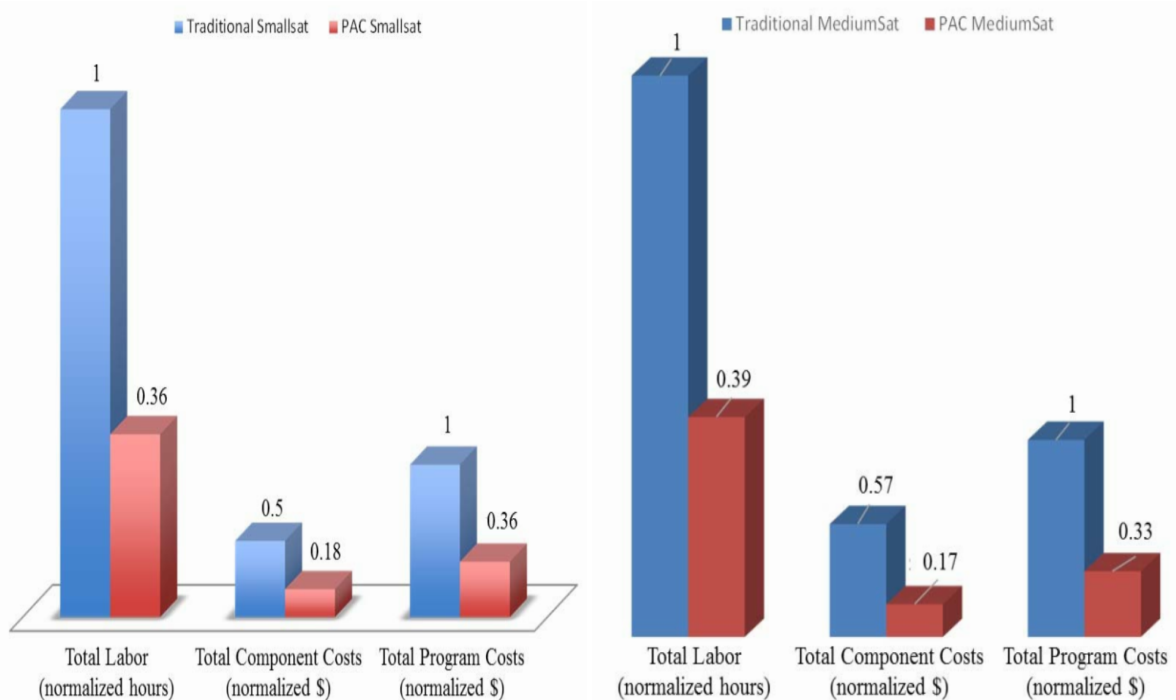
Figure 2-12: Schematic of Standard Hosted Payload Assembly (HPA), courtesy of [9]

This technology permits payload incorporation directly without the use of the POD chassis. The constraints on the payload for use of the HPA without requiring further mission specific analysis are as follows:

- Payload mass is within 15-60 kilogram margin.
- Payload center of gravity is within 15 centimeters of the POD chassis center and within 15 centimeters of POD Chassis Payload Deck.
- Payload is well fastened with respect to the POD chassis - one fastener per 5 centimeters of payload mounting edge distance.
- Payload has a fundamental frequency $f_n \geq 200Hz$ or $50Hz < f_n < 75Hz$.
- Payload footprint follows mass guidelines outlined: 15-30 kg corresponds to 20cm x 20cm / 30-60 kg corresponds to 30x30 cm.

A paper from 2015 delves into the final stages of project Phoenix, namely the Satlets and their design philosophy [9]. A satlet is defined as "a cellularized satellite architectural unit" designed with the express purpose of breaking the mass-performance relationship established by traditional monolithic space systems. The value proposition for such systems includes

decreased costs per kilogram (expected results are of an order of magnitude less than traditional spacecraft), increased redundancy and the possibility of achieving overall reliability comparable to traditional systems, whilst at the cell level reliability is much lower. The work here mainly focuses on homogeneous satlets, to be more specific, the Hyper-Integrated Satlet (HISat) developed by Nova Wurks Inc. The given design shows significant cost reductions compared to traditional design in all categories (labor, component and total program) for both SmallSat (less than 1500 pounds) and MediumSat (over 1500 pounds) classes, as illustrated in Figures 2-13a and 2-13b, for small and medium satellites respectively, courtesy of [9].



(a) Comparison between costs for traditional and HISat- (b) Comparison between costs for traditional and HISat-based satellite bus and its integration and testing (Small- based satellite bus and its integration and testing (MediumSat class))

Figure 2-13: Results of cost comparisons between HISAT and monolithic designs

The User Defined Adapter (UDA) developed by NovaWurks serves the purpose of exchanging power and data as well as employing required thermal management between the Satlet cells and payload. The capabilities of the UDA scale up as a function of number of attachments to the payload module (the more UDA connected to the payload directly, the higher the capabilities). Although the power and data capabilities are not specified, it is reported that the UDA is capable of driving up to 10 W of heat transfer at a 5 K temperature differential. As for the capabilities of the HISat cells, these can be classified into two types - one for actuation (carrying thrusters or reaction wheels and presents low computing capabilities) and one for attitude determination and computing (containing processors as well as any sensors necessary for the Attitude Determination and Control Subsystem - ADCS). Each cell includes a low-power main processor based on microprocessor technology with a projected performance range of 10000 MIPS, an initial memory capacity of 1 GB of RAM and 32 GB Flash Memory

storage.

In order to demonstrate the feasibility of this cellularized concept, [9] proposes a demonstration mission named the eXperiment for Cellular Integration Technology (eXCITe) whose primary goal is to advance the TRL of this technology to 9. The spacecraft comprises of a Package of Aggregated Cells (PAC) of twelve HISats hosting multiple payload interface experiments and is meant to be launched in Low Earth Orbit (LEO). Although the eXCITe concept is planned to be assembled on ground, it is mentioned that pre-launch assembly, or even on-orbit assembly is possible (using astronauts, teleoperated robotics or even self-assembly). [9] also explores future applications of Satlets, providing a few conceptual systems that make use of said building blocks, as illustrated in Figure 2-14.

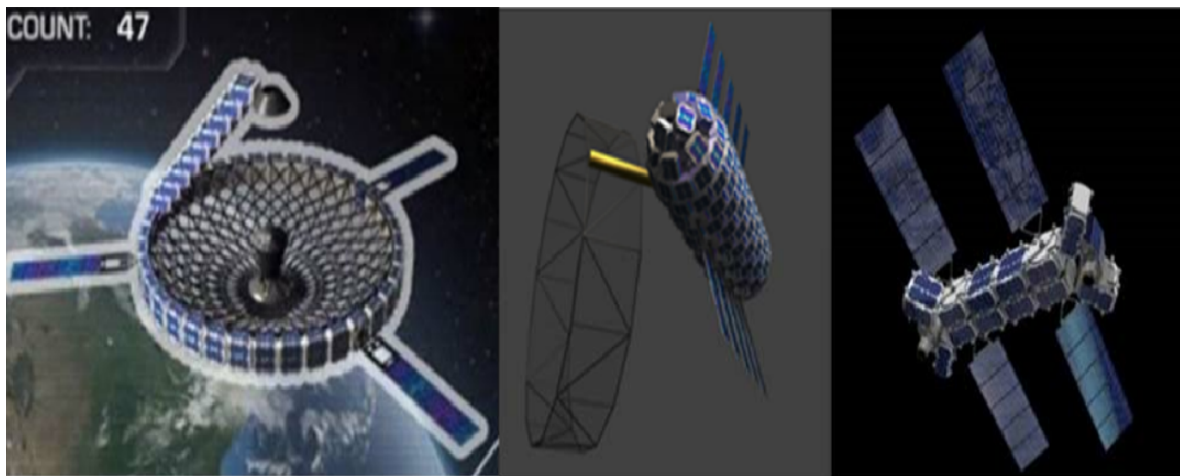


Figure 2-14: Conceptual Satlet-based systems, courtesy of [9]

2-4 "Jog" stage - Current State-of-the-Art

In this final stage of development of OOA, it was decided to include not only demonstration missions but also the current state-of-the-art standardized interfaces that enable such technology. In terms of demonstration missions, these can be classified based on the type of assembly used into two different classes: robotic free-flying assemblers and self-assembly.

The first example of robotic OOA is the Commercial Infrastructure for Robotic Assembly and Services (CIRAS) project, which employs two tendon actuated lightweight in-space manipulator (TALISMAN) arms, each outfitted with an Intelligent Precision Jigging Robot (IPJR). The TALISMAN arms were developed by NASA and leverage lightweight joints which provide a wide array of motions [34]. A composite version of this arm has reach and tip force capability comparable to that of the Shuttle Remote Manipulator System (SRMS) whilst occupying a seventh of the volume and weighing only a tenth of the mass. Up to date, two prototypes have been created to demonstrate the TALISMAN architecture, a 15m version of the arm and a 300m system assembled in-situ which enables advanced on-orbit assembly operations. Initial ground testing was performed so that target tracking, and robotic motion were demonstrated as illustrated in Figure 2-15, courtesy of [35], as well as the capability of assembling solar array elements on a truss structure.

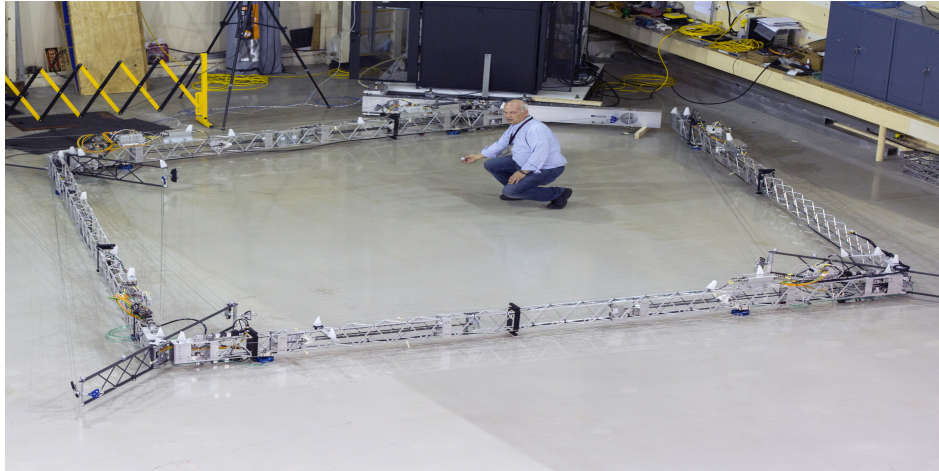


Figure 2-15: TALISMAN robotic arm ground testing

The IPJRs, as suggested by their name, primarily perform jiggling operations, however their functionality goes beyond that, as they have the added capability of providing support and location data on structural elements not only prior but during welding operations as well. As such, they can serve one of three primary functions: as a TALISMAN tool repositioning configuration, a separate end-effector, or even a relative positioning tool capable of assembling subsystems onto a truss structure backbone [34]. The accuracy and dexterity of this system was tested through experiments and assembly demonstrations [36] which served in identifying three factors that had major contributions in error generations:

- Welding was prone to positioning error, hence heat was being applied unevenly.
- Error correction algorithm did not correct errors that entered the boundary, instead resorted to the final pose near acceptable boundary.
- Solar panel weight caused unexpected compression in the joints once IPJR released them.

In order to solve these problems, in 2017, the NASA Intelligent Jiggling Assembly Robot (NINJAR 2.0), an enhanced version which made use of IPJR technology, was tested on the ground, demonstrating its ability to move and manipulate objects along a truss structure [37]. This was a first successful step necessary before the Orbital ATK team could integrate their Strut Assembly, Manufacturing, Utility & Robotic Aid (SAMURAI) into the process. This collaborative effort was needed as the intent was for the SAMURAI to pass strut elements to the future NINJAR 3.0 whilst also taking care of pose estimation and positioning of assembly elements. Figure 2-16 illustrates the results of the ground testing where NINJAR successfully build a cuboid structure:

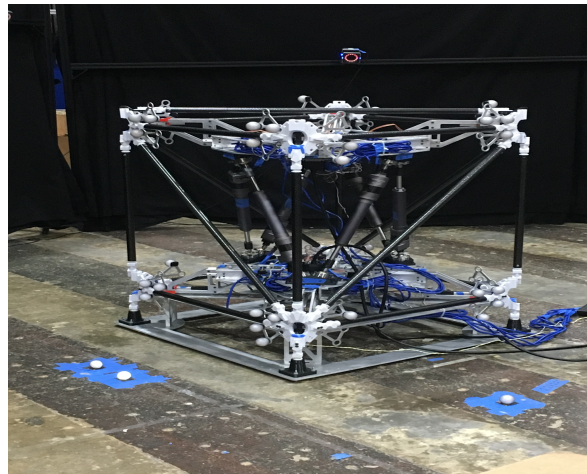


Figure 2-16: NINJAR ground testing, courtesy of NASA

Since the CIRAS project combines the long reach of the TALISMAN arm and the enhanced assembly and joining capabilities of IPJRs, [36] proposes the use of CIRAS to assemble a large Solar Electric Propulsion (SEP) vehicle, consisting of a bus and two solar array elements which would be assembled once injected on the desired orbit. The proposed concept investigated in [36] is a space tug with solar array elements capable of supplying between 250 kW and 500 kW to the ion engines used as payload.

The second representative mission that employs robotic operations is the Archinaut, or the Versatile In-Space Robotic Precision Manufacturing and Assembly System, a collaborative effort between NASA and Made In Space Inc. This project is essentially a free-flying system whose main goal is to combine precision robotic assembly capabilities with additive manufacturing. The advantages of this system would primarily be in mass optimization and risk reduction. The former would be achieved due to the fact that additive manufacturing on orbit would not require structural overconstraining necessary to withstand launch loads. The latter advantage arises from the use of common manufacturing materials, thus allowing robust systems build from components that are easily replaceable [38]. For fabrication purposes, the Archinaut employs DARPA's Scanning and Additive Manufacturing End-Effector (SAMEE) which also permits surface characterization, thus allowing for in-situ verification of the assembly process. It is important to mention that the TRL of Archinaut was raised to 6 on June 2017 following testing in representative vacuum and thermal conditions at the NASA Ames Engineering Evaluation Laboratory (EEL). These tests also marked the first and largest structure ever produced through additive manufacturing in relevant space conditions.

Visiting the Archinaut project website reveals two different possible applications of this technology in OOA implementations: the DILO and the ULISSES. The former stores deployable reflector panels during launch which are subsequently assembled and fixed in space. The edge alignment is verified through a laser based end-effector, and once all panels are fixed, they are deployed into their flight configuration and a boom is constructed using additive manufacturing. This is followed by the final step involving the in-situ verification for assembly flaws. Although this mission fits more thoroughly under the self-assembly classification, it was included here so as to avoid unnecessary confusion by quoting the Archinaut project in both classes. Conceptual illustrations of the DILO satellite are provided in Figure 2-17.

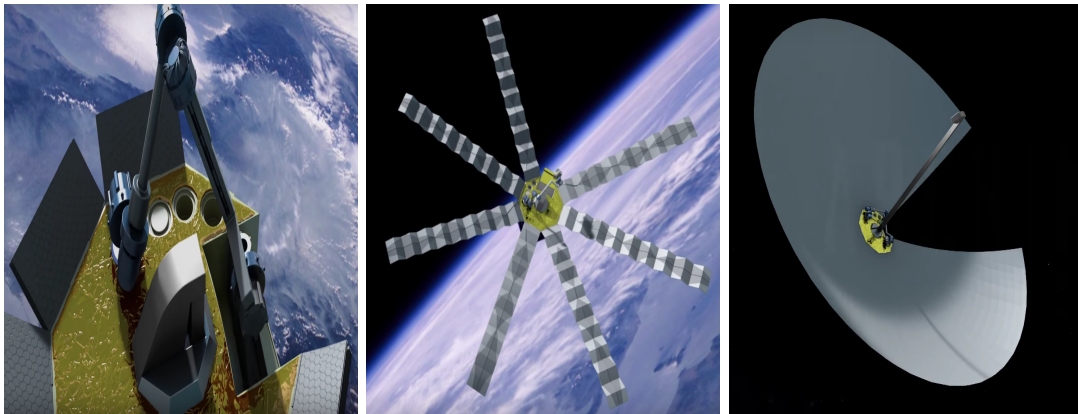


Figure 2-17: DILo conceptual illustrations of different assembly stages, courtesy of NASA/Made In Space

The ULISSES spacecraft on the other hand is a free-flying version of the Archinaut concept, employing three robotic manipulator arms to assemble the structural elements it manufactures in the space environment. The concept behind its operation can be structured into four actions: manufacturing of nodes, manufacturing of struts, mating of structural elements and autonomous assembly of structural elements into a truss, as shown in Figure 2-18, courtesy of [38].

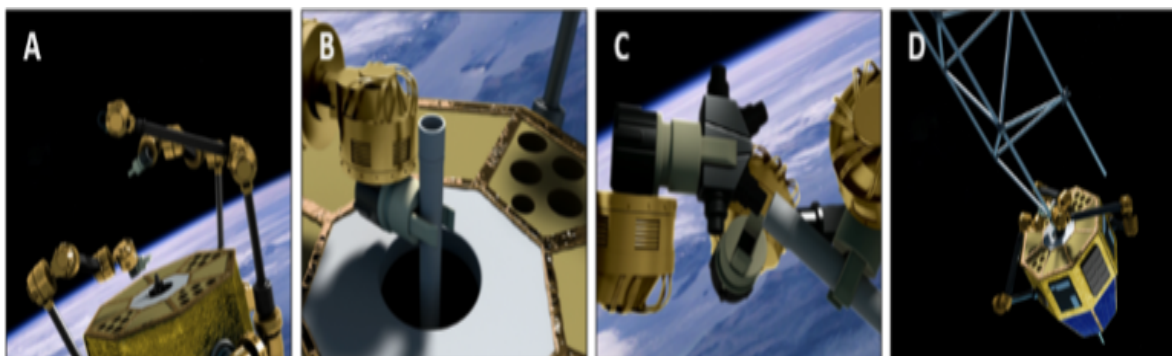


Figure 2-18: ULISSES manufacturing A) nodes and B) trusses, C) mating of structural elements, and D) truss assembly

Moving on to self-assembly concepts, the most promising mission is the Dragonfly project, a collaboration between NASA and Space System Loral (SSL) whose main goal is to enhance satellite capabilities by leveraging OOA technologies. The main application of this project is GEO communication missions. Initial ground testing was performed in 2017 [39] focusing on demonstrating the feasibility of robotic installation and reconfiguration of reflector antennae. The aim is to eventually include 3D printing capabilities (similar to Archinaut) so as to produce the antennae to be attached according to stakeholder requirements [40]. The main advantages of this methodology are upgradeability, reconfigurability and robustness in the communication domain. This technology promises to not only create but assemble antenna elements such that performance constraints can be satisfied in an active way. If higher data quality is required, an additional antenna can be produced and fitted.

Although Dragonfly provides some reasonable advantages for OOA, there are two distinct limitations when considering this implementation. Firstly, stringent collision avoidance and proximity operations requirements arise when attempting to utilize this approach for other assembly operations and the robotic manipulator employed for self-assembly has significantly reduced reach making it difficult to achieve scalability in design. Furthermore, the self-assembly itself poses the issue of creating value for a single satellite whereas free-flying robotic assembly can be deployed to aid various different missions, providing additional value with each successful use. In spite of these constraints with regards to scaling up to larger systems, reach and workspace restrictions, the Dragonfly project can at least produce enabling demonstrations for robotic manipulators meant for self-upgradeability. The envisioned concept of operations for Dragonfly is illustrated in Figure 2-19, courtesy of NASA.



Figure 2-19: Dragonfly concept of operation, courtesy of NASA

The last mission utilizing self-assembly comes from the field of small satellites in the form of the OOAN project developed by NASA [10], [41]. This mission revolves around the autonomous rendezvous and docking of 3U CubeSats through the use of permanent magnets. The spacecraft are equipped with Carrier-Phase Differential Global Position Systems (CDGPS) for use in relative position estimation, and a reaction control system (RCS) used in rendezvous and close proximity operations. The basic idea involves a leading satellite and a follower one, that engages its RCS once the two CubeSats are aligned along the local v -bar direction of the Local Vertical Local Horizontal (LVLH) frame (their Z-body axis). Four cold gas thrusters are strategically positioned along the spacecraft frames and provide the means of translational motion preceding the entry of the follower satellite into the sphere of influence of the leader's magnet. A docking schematic illustrating the OOAN concept is provided in Figure 2-20.

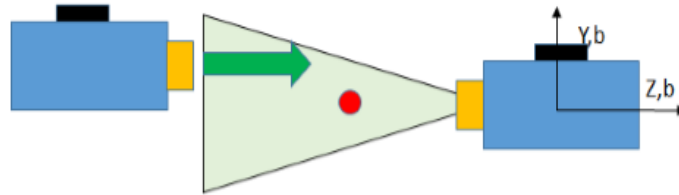


Figure 2-20: OOAN docking schematic, courtesy of [10]

The distinct advantage provided by making use of magnetic docking is the reduction in high precision sensors necessary during close proximity operations, which are the final and most risky part of the assembly process. There are also a couple of limitations involved, namely the limited range of the magnets as well as the fact that a certain distance is required between the two satellites for the system to work. The latter entails the fact that adding multiple such interfaces along different sides of each module may negatively affect the performance of the OOAN concept.

2-4-1 Current State-of-the-Art Interfaces

A total of four different standardized interfaces were selected as state-of-the-art based on their capabilities, as well as ease of assembly configurations:

- Hyper-Integrated Satlet (HISat) interface - created by NovaWurks, in collaboration with the Defense Advanced Research Projects Agency (DARPA), this project promoted the homogenous modularity approach to satellite design with the invention of the HISat. These small satellites are envisioned to be assembled on ground in various flight configurations depending on mission requirements. Although no information has been found on the actual interface design between the satlet elements, [9] does state that capabilities for fuel transfer exist at the least, with plumbing, tankage, valve and pump elements present in each HISat element. Furthermore, thermal load transfers are passive, being ensured through wall-to-wall conduction or radiation. It is also expected, based on possible Satlet designs in [9] that a mechanical interface exists, most likely some form of screw assembly based on the Satlet design illustrated in Figure 2-21, courtesy of [9]. In spite of the lack of information on actual performance parameters and physical structure, this project is mainly included due to the secondary interface created for the purpose of interfacing a payload with the HISat called the User Defined Adapter (UDA). This element is capable of driving up to 10 W of thermal load at a 5 K temperature difference, effectively including the payload into the overall system thermal control loop. A CAD diagram of the UDA and its associated block diagram are illustrated in Figure 2-22, courtesy of [9], [11].

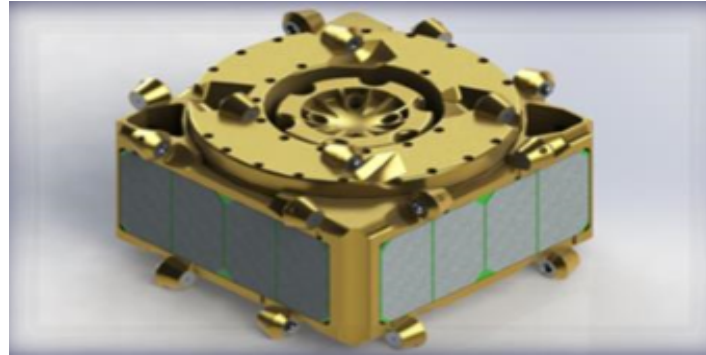


Figure 2-21: HISat design, courtesy of [9]

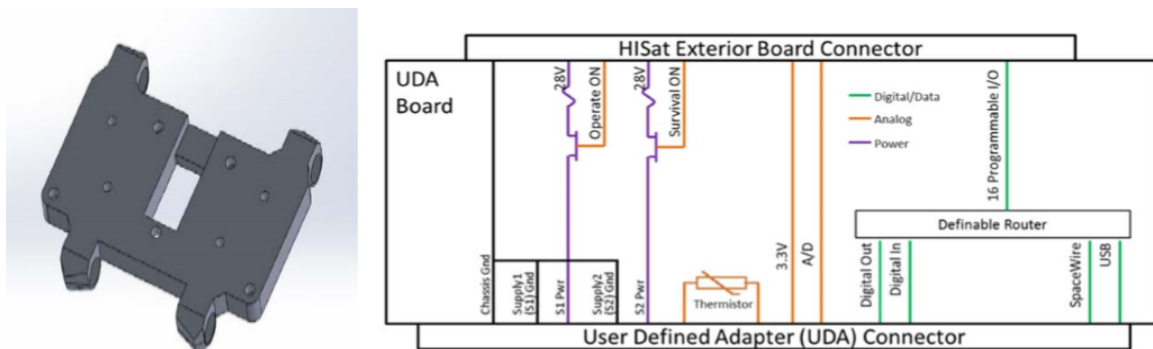


Figure 2-22: UDA plate CAD (left-hand side) and block diagram (right-hand side), courtesy of [11] and [9], respectively

- Self-assembling Wireless Autonomous and Reconfigurable Modules (SWARM) universal interface [12] - designed in the Space Systems Laboratory of the Massachusetts Institute of Technology (MIT), SWARM represents a test-bed for modular spacecraft systems capable of self-assembly and reconfiguration through the use of wireless communication. The interface that makes this possible is capable solely of mechanical locking and electrical transfer. This is due to the fact that ease of manufacturing is one of the design drivers in this undergraduate project. As such, fluid transfer was eliminated as a design requirement in order to maximize undergraduate involvement in both design and manufacturing. Furthermore, due to wireless communication being a baseline feature of the system, data transfer is deemed unnecessary for the interface element. With regards to structure, a CAD model is illustrated in Figure 2-23, courtesy of [12], showing the basic elements of the interface. One should note the pin head and corresponding entrance are both chamfered in order to reduce alignment constraints. The assembly method employed in the final proximity operations and eventual docking of two of these interfaces is electromagnetic attraction. For more specifications and design details, the interested reader is referred to [12].

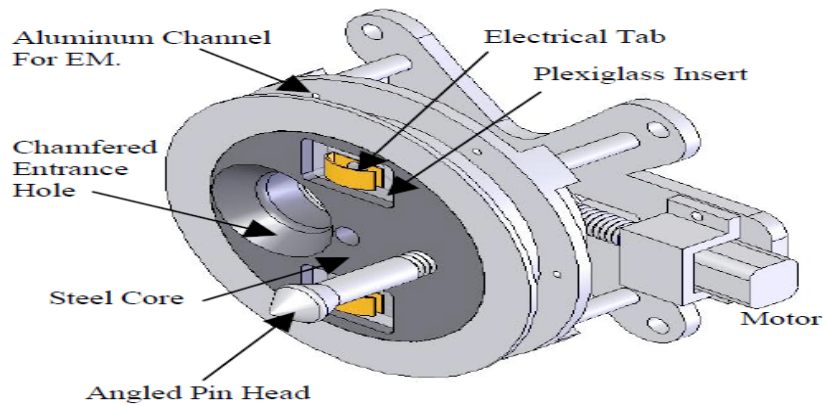


Figure 2-23: SWARM standard interface CAD, courtesy of [12]

- intelligent Building Blocks for On-Orbit Satellite Servicing ("iBoss") [13], [42] - a project funded by the German Aerospace Center (DLR), aims at exploiting the benefits of modular architectures and standardization with the aim of OOS operations. This endeavor focuses around two elements, functional modules and a 4-in-1 standardized interface design capable of docking as well as transfer of power, data and thermal loads. The design of the latter consists of a thermally conductive layer, an electrical interface made out of two isolated copper rings acting as positive and negative poles, a mechanical docking part and a central data link, as illustrated in Figure 2-24, courtesy of [13]. It is important to note that in this case, robotic assembly would be employed to fit the modules together, hence no magnetic element is present. On the other hand, a specialized tool tip is designed for the robotic arm that fits with the standardized interface and provides power to the module element whilst it is connected to the robotic arm. This is important as it explores the option of specific tool creation to fit the interface instead of creating an interface that will comply with current robotic standards.

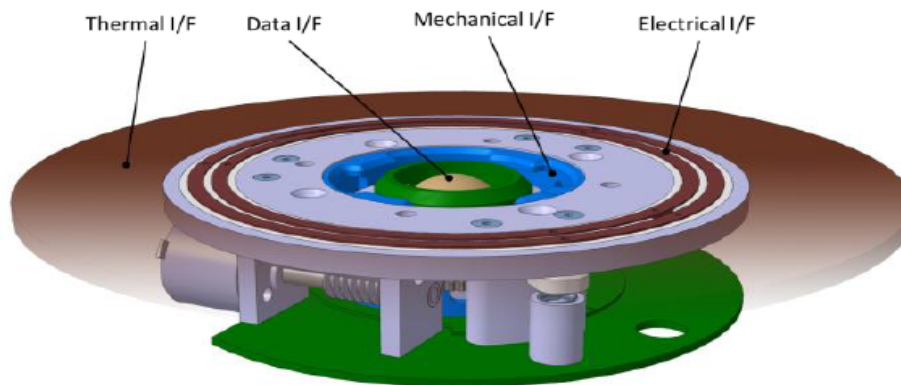


Figure 2-24: "iBoss" interface CAD, courtesy of [13]

- Standard Interface for Robotic Manipulation (SIROM) [14], [43], [44], [45]- a European project primarily developed in Spain, SIROM is a 4 in 1 multi-functional intelligent

interface that combines mechanical, electrical, data and fluid transfer capabilities in a single design. The applications of this project include OOS, OOA, refueling, payload upgrade or replacement, active debris removal and robot tool exchange. The idea behind the design of SIROM includes a combination of a custom end-effector and active payload systems which would enable the design of easily serviceable/upgradeable modular and re-configurable space systems. SIROM is equipped with redundant thermal patches, data and power connectors, and pin holes, such that four-degrees of axial symmetry are enabled. Out of all the options considered up until now, SIROM has the highest technical performance out of all interfaces considered. Figure 2-25 shows a schematic of SIROM with all relevant transfer connectors outlined.

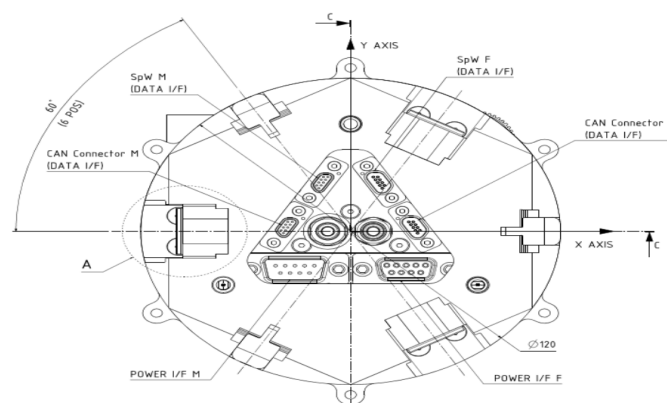


Figure 2-25: Schematic of SIROM interface design, courtesy of [14]

A summary of performance parameters and dimensions of all the interfaces described up until now is provided in Table 2-1, courtesy of [12], [13], [42], [14], [45]. The UDA (HiSat interface) is excluded from this as no information is available except for its dimensions.

Table 2-1: Main dimensions and performance parameters of existing SoA interfaces

SoA Interfaces	SWARM	iBoss	SIROM
Tension (max)	N/A	6000 <i>N</i>	1300 <i>N</i>
Compression (max)	N/A	6000 <i>N</i>	5000 <i>N</i>
Shear/Radial (max)	N/A	400 <i>N</i>	5000 <i>N</i>
Bending (X-axis moment)	N/A	400 <i>Nm</i>	150 <i>Nm</i>
Torque (Y-axis moment)	N/A	400 <i>Nm</i>	420 <i>Nm</i>
Bending (Z-axis moment)	N/A	400 <i>Nm</i>	150 <i>Nm</i>
Data rate	0.9216 Gbps	1 Gbps	0.322 Gbps
Electrical power transfer	N/A	5 <i>kW</i>	42 <i>W</i>
Voltage rating	5 <i>V</i>	100 <i>V</i>	20-34V (28V op)
Heat transfer coefficient	N/A	600 $\frac{W}{m^2 \cdot K}$	N/A
Operational temperature	N/A	-50/70 °C	-40/100 °C
Dimensions:			
Diameter	0.076 <i>m</i>	0.119 <i>m</i>	0.132 <i>m</i>
Height	0.038 <i>m</i>	0.048 <i>m</i>	0.1265 <i>m</i>

It will later become clear that the interfaces described here are of much lower dimensions than the interface that is designed as a result of this thesis, thus for a comparison in performance between said thesis result and the most high performance SoA interface (SIROM), a downscaled model is also produced and analyzed.

2-5 A different approach to modularity - Fractionated spacecraft concept

In spite of the existence and study of modular concepts for a significant amount of time, some researchers propose a different solution to make up for the disadvantages of traditional monolithic spacecraft: fractionated systems. This idea forgoes the necessity of mechanical interfaces, instead focusing on a cluster of free-flying modules which cooperate and communicate as needed during the mission's operational lifetime. The first mention of such a concept comes from a study from the Massachusetts Institute of Technology (MIT) in 2005 [46], which tries to assess the flexibility endowed by such a design. This paper tries to go a step further from classical modular systems by considering a spacecraft that is reconfigurable to a certain extent, thus being able to adapt to likely changes in requirements or even environment during mission operations. It is further postulated that due to the ability to reconfigure, add or exchange modules independently from others, fractionated concepts may offer the added advantage of reusability over several missions. As with modular concepts, a distinction needs to be made between homogeneous and heterogeneous fractionated spacecraft, of which the latter is addressed in said paper from MIT. The vision explored here is that a free-flying payload is supported by other (also free-flying) modules whose sole role is providing support, thus forming an on-orbit infrastructure.

In order to assess the flexibility of this concept, a multi-attribute trade-space exploration methodology is implemented, which has a customer-centric focus. The systems considered have the same performance levels and are built surrounding the same payload, thus what is examined is the variation in value delivered to the customer with respect to the following attributes: mass, maintainability, scalability, flexibility and responsiveness. The architectures investigated are, of course, defined by a series of design parameters which form the design vector. Subsequently varying these values results in the trade-space considered in this study. Although the mass is a clearly defined concept, the other four attributes are not, thus some definitions are provided for clarity:

- **Maintainability** = "the ability of a system to be kept in an appropriate operating condition" [47]
- **Scalability** = "the ability of a system to maintain its performance and function, and retain all its desired properties when its scale is increased greatly without having a corresponding increase in the system's complexity" [47]
- **Flexibility** = "the ability of the system to be modified to do jobs not originally included in the requirements definition" [48]
- **Responsiveness** = "the ability to meet changing requirements quickly" [49]

These are evaluated based on the response the system shows to a change, further divided into three criteria: change type, response type, and response time. This leads to the classification illustrated in Figure 2-26, courtesy of [46].

	Change in requirements			Change in conditions				Type of response				Time of response			
	No change	Higher performance	New function	No change	Internal	Interface	Environment	No active response	Reconfiguration	Subtraction of elements	Addition of elements	Exchange of elements	Short-term	Medium-term	Long-term
Maintainability	X				X							X	X	X	
Scalability		X		X					X		X	X	X	X	X
"Flexibility"			X	X					X	X	X	X	X	X	X
Responsiveness		X	X	X					X	X	X	X	X	X	

Figure 2-26: Definition of attributes

The architecture trade space investigated is reliant on four design parameters: fractionation level, technologies used, number of modules, and subsystems contained therein. Additionally, three different types of missions are investigated: navigation, communication and sensing. The cost is also considered, the estimations used being based on subsystem masses [50]. Finally in order to evaluate each of the four attributes defined previously, three distinct scenarios are envisioned:

- Scenario 1 - An internal failure occurs in the system. This is used to evaluate maintainability.
- Scenario 2 - An increase in level of performance is required. Based on this scalability can be quantified.
- Scenario 3 - A new function is required of the system (essentially a change of payload). This is used to evaluate both flexibility, as well as responsiveness.

The results of this study show that the effect of fractionation on mass has a tendency to induce mass penalties. The sensing mission is the only one that shows slightly less mass than traditional options, whereas on the other end of the spectrum, the navigation mission shows a mass penalty between 220% and 300%. An interesting conclusion with regards to this is that the fractionation of the power system produces the largest penalties, mainly due to additional hardware required both for power transmission and power generation. On the other hand, the grouping of propulsion and attitude control subsystems into the same module seems to lead to improvements in mass.

Whereas some minor improvements were registered with respect to mass in a specific mission type and fractionation architecture, fractionation only shows penalties when considering

costs, with the lowest being registered for sensing missions (190% - 250 %), and highest for navigation concepts (270% - 350%).

When considering maintainability, the results are fairly easy to predict - the lower the mass and cost of the module containing the subsystem that registers the internal failure, the lower the penalty for replacement as opposed to monolithic spacecraft where the whole system would need to be replaced.

As for scalability, at complete fractionation the smallest payload module corresponds to the communications mission, weighing approximately 45% of the mass of the monolithic spacecraft, while the highest payload module with respect to weight corresponds to the sensing mission, at 47% of the mass of the monolithic spacecraft. Based on this the costs for upgrading (effectively replacing) the communications mission payload module are less than 40% of the cost of the monolithic spacecraft.

When considering flexibility, the best results are achieved for the communications mission which results in the most light-weight payload module (30% of whole spacecraft), and the worst correspond to the sensing mission (45%). This results in a cost of only 25% that of a monolithic spacecraft for the communications payload of a fractionated architecture.

Finally, the shortest cycle with respect to the responsiveness criterion is registered for the communications mission, evaluated at 30% that of the monolithic equivalent system.

This study thus proposes that valuing the latter four attributes higher than traditional spacecraft design drivers such as mass and cost will lead to the preference of fractionated systems over monolithic ones. It is further mentioned that obvious technical risks exist for such concepts, however many advantages and possible synergies with other concepts could potentially outweigh the disadvantages of fractionated systems.

Following this study from MIT, in 2006, scientists from the Defense Advanced Research Projects Agency (DARPA) publish a paper describing the value proposition of fractionated spacecraft [51]. They identify a series of problems with traditional spacecraft designs such as the high costs and long timeframes associated with creating a system that can deliver a certain capability robustly in the face of uncertainty, as well as the complexity and trends that stem from this. When considering monolithic designs, an abundance of uncertainties is identified, from technical ones, such as the change in demand for capabilities during a spacecraft's operational lifetime caused by the long time frames in production as well as long life cycles such missions are designed for, to associated cost, schedule and value uncertainties [51], [49]. To tackle these, classical design dictates a need for robustness which in turn creates a more complex system. Furthermore, in order to counter any failures or uncertainties that the mission may deal with, extra fail-safes and back-up systems are added, which again increase the overall complexity of the system. This has led to a requirement-centric minimum-cost approach which is fairly typical of satellite design at the time of writing. DARPA proposes that a change to fractionated spacecraft designed and procured using a value-centric mindset could be a potential solution.

The first advantage proposed is the ability to adjust the capabilities of a fractionated spacecraft during its lifetime, instead of projecting high requirements years in advance at the start of the design. Such incremental and scalable deployment could have a significant impact on the business cases of various mission types. The second advantage offered relates to the option of substituting, removing or augmenting an existing module in such a system, or even

utilizing a module in a different mission altogether. This is expected to provide flexibility throughout the operational lifetime of the system, which in turn adds robustness. The deferral of specific design decisions to later in the production stages of such a system is also quoted as an advantage, the comparison being made to acquiring and holding options in the financial sector, thus not only diversifying risk but also reliability. In other words, the value proposition proposed by DARPA [51] can be classified into four distinct concepts:

- "Portfolio Optimization - Diversification of Risk & Reliability Tailoring" - this refers not only to cost variance expected for total launch costs but also to the risks associated to potential launch failures, or subsystem failures. Essentially compartmentalizing the system leads to reduced costs and scheduling penalties when replacing said module instead of the system as a whole. It is also considered that in a homogeneously fractionated system, a module failure does not mean a complete loss but a reduction in overall capability.
- "Spatial Distribution - Eliminating Fragility of Complex Systems" - in essence the distributed nature of such systems would reduce the risk as well as impact of any failures. Furthermore, since some requirements are directly dictated by the payload itself, there will be less strict equivalents for the non-payload modules, leading to simpler subsystems. When considering classified payloads, these can be developed separately from the rest of the spacecraft, thus reducing the associated security costs.
- "Cost Considerations" - this includes all costs facets discussed previously, from launch, to maintenance, impacts caused by upgrading or changing the design, as well as diversification of component choices.
- "New Paradigms" - a number of concepts are explored here, from the potential implementation of short design-build-test and design-build-fly development cycles, to fractionation acting as an enabler for responsive space launch viability both economically, as well as from the point of view of requisite launch rates and volumes. Taken to the extreme, this concept could supersede the need for large rigid structures, instead using a fleet of utility modules as support, thus only requiring the payload module as the main cost for the mission stakeholders.

This proposition is followed by a mapping of the main issues preventing the implementation of fractionated architectures: value-centric acquisition, cluster flying, data transmission, fractionated navigation, distributed computation and data resources, power transmission, force and torque transmission, and finally a demonstration program [51], [49]. These lead to the conceptualization and proposal of System F6 (Future, Fast, Flexible, Fractionated, Free-Flying Spacecraft). The preliminary design phase of this project was awarded to four separate competing entities: Boeing, Lockheed Martin, Northrop Grumman and Orbital Sciences, starting in February of 2008 and concluding in February of 2009 [52]. This phase mainly revolved around the development, validation and demonstration of a Value-Centric Design methodology and associated tools that could support the design of an optimized fractionated architecture.

This methodology was designed with the primary aim of quantitatively comparing value and cost of traditional spacecraft designs with systems built to adapt to new requirements, and

that are less likely to experience cost growth due to unforeseen or undesirable circumstances. As such a number of key definitions is given to support this framework:

- Value-Centric Design = "The incorporation of value metrics, in particular net value and the variance in net value, into Systems Engineering"
- Flexibility = "The ability of a system to change on demand. This incorporates scalability, evolvability, maintainability, and adaptability"
- Robustness = "The intrinsic ability of a system to maintain functionality in response to unforeseen circumstances. This incorporates reliability, survivability, resistance to fragility, and fault tolerance"
- Responsive Space = "The capability of space systems to respond rapidly to uncertainties, including technical uncertainty, environmental uncertainty, demand uncertainty, requirements uncertainty and funding uncertainty"

Using this framework, rather than minimizing risk, a Pareto frontier of maximized risk-adjusted net values will be generated for possible investments. Similarly, each design choice will result in an associated variance in value and cost. Thus risk mitigation is also included in the design trade process instead of being a separate entity, as mitigation strategies are selected to trade net value against reductions in the variance of net value. With respect to acquisition, the choices that maximize net value for a given cost are preferable. This process is explained in an overly simplified manner here, however much more detail is given as to the inner workings of such a methodology in [52]. The results of Phase 1 of the F6 program included the development of various tools and models to quantify net value which can be classified into three types: cost, benefit and risk evaluation models.

The first type no longer consist of solely point estimates, but incorporate probabilistic simulation aspects which account for launch failures, development delays and component failures whilst on-orbit, which enhance the familiar component-level manufacturing, development, launch and post-launch system operation cost models used in monolithic designs.

As for the benefits models, a common measure was used as a basis for all models developed by the different teams, namely the timeframe during which the spacecraft was operational transmitting data to the ground. Whilst the Orbital Sciences Team focused on the pricing for the data feed based on market dynamics, Boeing approached this problem by using a conservative estimate of system cost as the pricing of data, ensuring a reasonable profit margin. Lastly Northrop Grumman estimated the value of service provided by their spacecraft using Multi-Attribute Utility Theory.

With regards to risk evaluation models, all teams used Monte Carlo simulations as a basis, but decided to highlight their results in very different ways. Whilst Lockheed Martin compared the expected net present value of alternatives with the standard deviation of net present value, Orbital Sciences focused on the net present value versus cost, and Boeing plotted benefit versus cost such that the benefit to cost ratio becomes a slope line between design point and origin. Finally, Northrop Grumman chose to showcase dimensionless utility as a function of cost.

Once this groundwork quantifying net value and its variance was implemented each team went on to optimize their fractionated concepts. The design space was generated differently based on each team's design logic - whilst Boeing parametrized said space and generated a factorial set of designs, Lockheed Martin employed MIT's Generalized Information Network Analysis tool, and Orbital Sciences resorted to Georgia Tech's GT-FAST automated design tool. The optimizer software tools themselves varied greatly from team to team as well. Lockheed Martin continued to use MIT developed frameworks, in this case Space Lab's Time-Expanded Decision Network, Orbital Sciences developed their own custom software dubbed PIVOT, and Boeing visually picked out the best design plot based off of a risk-adjusted benefits to cost plot.

The conclusions of this phase can be summarized as follows:

- Whilst on-orbit servicing can definitely provide value, deterministic comparative cost analysis does not make this readily apparent. As such not only must benefits be estimated along with cost, but also a probabilistic analysis is essential.
- Several configurations with higher numbers of modules (or higher degree of fractionation) were estimated to exceed the cost of traditional spacecraft, on the other hand all fractionated configurations provided better utility in comparison.
- According to Boeing an eight module architecture showed higher benefit to cost ratio in spite of having a higher cost than monolithic systems. Furthermore it was indicated that the steepest jumps with respect to benefit to cost ratio were registered when separating into two or three modules.
- Lockheed Martin registered a 10% - 20% increase in expected net value when compared to traditional spacecraft when using two or three modules.
- Two teams noted the critical importance of technology readiness level (TRL) in module configuration. Boeing's results found that isolating low TRL components in isolated modules improved the overall value of a system, whilst Lockheed Martin found that it is good practice to include similar TRL components in the same module as compared to spreading them across multiple modules.
- Fractionated architectures overall showed less risk when faced with uncertainties such as random changes in environment or even in requirements.

Based on all of these results it was proposed to refine the Value-Centric Design methodology in Phase 2, whilst also delving more deeply in the areas of risk management, value-based acquisition and subcontracting, dynamic project management and benefit assessment [52]. A paper followed shortly after this describing how DARPA intended to bridge the results of their work in Phase 1 to a potential plan for transitioning into reality [53]. This work not only considers the four key enabling technologies necessary for F6 to be a success (Networking, Wireless Communication, Cluster Flying and Distributed Computing) but also summarizes work already performed in these sectors of technological development. Following some demonstration of cluster flight by DARPA's Orbital Express program as well as NASA's Demonstration of Autonomous Rendezvous Technology (DART), the next step taking place at the time of writing of [53] was the testing of the Synchronized Position Hold Engage Reorient Experimental

Satellites (SPHERES) developed by MIT, being used on the ISS. The conclusion of this paper is that in order to actually be able to proceed with a full scale version of Project F6 an on-orbit demonstration involving microspacecraft would be critical, albeit not the most optimal envisioning of fractionated spacecraft concept.

In spite of this promising start for Project F6, DARPA cancelled it in 2013, however several works were published thereafter that showed that this in no way was a waste of time, and that a lot of the research done on this concept could be applied or repurposed for different projects. One such paper explores the concept of optimal modularity of a fractionated spacecraft, even developing a model based on a simplified F6 architecture [54], whilst yet another paper published in 2014 verifies the Cluster Flight Application (CFA) developed by DARPA, using MATLAB simulations and high-fidelity embedded FSW simulation [55]. Even more recently, in 2018, [56] showcases the advantages of the Adaptable System Design and Analysis (ASDA) tool developed during Project F6, as a way to convert an advanced technology into components, bus or launch vehicle and then propagate that change into the operation and cost arena [56]. Such a tool could potentially improve concept development, planning and fast-track the implementation of novel systems.

Interest in the topic of fractionated architectures has not completely died down with the ceasing of Project F6, as even other sources aside from DARPA investigate enabling technologies for such concepts, such as hardware-in-the-loop simulation systems for fractionated spacecraft clusters [57] which are not exclusive to this topic but can ultimately be applied to proximity free-flying spacecraft as well. Finally, for a more in-depth discussion on what distributed satellite systems have to offer, including the trends, challenges and prospects for the future, the interested reader is referred to [58] which not only synthesizes work done on fractionated spacecraft but aims at providing an overview of all progress achieved in the fields enabling such concepts as well.

2-6 Value proposition and current needs of OOA

On-orbit assembly offers a range of advantages, both in the short-term and the long-term. The Space Science and Technology (S&T) Partnership Forum established in 2015 has attempted to quantify some of these benefits as well as tackled the main needs to be satisfied so that OOA is a success in two major works [59], [18]. The first study deals with the value proposition, strategic framework as well as defining the capability needs required for OOA to succeed, whereas the latter treats these needs in a more organized manner, mapping and prioritizing them with the goal of near-term demonstration in mind. The structure through which the S&T develops a value proposition for OOA starts with identifying the stakeholder's and their expectations:

- Resilience
- Military utility
- Upgradeability
- Scientific progress

- Space exploration
- Persistence

Using these as input, the S&T define an enterprise value as a function of cost (reduction), performance (increase) and time contribution. The latter refers to reduction in technology refresh time. This value is guided by Equation 2-1, courtesy of [59]:

$$OOSEnterpriseValue = \frac{f_p(\text{performance})}{f_c(\text{cost}) \cdot f_t(\text{time})} \quad (2-1)$$

The final step involves determining the alternatives for collaboration so as to deliver said value. Four common stakeholder goals were selected based on multiple technical interchange meetings (TIMs):

- Supports near-term demonstration
- Affordable
- Lower cost
- Industry transitioning

The results of this process lead to five main design drivers: stability, assembly, upgradeability, scalability and interfaces. Furthermore a first draft of capability needs as well as their definitions is compiled in [59], structured as follows:

- Deployables
- Structural Assembly
- Connecting Ancillary Utilities
- Ability to disjoin
- Sensing, Modeling, Simulation, Verification
- Interoperability
- Automation/Autonomy
- Precision
- Adaptive Correction
- Design
- Tunability
- Stability
- Standard Interfaces

- Docking/Berthing

Each of these classes have sub-needs defined, however due to space concerns, these are not included here. As such, the curious reader is referred to [59] for more details.

The second study from S&T firstly defines costs associated with demonstrating the needs described above. Starting from the identification of three main cost factors, namely payload, payload certification and payload launch mass costs, [18] defines a different framework for evaluating cost since the scope of said study did not allow for direct quantification of said costs in dollar values. As such the following classes are defined: none, minor, significant and major. Using these classes weights and scores are given to the needs enabling OOA. Furthermore, S&T compile a list of potential demonstration platforms such as the ISS, the James Webb telescope, Restore-L, Robotic Servicing of Geosynchronous Satellites (RSGS), and Commercial Infrastructure for Robotic Assembly and Servicing (CIRAS) missions. Quantifying these platforms using Quality Function Deployment (QFD) techniques, five distinct levels of readiness are defined: none, minor, significant, major and cannot support. Following this, three main scenarios are defined for the application of OOA:

- Large Space Telescopes
- Space Vehicle Hub and Transfer Facility
- Communications Hub

Interestingly enough an earlier paper published in 2016 [60] investigates commercial applications of OOA and identifies a case that is not present here which they present as a low hanging fruit - OOA of Radio Frequency Apertures. This presents a similar operational case as space telescopes but with lower requirements with respect to alignment tolerances. The results of the S&T analysis, courtesy of [18], consist of a list of twenty capability needs ranked from highest to lowest priority, as follows:

1. Fail-safe modes of behavior on failure detection
2. Modular design
3. Soft docking/berthing of modules
4. A limited number of standard mechanical, electrical, thermal and fluid connection approaches with well-characterized properties
5. Standard protocols and ports to accommodate visiting vehicles and communication traffic
6. Means of verifying the continuity of interface connections/disconnections
7. Design for serviceability
8. Modeling and simulation for verification and validation
9. Modeling and simulation for assembly sequencing/planning

10. Ability to reversibly assemble structural, electrical and fluid connections
11. Standard but secure communication protocols to accommodate interaction with other (TBD) associated systems
12. Quantitative performance prediction for autonomous systems
13. Design for assembly
14. Ability to assemble high stiffness structures
15. Known precision limits of any and all assembly agent elements across the assembly site's environmental envelope
16. Robotic assembly with joining
17. Ability to route electrical power and data across assembled joints
18. Ability to disconnect structural, electrical and fluid connections without propagating damage to other system components
19. Ability to route fiber optical conductors across joints
20. Intelligence to make stereotyped decisions correctly without human input

A full list of the prioritized enabling capabilities as well as their scores is offered in Appendix A of [18] however they will not be included here. What is important to note is that, out of the priority list above, the interface design aims to satisfy quite a number of these, namely numbers 2, 4, 6 (to a minimal extent), 7, 8, 10, 13, 14, 17 and 18. As such, the interface design presented in this work aims at addressing half of the top twenty needs prioritized by the S&T study.

Although this thesis only focuses on OOA, it is important to note that this is an enabling technology for an even higher tier step in space development, space manufacturing. Interestingly enough, [39] defines a couple of near-term business cases for such technology: Nanosatellite Trusses and Antennae in LEO, and GEO Satellite Solar Panels and Structure Repairs. This is included not only for completeness but to give a glimpse of what the next future step could be should OOA become a common design methodology.

Need Analysis on Space Telescopes for OOA

This chapter details the need analysis of space observation missions meant for on-orbit assembly, which is used as a basis for generating the detailed design requirements for the inter-modular standard interface. Section 3-1, the reasoning behind the choice in mission type and assembly type is discussed. Based on technological trends observed from current and future space telescope missions taken as reference, a preliminary list of top-level requirements is defined in Section 3-2. Subsequently, the preliminary sizing of the optics system is performed in Section 3-3, where a decision is made on the degree of modularity of the optics, as well as the way in which the system will be broken down into modules. Section 3-4 discusses the envisioned spacecraft configuration, expanding the trait of modularity from only the optics, to the whole system. This is followed by Section 3-5 which discusses the choice of orbit. Using the selected orbit, the perturbations expected are discussed in Section 3-6. The requirements imposed by launcher selection are discussed in Section 3-7. A first-order estimation of the temperature of equilibrium for the given orbit is made in Section 3-8. Using the number of modules as a basis, Section 3-9 estimates the housekeeping data required for such a spacecraft. Section 3-10 formulates some requirements and guidelines for the design of the assembler. Due to the fact that focus will be on the inter-modular interface, the design of the assembler subsystems will not be pursued in this work, however some capabilities with respect to the robotic system will be specified. Finally, an overview of the concept of operations for the whole system as well as a definition of its structure, and functionality of the interface to be designed is presented in Section 3-11.

3-1 Mission and Assembly Type

Through the literature study it was observed that there is not only an increasing interest in OOA [59], [18], [60], but also a desire for increasingly larger space telescope apertures [61], [62], [63], [64], [65], [66]. Furthermore, at this point in time, with the launch of the JWST

[67], [68], [69], [70], the current size limit permitted with existing launch vehicles has been hit. This is confirmed by the NASA iSAT study [71], [72], [73], [74], [75] which also estimated that if one were to consider future launchers (those existing at a conceptual level at present), the maximum size of aperture diameter that could be launched would be 15 meters. As telescope performance is directly correlated with aperture size, coupled with the limitations of current launchers with respect to spacecraft size, one can assume that applying OOA technology to space telescopes is one of the only ways (aside from OOM) that could create very large scale space observatories. As such, it is henceforth assumed that the type of mission that is best suited for analysis when using OOA would be observation missions with large aperture sizes.

Now that the mission type has been chosen, it is important to consider the type of assembly to be used on orbit as this influences the requirements of the modules themselves, potentially influencing the interface design to a certain extent. The two main options considered here are self-assembly and a free-flyer assembler spacecraft. The critical challenges raised by both concepts are workspace limitations (or reach), as well as proximity operations and the sensors required to perform them. In spite of advances in robotic arm technology [76], [26], [28], [27], [7], there are limits to the range of motion of such systems (in other words the size of the workspace). The literature study found that the TALISMAN arms have the longest reach up to date [34], namely 15 meters when fully extended. Although this constitutes a feasible solution for self-assembly, it is assumed that, at the maximum reach of 15 meters, the TALISMAN arms have a limited performance with respect to workspace size. This means that, assuming the robot arm is mounted at the center of the structure, a maximum size of under 30 meters diameter would be achievable using this system. This constitutes the current technological limitations with respect to the reach a static self-assembly system can achieve. Based on this information, it can be concluded that for structures exceeding that scale, self-assembly would only be possible either through the use of robotic systems that have not been designed or tested yet (which presents a high technological risk) or by moving the mounting point of the robotic arm as the structure gets assembled. This involves some degree of risk as detachment of a critical part used in assembly can, in the worst case scenario, result in the complete loss of this system or failures caused by reattachment at a different location. The loss of a system as critical as this during OOA would spell the end of the mission, hence this is considered a critical disadvantage of self-assembly. Furthermore, whilst still exploring the topic of workspace limitations, the positioning of the mount for the robotic arm drastically affects the position of the workspace thus, being able to move said mounting point may offer advantages in specific proximity operations (e.g. a more favorable angle under which robotic assembly would become easier). Due to this fact, it is assumed that a free-flyer system offers distinct advantages during proximity operations in comparison to self-assembly.

In addition to the limitations of reach one can also consider the impact launcher limitations have on the design of a space telescope to be assembled in orbit. When considering self-assembly with a system similar in performance to the TALISMAN robotic arm, it can be assumed that having this subsystem already assembled to a specific module during launch raises extra considerations with respect to launcher volume and weight limitations, as well as the need for sufficient structural strength to survive the launch loads. If the arm is packed separately, although volume and weight will be lower, more stringent requirements will be imposed on the rest of the system (i.e. modules) so that these can rendezvous and assemble with the robotic arm. This creates another assembly phase that is just as, if not more critical than the assembly of the full telescope, as having a separated robotic arm with no

power and control systems attached raises an entirely new issue of assembly. On the other hand, when considering the free-flyer option, all the sensing capabilities needs and associated requirements can be passed on to the assembler spacecraft instead of the modules. This may lower the size, weight and volume of specific modules, as well as their design cost by effectively switching the extra systems necessary to the assembler satellite. Of course, this would mean that said spacecraft would have some limitations with respect to launch vehicle selection, however it would also require a smaller robotic arm due to the possibility of moving around the structure to be assembled. Last but not least, when considering costs, the option of using the assembler for multiple missions will inherently add to the value of the system and potentially offset some of the production costs. If the self-assembly option is chosen, using this system to assemble a different mission comes with the inherent risk of compromising both missions due to the proximity required during the assembly phase (in other words the reach limitations mentioned previously). This is considered to be an unacceptable risk for any potential stakeholder that would make use of such a system. On the other hand, a free-flyer assembler satellite can be equipped with sufficient fuel to actually service multiple missions, thus offering the opportunity of cost reduction. As such, due to the desire to minimize the impact of assembly choice on the space telescope system, reach and workspace limitations, as well as the potential cost savings involved in this choice, it is assumed that a free-flyer assembler spacecraft is the best option to use for the interface design detailed in this work.

3-2 Top-level mission requirements

In order to create a flexible interface that can be used for a range of future applications in modular space telescopes, it is important that it satisfies a wider range of requirements than those prescribed by a singular mission design. The goal is not to focus on a point design, but rather to find a reasonable range of expected requirements of space telescopes to be launched in future years. Towards this end, a number of existing, planned and conceptual missions involving space observatories (Hubble [21], Spitzer [77], Kepler [78], Herschel [79], Transiting Exoplanet Surveillance Satellite or TESS [80], James Webb [68], [69], Wide-Field Infra-Red Survey Telescope or WFIRST [81], and ATLAST [61], [62], [63]) were compiled and evaluated based on their size, electrical power, communication and instrument characteristics, as illustrated in Tables 3-1 and 3-2.

Table 3-1: Characteristics of reference space telescopes - Part 1

Reference mission	Power	Data rate	Number of pixels	Aperture size	Year of launch
Hubble Space Telescope (HST)	2100 W	1.908 Mbps	35 Mpix	2.4m	1990
Spitzer Space Telescope	375 W	2.2 Mbps	0.26 Mpix	0.85m	2003
Kepler	615 W	4.33 Mbps	95 Mpix	1.4 m	2009
Herschel Space Observatory	1200 W	130 kbps	648.3 kpix	3.5 m	2009

Table 3-2: Characteristics of reference space telescopes - Part 2

Reference mission	Power	Data rate	Number of pixels	Aperture size	Year of launch
Transiting Exoplanet Surveillance Satellite (TESS)	415 W	100 Mbps	16 Mpix	N/A	2018
James Webb	2000 W	2.723/28 Mbps	57 Mpix	6.35m	2021
Wide-Field InfraRed Survey Telescope (WFIRST)	3200 W	0.9 Gbps	288 Mpix	2.4 m	2025
Advanced Technology Large-Aperture Space Telescope (ATLAST) 9.2	5700 W	600 Mbps	1-1.6 Gpix	9.2 m	2020 decade
ATLAST 16.8	≈ 10000 W	600 Mbps	1-1.6 Gpix	16.8 m	2020 decade

A few observations can be made when grouping together some of the missions in Tables 3-1 and 3-2. First of all, the final two entries refer to a NASA project that considered space observatories of multiple sizes, making use of the same baseline instruments, hence the numbers correspond to the aperture sizes. When considering this fact, one can draw the conclusion that scaling up the system would increase the average power required. However, considering only the instruments are the same, it can be inferred that most of the extra power requirement will come from the attitude determination and control, propulsion (due to the use of ion thrusters which consume electrical power), and thermal subsystem. Another potential contributor is the power subsystem, under the assumption of higher power dissipation with increasing size, however this is expected to be much lower than the contribution of the aforementioned subsystems.

A second important observation can be made when considering the WFIRST mission, which makes use of a very similar optics system as the HST, with the exact same primary mirror diameter, but with state-of-the-art instruments. This means that when comparing the two, one can determine the effect more performant scientific instruments have on the requirements of the spacecraft. In this case, the power increases by more than 50%, and the data rate as well as number of pixels increase by at least one order of magnitude. This hints at the fact that the better the instruments, and the higher their pixel count, the higher the corresponding power usage and data rates, however this remains to be confirmed by evaluating the whole data-set.

Finally, when perusing the data rates, the observant reader may notice that both the Kepler and the James Webb telescope have two entries for data rate, the lower one corresponds to the scientific data production, whilst the higher value is related to the rate at which data is

transmitted back to Earth. The highest of these will be used in the evaluation. This is due to the fact that there is no guarantee that an interface will not be present between the data storage system and the communication subsystem. Since in both cases the higher value is at least an order of magnitude higher than the data collection rate, Chapters 4, 5 and 6 will investigate the idea of creating a range of interfaces, with different data transfer capabilities. The idea of a suite of interfaces is desirable as it can reduce the costs associated with using a very high performance interface for all the modules, versus using it only for the primary communication path.

Using this data, the evolution with respect to size, power requirements, data rates necessary for communication, as well as number of pixels can be seen with respect to time, as shown in Figure 3-1.

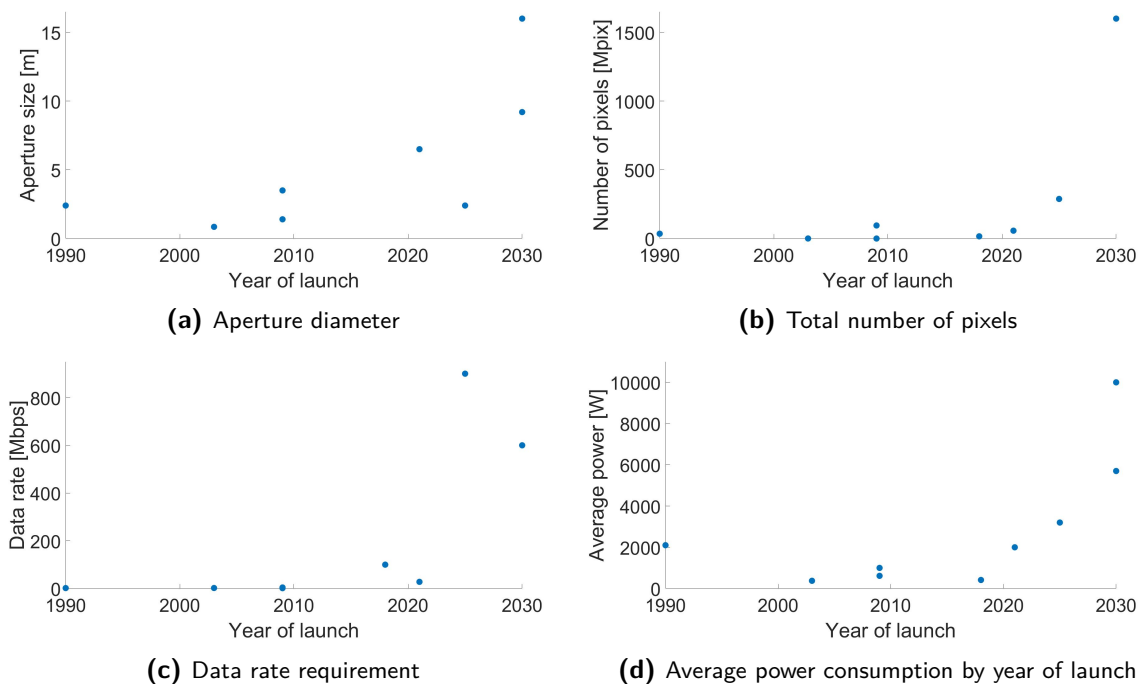


Figure 3-1: Evolution of mission parameters over time

The first observation one can make when considering these graphs is an increase over time in both aperture size and number of pixels of instruments used. The data rates seem to follow suit, except in the case of WFIRST, which can be seen as an outlier with its data rate of 0.9 Gbps. This is further confirmed when considering the fact that the ATLAST mission has 4 to 6 times the number of pixels compared to WFIRST, however its data rate requirement is only 0.6 Gbps. This is most likely due to the fact that some form of data compression techniques are used in the ATLAST project, whilst the WFIRST mission only indicates the rates at which its instruments gather data, most likely in uncompressed form.

The average power consumption on the other hand, does not really present any trends that are consistent throughout the considered timeframe - from 1990 to 2030. At first, it seems that power requirements went down with time, as instruments were optimized, however, starting from 2018, a clear increase can be observed. This can be partly attributed to more

performant instruments having higher power requirements, but one should also consider that the last two data points make use of electric propulsion, which explains the dramatic rise in power requirement in comparison with all the other reference missions. In order to gain more information into power usage trends, one can rearrange the reference missions in order of increasing power consumption. The results with respect to number of pixels and data rate are illustrated in Figure 3-2.

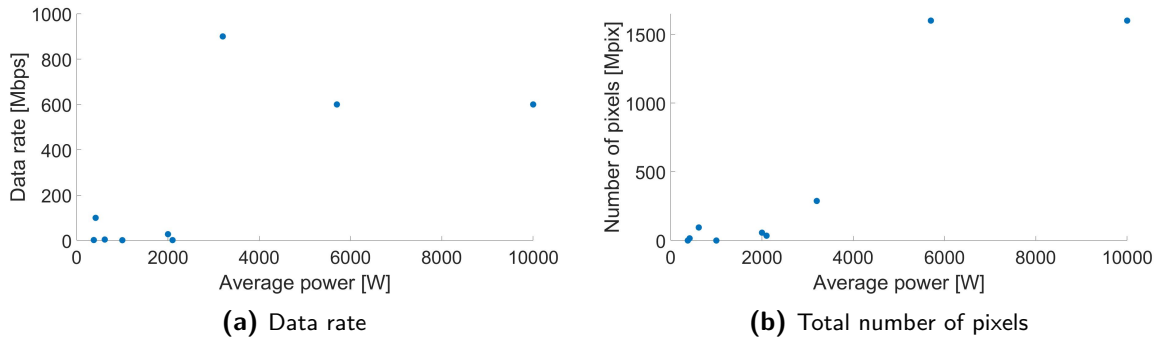


Figure 3-2: Mission parameter evolution with increasing power usage

It can be seen that higher power consumption seems to be correlated with larger numbers of pixels, however data rates do not seem to follow as clear a trend. When considering data rate evolution with respect to increasing pixel count, as shown in Figure 3-3, the reason for this deviation becomes clear.

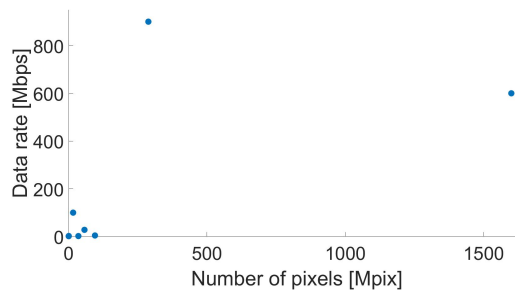


Figure 3-3: Data rate ordered by increasing number of pixels

The data from the reference missions shows a very low correlation between the required data rate and the number of pixels. This is partly due to the fact that communication data rate is used as a basis for this analysis, meaning that some of the data points consider short transmission windows, requiring much higher rates than the scientific data collection rate. Another potential reason for the lack of correlation between these two parameters is the choice of compression algorithms on which, especially for missions that are still under development, no information was found. Due to this result, it is deemed important to pursue both total number of pixels and data rate trends in the rest of the analysis.

The final aspect to consider is how the mission parameters vary with increasing aperture size. This is important mainly due to the existence of conceptual missions with even larger

apertures like the Giant Orbiting Astronomical Telescope (GOAT) [64], with a 25 m diameter primary aperture, the Thirty Meter Space Telescope (TMST) [65], and the Robotically Assembled Modular Space Telescope (RAMST) [66], a 100 m diameter concept. In order for an interface to be flexible enough to be usable in projects such as these, it is imperative to see if any correlation is found between increasing aperture size and the rest of the mission parameters. Thus, rearranging with respect to increasing aperture size yields the results in Figure 3-4a, for number of pixels, and Figure 3-4b, for power.

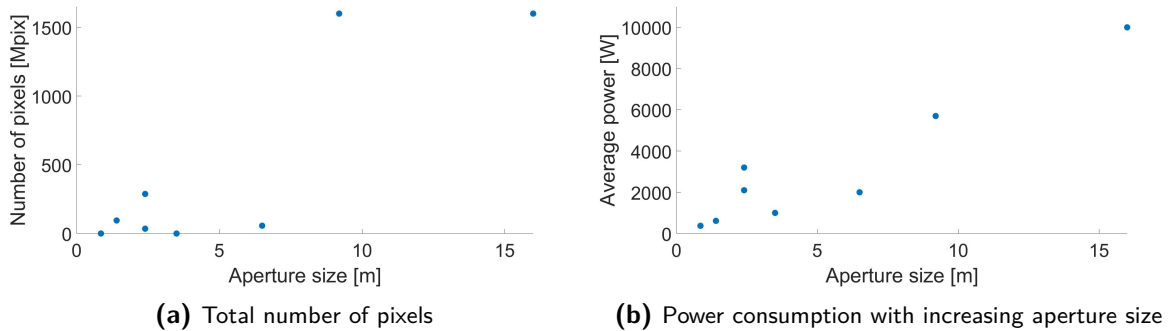


Figure 3-4: Evolution of pixel count and power consumption with increasing aperture size

Even though some correlation can be seen between aperture size and power usage, the number of pixels do not follow the same trend. This is due to the fact that to improve the resolving power of a telescope one can either increase the diameter of the primary mirror, or increase the number of pixels of the detector. As such, there is not much, if any correlation between increasing size and the pixel count. A similar conclusion can be drawn about the data rate, both of which are dependent mainly on the choice of instruments, not the size of the optics.

To summarize, the following observations that affect the interface design can be made based on the reference mission data:

1. There is a clear trend of increasing aperture size over time, confirming the needs described by literature.
2. With increasing aperture size, power usage seems to follow suit.
3. With the passage of time, more powerful instruments are used, with higher pixel counts.
4. Data transmission requirements also increase with time.
5. Although there is a direct correlation between number of pixels and the rate at which scientific data is generated, a correlation between the transmission rate and pixel count was not at all obvious.
6. There does not seem to be a size limit for space observatory primary apertures, based on conceptual missions like GOAT, TMST and RAMST.

Based on the fifth observation, one can conclude that the aperture size can be treated separately from the parameters that are only influenced by the choice of instruments, namely the

pixel count and the data rate. In the case of these two parameters, over a timeframe spanning from 1990 to 2030, the maximum values projected are 0.9 Gbps, for data rate, corresponding to the WFIRST mission, and 1-1.6 Gpix, as total number of detector pixels, for ATLAST. When considering these two missions, a big discrepancy can be seen between the pixel count and data rate, as seen in Table 3-3.

Table 3-3: Comparison between WFIRST and ATLAST w.r.t. data rate and pixel count

Parameter	WFIRST	ATLAST
Number of pixels	288 Mpix	1-1.6 Gpix
Data rate	900 Mbps	600 Mbps

As stated previously, where available, the data rate for communication was used in the analysis. In the case of WFIRST, the data rate projected is the instrument data generation rate, under the assumption of constant communication, whilst for ATLAST, 600 Mbps is used for communication, within specified time windows. However, it was also concluded that there should be a correlation between number of pixels and data rate hence this result is a bit strange. Since the total data production based on 16 bits per pixel is:

$$D_{generated_{WFIRST}} = 288 \cdot 10^6 \cdot 16 = 4.608Gb(\text{every } 5.5 \text{ seconds}) \quad (3-1)$$

$$D_{generated_{ATLAST}} = 1.6 \cdot 10^9 \cdot 16 = 25.6Gb(\text{no time interval available}) \quad (3-2)$$

There are only two possible explanations for this discrepancy: the use of a compression algorithm for the ATLAST mission, or a very long time interval between the images taken. The latter explanation is found to be less likely since the ATLAST mission further accounts for transmission windows, unlike WFIRST. This would by all means indicate a higher data rate requirement, which is not the case here. As such, since the difference between the data rates is a factor of 50% from ATLAST to WFIRST, it is assumed that a data rate requirements of 0.9 Gbps is a reasonable estimate for space observatory system evolution. This is under the assumption that compression will be used, allowing for even greater pixel counts than for the ATLAST mission. This would improve resolving power, which is one of the main needs of future space telescopes. Based on the ATLAST reference, assuming a 0.9 Gbps data rate transfer is feasible, hence a 50% increase in data rate from the baseline design would result in the possibility of transmitting an amount of data a factor of 1.5 larger:

$$D_{adjusted} = 1.5 \cdot 25.6Gb = 38.4Gb \quad (3-3)$$

Which results in 2.4 Gpix, provided the each pixel corresponds to 16 bits. This 50% margin on both data rate and pixel count is taken as safety to ensure the interface can be used in future, more data intensive applications. The data rate value will henceforth be used as a requirement for the interface design, in Chapter 4.

Moving on to primary aperture diameter, the first conclusion mentions the trend of increasing size, whilst the last admits no limit to this trend as of the time of writing. In this regard,

it is hard to arrive at a reasonable answer based solely on this analysis. Luckily, a workshop covering in-Space Assembly of Telescopes [72], conducted by NASA, studied the topic of when it is advisable or even advantageous to make use of OOA methods for space observatories. Three important results of this study [71], [73] need be quoted:

- It appears that the largest conventional space telescope design deployed from a future fairing of 8-10m (SpaceX's Big Falcon Rocket, or NASA's SLS) is 15m in size.
- Due to the risk advantages provided by OOA, this may be a preferred implementation approach in comparison to single launches for 10m class or larger apertures.
- OOA may offer cost reduction opportunities for aperture diameters of 15 m or less, however this is ultimately dependent on the point design.
- Due to the scalable nature of OOA, there is no inherent issue in designing apertures larger than 15m.

In light of this information and the reference missions, a primary aperture of 15 m will be used as a reference for this conceptual design. The reasoning is to use this as a first order estimation for the perturbations the system will experience during assembly, launch and potential servicing, which can then be translated into mechanical requirements for the interface design.

The problem arises when considering primary diameter in relation to power, since the latter ultimately depends on the design implementation, and how many subsystems make use of electrical power. One example of this is the thermal system, which can be passive or active, the former not using any power, whilst the latter does. Another example that has already been mentioned is the use of electric propulsion, which can have a sizable influence on power usage, depending on the scale of the system and its requirements. In spite of this fact, some degree of correlation was found between average power and aperture size for the sample space used in this section. Considering that the chosen aperture size is 15 meters in diameter, as opposed to ATLAST's 16 meter variant, a lower power rating can be expected. Furthermore, since the focus of the thesis work is the interface design with the restriction of fluid transfer not being considered, a propulsion subsystem is not considered for the purpose of this conceptual design. Considering ATLAST makes use of electric propulsion, this means the power usage should be even less if one eliminates this subsystem. Of course, this will cause some restrictions on orbit which will be discussed in Section 3-5. For now, the lack of electric propulsion and difference in size is assumed to account for about 20% decrease [82] from the 16 meter diameter ATLAST concept, resulting in an estimated power usage of:

$$P_{req} = 80\% \cdot P_{ATLAST16m} \approx 8kW \quad (3-4)$$

In order to find out what voltage the inter-modular interface will need to accommodate, the European Cooperation for Space Standardization provides documentation of common standards used by industry. The standards dealing with electronics, namely ECSS-E-ST-20C, state that for a fully regulated bus, the bus voltage will be 28V, if the power consumption is smaller or equal than 1.5 kW, 50V, for power up to 8 kW, or 100V and 120V for higher power usage. As mentioned in the literature study in Chapter 2, power transfers at low voltage have

already been performed by other interface candidates. However, due to the high power requirement, the interface design should consider both a 50 V and a 28 V variant. Furthermore, when considering electronic components, it is the norm to account for voltage variation, also called transients. With regard to this, ECSS-E-ST-20C states the following:

"i. With a fully regulated bus in nominal operation the bus voltage transients shall be:

1. for load transients of up to 50% of the nominal load not exceed 1% of its nominal value
2. for any source and load transients remain within 5% of its nominal value"

Using the more conservative value provided in the second point will yield a voltage transient of:

$$\Delta V_{low} = 28 \cdot 5\% = 1.4V \quad (3-5)$$

$$\Delta V_{high} = 50 \cdot 5\% = 2.5V \quad (3-6)$$

The final top-level requirements synthesized by this analysis create an envelope of modular space observatory missions for which the interface can be used, as shown by Table 3-4.

Table 3-4: Top-level requirements and interface applicability

Parameter	Value up to which interface can be used
Aperture size	15 meters and possibly above
Data rate	0.9 Gbps
Power usage	8 kW

The aperture size chosen above is mainly driven by the findings of the iSAT study from NASA. The main arguments are: the limit of space telescopes that use launchers that are currently being developed is 15 m diameter, cost savings are possible in the 5m to 15 m range, and, last but not least, primary mirror diameters of over 15 m are only possible through OOA (when considering launch opportunities that either exist or are currently being developed). The choice of data rate was driven by considering the number of pixels and data rates of the top two reference missions in these categories (WFIRST and ATLAST). The logic was that although the latter has a much larger pixel number (refer to Table 3-3), the data rate of the former is 50% higher. Since the ATLAST mission is a much newer concept that utilizes a much more powerful instrument it is assumed that difference is caused by novel data compression techniques. As such, using a data rate requirement similar to WFIRST, but with the same data handling algorithms as ATLAST, it would be possible to account for a 50% increase in pixel count (refer to 3-3 and paragraphs above and below). This was deemed as a sufficiently high margin so as to account for instrument evolution over time. Lastly, the power requirement is derived from the mission with highest consumption, in Equation 3-4.

The reason why an even higher aperture can potentially be achieved using the same interface design is that part of the structural constraints will arise from size, whilst others from launcher

constraints, as discussed in Section 3-7. This means that, if launcher constraints far exceed the magnitude of the disturbances in the micro-gravity environment in which assembly will take place, then the interface is still viable. However, it should be noted that a more detailed analysis of the mission-specific orbital perturbations will be necessary for any conceptual mission that wants to use this interface design to make sure that the interface can satisfy the structural needs of the system. A discussion on what these limiting loads are will be provided in Chapter 4. Furthermore, since it is desirable to have an interface that can compete with current state-of-the-art designs, it is probable that the performance will exceed both the requirements driven by launch loads and those accounting for on-orbit disturbances, thus making the scaling up of future space telescopes even more viable. Since both the power and data rate requirements for the interface have been established, the only transfer types left are thermal and mechanical. In order to establish requirements for the mechanical connection the interface should satisfy, it is imperative to investigate the on-orbit disturbances felt during the mission lifetime, as well as launch loads the modules will be subjected to. However, in order to estimate the orbital perturbations, one must first determine the size and orbit of the conceptual space telescope.

3-3 Modular Optics Considerations

When considering a modular aperture with a 15 meter diameter, it is important to envision what shape the elements will have to achieve a somewhat circular shape. For a top-level estimation, a hexagonal shape is considered to be the most appropriate for space telescopes, both due to its efficiency in space filling, as well as the fact that hexagonal mirror elements have been produced to date, hence are easier to manufacture. A very important design problem that will need to be solved for any conceptual telescope using the interface described in Chapter 6 is the number of modules the telescope will be separated into. The reason this is important from the perspective of the interface design as well, is because the extra housekeeping data generated by each interface in order to detect failures and diagnose their location is directly influenced by the number of modules that make up the system, as will be discussed in Section 3-9. The dimensions of the modules will be constrained to some extent by mirror production capabilities. In order to compute them, the area of the primary mirror must first be computed, using Equation 3-7.

$$A_{primary} = \pi R^2 = \pi \cdot 7.5^2 = 176.71m^2 \quad (3-7)$$

The area of a hexagonal module is given by Equation 3-8, where a is the length of the hexagon's side, which is equal to the radius of the circle inscribed by the hexagon.

$$A_{hex} = \frac{3\sqrt{3}}{2} \cdot a^2 = \frac{3\sqrt{3}}{2} \cdot R_{hex}^2 \quad (3-8)$$

A primary aperture with a slot in the center through which light is gathered by the instrument detectors, in modular form, using hexagonal elements can only be made as close to circular as possible using concentric circles made up of joined hexagons - i.e. 6, 18, 36, 60, etc. In order to find how big the hexagonal mirrors will be depending on the number of volumes one makes use of the following equation:

$$A_{primary} = (n + 1) \cdot A_{hex} \Rightarrow a^2 = \frac{A_{primary}}{\frac{3\sqrt{3}}{2} \cdot (n + 1)} \quad (3-9)$$

Using the numbers for concentric circles made out of hexagons yields the results in Table 3-5.

Table 3-5: Combinations of module number and corresponding size

Number of modules (n)	Size of hexagon side (a)
6	3.117 m
18	1.892 m
36	1.356 m
60	1.056 m
90	0.86 m
126	0.732 m
168	0.6344 m
216	0.56 m
270	0.501 m
330	0.453 m
396	0.414 m
468	0.381 m

Under the assumption that each hexagonal mirror element will have the same surface area as the module it sits on, even 90 modules are sufficient considering the existence of hexagonal mirrors with very low RMS (in the order of 20 nm or less) with size of 1.45m from edge to edge [83]. However one must keep in mind the fact that the JWST [67] uses even smaller mirrors of 1.32m in dimension from edge to edge, and they are custom made. This means that the production costs for this size of mirrors will far exceed the costs of sizes that can be mass produced. In order to ensure flexibility of use with both custom made and mass-manufacturable mirror types (0.3-1 m sizes [84]), it is important to give up on the idea that a single module needs to be the same size as the mirror element connected to it. This means that the shape of the modules does not necessarily need to be hexagonal, as multiple elements will be used to support any given mirror element. Given this, it is decided to switch to a cubic module shape, since although a square is significantly less efficient in covering a large circular surface area, the number of interfaces on each module decreases by 33%, and the assembly is simpler, as will be seen in Section 5-1.

Switching to cubic modules raises a new problem, namely how to constrain the interface dimensions rigorously whilst also making sure any type of optics can be used. In this case, since the goal is to allow as many types of optics as possible, it is decided to constrain the modules to be able to fit the smallest type of state-of-the-art mirrors available. In this case this corresponds to the Autonomous Assembly of a Reconfigurable Space Telescope (AAReST) mission [85], [86] which makes use of deformable mirrors to actively maintain aperture shape. These mirrors are circular and have a maximum diameter of 0.4m. With this in mind a cubical module with edges of 0.4m is the minimum size for which a single module can fit this mirror. This is found to be a sufficiently small value for the mirror size and will be used in order to estimate a maximum value for housekeeping data production in Section 3-9. An estimation

for the number of such modules necessary for a 15 m diameter primary aperture is then given by:

$$A_{primary} = n \cdot A_{module_{top}} \Rightarrow 176.71 = n \cdot 0.4^2 \quad (3-10)$$

Where n is the number of modules. This results in 1101 modules.

3-4 Spacecraft Configuration

After considering the separation into modules, it is necessary to consider if the spacecraft can be modularized even further. Based on the expectation of high stability requirements for the primary optics due to the use of modularity, a static wave-front error in the order of 7 nanometers is not out of the question, based on reference missions such as JWST [70] and ATLAST [61]. In order to achieve this stringent requirement, two distinct classes of options can be adopted: the use of some form of support structure (e.g. deployable truss modules - DTMs [87]), or active actuators (e.g. those used by the James Webb Space Telescope [70]). Whatever the choice, the next consideration would be if this optics system should be an integrated part of the modules, or packaged separately (all the mirrors together, for example) in a structure capable of ensuring no damage when subjected to launch loads. The use of any of the aforementioned structural options creates three distinct layers for the part of the spacecraft containing the primary aperture:

- Mirror elements
- Supporting structure/actuators
- Module subsystems

The choice in packaging into a launcher will be affected by the separation of these layers during assembly. With this in mind one can consider three different configurations which effectively change the definition of a module: a) each module is comprised of all three layers, b) each module is comprised of one or two layers with the rest being considered as auxiliary parts, and c) each module is composed of only one layer. In the first case, where all three layers are integrated into a single module, launch options will be severely limited due to the presence of the mirror elements which are assumed to be the most fragile element. This will have an effect on both cost and scheduling due to the inability to make use of all launch opportunities.

On the other hand, the second scenario offers the possibility of either separating the most fragile layer from the modules, or grouping both the support structure and mirror layer together whilst the module subsystems are launched independently. The choice between these two cases is highly dependent on what the supporting structure is made out of. If actuators are chosen, then these will need to be grouped with the module subsystems layers so that they are integrated with the power subsystem. If deployable structures are selected, fixing them to the mirror elements before launch is an option, however it may require said structures to be deployed during launch, which would affect how much volume they take up,

again affecting how long the launch of the full system will take and overall cost incurred (assuming multiple launches).

The last scenario would entail a full separation of the three layers. The advantages of this configuration are the flexibility of deployment with respect to launch, as the modules containing the subsystems could be launched using any existing options. This is also potentially true for the supporting structure, assuming that deployable structures are used. Since these would not be attached to anything, they could be launched whilst being stowed, thus occupying the least amount of volume. The only constraint for launcher availability would then be for the mirror layers, however packing them with methods that ensure cushioning and shock absorption could be a viable method of expanding the list of usable launch vehicles. On the other hand, if actuators are chosen as the middle layer, the disadvantage of having to connect these to the power subsystem on-orbit arises. Due to the flexibility in launch vehicle choice (which can also potentially fast-track the schedule from first launch to spacecraft nominal operation), as well as efficient use of volume, this option is chosen as the configuration for which the interface will be designed. As such, henceforth a module will be defined as an element of the module subsystem layer, and the interface will be designed so that this layer can be assembled on orbit. The other two layers are considered as auxiliary parts which do not generate any specific interface requirements so as to not excessively broaden the scope of this work. This will have the effect of lowering the requirements for the interface, but raising the required capabilities of the assembler, as it should be capable of assembling not only the modules together, but the auxiliary layers as well.

For the remainder of the discussion, it is assumed that these three layers are detachable, and the combinations of layers will be discussed. In the event of three different layers to be assembled, a DTM structure - as the support layer - will be most conducive for assembly, as it provides an easy to assemble skeleton for all the subsequent connection operations. Assuming the use of such a structure will mean that this will take priority over the mirror layer in the assembly phase. Upon completion of the structural support, the mirror elements can be fixed to this using pre-designed fixtures. Assuming further actuation is necessary, this will most likely be packaged with the module subsystems in the event of using a deployable structure. Thus, the final step will be the attachment of modules, through (desirably) the same inter-modular interface design, described in Chapter 6.

Combining the mirror elements and structure in a pre-assembled module only holds minor advantages in simplified assembly operations, however it restricts the design space for support structure to non-deployable systems, which could result in a system that is unnecessarily heavy. However, there is another, more feasible combination, namely to have the whole assembly fixed into modular elements containing all three layers, thus decreasing the complexity of required operations significantly (an example of this is the AAReST mission [86]). This would most definitely reduce the requirements for the robotic payload of the free-flyer assembler, however this could potentially result in a very specialized system. Thus the assembler would be less flexible in dealing with general assembly tasks for any systems not using the same standardized interface that it was designed for. Although this is not evaluated as a viable choice, it is considered for completeness. As mentioned above for this interface design it is considered that three distinct layers will be present in the telescope design as illustrated in Figure 3-5.

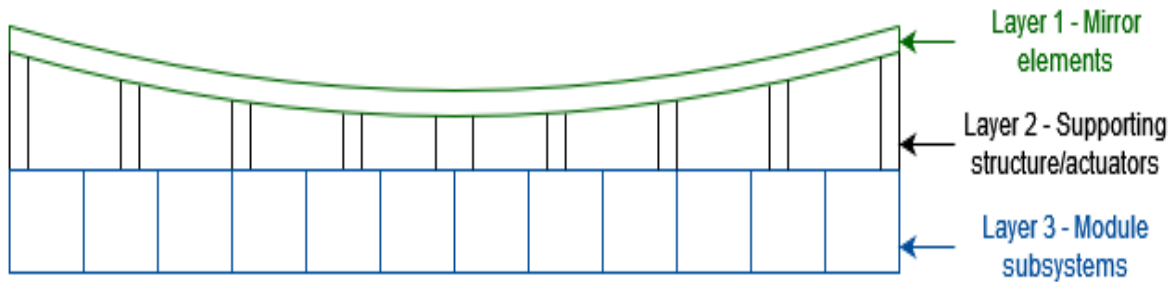


Figure 3-5: Telescope primary aperture design separated in layers - Mirrors, supporting structure, modular platform containing operational subsystems (from top to bottom)

The first layer makes up the primary mirror itself, and any type of mirror of any size can be used, depending on the size of aperture required. The support structure could either be fixed or made out of deployable truss modules (DTMs) [34]. This is possible due to the fact that most subsystems are delegated to the modular bottom layer. With this design this latter layer would be assembled before the top-most layer, which would then be fixed or assembled on top of it (depending on the choice of design). The third layer composed of the modules would be assembled first and used as a foundation on which the other layers can sit upon. This presents advantages in packing and deploying such a system as the top two layers could be packed more efficiently and launched independently from the modules, but also in terms of servicing as, depending on the ratio between the second layer dimensions and module size, these can be taken out without compromising the primary mirror. Furthermore, due to this separation into layers, one could make use of this type of interface in a number of other mission types that use large platforms (similar to the third layer), such as communication or even solar collection farms. It is important to note that the interface will be designed in such a way so as to permit the assembly and functioning of the bottom-most layer containing all operational subsystems.

3-5 Astrodynamics

When considering observation missions in general, it is desirable to either perform scientific measurements that have not been done up until the present, or enhance existing scientific data with higher resolution data or higher pixel counts, for example. As such, an approach to enhancing scientific return can be to improve existing concepts to a significant degree. Two missions are considered for reference here, HST [21], from the perspective of a successful modular space telescope mission, and the JWST [68]. Other missions such as AAReST [85], [86], ATLAST [61], GOAT [64], TMST [65] and RAMST [66] exist on a conceptual level at the time of writing, with demonstrations pending. Due to this fact, HST could be used as a preliminary starting point. The major limitations of this mission are its low altitude orbit and the size of the primary aperture of the telescope. Thus, one could improve the scientific return by opting for an orbit farther away from both the Earth and, potentially, the Sun. The reason for this is that in the case of measurements in the infra-red (IR), any thermal influence can potentially make small signatures invisible due to the source's strength in the IR spectrum. This means that protection from the Sun and its thermal influence is a critical factor for scientific data based on IR measurements such as asteroid detection. When considering

solely Hubble, Geosynchronous Earth Orbit (GEO) or Sun-Earth Lagrange 2 (SE-L2) would radically reduce the thermal influence of the Sun and Earth on the instruments. The latter option seems to be a more and more attractive deployment point as time goes on, and is the target orbit of the JWST, the reasons for which will be explained.

The SE-L2 point, due to its large distance from the Sun, provides a thermally stable environment with minimal IR influence from both the Sun and the Earth, with only the Sun-direction being excluded from viewing in order to avoid blinding the instruments. Additionally, the radiation environment is less strong at this distance than it is for LEO or GEO. However, the drawbacks of this option are the very long transfer time to reach said orbit, communication delay due to the large distance between the spacecraft and Earth, as well as the fact that the orbit is unstable, resulting in necessary maneuvers every 30 days. In spite of this, orbits around SE-L2 would not be very costly to maintain with regard to propellant consumption. However, this option would in any design version need to have some form of propulsion capability, due to there being no possibility of direct orbit injection. Current observation missions planned for SE-L2 include the James Webb Space Telescope (JWST) [68], and ATLAST [61].

On the other hand GEO provides less communication delays, thus more control from ground during sensitive operational phases, as well as the ability to directly inject the spacecraft into orbit using certain launchers whilst no propulsion would be necessary for orbit-keeping. Conversely, the drawbacks compared to SE-L2 are a less stable thermal environment and higher radiation energy. Nevertheless, with regards the HST's orbit, the thermal environment is much more stable. Due to the fact that this mission aims at using OOA as an integral technology to be demonstrated, the only way to ensure minimization of risk is increasing the supervisory role of the ground segment during the assembly phase. Since this is the most critical technology, the value of lessening communication delays far outweighs that of the observational merits of SE-L2. As such, GEO is chosen as the orbit, due to its low communication times, more qualitative scientific output with comparison to LEO, and the possibility of not using a propulsion system - which would be a definitive improvement in both total system weight, and cost. Since the orbit has been chosen, the associated disturbances can now be calculated.

3-6 Attitude Determination and Control subsystem

In order to determine the perturbations the interface structure needs to withstand, one must first compute the disturbances the spacecraft will be subjected to during its operational lifetime. These disturbances arise from four sources: aerodynamic drag, gravity, solar pressure and magnetic fields of planets in the immediate proximity. In the case of GEO, the aerodynamic drag will not be a concern due to the orbital altitude being higher than that of the atmosphere. Thus, only the other three perturbations will be considered. In order to calculate the gravitational disturbance, one can use Equation 3-11 [50].

$$T_g = \frac{3\mu_E}{2R^3} \cdot |I_z - I_y| \cdot \sin(2\theta) \quad (3-11)$$

Where μ_E is the Earth gravitational constant, R is the distance from the spacecraft to the center of the Earth, I_z and I_y are the mass moments of inertia around the Z- and Y-axis,

respectively, and θ is the angle between the local vertical and the principal Z-axis. In order to calculate a first order estimation of the moments of inertia around the Z- and Y-axes, it is important to have a simplified view of the spacecraft. Assuming an on-axis Ritchey-Cretien optical system, the primary and secondary mirrors can be simplified to thin disks with individual masses, whilst the surrounding structure can be modelled as a thin walled hollow cylinder, of neglectable thickness in comparison to the other dimension. This simplification results in the X and Y moments of inertia to be equal, due to symmetry. The equation for mass moment of inertia around the viewing (Z-) axis can be computed using Equation 3-12:

$$I_z = I_{z_{primary}} + I_{z_{secondary}} + I_{z_{structure}} \quad (3-12)$$

The moments of inertia of the primary and secondary elements is computed using Equation 3-13, for thin disks, whilst that of the structure element is calculated through Equation 3-14, for hollow cylinders of neglectable thickness.

$$I_{z_{disk}} = \frac{1}{2}m \cdot R^2 \quad (3-13)$$

$$I_{z_{cylinder}} = m \cdot R^2 \quad (3-14)$$

Where m is the component mass and R its distance with respect to the rotation axis going through the centroid of the structure. The primary mirror mass will be calculated based on the expected areal density of mirrors for the ATLAST study, 15 kg/m^2 . This results in a primary mirror weight of:

$$m_{primary} = \pi \cdot R_{primary}^2 \cdot 15 = 2650.72 \text{ kg} \quad (3-15)$$

Assuming the ratio between the primary and secondary mirrors is similar to HST and WFIRST results in secondary mirror diameter a factor of 3 smaller than the primary. Thus, the weight of the secondary mirror can be estimated as:

$$m_{secondary} = \pi \cdot R_{secondary}^2 \cdot 15 = 294.52 \text{ kg} \quad (3-16)$$

Assuming that 30% of the whole system is the structural subsystem, and that 80% of this structure will be used for the cylinder results in a mass fraction of:

$$m_{cyl} = 30\% \cdot m_{total} \cdot 80\% = 0.24 \cdot 30000 = 7200 \text{ kg} \quad (3-17)$$

If the rest of the satellite mass, excluding the secondary mirror, is concentrated around the primary mirror location, this can be included in the primary disk simplification. The weight of this section is thus:

$$m_{primary_{disk}} = m_{total} - m_{cyl} - m_{secondary} = 30000 - 7200 - 294.52 = 22505.48 \text{ kg} \quad (3-18)$$

This yields the following moments of inertia:

$$I_{z_{primary}} = \frac{1}{2} \cdot m_{primary_{disk}} \cdot R_{primary}^2 = \frac{1}{2} \cdot 22505.48 \cdot 7.5^2 = 632966.625kg \cdot m^2 \quad (3-19)$$

$$I_{z_{secondary}} = \frac{1}{2} \cdot m_{secondary} \cdot R_{secondary}^2 = \frac{1}{2} \cdot 294.52 \cdot 2.5^2 = 920.375kg \cdot m^2 \quad (3-20)$$

For the structure, it is assumed that an 8 meter distance between the primary and secondary mirrors is sufficient for this conceptual application, resulting in:

$$I_{z_{structure}} = m_{cyl} \cdot R_{structure}^2 = 7200 \cdot 4^2 = 115200 \quad (3-21)$$

$$I_z = I_{z_{primary}} + I_{z_{secondary}} + I_{z_{structure}} = 749087kg \cdot m^2 \quad (3-22)$$

In order to calculate the mass moment of inertia around the Y-axis, the disks elements will be treated as point masses, whilst the cylinder is governed by Equation 3-23.

$$I_{y_{cylinder}} = \frac{m_{cylinder}}{12} \cdot (6R_{cylinder}^2 + h^2) \quad (3-23)$$

Where h is the distance between the two mirrors in this case. This results in the following individual components:

$$I_{y_{primary}} = m_{primary} \cdot \left(\frac{h}{2}\right)^2 = 360087.68kg \cdot m^2 \quad (3-24)$$

$$I_{y_{secondary}} = m_{secondary} \cdot \left(\frac{h}{2}\right)^2 = 4712.32kg \cdot m^2 \quad (3-25)$$

$$I_{y_{structure}} = \frac{7200}{12} \cdot (6 \cdot 16 + 10.5^2) = 600 \cdot 401.5 = 240900kg \cdot m^2 \quad (3-26)$$

Adding these components together results in the total moment of inertia around the Y-axis:

$$I_{y_{total}} = I_{y_{primary}} + I_{y_{secondary}} + I_{y_{structure}} = 605700kg \cdot m^2 \quad (3-27)$$

Substituting the gravitational constant ($3.986 \times 10^{14} \frac{m^3}{s^2}$), the orbital altitude for GEO, as well as the moments of inertia and assuming $\theta = 10^\circ$ (since the spacecraft is fairly symmetric hence mass balance could potentially be adjusted better) results in a gravitational perturbation of:

$$T_g = \frac{3 \cdot 3.986 \cdot 10^{14}}{2 \cdot 42164144^3} \cdot |749087 - 605700| \cdot \sin(20) = 7.97625 \cdot 10^{-9} \cdot 49041.24229 = 3.91165 \cdot 10^{-4} Nm \quad (3-28)$$

Equation 3-29 [50] is used to estimate the perturbation caused by the magnetic field of the Earth on the spacecraft.

$$T_M = D \cdot B = D \cdot \left(\frac{M}{R^3} \cdot \lambda \right) \quad (3-29)$$

Where D is the residual dipole moment of the spacecraft, B is the magnetic field strength, M is the magnetic moment of the Earth multiplied by the magnetic constant ($= 7.8 \cdot 10^{15} T$), R is the distance between the spacecraft and the Earth's center, and λ is the unitless function of magnetic latitude, ranging from 1 at the magnetic equator to 2 at the magnetic poles. For Class III spacecraft (for which magnetic torque is much smaller than the other disturbance torques) the residual dipole moment can be estimated using Equation 3-30. Assuming a similar mass to the ATLAST 16.2 meter concept, with a mass margin (since the chosen conceptual mission has a 15 meter diameter primary aperture) will result in:

$$D \approx 10^{-2} \cdot m_{spacecraft} = \frac{30000}{100} = 300 A \cdot m^2 \quad (3-30)$$

Assuming an equatorial orbit, hence $\lambda = 1.2$ and substituting in Equation 3-29, results in a magnetic torque of:

$$T_m = 300 \cdot \left(\frac{7.8 \cdot 10^{15}}{42164144^3} \cdot 1.2 \right) = 300 \cdot 1.248665134 \cdot 10^{-7} = 3.746 \cdot 10^{-5} Nm \quad (3-31)$$

Finally, the torque caused by solar pressure can be calculated using Equation 3-32 [50].

$$T_{sp} = \frac{\Phi}{c} \cdot A_s \cdot (1 - q)(c_{ps} - c_m) \cdot \cos(\varphi) \quad (3-32)$$

Where Φ is the local solar flux, c is the speed of light, A_s is the sunlit surface of the spacecraft, q is the reflectance factor ranging from 0 to 1, φ the angle of incidence of the Sun, and c_{ps} and c_m are the centers of solar pressure and mass, respectively. In order to calculate the maximum local solar flux felt during the mission one need only multiply the value on Earth (at 1 Astronomical Unit - AU) with the ratio of squared distances from the Sun in AU. One Astronomical Unit corresponds to a value of $1.496 \cdot 10^8 km$ In order to compute the closest distance from the spacecraft to the Sun during its lifetime, in AU, one can make use of Equation 3-33.

$$R_{S/C} = 1 - \frac{a}{1.496 \cdot 10^8} \quad (3-33)$$

Where a is the semi-major axis of the chosen orbit, in this case 42164.144 km. Substitution will result in a distance of:

$$R_{S/C} = 1 - \frac{42164.144}{1.496 \cdot 10^8} = 0.99972AU \quad (3-34)$$

The ratio of squared distances is then calculated to be:

$$\frac{R_{Earth}^2}{R_{S/C}^2} = \frac{1^2}{0.99972^2} = 1.00056 \quad (3-35)$$

The local solar flux is thus:

$$\Phi = 1366 \frac{W}{m^2} \cdot 1.00056 = 1366.77 \frac{W}{m^2} \quad (3-36)$$

Assuming the worst case solar incidence angle ($\varphi = 0^\circ$), a reflectance factor of $q = 0.6$ and a maximum distance between the center of mass and the center of solar pressure of one meter results in a solar pressure disturbance of:

$$T_{sp} = \frac{1366.77}{3 \cdot 10^8} \cdot \pi R_{primary}^2 \cdot (1 + 0.6) \cdot 1 \cdot \cos(0) = 1.2882 \cdot 10^{-3} Nm \quad (3-37)$$

It is worth mentioning that the surface area is calculated under the assumption that the backside of the primary mirror will be the Sun-oriented face.

In order to select and size the actuators used in attitude control as well as identify the interface requirements, one must first compute the maximum disturbance a reaction wheel would have to counter, including a margin factor for safety, as shown in Equation 3-38.

$$T_c = T_D \cdot MF = \max(T_g, T_s, T_m) \cdot MF \quad (3-38)$$

Where T_g , T_s and T_m are the gravitational, solar pressure and magnetic disturbances, respectively, and MF is the margin factor. Using a safety factor of 10% yields a maximum torque requirement of:

$$T_c = 1.224 \cdot 10^{-3} \cdot 1.1 = 1.3464 \cdot 10^{-3} Nm \quad (3-39)$$

This result represents the maximum expected orbital perturbation during mission lifetime. However, as mentioned previously, this is not the only source of mechanical constraints for the interface design - the launcher mechanical environment is also a concern.

3-7 Launcher Considerations

The last element needed to establish a range of structural requirements for the detailed interface design phase is the launch vehicle. For conventional satellites, these are usually the highest loads experienced during the mission lifetime, hence the structural subsystem becomes overconstrained in order to account for this. In the case of modular structures to be assembled in space, this can be avoided by distributing weight across multiple modules, making the requirements less strict. However, mechanical environments inside launch vehicles vary, hence a point design will usually aim to satisfy particular launch conditions. Since the approach for interface design described by this thesis involves flexibility as a critical aspect, one can develop an envelope of worst-case conditions based on existing launchers. The data describing the mechanical environment for a range of existing launch vehicles, with respect to required natural frequencies, as well as quasi-static loads (QSL), was compiled from the respective user manuals [88], [89], [90], [91], [92], [93], into Tables 3-6 and 3-7.

Table 3-6: Mechanical environment constraints for considered launch vehicles - Part 1

Launcher	Natural frequency (lateral)	Natural frequency (longitudinal)	Max QSL (lateral)	Max QSL (longitudinal)
Vega	$f \geq 15$ Hz	$20 \text{ Hz} < f < 45 \text{ Hz}$ or $f \geq 60$ Hz	± 0.9 g	-5g (compression) +3 g (tension)
Vega C (single launch config)	$f \geq 12$ Hz	$f \geq 20$ Hz	± 1.35 g	-5 g (compression) +3 g (tension)
Vega C (dual launch config) upper S/C	$f \geq 12$ Hz	$f \geq 20$ Hz	± 2.5 g	-7.7 g (compression) +3.3 g (tension)
Vega C (dual launch config) lower S/C	$f \geq 12$ Hz	$f \geq 20$ Hz	± 2 g	-7.7 g (compression) +3.3 g (tension)
Soyuz	$f \geq 15$ Hz	$f \geq 35$ Hz	± 1.8 g	-5 g (compression) +1.8 g (tension)
Ariane 5	$f \geq 10$ Hz ($M \leq 4500$ kg) $f \geq 8$ Hz ($M > 4500$ kg)	$f \geq 31$ Hz ($M \leq 4500$ kg) $f \geq 27$ Hz ($M > 4500$ kg)	± 2.0 g	-6 g (compression) +2.5 g (tension)
Atlas V	$f \geq 8$ Hz	$f \geq 15$ Hz	± 2.0 g	-6 g (compression) +2 g (tension)
Delta IV Heavy	$f \geq 8$ Hz	$f \geq 30$ Hz	± 2.0 g	-6 g (compression) 2 g (tension)
Falcon 9	N/A	$f \geq 35$ Hz	± 2.0 g ($M > 4000$ lbs) ± 3.0 g ($M < 4000$ lbs)	-6 g (compression) +2 g (tension) ($M > 4000$ lbs) -8.5 g (compression) +4 g (tension) ($M < 4000$ lbs)

Table 3-7: Mechanical environment constraints for considered launch vehicles - Part 2

Launcher	Natural frequency (lateral)	Natural frequency (longitudinal)	Max QSL (lateral)	Max QSL (longitudinal)
Falcon Heavy	N/A	$f \geq 35$ Hz	± 2.0 g (M > 4000 lbs) ± 3.0 g (M < 4000 lbs)	-6 g (compression) +2 g (tension) (M > 4000 lbs) -8.5 g (compression) +4 g (tension) (M < 4000 lbs)

The only unknowns are the lateral natural frequency requirements for Falcon 9 and Falcon Heavy. Due to the fact that a clear difference between lateral and longitudinal natural frequency requirements can be seen in all launcher candidates, it is expected that the lateral frequency for the Falcon variants will follow the same trend. Since all the other candidates show a required lateral frequency of 15 Hz or above, this will be used as the worst-case scenario. Using the worst-case conditions for QSL, and taking into account all frequency requirements results in the envelope of parameters presented in Table 3-8.

Table 3-8: Mechanical environment constraint envelope for considered launch vehicles

Natural frequency (lateral)	Natural frequency (longitudinal)	Max QSL (lateral)	Max QSL (longitudinal)
$f \geq 15$ Hz	$35 \text{ Hz} \leq f \leq 45 \text{ Hz}$ or $f \geq 60$ Hz	± 3.0 g	-8.5 g (compression) +4 g (tension)

One can clearly observe that the loading factors for all launchers, as well as for the worst-case scenario, have much higher values for longitudinal constraints, than for lateral. This raises the question of module shape and how that shape fits in a launcher. Depending on the positioning of the interfaces on these cubical module elements, it should either be designed to support only lateral loads - e.g. no interfaces are present on the top or bottom faces -, or both longitudinal and lateral, in the case of interfaces on all faces of the modules. This will yield two limit cases, as illustrated by Table 3-9.

Table 3-9: Limit summary of mechanical environment constraint envelope for considered launch vehicles

Case type	Natural frequency	Max QSL
1. Interfaces only on lateral sides	$f \geq 15$ Hz	± 3.0 g
2. Interfaces on all sides	$35 \text{ Hz} \leq f \leq 45 \text{ Hz}$ or $f \geq 60$ Hz	-8.5 g (compression) +4 g (tension)

Since the difference in load cases is quite high, it is expected that the first case will yield a less overconstrained design for the interface, but will be limited in how the modules can fit together, whilst the latter will most likely be a heavier version, more constrained from a mechanical point of view. This thesis will focus on the first case, due to the fact that

the main modular structure necessary for space telescopes is the primary aperture, which implies a lateral connection with respect to the cube-shaped elements mentioned before. The drawbacks of this method are:

- No additional layer can be affixed to the top/bottom faces - this means that only one planar layer can be created with this technique, which may be suitable for large apertures (which can be seen as increasing in dimensions only in one plane), but not so much for other systems that require 3D scaling, for example space stations or even space cities.
- Modules need to be packaged in the launcher with a certain orientation - which is an inconvenience that can most probably be avoided given sufficient planning in the early design phases

In spite of these drawbacks, it is expected that the advantages brought by the modular implementation of space satellites using this approach far outweigh these concerns that can be addressed during a detailed phase of any point design. Since both the structural and electrical requirements for the interface have been established, the only classes left for evaluation are the thermal environment and bus data rate. The latter is important mainly due to the fact that the scientific data rate requirement is very high, hence two different versions of interface can be designed - one for high data rate transfer, for the scientific return and communication lines, and the other for bus, as well as interface housekeeping data.

3-8 Thermal subsystem

In order to gain a measure of how much thermal control is needed and of what type in order to keep all components within their temperature range, one must first estimate the thermal properties of the outer surface of the spacecraft in its operational conditions. Simplifying the structure to a flat plate with one side normal to the Sun and the other insulated, one can calculate the heat energy going in and out of this plate using Equations 3-40 and 3-41, respectively [50]:

$$Q_{in} = J_t \cdot A_\alpha \cdot \alpha \quad (3-40)$$

Where J_t is the local thermal flux, A_α is the projected area of the Sun towards the plate, and α the absorptivity of the surface.

$$Q_{out} = A_\varepsilon \varepsilon \sigma T^4 \quad (3-41)$$

Where A_ε is the radiating surface area, ε the emissivity, σ the Boltzmann constant (equal to $5.67051 \cdot 10^{-8} \frac{W}{m^2 \cdot K^4}$), and T the absolute temperature in Kelvin. By writing the heat balance ($Q_{in} = Q_{out}$), and solving for the temperature one arrives at Equation 3-42.

$$T = \sqrt[4]{\frac{A_\alpha}{A_\varepsilon} \cdot \frac{\alpha}{\varepsilon} \cdot \frac{J_t}{\sigma}} \quad (3-42)$$

The area ratio is equal to one, under the assumption of a flat plate, thus the absolute temperature becomes a function of $\frac{\alpha}{\epsilon}$. Assuming white paint will result in this ratio being equal to 0.13, thus Equation 3-42 becomes:

$$T = \sqrt[4]{0.13 \cdot \frac{J_t}{5.67051 \cdot 10^{-8}}} \quad (3-43)$$

The only unknown left is the thermal flux J_t , which is the summation of three components: solar radiation, planetary albedo and planetary radiation, as illustrated in Equation 3-44.

$$J_t = J_{solar} + J_{albedo} + J_{planetary} \quad (3-44)$$

The albedo radiation is governed by:

$$J_{albedo} = J_{solar} \cdot a \cdot F \quad (3-45)$$

Where a is the albedo of the Earth (0.33) [15] and F is the visibility factor which can be found to be 0.003, using Figure 3-6, courtesy of [15].

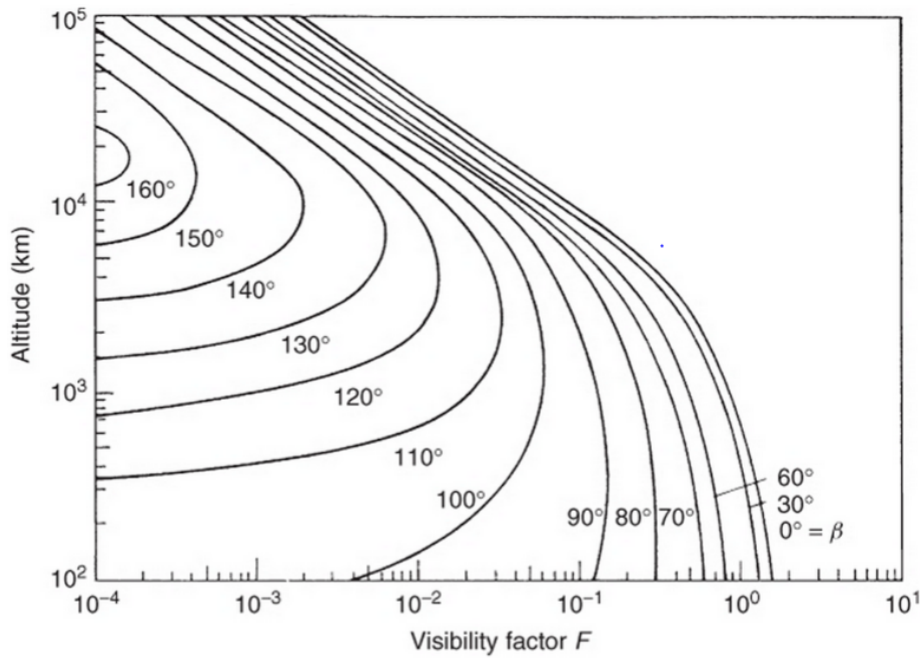


Figure 3-6: Visibility Factor (F), courtesy of [15]

This results in an albedo radiation value of:

$$J_{albedo} = 1366.77 \cdot 0.33 \cdot 0.003 = 1.3531023 \frac{W}{m^2} \quad (3-46)$$

As for planetary radiation, it can be assumed that the Earth radiates with an intensity of $237 \frac{W}{m^2}$, hence the total thermal flux is given by Equation 3-47.

$$J_t = 1366.77 + 1.3531023 + 237 = 1605.1231 \frac{W}{m^2} \quad (3-47)$$

Substituting into Equation 3-42 results in an absolute temperature of:

$$T = \sqrt[4]{0.13 \cdot \frac{1602.1231}{5.67 \cdot 10^{-8}}} = 246.2K \quad (3-48)$$

Based on the instruments used in the reference missions in Section 3-2, some need to be kept under 170K, with others under 100K. Hence it is expected that a detailed thermal design will be necessary. However, this work cannot be undertaken during this thesis due to scope constraints, thus the only thing that can be specified at this stage is to explicitly state the capability to transfer thermal loads as a design goal for the inter-modular interface. Furthermore, due to the thermal sensitivity of the instruments it is expected that this capability is only necessary at times, depending on which face the interface is on (e.g. a thermally conductive interface should not create a heat path towards heat sensitive components). As such, it would be desirable if the thermal capability could be integrated with the interface only at request, implying a detachable extension. This will be investigated as a goal, not a requirement, in Chapter 4. Finally, from an interface design perspective, the last requirement can be derived when identifying the bus and housekeeping data requirements for such a conceptual space telescope system.

3-9 Command and Data Handling subsystem

The Command and Data Handling (CNDH/C&DH) subsystem can be seen as the brain of the spacecraft. It ensures all the necessary inputs arrive to all the correct systems, schedules all autonomous tasks and stores any data that cannot be transmitted so as to be sent during the next communication window. The estimated data rate is 0.9 Gbps scientific return from the instruments, however one need also take into account housekeeping and bus data rate for the interface variant that does not deal with the instrument data or the communication lines.

Extra housekeeping data flows arise due to a critical difference between modular implementations and monolithic ones - the ability to detect faults internally and diagnose based on internal measurements. The problem can be framed as such: considering a local failure in one of the modules, what is the minimum data (and sensors) one would need to detect the problem and its location, be it an interface or within a module. With this in mind, a series of initial housekeeping data parameters are established, assuming the interface is capable of docking/undocking (including ensuring structural stability whilst docked), as well as transferring power, thermal loads and data.

- Structure/mechanism - "locked/unlocked" status; value is allocated to a char type, corresponding to 8 bits
- Power - both voltage and current intensity values; each value is allocated to a float type, corresponding to 32 bits

- Thermal - temperature at interface and module temperature values; each value is allocated to a float type.

Defining n_{mod} as the number of modules and n_{faces} as the total number of faces per module, one can write the total data required for interface-related housekeeping as:

$$d_{hk} = d_{struct} + d_{power} + d_{thermal} = n_{mod} \cdot n_{faces} \cdot 8 + 2 \cdot n_{mod} \cdot n_{faces} \cdot 32 + n_{mod} \cdot n_{faces} \cdot 32 \text{ bits} \quad (3-49)$$

Where d_{struct} , d_{power} , $d_{thermal}$ are the housekeeping components indicating properties related to docking state, power transmission, and thermal control, respectively. Rewriting Equation 3-49 more conveniently yields:

$$d_{hk} = 8 \cdot n_{mod} \cdot 13 \cdot n_{faces} \text{ bits} \quad (3-50)$$

Using the maximum expected value for number of modules of 1101 as discussed in Section 3-3, and $n_{faces} = 4$ corresponding to cubical modules (with only the top and bottom not using the interface) results in:

$$d_{hk} = 458016 \text{ bits} = 0.458 \text{ Mb} \quad (3-51)$$

One could also account for the possibility of the other subsystems being modularized further. Using a 20% margin on the number of modules in order to account for this will yield:

$$d_{hk} = 0.5496 \text{ Mb} \quad (3-52)$$

This value will be used as a conservative estimate for the data rate. Assuming these parameters are generated once every tenth of a second would result in a data rate of:

$$DR_{hk} = 0.5496 \cdot 10 \text{ Mbps} = 5.496 \text{ Mbps} \quad (3-53)$$

This value needs to be added to the expected bus data rate in order to estimate the requirements for the low data rate variant of interface. Since the most commonly used spacecraft buses are the MIL-STD-1553B [94], and CAN [95], the ESA alternative, and both their bus data rates are in the order of 1 Mbps, the required housekeeping data rate becomes:

$$DR_{req} = 5.496 + 1 \text{ Mbps} = 6.496 \text{ Mbps} \quad (3-54)$$

Storage will not be considered for this conceptual design, since it does not affect the interface in any way. However, it is mentioned that recommended options, based on data traffic expectations for the future, include Hard-Disk Drive (HDD) or Solid State Drive (SSD) with the latter being recommended for compactness, and lack of moving parts.

3-10 Robotic Assembler

The robotic assembler's main role during this conceptual mission is to assemble the individual modules together into the space telescope. In the envisioned free-flyer version chosen for this mission, the robotic agent would have all the capabilities of a spacecraft coupled with a robotic payload capable of completing its assembly task successfully. As the main focus of this work is the detailed design of an inter-modular interface, the design of the assembler cannot be treated here, and is thus considered a task for future study. However, a list of potential constraints and critical considerations is included for completeness:

- When docking with the assembled system, the assembler agent shall make use of the same inter-modular interface.
- The robotic payload shall be able to handle the connection of two modules using the interface described in this work.
- Trade-off between universal grapping fixtures and specific end-effector tools usable solely with this interface design.
- Investigate optimized motion and path planning algorithms for assembly.
- Trade-off using C&DH subsystem of assembler for full system upon docking or using separate C&DH subsystems for the telescope and assembler (or a combination of the two for the docked configuration).
- Investigate the possibility of using a communication subsystem only on the assembler as opposed to a smaller one for the assembler, for control during assembly, and a larger, higher gain one for the telescope, to ensure large amounts of scientific return.
- Possibility of refueling made viable once number of potential servicing targets increases (in the long-term).
- Investigate using ADCS of assembler for partial control during docked configuration.

3-11 Concept of operation (CONOPS)

The concept of operations, or CONOPS for short, represents an overview of the operations of the spacecraft during its entire lifetime. In the case of a modular space telescope to be assembled on orbit, one can separate the mission into four distinct phases: launch and orbit injection, assembly, nominal operation, and end-of-life or disposal.

Starting with the launch and orbit injection phase, as discussed in Section 3-5, the chosen orbit is a geosynchronous one. Potential options exist based on the choice of ground station. Assuming the use of the Deep Space Network, with a 34 meter diameter BWG antenna due to the high data rate possibilities achievable in the Ka-band, three different locations are available: Goldstone, California; Madrid, Spain; Canberra Australia. The choice between these will depend on a detailed market analysis, as well as the nature and nationality of the stakeholders invested in this mission. Considerations and requirements for this stage include:

- No propulsion capability for the space telescope requires that the modules be injected directly into the orbit where the system will be assembled, in this case GEO.
- The modules can be scheduled for orbital insertion in a series of launches, not all at once. This may allow some cost savings, as well as offsetting the effects of scheduling risks (e.g. delays with module components before integration).
- The order in which sent modules will be assembled
- Grouping of modules within chosen launcher(s)
- Separate packaging for mirror elements and joining with structure is performed on orbit vs. mirrors are each attached to a module during launch.
- Time required to assemble given number of modules

As the order of assembly impacts the necessary grouping of the modules to be packaged per launch, and the assembly time is a good indication for scheduling subsequent launches so that the full system is operational within a certain time frame, it is clear that the formal definition of the assembly phase will have a measurable impact on the overall project. However, this is work to be done during a potential detailed design phase, which is not the case for this work. In spite of this, due to the importance of this assembly phase, a couple of scenarios are evaluated here.

The final consideration for the assembly phase would be the packaging method for the mirror elements provided they are treated as a singular layer of the assembled structure. It would be recommended, considering the fragility of these components, to design a structure capable of fitting inside the selected launcher and safely transporting the mirrors into GEO with no damage whatsoever. However, this raises the question of disposal of said mirror-carrier - the options for which range from de-orbiting for reuse, attachment to the assembled structure, or permanent disposal. Provided multiple space telescopes using similar modular architectures are envisioned, the use of a transportation module for mirror elements from Earth to GEO could be a feasible investment, however this is considered the realm of future study. The current preferred configuration would be a three-layered structure to be assembled on orbit, ensuring a wide range of servicing and assembly operations, thus increasing the possible servicing missions assembler can contribute to, effectively increasing potential revenue assuming sufficiently developed infrastructure.

During the nominal operation phase, the assembler will be docked with the space telescope and the system will be performing its scientific goals and transmitting this data back to Earth. The only consideration here is the eventuality of a servicing event in which case the following step approach will be used:

1. The housekeeping data indicating a fault is sent as a high priority message to the C&DH subsystem.
2. The C&DH evaluates the housekeeping data and sends a preliminary analysis indicating suspected location of fault.
3. The results of this analysis and the data used as input are sent to the ground station for interpretation.

4. The ground operators decide if self-diagnosis is correct or more information is necessary.
5. In the case of the latter option, the signal is given for the assembler to un-dock and perform visual inspection around a target area.
6. Once sufficient data to isolate the location and nature of problem, servicing can be considered.
7. In the event of an interface malfunction, it is attempted to rotate the modules (if possible) so as to make use of redundant elements currently not connected to any module before resorting to a module replacement.
8. If the failure is internal to one of the modules, a replacement will need to be sent before servicing can occur. The assembler will dock with the system or remain in docked position awaiting the replacement module, upon which servicing can occur.
9. Ground operators will communicate the estimated time/date of arrival of the spare module, as well as the proposed servicing approach.

In the case of servicing other nearby satellites with the assembler, the process is very similar to the above steps, minus the self-diagnosis phase. In this case, the ground operator would signal the need for servicing, location of the target and estimated time of arrival of spare parts. Shortly before rendezvous, the servicing plan will be uplinked to the free-flying assembler, which will return to dock with the space telescope upon completion of its task. Assuming sufficient servicing and/or assembly operations are performed successfully, it is expected that increasingly less oversight will be needed during such phases from human operators. Full autonomy would thus become the natural next step in the evolution of this technology.

The plan for end-of-life operations is not set at this point in the design, however, varying options exist depending on the success of this mission. Assuming the standard interface is a success and is imposed as a standard for modular architectures, it is completely feasible to imagine a semi-permanent observatory with regular technological updates through module replacement. Furthermore, assuming the need for such a telescope is at an end, or better locations need be investigated, the modular architecture allows for reuse of working modules in other subsequent missions as well. This means that it is possible to create a mission that will use components of this modular conceptual space telescope once it no longer provides any value. Of course, some elements that degrade over time in the space environment like solar panels and electronics systems would need to be discounted and disposal processes need to be considered for these as well. Although the actual choice in the options discussed until now heavily depends on the success of the inter-modular interface, it is clear that such an event would allow for much more flexibility not only in design, but in end of life operations as well. This aspect as well as the potential of reusing parts of existing space assets to create higher performance missions with lower costs are two critical advantages of transitioning to modular architectures.

Detailed Interface Design - Preliminary design

There are no thermal requirements, however the goal is to have some extent of thermal power transfer from module to module. This is not stated explicitly in the requirements, as seen below:

- MIST-E-1.0: Interface design shall consider two options - a lower, and a higher power implementation corresponding to ≤ 1.5 kW, and ≤ 8 kW, respectively.
- MIST-E-1.1: Interface shall be able to pass 8 kW of electrical power from module to module.
- MIST-E-1.2: Interface shall be able to pass voltages of 28 ± 1.4 V in the case of the low power implementation.
- MIST-E-1.3: Interface shall be able to pass voltages of 50 ± 2.5 V in the case of high power version.
- MIST-D-1.0: Interface design shall consider two options - a lower data link version for bus and housekeeping, and a higher data link version for scientific instruments.
- MIST-D-1.1: The high data rate version shall be able to transfer data at speeds up to 0.9 Gbps.
- MIST-D-1.2: The version in charge of housekeeping shall be able to transfer data at speeds up to 6.496 Mbps.
- MIST-S-1.0: The interface shall have a lateral natural frequency of at least 15 Hz.
- MIST-S-1.1: The interface shall have a longitudinal natural frequency above 60 Hz.
- MIST-S-1.2: The interface shall be able to withstand lateral launch loads of ± 3.0 g.

- MIST-S-1.3: The interface shall be able to withstand longitudinal launch loads of 8.5g in compression and 4.0 g in tension.
- MIST-S-1.4: The interface shall be able to withstand orbital perturbations up to $1.3464 \cdot 10^{-3} Nm$ on fully assembled system.
- MIST-S-1.5: The load bearing capabilities of the interface shall be comparable to current state-of-the-art options.
- MIST-S-1.6: The interface design shall allow for easy assembly and disassembly in order to facilitate servicing.
- MIST-S-1.7: The interface dimensions shall not exceed 0.4 by 0.4 *m*.
- MIST-S-1.8: The interfacing (height) dimension shall not exceed 0.02 *m*.

The letters MIST correspond to modular interface for space telescopes, whilst E, D and S correspond to electrical, data and structural subsystems respectively.

Now that the requirements have been defined, the remainder of this chapter is structured as follows: Section 4-1 treats the preliminary design of the interface, whilst Section 4-2 elaborates on the setup of all simulation types. Finally, Section 4-3 details the results thereof.

4-1 First Iteration of Interface Design

In this section, the design philosophy behind the modular interface will be explored, as well as the design choices that led to this preliminary design. In Subsection 4-1-1, the design choices will be explained that lead to the preliminary version of the interface. This is followed by the choice of material, as well as end-connectors for both data and electrical needs, covered in Subsection 4-1-2.

4-1-1 Preliminary Interface Design (MIST V0.0)

Existing interface design show a fairly high variability in design, however most of them require a lateral distance to be available for both assembly and disassembly. In the context of a space telescope, if one keeps the previous definition established in Chapter 3, one can identify a few layers that are stacked vertically: a base made out of the modules, a support layer for the main mirror aperture and the mirror aperture. Keeping this in mind, any direction in the plane of the layers can be defined as lateral. The problem with requiring a lateral spacing for disassembly is when one considers servicing of the most central module. If any of the existing standardized interface designs would be used, servicing the central module would entail disassembly of the whole structure so that the target module is accessible. This would imply that during this process the modular spacecraft would have to cease any functions that involve more than a single module, which results in a very long time where the spacecraft is effectively inactive. This is a very big problem since this means a single module failure could cripple the entire operational capability of the whole.

A solution to this would be utilizing a design that permits assembly along the vertical axis. This not only solves the problem of servicing, but can also simplify some of the proximity operations, thus requiring less sensors for precision alignment as the modules themselves can be used as both support and guide for the assembler unit. The drawback to such a system is that it requires an extra moving component that will take loads in the direction of assembly, henceforth referred to as vertical shear loads. Since moving components are generally avoided due to the risk of failure, it is desirable to simplify this locking mechanism as much as possible. With regards to the vertical assembly geometries, a few different geometries can be considered, as shown in Figure 4-1.

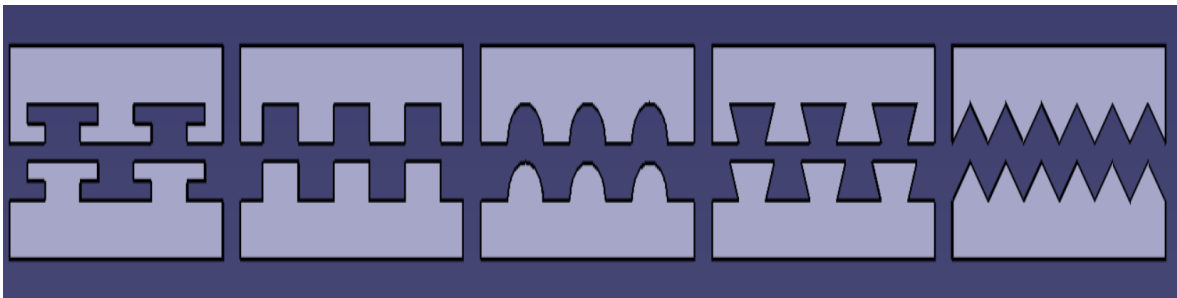


Figure 4-1: Top view of cross-sectional geometries considered for use in vertical assembly system

Out of these geometries only two of them can support tensile loads as well as vertical and lateral bending moments, namely the first and fourth, henceforth referred to as T-section and trapezoidal versions, respectively (in the industry, such linear slide systems are called box gib and dovetail, respectively). This implies that any choice outside of these two would require the aforementioned locking mechanism made for shear to also bear other types of loads. This is deemed to be unfavorable as it raises the complexity of the mechanism, hence heightening the risk of failure of the interface itself. As such, the two candidates left remain the T-section and trapezoidal options.

If one were to consider two plates identical in dimension with the same number of elements (T-shaped or trapezoidal), at first glance, the latter would be more resistant in tension, lateral shear, vertical and lateral bending moments, as well as twist. This is mainly due to the fact that a larger effective area would be used to take up the load. However, the T-shaped option offers increased stiffness and strength due to its ability to distribute loads efficiently in both X and Y directions [96], [97], [98].

Now that the choice of sliding assembly geometry is done, it is important to consider the locking element preventing motion in the vertical direction. One could consider different shapes that could bear the vertical shear load better, however there is also another matter to consider - flexibility. When aiming to produce a standardized interface it is important for it to be usable with various different concepts, otherwise it will only be usable by a select range of designs. As such, a certain degree of freedom of design or adaptation should be offered so that any space telescope concept can adapt this interface concept to their design requirements. This covers not only system requirements such as data and electrical transfer capabilities, but also subsystem requirements such as locking system actuation. If one were to consider linear actuation for this system, the options can be categorized into two classes

- rotating and non-rotating. With this in mind, a cylindrical locking system would offer the greatest flexibility in terms of actuator choice as it permits the use of both aforementioned classes. Furthermore, when considering the choice of T-section geometry, it is clear that the locking mechanism would have to be compact so as not to compromise the resistance of the section it goes through. As such, a circular cross-section, or in other words a cylindrical system, offers the perfect solution.

Combining the locking cylinder with the sliding assembly concept, and scaling to satisfy the MIST-S-1.7, MIST-S-1.8 dimension requirements leads to what will henceforth be referred to as MIST V0.0. This interface is comprised of three elements, two plates and the central locking cylinder, which are shown in Figures 4-2.

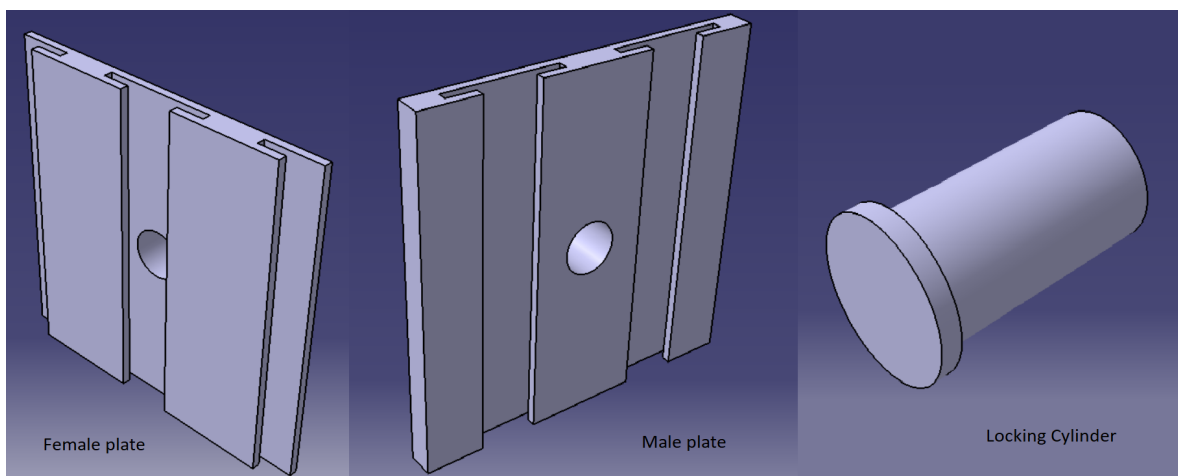


Figure 4-2: Overview of MIST interface components (V0.0)

With respect to the main dimensions a few constraints apply:

1. The female plate shall have two T-sections
2. To ensure structural integrity, the width of the lateral sections will be double the thickness of the vertical sections.
3. To avoid meshing issues, as well as to simplify manufacturing, whole numbers will be used for the first iteration of dimensions.

The first constraint will result in the male plate consisting of a full, central, T-section, and two halves, placed laterally. In order to satisfy the other two constraints, the notation shown in Figure 4-3 is used, where any whole T-section corresponds to a dimension of $4 \cdot x$, and the halves will correspond to $2 \cdot x + e$. The extra unknown e is added in so as to guarantee that any remainder from the first order dimension calculation will be shifted to the outside edges, ensuring their strength, as well as guaranteeing integer values for x .

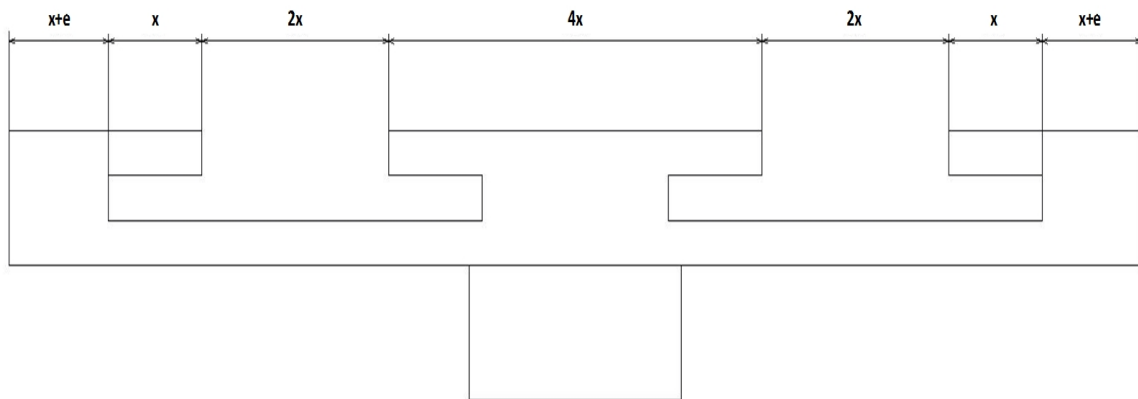


Figure 4-3: MIST V0.0 dimension notation for first order estimation

Based on this notation, Equation 4-1 can be compiled for the major dimensions of the T-sections.

$$2 \cdot x + e + 2 \cdot x + 4 \cdot x + 2 \cdot x + 2 \cdot x + e = W_{plate} \quad (4-1)$$

Grouping terms and substituting 400mm for the W_{plate} , which corresponds to the width of the plate, results in Equation 4-2:

$$12 \cdot x + 2 \cdot e = 400mm \quad (4-2)$$

Solving for maximum x and minimum e , whilst also constraining them to be whole numbers, leads to:

$$x = 33mm \quad e = 2mm$$

The height of the T-sections is chosen to be 20 mm in order to minimize the size of the interfacing elements. This serves to reduce volume that can not be used for other spacecraft sub-systems. The diameter of the central connector is chosen to be 60 mm, so as to ensure that at least 3 mm are left on each side from the edges of the hole to the sides of the T-flange. Due to space constraints, the full technical drawings of all the interface components will be included in Appendix A, Figures A-1, A-2, A-3, corresponding to the male plate, female plate, and locking cylinder, respectively.

In order to make a comparison with existing interfaces, MIST V0.0 needs to be scaled down to a W_{plate} of 120 mm, corresponding to the maximum lateral dimensions of existing state-of-the-art interfaces [43]. This results in Equation 4-3:

$$12 \cdot x + 2 \cdot e = 120mm \quad (4-3)$$

Solving for x and e in a similar fashion leads to:

$$x = 9$$

$$e = 6$$

The height of the T-sections for the scaled down version is restricted to 10 mm, so as to have similar dimensions as the existing interface concepts it will be compared to. The locking cylinder diameter is chosen to be 16 mm so as to allow for sufficient space to mount both electrical and data connectors, whilst keeping a 1 mm distance from the sides of the vertical section of the T. Similarly to the full-scale model, the technical drawings showing all dimensions are included in Appendix B, Figures B-1, B-2, B-3, corresponding to the male plate, female plate and locking cylinder, respectively.

4-1-2 Selection of Material, Data and Electrical Connectors

Since the design philosophy as well as major changes leading to different iterations of the MIST interface have been covered, it is time to explain the selection of materials and end connectors. When considering the former, a list of materials commonly used in spacecraft was compiled, the parameters of which are described in Tables 4-1 and 4-2. The data for the Titanium and Aluminium alloys was compiled from ASM MatWeb [99],[100], the properties of the Sintered Silicon Carbide from AZo Materials [101], and the properties of the carbon composites are courtesy of the Mechanical Engineer's Handbook [102]. As for the M55J and T800 composites, most of the data was compiled directly from Toray's manuals [103], [104], except for the densities which were computed using the individual densities of the carbon fibers and epoxy, with a 60% fiber ratio.

Table 4-1: Materials considered and their mechanical properties - Part 1

Material	Density (ρ)	Modulus of Elasticity (E)	Modulus of Rigidity (G)	Specific Thermal Conductivity
Titanium				
Ti-6Al-4V	4430 $\frac{kg}{m^3}$	113.8 <i>GPa</i>	44 <i>GPa</i>	6.7 $\frac{W}{m \cdot K}$
Al 7075-T6	2810 $\frac{kg}{m^3}$	71.7 <i>GPa</i>	26.9 <i>GPa</i>	130 $\frac{W}{m \cdot K}$
Sintered Silicon Carbide (SSiC)	3100 $\frac{kg}{m^3}$	400.1 <i>GPa</i>	175.475 <i>GPa</i>	100 $\frac{W}{m \cdot K}$
<i>UHM^{pitch}</i>				
Carbon	1800 $\frac{kg}{m^3}$	165 <i>GPa</i>	63 <i>GPa</i>	110 $\frac{W}{m \cdot K}$
<i>UHM^{PAN}</i>				
Carbon	1660 $\frac{kg}{m^3}$	110 <i>GPa</i>	41 <i>GPa</i>	14 $\frac{W}{m \cdot K}$
<i>UHS^{PAN}</i>				
Carbon	1610 $\frac{kg}{m^3}$	63 <i>GPa</i>	21 <i>GPa</i>	4.8 $\frac{W}{m \cdot K}$
<i>M55J</i>	1586 $\frac{kg}{m^3}$	338 <i>GPa</i>	N.A.	155.6 $\frac{W}{m \cdot K}$
<i>T800</i>	1520 $\frac{kg}{m^3}$	163 <i>GPa</i>	N.A.	11.3 $\frac{W}{m \cdot K}$

Table 4-2: Materials considered and their mechanical properties - Part 2

Material	Yield Strength Tension (σ_{Y_t})	Yield Strength Compression (σ_{Y_c})	Yield Strength Shear (τ_Y)
Titanium Ti-6Al-4V	880 MPa	970 MPa	-
Al 7075-T6	503 MPa	503 MPa	331 MPa
Sintered Silicon Carbide (SSiC)	320.35 MPa	3203.65 MPa	-
<i>UHM^{pitch}</i> Carbon	900 MPa	280 MPa	41 MPa
<i>UHM^{PAN}</i> Carbon	1380 MPa	760 MPa	80 MPa
<i>UHS^{PAN}</i> Carbon	3500 MPa	1380 MPa	80 MPa
<i>M55J</i>	2020 MPa	890 MPa	68 MPa
<i>T800</i>	3290 MPa	1490 MPa	135 MPa

Although the composites show the highest strengths with respect to tensile loading, they are very bad with respect to shear. Furthermore, it is important to consider that the strengths shown above are all for in-plane or along fiber, in the other directions the materials are much weaker. This is the main reason for not choosing these options. As for the SSiC, it is a ceramic material which inherently means it is brittle. The observant reader will notice that for this material the strength registered is actually the ultimate strength since ceramics do not present elastic behaviour. Considering that the density of the material is quite high and no resistance was found for shear, this material is discounted as a choice. From the remaining two materials, the Ti-6Al-4V and Al 7075-T6, the latter is chosen for fairly consistent strength in all directions, good thermal conductivity and low density. This choice will ensure that the interface is light weight and is capable of passing a fair amount of heat without requiring any extra thermal subsystem addition to the interface itself, thus simplifying the design.

For the data connector, the shape and fastening mechanism are critical as these have a major influence on the complexity of the mechanisms necessary, as well as contributing as a risk factor for failure. In the case of ends that require additional motion to fasten the connection once coupled (e.g. bayonet or screw-in types), an additional actuator would need to be involved in the design. Such additions would add unnecessary complexity to the interface whilst the only advantage they would bring is superior fastening of the connection once achieved. Considering the interface design described up until now this is not required, since the central locking system already fastens the system sufficiently. As such, these types of connectors are discounted as options, thus leaving only plug-in and push-pull connector types in the discussion. If one were to consider solely the radiation reinforced alternatives qualified for space usage, there are numerous iterations of high data rate cables that conform to the SpaceWire standard, such as those offered by Axon [105], or even Gore [106]. In the case of

the latter, data rates up to 400 Mbps are achieved which is not sufficient for the application at hand, but Axon offers much higher speed cables up to 10 Gbps or even 40Gbps for their AxoMach versions [107]. This is a performance much higher than the requirements set for this interface design, however this is not the main reason for discounting this choice. The types of cables offered by both of these companies, as well as many others that offer connectors that adhere to the Spacewire standard, are of the push-pull type, with pins as ends. The issues with pin configurations are two-fold - firstly, they require precise alignment, and secondly due to the dimensions of said pins the risk of damage arises when connecting and disconnecting repeatedly or when shocks are involved.

This does not pose a problem in traditional spacecraft design as all systems are assembled on the ground, never to be disconnected or reconnected. In the case of a modular system where the intent is not only to assemble a large scale spacecraft but also to enable the possibility of servicing and replacement of modules, this becomes an issue that needs to be addressed. Due to this very reason it was decided to also consider options that are not normally used in space design, but that may be tailored to be used as such in the future. When considering costs, availability, compactness, technological progress over a limited time span as well as innovation, the first thing that comes to mind is the USB cable. Due to its heavy usage in the industry as well as day to day activities, this type of connector has evolved through leaps and bounds, especially when considering data rates achievable. The most important factor that cannot be overlooked is that the end-connectors for such systems have also evolved over time leading to a fairly recent model using magnets to connect and disconnect part of the end of such a cable. This technology ensures that very little force is applied to the actual end-connector thus minimizing the risk of damage. Furthermore, the very slight magnetic force produced by this system actually enhances alignment, without any additions of fancy sensors that ensure it. For a system such as MIST this is a very alluring solution. The choice of using this technology comes with numerous advantages, from ready availability, to low cost, ease of assembly, and lower risk of damage. It can also be further argued that compactness also plays a key role as even smaller interface models can be built based on the design logic explained up until now (a good example of this being the scaled down version of MIST). The only disadvantage is that this type of connector has not yet been used as a solution for traditional spacecraft, thus no thoughts have been given on radiation reinforcing it to withstand the space environment. However, if this type of data connector were to be included into a design meant as a next stepping stone in space design, which enabled future progress at an accelerated rate, such as a flexible concept for large scale space assembly, the aforementioned disadvantage seem insignificant and easily resolved. As such, it is decided to use a magnetic USB cable as the data transfer mechanism. The USB chosen for the manufactured interface was a NetDot 3rd Generation cable readily available on Amazon [108] as not only is it low cost, but more importantly it offers a magnetic system allowing for data connection irrelevant of rotation between the ends (360° alignment).

When considering the electrical connector, the main criteria of choice were alignment considerations and ease of contact. As such any types involving pins were discounted from the search for the same reasoning mentioned above, and the only types considered were spring-loaded connectors and electrical tabs. When considering the design of MIST, it was important to consider how easily contact could be made with each type of connector. For the former option, even a slight distance between the two ends allows for the connection to be successful, however physical contact is required for the latter. For this reason as well as compactness,

spring-loaded connectors were chosen for MIST. For the full-scale interface the LSH High Power Connector [109] was selected as an option, however this is a mere recommendation based off of the chosen requirements. Given lower or higher requirements, the design can be easily adjusted to accommodate for a different connector. As for the scaled-down interface (in other words the one that was manufactured), Mill-Max 821 Spring-Loaded Pogo Pin Header Strip with 2 pins [110] was selected as a solution.

4-2 ANSYS simulation setup

In order to evaluate the load tolerances for the various versions of the interfaces, ANSYS Workbench was selected as the most suitable candidate. This software has multiple advantages, amongst the most important being the capability of performing finite-element analysis (FEA), as well as the ability of importing and editing pre-existing CAD models.

When using such a program, the first step is to set up the type of simulation, in this case, Static Structural, as the goal is to find the limit loads of the interface assembly. The next step is a decision on what exactly should be simulated, either the actual load case or a simplified assembled state or both. In other words, one can choose to import the whole assembly into the simulation environment and evaluate the results of the actual load cases, or import elements one by one and simulate the assembled state for each one. For the purposes of this thesis, it was decided that both types of simulations will be performed, as more information can be gained by correlating the results of both types of simulations (e.g. what the weaker element of the assembly is, how much more resistant the assembled state is versus the disassembled state under similar loading conditions). As such the simulations can be categorized as:

1. Assembled state of male and female plates (single component)
2. Assembly load evaluation (major components assembly)

4-2-1 Assembled state simulation setup

Once the simulation object and type have been selected, the Design Modeler module can be used to import pre-existing CAD models, as well as edit them. The main need for editing is for establishing coherent constraints based on how the interface will be included in a spacecraft assembly. In other words, only the plate elements of the interface will be considered as part of the spacecraft walls, whilst the T sections will be external so that assembly can take place. As such, these need to be separated so that the lateral surfaces of the plates can be fixed, as shown in Figures 4-4a, and 4-4b, corresponding to the simulations of the male and female plate, respectively.

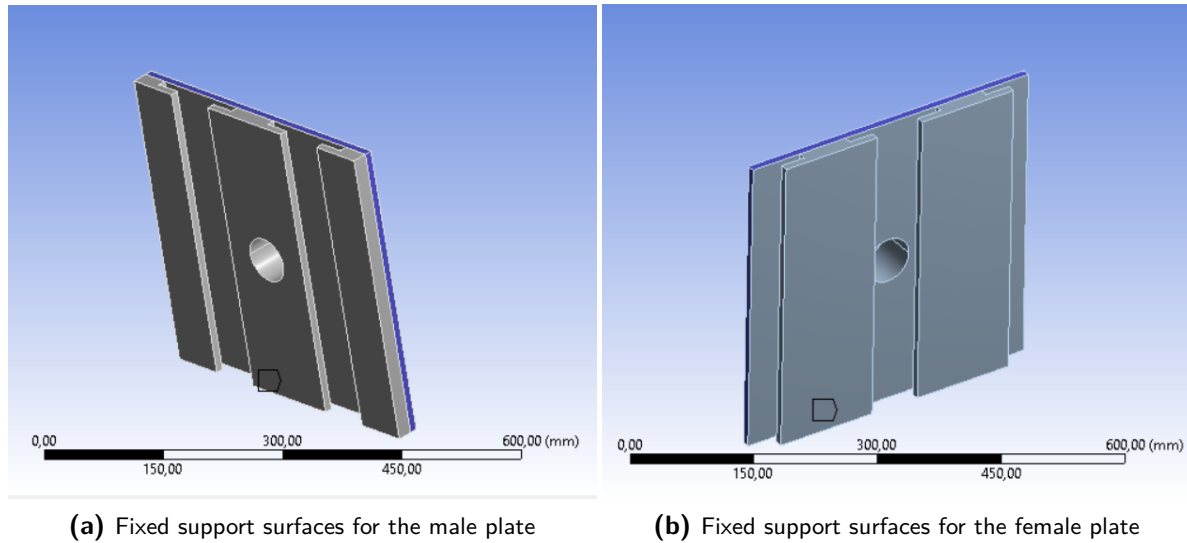


Figure 4-4: Assembled state simulation - fixed support constraints

It is necessary to mention that the same principle applies to all versions of the interface, as such only the first version is shown for clarifications on simulation setup. Now that the object of the simulation has been imported and edited, the next step is to add the material of the object to be evaluated. As established previously in Subsection 4-1-2, an Aluminium alloy will be used for the physical implementation of the interface. ANSYS permits to tailor material properties to any need, or directly import existing materials from their in-built material library. In this case, the material library included the Aluminium alloy T60.

Once this material is applied to the simulation object, the next phase is to define a mesh. Using the function body sizing, a mesh with a specific (user inputted) size of mesh element can be created. For consistency reasons, the same element size will be used for both the assembled state and assembly simulations. In consequence, the element size is chosen to be 10 mm, for reasons that will be elaborated on in Subsection 4-2-2.

The next step is to select the boundary conditions and their type. In this case Fixed Support is used, as shown in Figure 4-4. This is sufficient with respect to constraints, as such only the applied load needs to be selected. The load cases evaluated in this simulation can be split into forces and moments. In the case of forces, a 10 kN baseline value will be used for stress calculation, while for moments a 1 kNm value will serve for stress evaluations. Both classes will be applied as surface loads or moments, respectively. A total of seven distinct load cases can be distinguished:

1. Tension, as shown in Figure 4-5

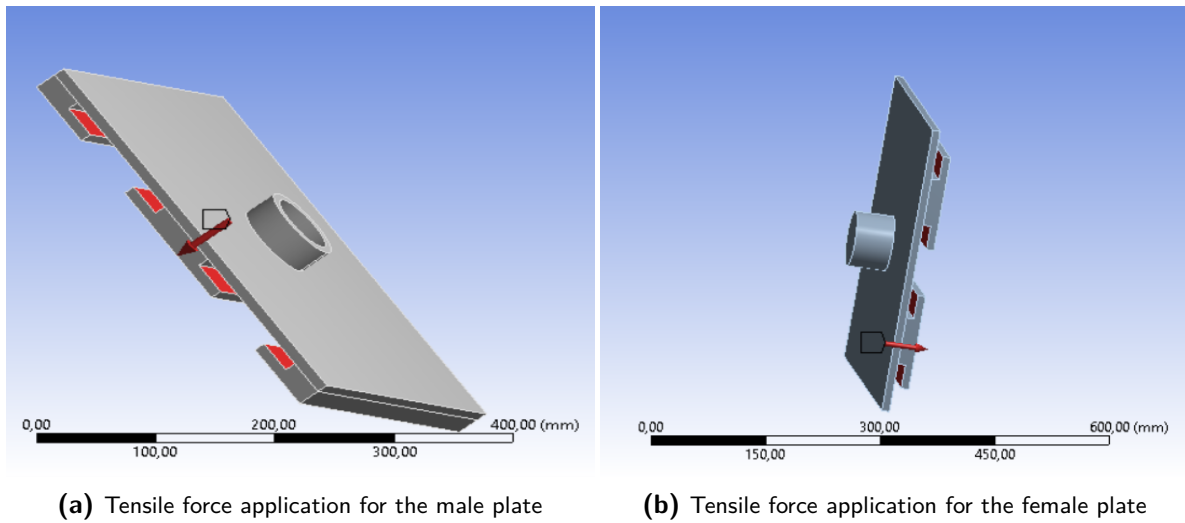


Figure 4-5: Tensile force direction and surface application for assembled state

2. Compression, as shown in Figure 4-6

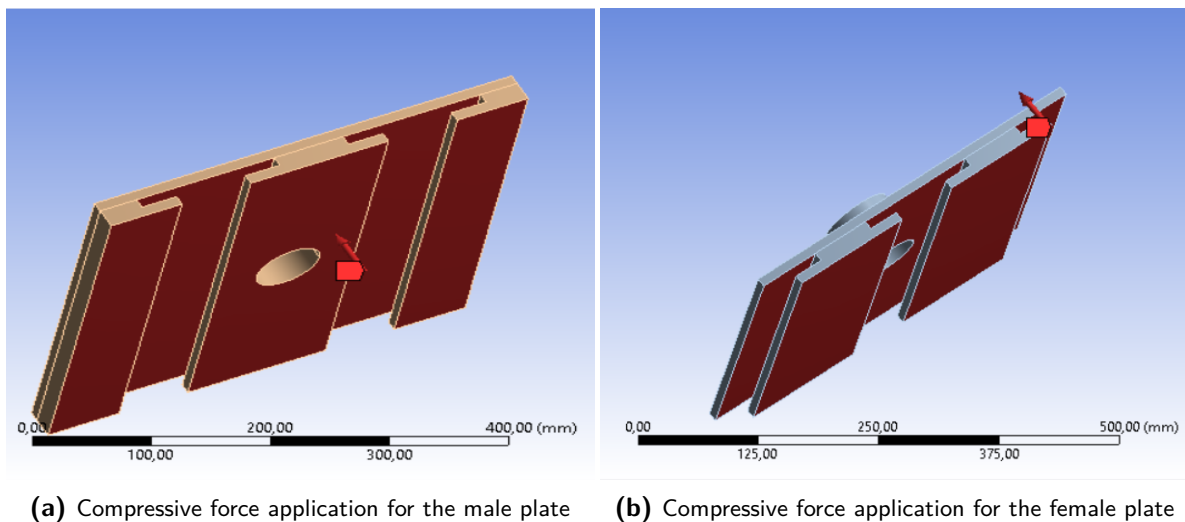


Figure 4-6: Compressive force direction and surface application for assembled state

3. Vertical Shear, as shown in Figure 4-7

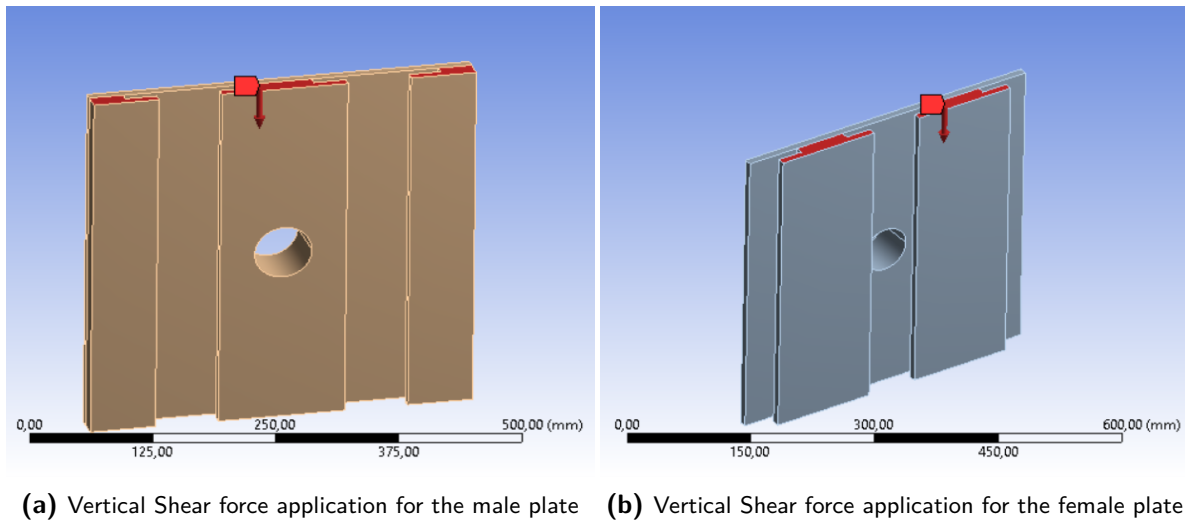


Figure 4-7: Vertical Shear force direction and surface application for assembled state

4. Lateral Shear, as shown in Figure 4-8

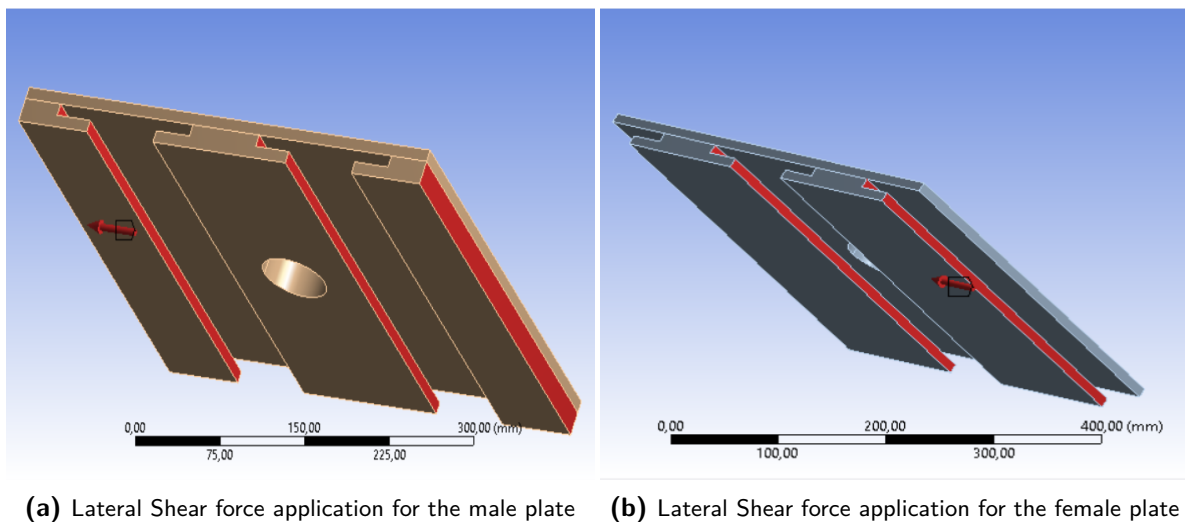
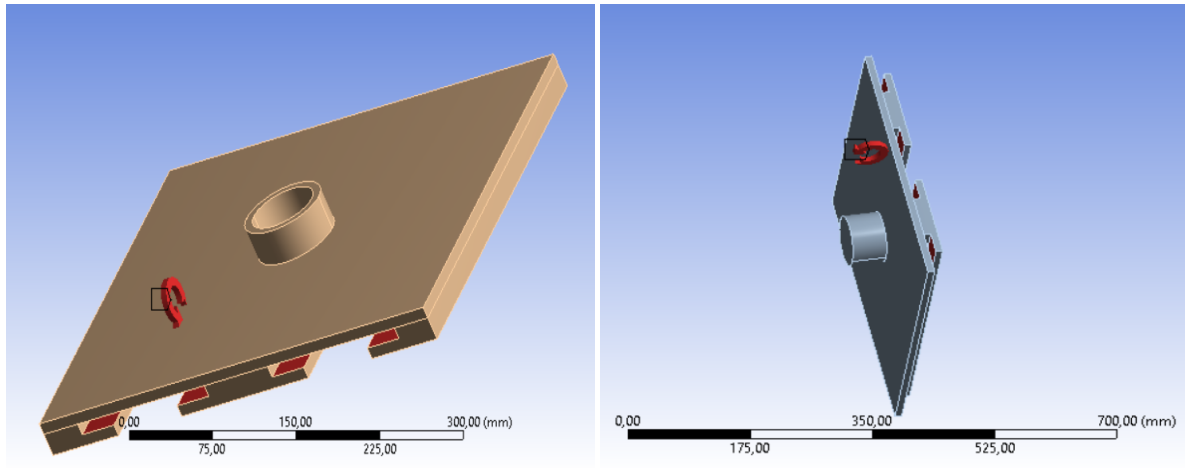


Figure 4-8: Lateral Shear force direction and surface application for assembled state

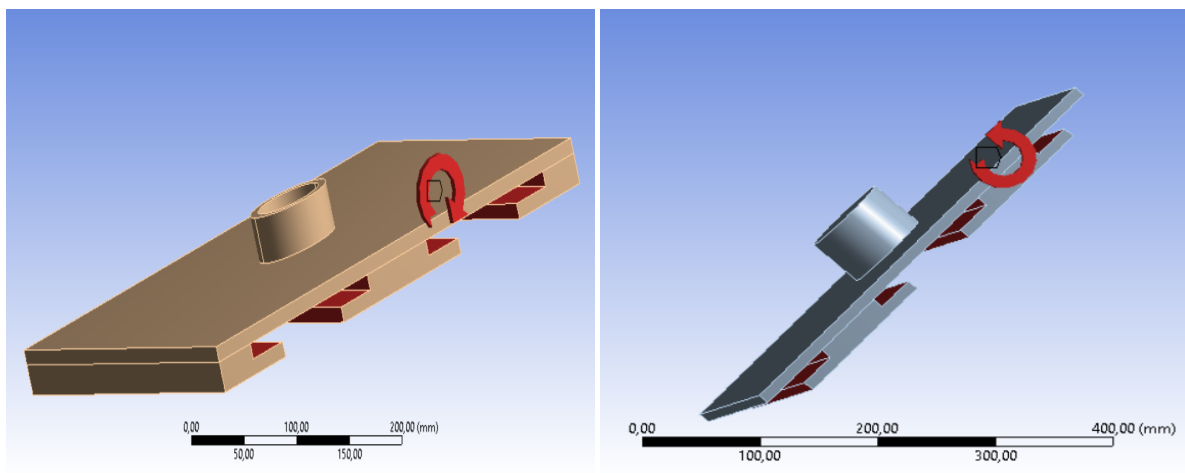
5. Vertical Bending moment, as shown in Figure 4-9



(a) Vertical Bending moment application for the male plate (b) Vertical Bending moment application for the female plate

Figure 4-9: Vertical Bending moment direction and surface application for assembled state

6. Lateral Bending moment, as shown in Figure 4-10



(a) Lateral Bending moment application for the male plate (b) Lateral Bending moment application for the female plate

Figure 4-10: Lateral Bending moment direction and surface application for assembled state

7. Twist moment, as shown in Figure 4-11

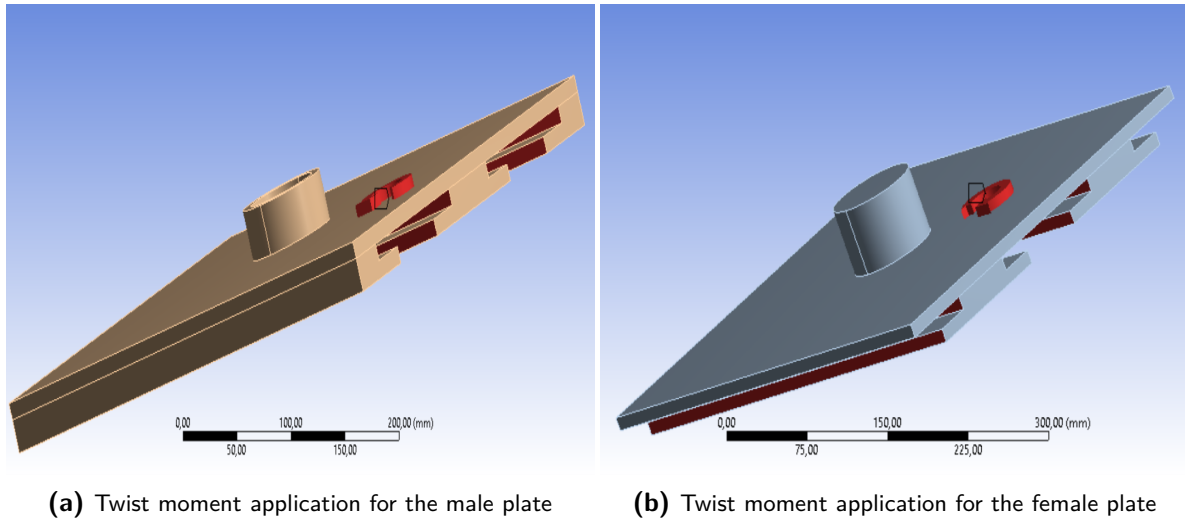


Figure 4-11: Twist moment direction and surface application for assembled state

In all the above figures, the red arrows indicate the direction of application, whilst the red surfaces are those on which the forces or moments are applied.

4-2-2 Assembly simulation setup

Similarly to the assembled state simulation, importing the geometry and adding material are done in the exact same way. One slight difference is that the editing is only performed on the female plate due to the decision to use it as the fixed element when considering loads and stresses. The selection of faces for which the fixed support constraint is used are shown in Figure 4-12.

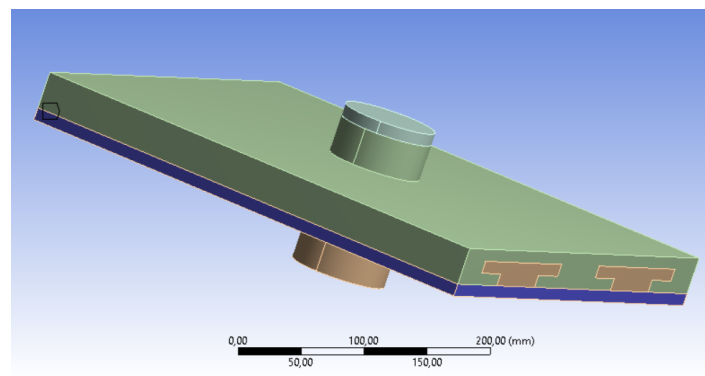


Figure 4-12: Assembly - fixed support constraints

The choice of fixing the female plate is due to the fact that higher stresses were expected when constraining the female plate to be fixed instead of the male plate. The main reason for this is that especially under tensile loads the thickness of the lateral plate sections not containing T-sections will cause a reduction in strength when compared to the male plate where the

lateral sections contain T-sections which would prevent deflection to a certain extent, thus distributing stress better. These expectations were also confirmed through simulation.

For the assembled state simulations, the fixed support constraints are sufficient, however for the assembly itself the contact surfaces need to be constrained as well. Bearing this in mind a few options are available, among which frictional contacts. For the purpose of this simulation, this type of contact is selected with a frictional coefficient of 1.2, corresponding to machined Aluminium alloys [111]. This is enough to satisfy all boundary conditions for the system. As such the only things missing are the mesh and load application.

With respect to the mesh, one would usually select as small a mesh size as possible in order to more accurately pinpoint potential stress concentration areas, as well as reduce errors between averaged stresses and unaveraged stresses computed by the finite element analysis. Furthermore a good rule of thumb when performing such simulations is that the mesh element size should never exceed the smallest dimension found in the object. In this case, the smallest dimension is the thickness of the T-sections, namely 10 mm for the full-scale model, 5 mm for the scaled down version. When using these sizes however, a relatively large difference can be found between the averaged stresses and unaveraged stresses, as will be seen in Sections 4-3 and 5-2. Normally a smaller mesh size would be in order, however when going below an 8mm sized mesh element, the total number of mesh elements exceeds the limits of the ANSYS license. This presents a unique problem as using a mesh element that cannot be multiplied by an integer to equal the smallest dimension of the object is usually inadvisable. The reason for this is that the point selection resulting from such a mesh would, quite often, not include points on corners, which are expected stress concentration points. Based on this reason and the software limitation for total element number it was decided to select 10mm as element size for the full scale model, and 5mm for the scaled down version (the one for performance comparison with existing interfaces).

Now that the mesh and constraints are set, the load cases can be defined. The application surfaces and force directions for each individual case are illustrated in Subfigures 4-13a, 4-13b, 4-14a, and 4-14b, for tensile, compressive, vertical shear, and lateral shear forces, respectively. Additionally, Subfigures 4-15a, 4-15b, and 4-15c, show the same thing for vertical bending, lateral bending, and twist moments, respectively.

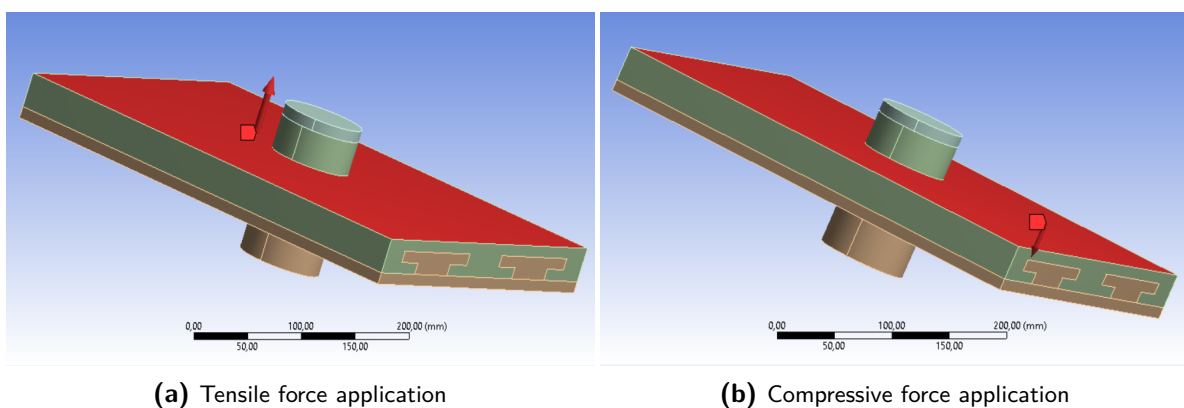


Figure 4-13: Tension and compression load cases - direction and surface application for assembled state

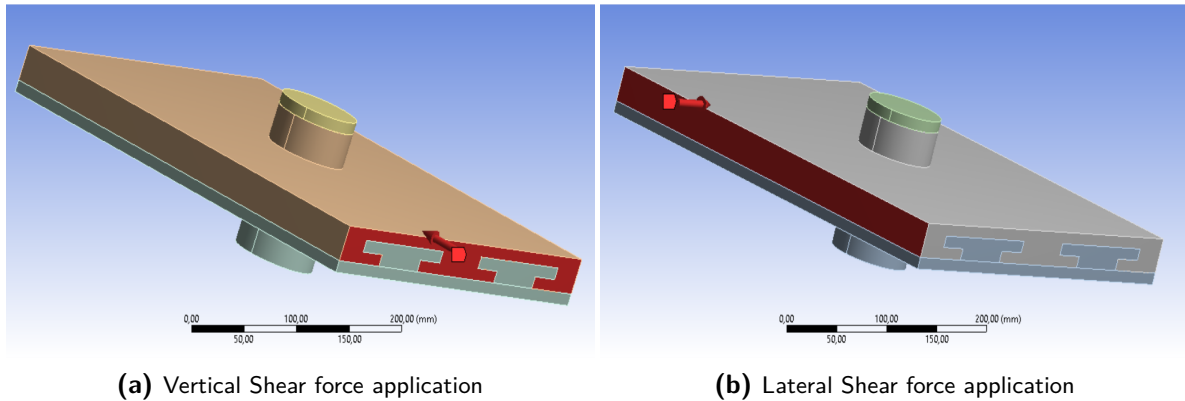


Figure 4-14: Vertical and lateral shear load cases - direction and surface application for assembled state

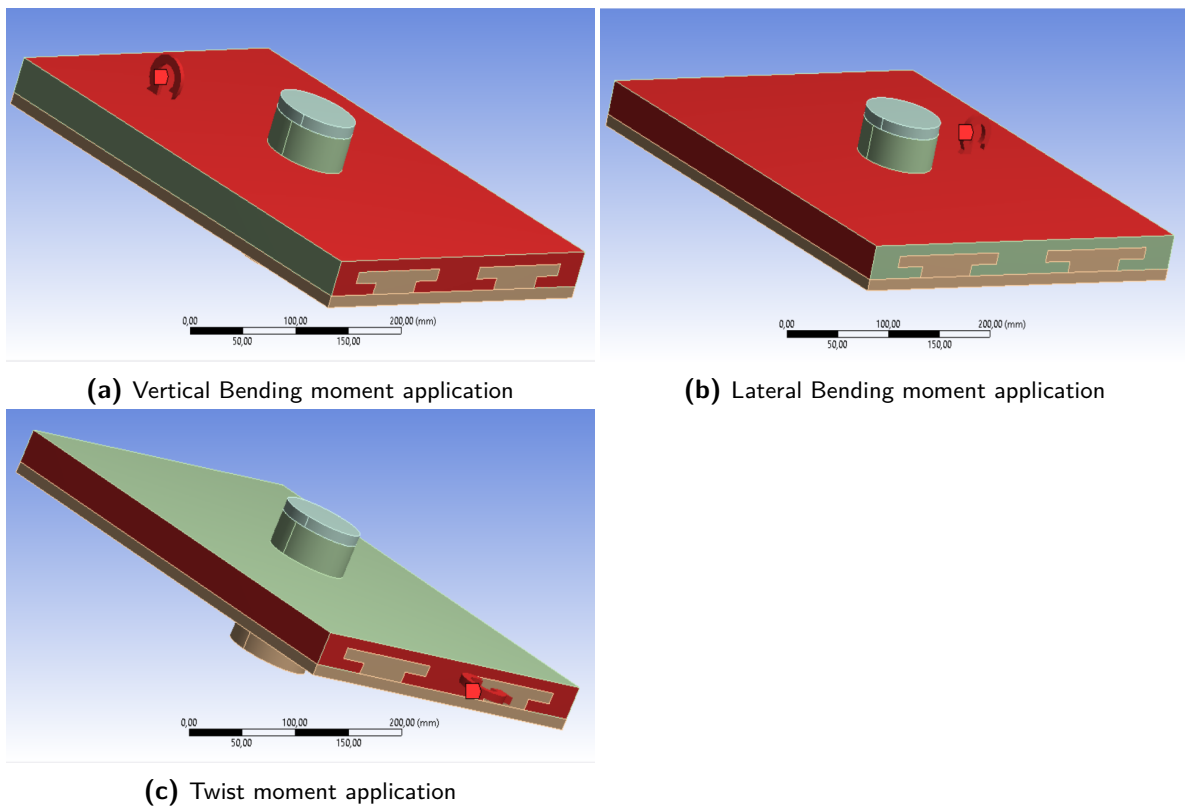


Figure 4-15: All moments - direction and surface application for assembled state

Similarly to the assembled state simulation, the baseline values for forces is 10 kN, and 1kNm is used for moments. Using the same simulation logic, the maximum values for each load case are computed using both Von Mises and shear stress failure criteria.

4-3 ANSYS simulation results for interface V0.0

The first tests performed were on MIST V0.0 under the assembled state conditions. For the tensile case the stress distributions are shown in Figure 4-16, with Subfigures 4-16a, and 4-16b corresponding to the Von Mises and maximum shear stress distribution for the male plate, and Subfigures 4-16c, and 4-16d, for the female plate.

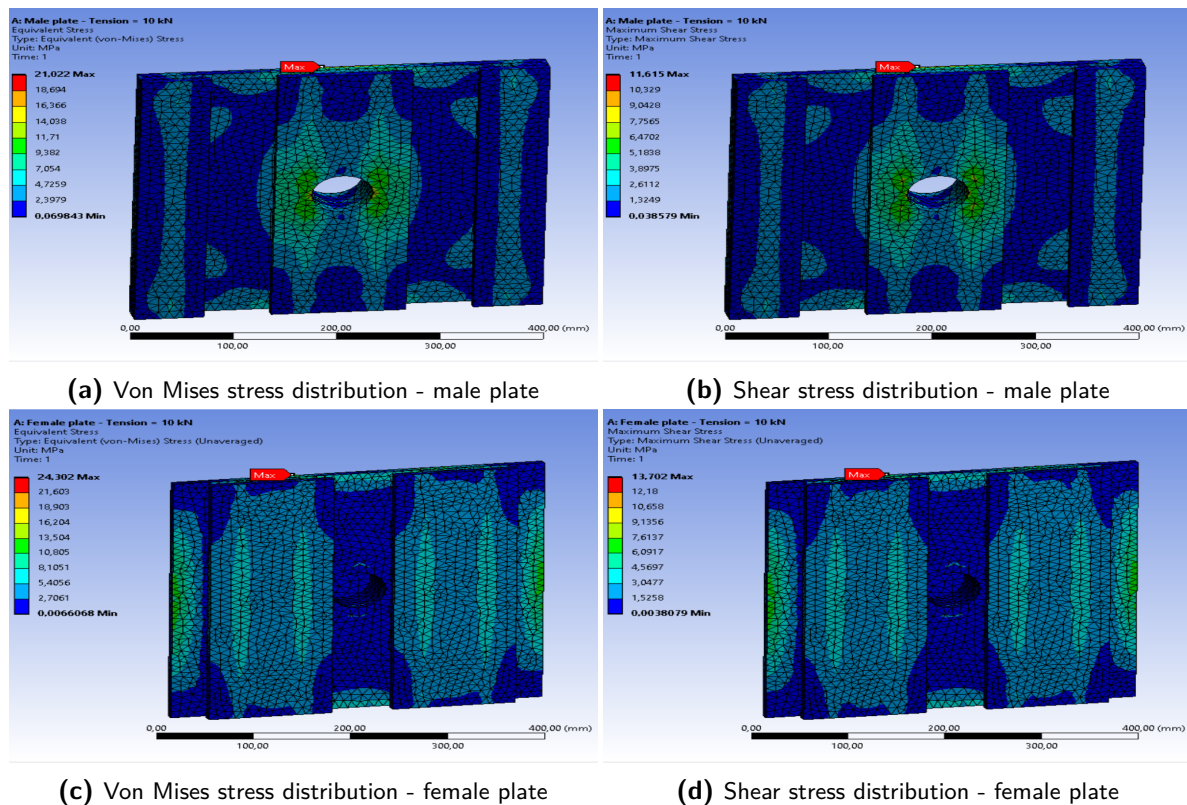
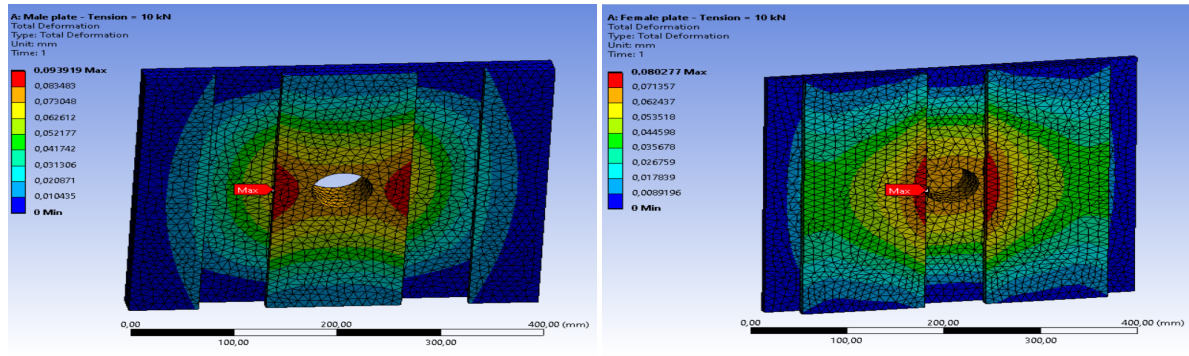


Figure 4-16: Stress distribution under 10 kN tensile load - Assembled state MIST V0.0

For the male plate, the stress is mainly distributed around the central part of the T-section, however the maximum stress found through simulation is at the top or bottom of said section, due to symmetry. Considering the maximum is exactly on an edge, it can be assumed that this is a stress concentration given by the mesh placement, and that the true maximum stress will occur around the central hole. However, the idea that this is the true maximum cannot be dismissed completely, as such this value will not be excluded when computing the maximum load for the tensile case.

Similarly, the maximum stress point for the female plate also occurs at the top of the plate, at the back of one of the T-sections. It is important to mention that symmetry applies here, as such there are actually four points where maximum stress occurs, two at each T-section, at the top and the bottom. This also seems to be a stress concentration as the maximum points of stress should occur towards the sides of the plate, where the resistance is weakest. This seems to be the case when considering the stresses along the sides of the female plate, where slightly lower values than the maximum are registered. This is expected due to the fact that

the tensile force is applied to the flanges of the T-sections. As for the male plate, this logic is not sufficient to discount the simulated results for peak stress, hence these will be taken into consideration when computing limit loads. The deformation associated this load case is shown in Figure 4-17.

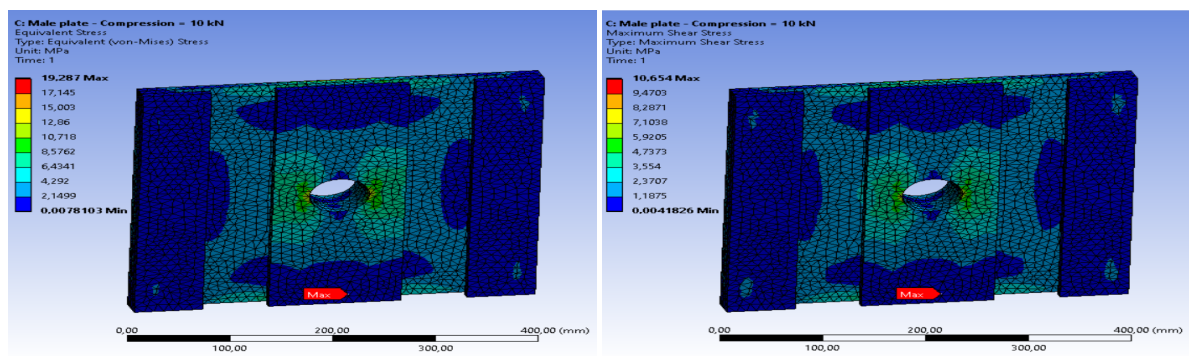


(a) Deformation of male plate (b) Deformation of female plate

Figure 4-17: Deformation under 10 kN tensile load - Assembled state MIST V0.0

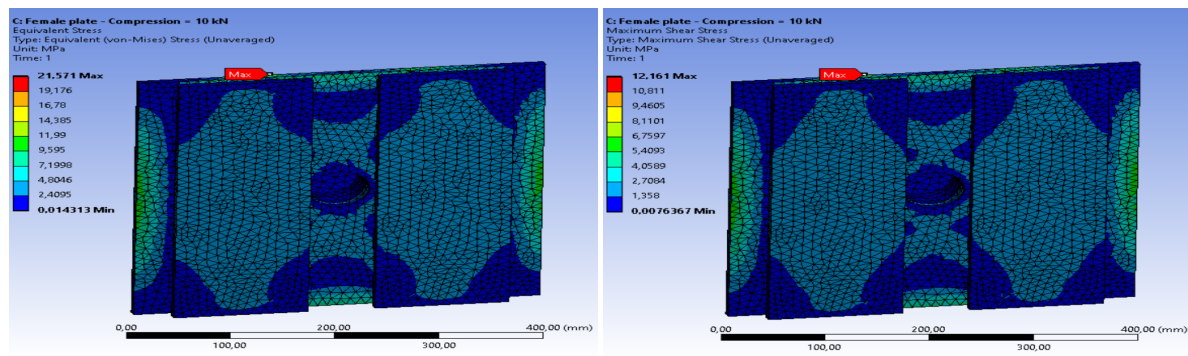
For the male plate, the maximum stresses seem to be concentrated around the edges of the flanges of the central T-section. This makes sense as the central hole somewhat compromises the structural integrity of the aforementioned section for tensile loads, and the edges will experience the highest stress due to the nature of the loading. Similarly, the central facing edges of the T-sections are the peaks for the female plate. One could even argue that the deformations of the two plates seem to be complementary in the case of tension.

The results of the compressive case with respect to stress distributions are shown in Figures 4-18 and 4-19, where Subfigures 4-18a, and 4-18b pertain to the Von Mises and maximum shear stress distribution for the male plate, and Subfigures 4-19a, and 4-19b, for the female plate.



(a) Von Mises stress distribution - male plate (b) Shear stress distribution - male plate

Figure 4-18: Stress distribution under 10 kN compressive load - Assembled state MIST V0.0 male



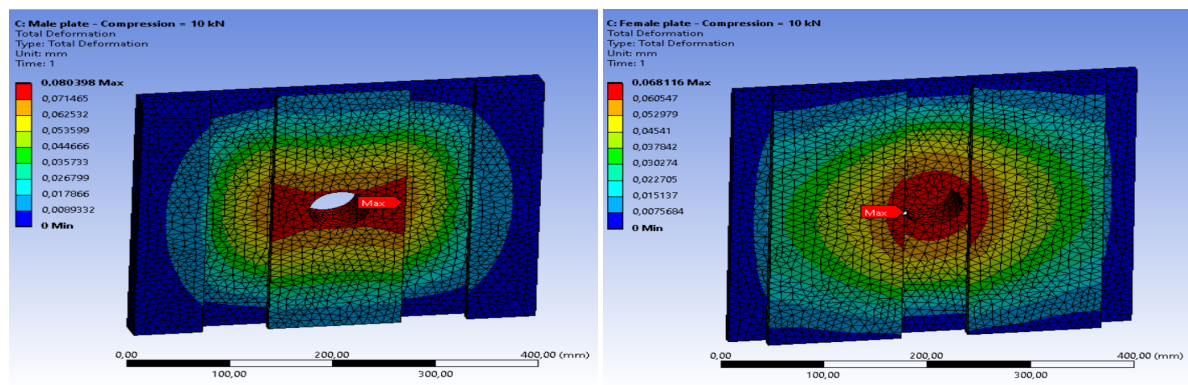
(a) Von Mises stress distribution - female plate

(b) Shear stress distribution - female plate

Figure 4-19: Stress distribution under 10 kN compressive load - Assembled state MIST V0.0 female

From the point of view of maximum stress points, a very similar situation to the tensile case can be observed. The male plate shows two symmetric peaks at the top and bottom of the central T-section, whilst the female plate shows four points of maximum, at the top and bottom of the two T-sections. The main difference in stress distribution for the male plate in the case of compression versus tension is the absence of higher stresses in the lateral T-flanges, and higher values on the plate sections connecting them. Whereas for the female plate, the stress is more evenly distributed across the T-sections, with no stress concentrations occurring at the points of connection between the lateral and vertical sections of the T-flanges.

The corresponding deformation is shown in Figure 4-20.



(a) Deformation of male plate

(b) Deformation of female plate

Figure 4-20: Deformation under 10 kN compressive load - Assembled state MIST V0.0

The deformation for both plates not only shows symmetry, but also the concentration of highest values towards the middle of the plates. This can be attributed to the fact that any hole or cylindrical cut-out present weakens the structure around said element. The deformation subsides the closer to the edges one looks, which makes sense considering the definition of fixed support constraints.

The results of the vertical shear load case are shown in Figure 4-21, where Subfigures 4-21a,

and 4-21b correlate with the Von Mises and maximum shear stress distribution for the male plate, and Subfigures 4-21c, and 4-21d, for the female plate.

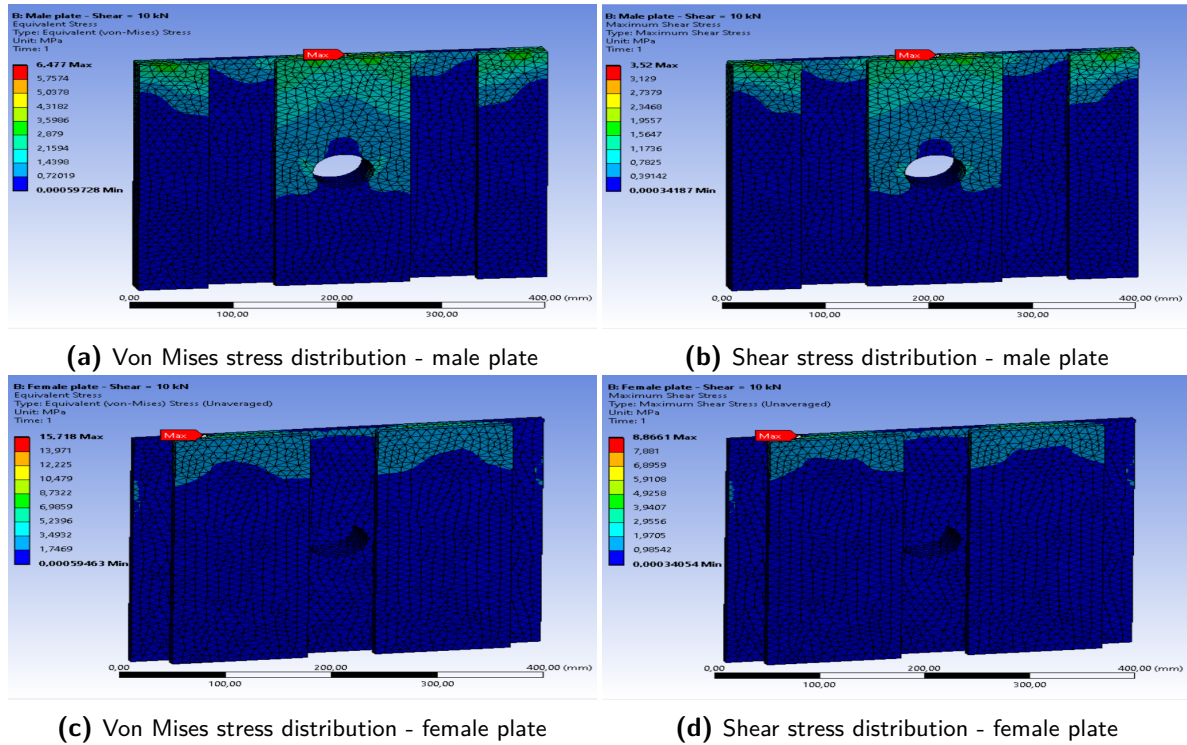


Figure 4-21: Stress distribution under 10 kN vertical shear load - Assembled state MIST V0.0

In the case of vertical shear, the stress is concentrated along the surface of application, namely the top of the plates. It decreases linearly towards the bottom, as expected. The male plate shows only one maximum, at the top of the central section, however two symmetrical points (with respect to maximum) can also be observed where stress peaks. As for the female plate, four points of maximum on each side of the T-sections can be observed, due to symmetry.

The resulting deformation is shown in Figure 4-22.

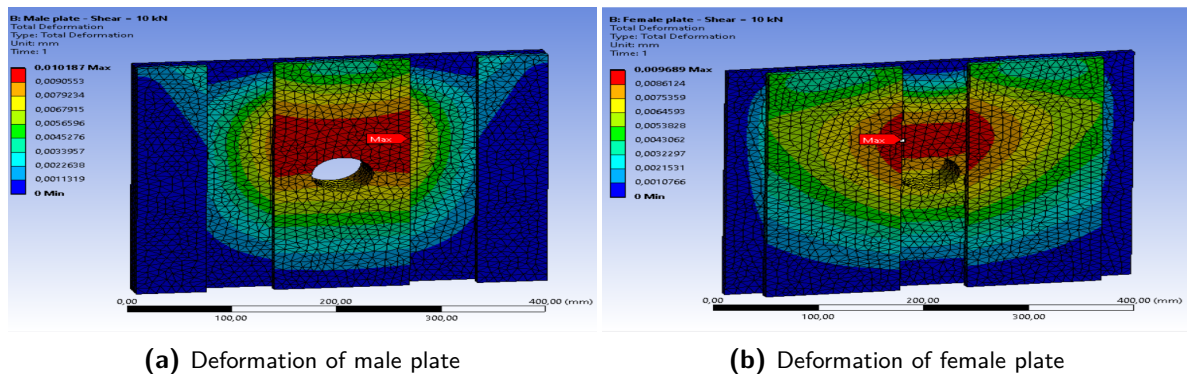


Figure 4-22: Deformation under 10 kN vertical shear load - Assembled state MIST V0.0

The deformation distribution shows symmetry with respect to the vertical axis, however the maximum is shifted upwards from the central part of each element. This makes sense, as the central hole or cylinder cut-out, in the case of the female plate, does subtract from the structural integrity of the element, however the load is focused on the top-most edge. As such, stress can be distributed fairly well until the point where structural strength is reduced, thus producing the patterns above.

The stress distributions resulting from lateral shear are shown in Figure 4-23, where Subfigures 4-23a, and 4-23b correspond to the Von Mises and maximum shear stress distribution for the male plate, and Subfigures 4-23c, and 4-23d, for the female plate, respectively.

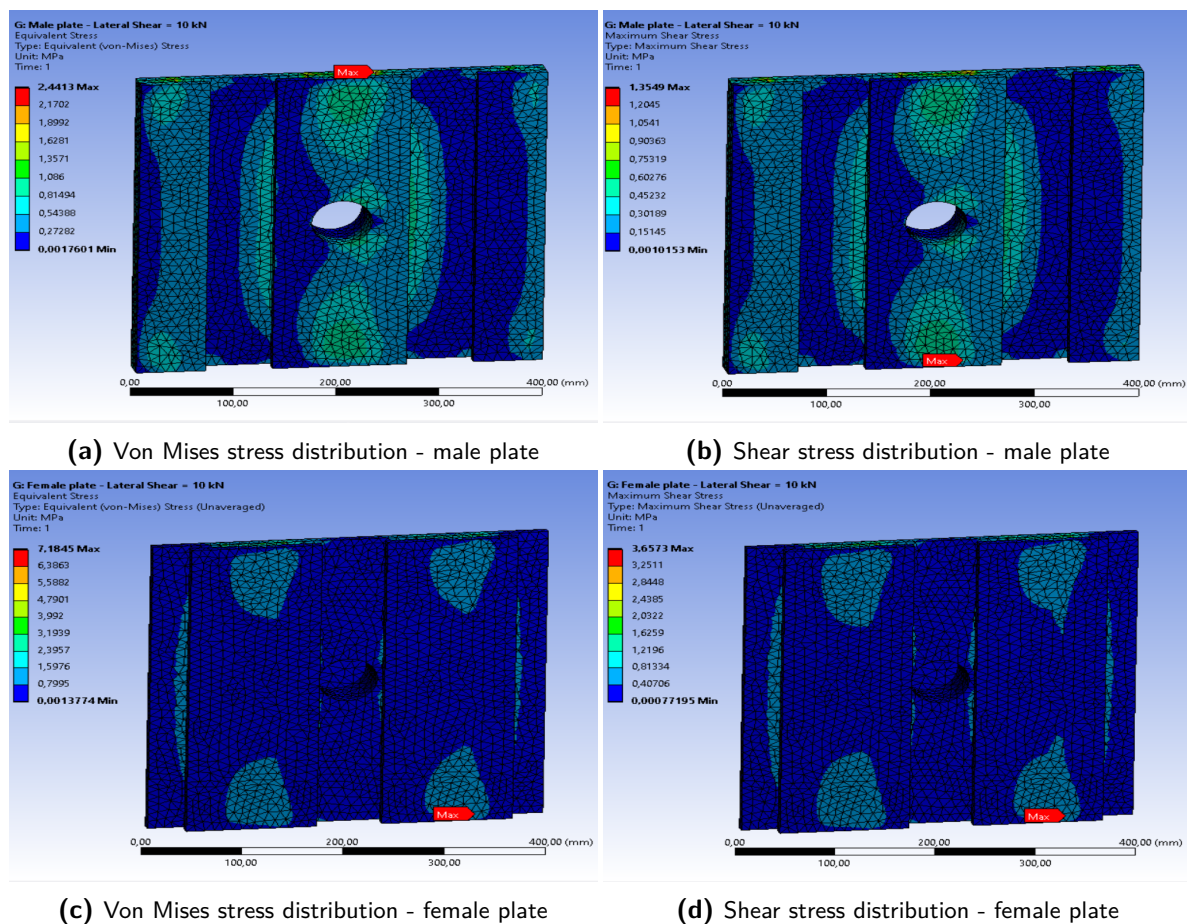


Figure 4-23: Stress distribution under 10 kN lateral shear load - Assembled state MIST V0.0

Under the load of lateral shear, the higher stress tends to be concentrated in the direction of force application. Even without considering the simulation setup, one can tell from the above figures that the force is applied from right to left. Again, the point of maximum stress occurs on the top/bottom of the central T-section, in the case of the male plate, and the two T-sections, in the case of the female plate. This is unexpected, but it cannot be dismissed in the process of calculating limit loads. The ensuing deformation is shown in Figure 4-24.

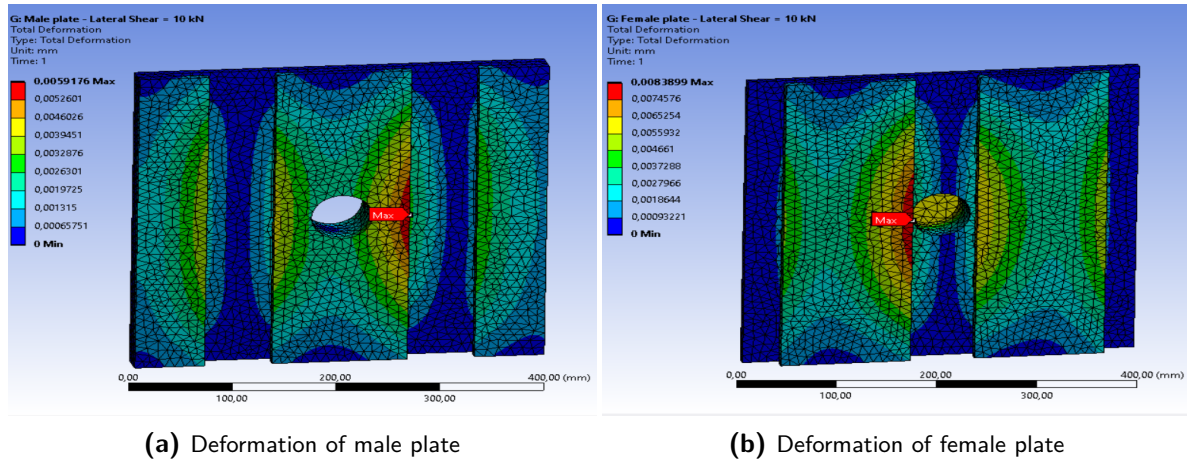


Figure 4-24: Deformation under 10 kN lateral shear load - Assembled state MIST V0.0

The peaks with respect to deformation occur on the right-hand side of the central T-section for the male plate. This is due to the combination of force application and the hole in the middle which compromises the structural integrity of the piece to a certain degree. For similar reasons, the maximum deformation for the male plate occurs on the left-hand side T-section due to the direction of force application, but towards the central cylindrical cut-out.

The stress distributions associated with the vertical bending moment case are illustrated in Figures 4-25 and 4-26, where Subfigures 4-25a, and 4-25b correlate with the Von Mises and maximum shear stress distribution for the male plate, and Subfigures 4-26a, and 4-26b, for the female plate, respectively.

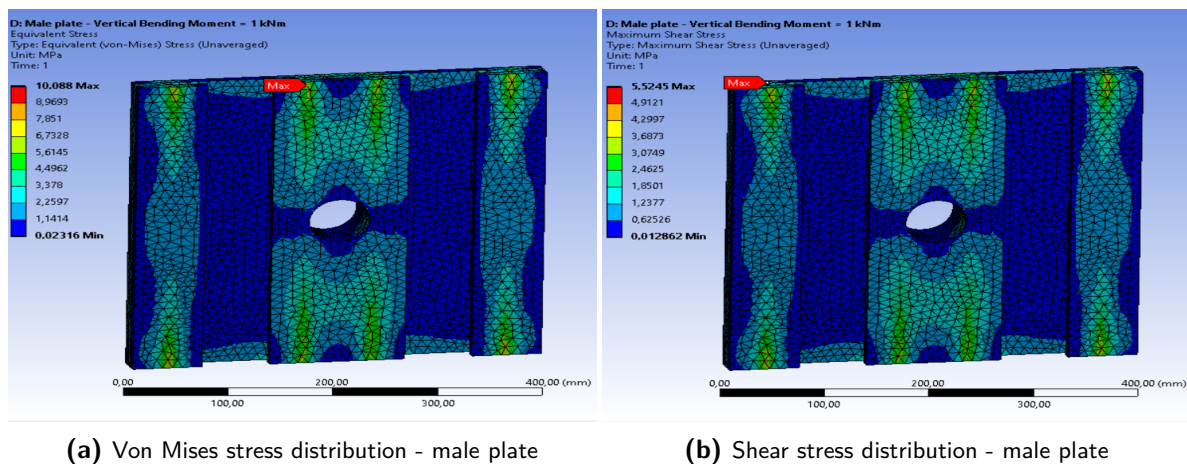
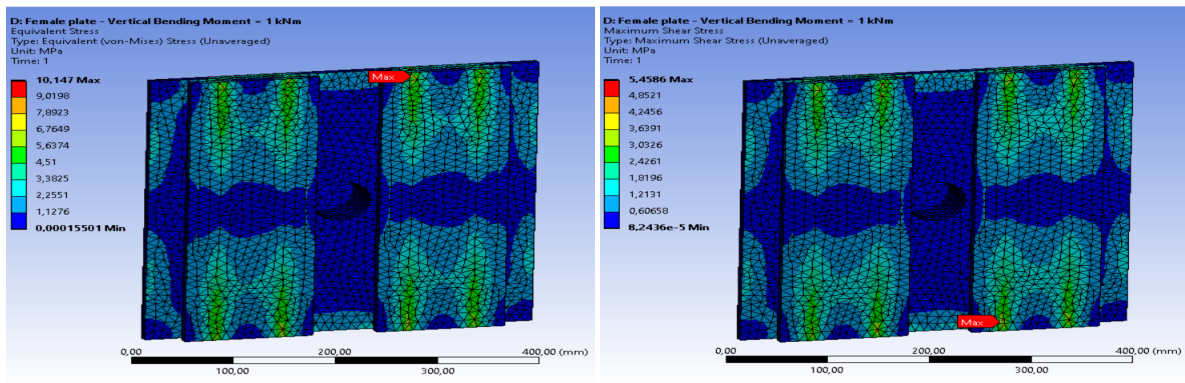


Figure 4-25: Stress distribution under 1 kNm vertical bending moment - Assembled state MIST V0.0 male

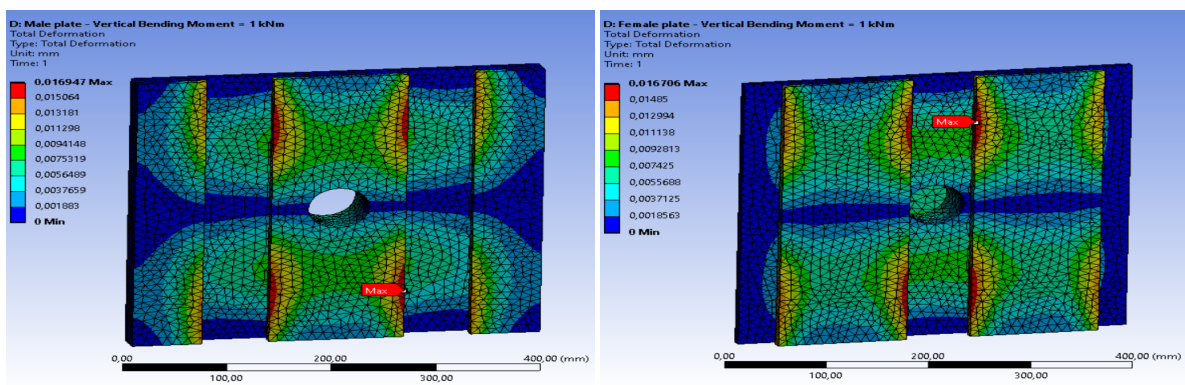


(a) Von Mises stress distribution - female plate

(b) Shear stress distribution - female plate

Figure 4-26: Stress distribution under 1 kNm vertical bending moment - Assembled state MIST V0.0 female

The stress distribution for both male and female plates show symmetry both along the vertical and the lateral axis. The peaks for the male plate occur on the central T-section again, two at the top, and two on the bottom, on each side of this element. To complement these results, the female plate shows similar positions for maximum values, two points on the top and two on the bottom, on the central-facing sections of the T-flanges. The resulting deformation is shown in Figure 4-27.



(a) Deformation of male plate

(b) Deformation of female plate

Figure 4-27: Deformation under 1 kNm vertical bending moment - Assembled state MIST V0.0

The peaks with respect to deformation follow a similar pattern to the stress ones. They occur symmetrically on both top and bottom, on the central or centrally-facing flanges of the T-sections respectively, depending on male or female. Furthermore, one can discern high values for deformation on the other T-section flanges, however they are not as high as the maximum points.

The lateral bending moment load case results with respect to stress distributions are shown in Figure 4-28, where Subfigures 4-28a, and 4-28b pertain to the Von Mises and maximum shear stress distribution for the male plate, and Subfigures 4-28c, and 4-28d, for the female plate.

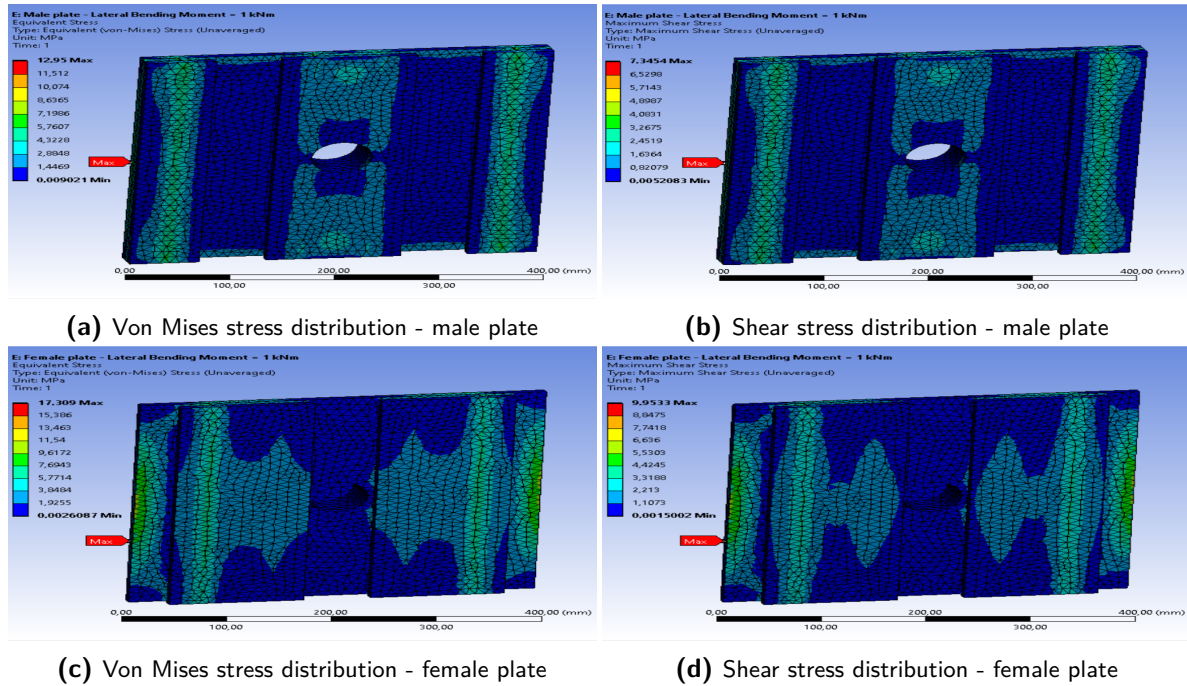


Figure 4-28: Stress distribution under 1 kNm lateral bending moment - Assembled state MIST V0.0

When considering the lateral bending moment case, one can discern concentrations of stress both along the middle T-section, as well as the sides, in the case of the male plate. The observant reader will notice a slightly greener hue on the edges, since these are the primary structural elements countering the load. The maximum point again occurs on the outside, in a section where no stress concentrations are observed around the peak. This is most likely a stress concentration caused by the mesh placement. In the case of the female plate, the highest stress occurs around the sides of the plate. This is due to the combination of load application and fixed support constraint definition. Four symmetrical points of maximum can be identified in the case of the female plate, two above and two below with respect to the lateral symmetry line, on each side of the element. The associated deformation is shown in Figure 4-29.

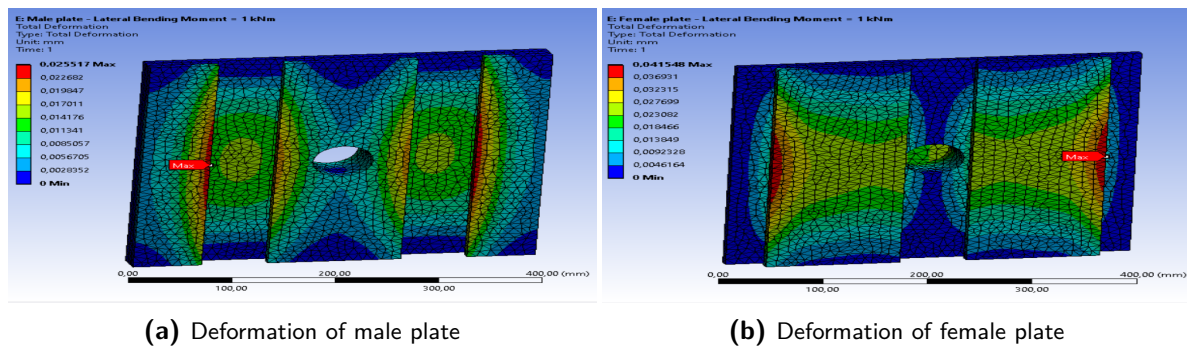


Figure 4-29: Deformation under 1 kNm lateral bending moment - Assembled state MIST V0.0

With regards to the deformation, the male and female plates show complementary behaviour. The maximum points occur on the outermost lateral flanges of the T-sections, the main structural elements that prevent motion in the lateral bending case. When considering the male plate, high concentrations can also be observed at the edges of the central T-section. This is due to the load surface definition including these flanges as well. This fact is further confirmed by the lack of such concentrations on the female plate in said area.

The stress distributions for the moment of twist load case are shown in Figure 4-30, where Subfigures 4-30a, and 4-30b corresponding to the Von Mises and maximum shear stress distribution for the male plate, and Subfigures 4-30c, and 4-30d, for the female plate.

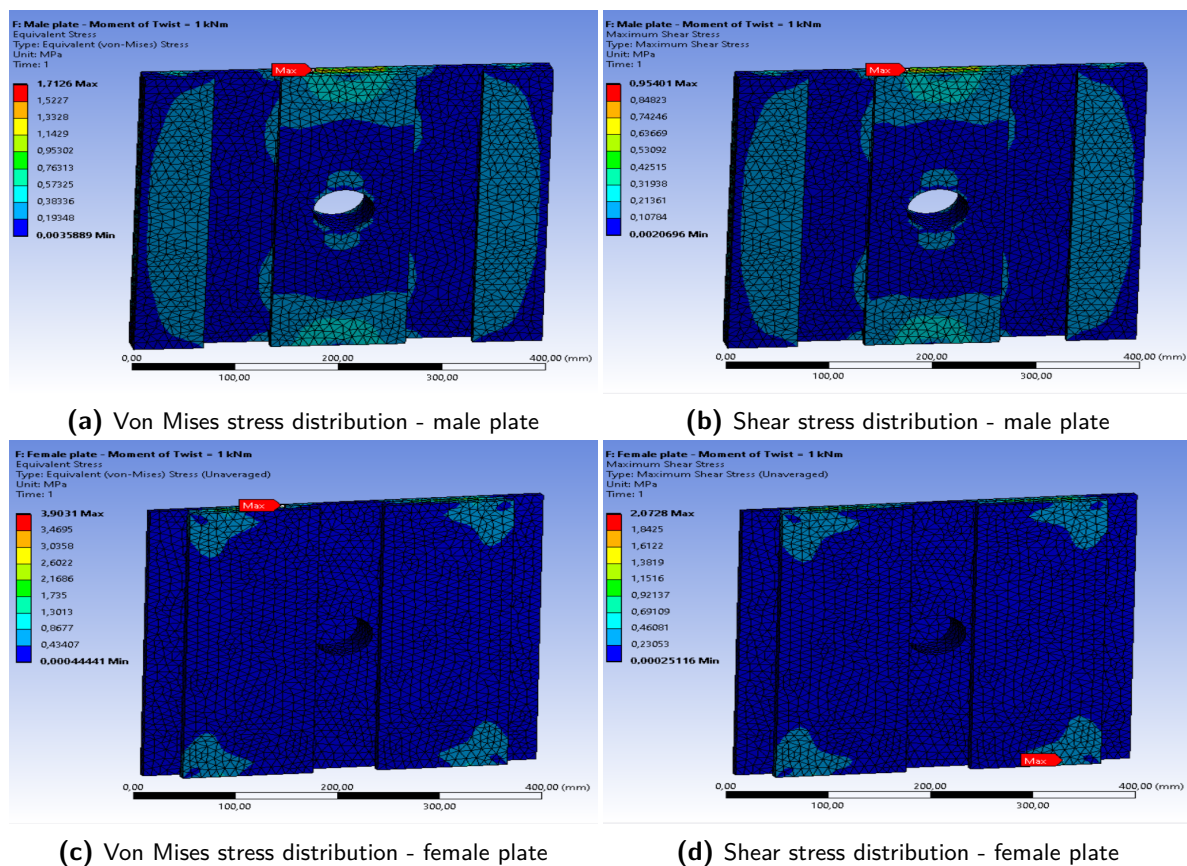


Figure 4-30: Stress distribution under 1 kNm moment of twist - Assembled state MIST V0.0

The stress resulting from the moment of twist loading seems to show somewhat circular distributions in the case of the male plate. The maximum points are four-fold, two on the top and two on the bottom of the central T-section. The stress is concentrated around these maximums as well as on the flanges of the lateral T-sections. In the case of the female plate, the stress is concentrated solely around the top and bottom of the outermost flanges of the T-sections. This can be attributed to the combination of load and constraint definition. The stress peaks are four-fold, symmetrically placed with respect to both vertical and lateral axes. The corresponding deformation is shown in Figure 4-31.

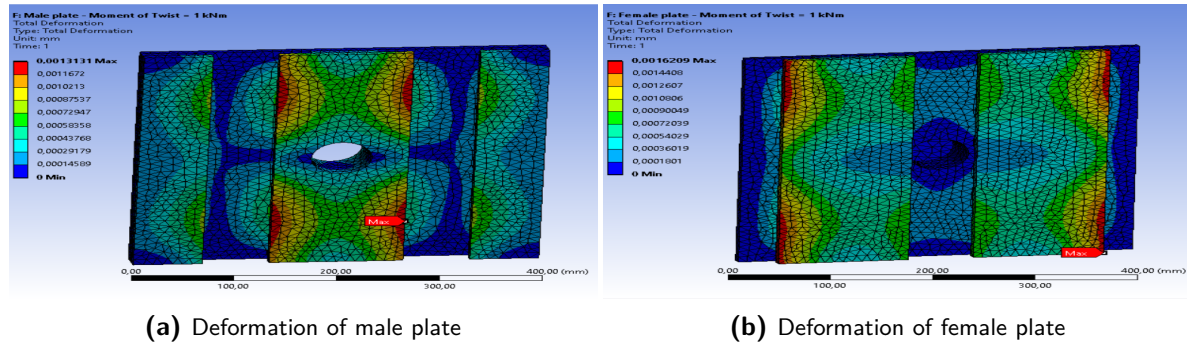


Figure 4-31: Deformation under 1 kNm moment of twist - Assembled state MIST V0.0

In this load case, the distribution of deformation in the female and male plates do not complement each other. Whilst the former shows peaks around the exterior edges of each T-section, the male exhibits maximums on the sides of the central T-section alone. This is mainly due to the way the force application is defined in ANSYS. Furthermore, one could argue that this can construe an additional reason to simulate the assembled state as well so as to confirm these results. With respect to the actual peaks, both plates exhibit four such points in symmetry around both vertical and lateral axes.

A summary of maximum Von Mises, shear stresses and deflection is compiled in Tables 4-3 and 4-4. This can be used to compare the differences between the assembled state simulation and the actual assembly correspondent. Furthermore, both averaged and unaveraged values are included both for completeness as well as to give a more in depth view of the accuracy and inner workings of the simulations performed.

Table 4-3: Part and assembly load simulation results MIST V0.0 (ANSYS) - Part 1

Loading case	Female Plate	Male Plate	Assembly
Tension - 10 kN			
Von Mises (avg)	17.714 MPa	20.31 MPa	12.794 MPa
Von Mises (unavg)	24.302 MPa	27.363 MPa	16.633 MPa
Max Shear (avg)	9.7341 MPa	11.217 MPa	7.0189 MPa
Max Shear (unavg)	13.702 MPa	15.207 MPa	9.2741 MPa
Deflection	80.277 μm	94.038 μm	46.879 μm
Compression - 10 kN			
Von Mises (avg)	15.725 MPa	18.775 MPa	4.5446 MPa
Von Mises (unavg)	21.571 MPa	25.37 MPa	7.7403 MPa
Max Shear (avg)	8.6397 MPa	10.295 MPa	2.4988 MPa
Max Shear (unavg)	12.161 MPa	14.093 MPa	4.4668 MPa
Deflection	68.116 μm	80.484 μm	14.398 μm
Shear (vertical) - 10 kN			
Von Mises (avg)	6.453 MPa	6.5101 MPa	9.6966 MPa
Von Mises (unavg)	15.714 MPa	14.226 MPa	10.695 MPa
Max Shear (avg)	3.4499 MPa	3.4664 MPa	5.0158 MPa
Max Shear (unavg)	8.8661 MPa	7.6655 MPa	5.601 MPa
Deflection	9.689 μm	10.272 μm	22.252 μm

Table 4-4: Part and assembly load simulation results MIST V0.0 (ANSYS) - Part 2

Loading case	Female Plate	Male Plate	Assembly
Shear (lateral) - 10 kN			
Von Mises (avg)	3.4145 MPa	2.5007 MPa	4.4482 MPa
Von Mises (unavg)	7.1845 MPa	4.6389 MPa	8.1711 MPa
Max Shear (avg)	1.9517 MPa	1.3904 MPa	2.4272 MPa
Max Shear (unavg)	3.6573 MPa	2.503 MPa	4.5488 MPa
Deflection	8.3899 μm	5.9049 μm	8.3282 μm
Lateral bending moment - 1 kNm			
Von Mises (avg)	9.8643 MPa	9.6995 MPa	9.8511 MPa
Von Mises (unavg)	17.309 MPa	12.684 MPa	16.615 MPa
Max Shear (avg)	5.3219 MPa	5.3767 MPa	5.4292 MPa
Max Shear (unavg)	9.9533 MPa	7.1806 MPa	8.9409 MPa
Deflection	41.548 μm	25.572 μm	50.593 μm
Moment of twist - 1 kNm			
Von Mises (avg)	1.7509 MPa	1.7562 MPa	2.972 MPa
Von Mises (unavg)	3.9031 MPa	3.3401 MPa	6.7572 MPa
Max Shear (avg)	0.99697 MPa	0.9798 MPa	1.663 MPa
Max Shear (unavg)	2.0728 MPa	1.8388 MPa	3.8795 MPa
Deflection	1.6209 μm	1.3182 μm	7.5502 μm
Vertical bending moment - 1 kNm			
Von Mises (avg)	6.1007 MPa	6.4835 MPa	8.5704 MPa
Von Mises (unavg)	10.147 MPa	10.072 MPa	13.294 MPa
Max Shear (avg)	3.3812 MPa	3.5681 MPa	4.5927 MPa
Max Shear (unavg)	5.4586 MPa	5.5738 MPa	7.2828 MPa
Deflection	16.706 μm	16.956 μm	28.39 μm

One of the first things that is readily apparent from these results is that there is a relatively large variation in results for the averaged and unaveraged stresses. As mentioned previously, these are mainly due to the mesh size, however this could not be reduced further due to program limitations. A summary of these differences in terms of percentile is illustrated in Tables 4-5 and 4-6.

Table 4-5: Percentile difference between averaged and unaveraged stress values - MIST V0.0 Part 1

Stress type	Sim type	Tension	Compression	Vertical Shear	Lateral Shear
Von Mises	Female	37.19 %	37.18 %	143.51 %	110.41
	Male	34.73 %	35.13 %	118.52 %	85.5 %
	Assembly	30.01 %	70.32 %	10.3 %	83.69 %
Shear	Female	40.76 %	40.76 %	157 %	87.39 %
	Male	35.57 %	36.89 %	121.14 %	80.02 %
	Assembly	32.13 %	78.76 %	11.67 %	87.41 %

Table 4-6: Percentile difference between averaged and unaveraged stress values - MIST V0.0
Part 2

Stress type	Sim type	Lateral Bending	Twist	Vertical Bending
Von Mises	Female	75.47 %	122.92 %	66.33 %
	Male	30.77 %	90.19 %	55.35 %
	Assembly	68.66 %	127.36 %	55.12 %
Shear	Female	87.03 %	107.91 %	61.44 %
	Male	33.55 %	87.67 %	56.21 %
	Assembly	64.68 %	133.28 %	58.57 %

The largest differences for all simulation types can be seen in the vertical shear and moment of twist loading cases. Interestingly enough, a factor of ten lower differences are found for the assembly when under vertical shear as compared to individual plates. This is suspected to be due to better load transfer through the structure as well as improved loading definition only possible when coupling the male and female elements as a whole. The tensile and shear cases show higher variation between averaged and unaveraged stresses for the assembled state simulations in comparison to the assembly one. This is most probably the result of load definition, as forces can be applied directly to the T-section flanges instead of being transmitted through interaction of the assembly. Due to these significant variations in stresses, one cannot discount these results as pure errors, and more simulations and testing would be necessary in order to fully validate the interface for launch. In this case, the safest solution is to guide oneself from the highest values, i.e. the unaveraged ones, when computing limit loads and using these as a first-order estimation that will need to be confirmed through thorough testing.

Another important observation one can make from the simulation results from Tables 4-3 and 4-4 is that the assembled interface outperforms both the male and female plates, with regards to maximum stress, under tension, compression and vertical shear loading. However, the opposite is true when considering lateral shear, vertical bending and moment of twist. In the case of the moment loading, this can be explained by the way the loads are defined with respect to surface of application. As all moments and forces except vertical shear are applied directly to the back of the non-fixed plate in the assembly, there are reaction forces and moments associated to such a load case. This, of course, results in higher stresses due to the load case not being as simple as for the assembled state case. Additionally, in the case of moment loading, the extra distance from the plate back (application surface) to the contact surfaces of the interface effectively create a larger moment arm, thus increasing the loading at the contact point. In the case of lateral shear a different phenomenon occurs where the surface on which the load is applied is much higher in the assembled state simulations than in the assembly one. This causes better load transmission throughout the structure for the male and female plates when simulated individually, whereas higher stress concentrations occur for the assembly. Another important observation is that under specific loading, such as vertical shear and moments, the deformation also shows higher peaks for the assembly in comparison to assembled state. This could be attributed to either the definition of the contact surfaces as frictional surfaces or the definition of fixed support constraints on a single plate instead of both, or even a combination of these two factors. Table 4-7 quantifies the differences with

respect to percentages between the different simulation scenarios, based on the unaveraged stress and deformation results.

Table 4-7: Percentile comparison between assembled state and assembly simulation - unaveraged stress results

Load case	Value	Male vs Female	Male vs Assembly	Female vs Assembly
Tension	Von Mises	+12.74 %	- 39.2 %	-31.56 %
	Shear	+10.98 %	-39.01 %	-32.32 %
	Deformation	+17.14 %	-50.15 %	-41.6 %
Compression	Von Mises	+17.61 %	-69.49 %	-64.12 %
	Shear	+15.89 %	-68.30 %	-63.27 %
	Deformation	+18.16 %	-82.11 %	-78.86 %
Vertical Shear	Von Mises	-9.49 %	-24.82 %	-31.94 %
	Shear	-13.54 %	-26.93 %	-36.83 %
	Deformation	+6.02 %	+116.63 %	+129.66 %
Lateral Shear	Von Mises	-35.43 %	+76.14 %	+13.73 %
	Shear	-31.56 %	+81.73 %	+24.38 %
	Deformation	-29.62 %	+41.04 %	-0.74 %
Lateral Bending	Von Mises	-26.72 %	+30.99 %	-4.01 %
	Shear	-27.86 %	+24.51 %	-10.17 %
	Deformation	-38.45 %	+97.85 %	+21.77 %
Moment of twist	Von Mises	-0.74 %	+31.99 %	+31.01 %
	Shear	+2.11 %	+30.66 %	+33.42 %
	Deformation	+1.5 %	+67.43 %	+69.94 %
Vertical Bending	Von Mises	-14.42 %	+31.99 %	+31.01 %
	Shear	-11.29 %	+30.66 %	+33.42 %
	Deformation	-18.67 %	+67.43 %	+69.94 %

It becomes readily apparent from the data above that the male plate outperforms the female one in tension and compression. This is to be expected considering the placing of the half T-sections laterally on the male plate which provide higher strength in the tensile case, and more surface area for stress distribution under compression. In all the remaining load cases except for twist, the female plate outperforms the male one by at least 10 %. The fact that there is an increase of over 100 % in deformation between the assembled state and assembly simulation under vertical shear may seem worrisome, however it is important to consider that in the grand scheme of things this represents a difference of around 10 μm which is acceptable under the defined loading.

Using a safety factor function coupled with the unaveraged values for Von Mises and maximum shear stress corresponding to the assembly simulation, the limit loads for each case can be computed, as presented in Table 4-8. The right-hand column of the table also mentions the failure criterion exceeded, be it either Von Mises or maximum shear stress.

Table 4-8: Maximum load bearing capabilities of MIST V0.0

Load case	Magnitude	Failure mode
Tension	151078 <i>N</i>	Shear
Compression	313472 <i>N</i>	Shear
Shear (vertical)	284569 <i>N</i>	Shear
Shear (lateral)	306289 <i>N</i>	Shear
Lateral bending moment	15638.411 <i>N · m</i>	Shear
Moment of twist	35378.483 <i>N · m</i>	Shear
Vertical bending moment	19196.654 <i>N · m</i>	Shear

The first noticeable fact is that for all cases, the failure criterion exceeded is maximum shear stress. Additionally, from the results above one can infer that, with respect to forces, the most favorable load cases for MIST V0.0 are compression and lateral shear, followed by vertical shear and tension. With regards to moments, the highest load tolerance, by almost a factor of two compared to the next case, is found in the case of twist, followed by vertical and lateral bending. These strengths are very advantageous for manipulating a large modular platform that makes uses of this interface concept.

It is very important to note that the limit loads are much higher than necessary for a 15m diameter primary aperture telescope. The reasoning for aiming for such loads is associated with the desire of creating a standardized interface that can be used as broadly as possible. By extension, this means that the higher the structural performance, the larger the telescopes this model can be used for without needing any adjustment. In the case of smaller projects, one could even use the same design logic presented in this work to downscale the interface for almost any size desired, the only size limit being a large enough central connector to fit both the electrical and data end-connectors.

The down-scaled version of the interface was also simulated so as to make a comparison between the MIST concept and existing interfaces of similar size [43], [12], [13], [42]. The results of said simulations are presented in Tables 4-9 and 4-10.

Table 4-9: Part and assembly load simulation results MIST V0.0 120x120 version (ANSYS) - Part 1

Loading case	Female Plate	Male Plate	Assembly
Tension - 10 <i>kN</i>			
Von Mises (avg)	65.859 <i>MPa</i>	73.64 <i>MPa</i>	47.233 <i>MPa</i>
Von Mises (unavg)	86.279 <i>MPa</i>	94.947 <i>MPa</i>	77 <i>MPa</i>
Max Shear (avg)	36.071 <i>MPa</i>	38.979 <i>MPa</i>	25.937 <i>MPa</i>
Max Shear (unavg)	48.566 <i>MPa</i>	53.545 <i>MPa</i>	41.028 <i>MPa</i>
Deflection	77.047 μm	85.126 μm	54.649 μm
Compression - 10 <i>kN</i>			
Von Mises (avg)	55.252 <i>MPa</i>	65.861 <i>MPa</i>	18.222 <i>MPa</i>
Von Mises (unavg)	72.245 <i>MPa</i>	80.725 <i>MPa</i>	21.402 <i>MPa</i>
Max Shear (avg)	30.269 <i>MPa</i>	33.508 <i>MPa</i>	10.018 <i>MPa</i>
Max Shear (unavg)	40.679 <i>MPa</i>	45.522 <i>MPa</i>	12.094 <i>MPa</i>
Deflection	61.759 μm	67.262 μm	12.152 μm

Table 4-10: Part and assembly load simulation results MIST V0.0 120x120 version (ANSYS) - Part 2

Loading case	Female Plate	Male Plate	Assembly
Shear (vertical) - 10 kN			
Von Mises (avg)	34.951 MPa	31.462 MPa	66.992 MPa
Von Mises (unavg)	95.602 MPa	71.527 MPa	71.924 MPa
Max Shear (avg)	18.3 MPa	17.108 MPa	36.555 MPa
Max Shear (unavg)	53.842 MPa	40.481 MPa	40.649 MPa
Deflection	15.41 μm	13.489 μm	88.294 μm
Shear (lateral) - 10 kN			
Von Mises (avg)	26.108 MPa	19.187 MPa	25.373 MPa
Von Mises (unavg)	53.649 MPa	32.943 MPa	55.089 MPa
Max Shear (avg)	14.692 MPa	10.438 MPa	14.412 MPa
Max Shear (unavg)	27.602 MPa	17.221 MPa	29.422 MPa
Deflection	14.53 μm	10.5 μm	16.304 μm
Lateral bending moment - 1 kNm			
Von Mises (avg)	139.88 MPa	160.42 MPa	150.55 MPa
Von Mises (unavg)	241.72 MPa	224.55 MPa	285.9 MPa
Max Shear (avg)	76.776 MPa	85.962 MPa	84.369 MPa
Max Shear (unavg)	132.96 MPa	116.74 MPa	151.98 MPa
Deflection	159.89 μm	116.1 μm	250.67 μm
Moment of twist - 1 kNm			
Von Mises (avg)	49.028 MPa	50.47 MPa	54.798 MPa
Von Mises (unavg)	113.88 MPa	92.27 MPa	149.16 MPa
Max Shear (avg)	26.783 MPa	27.67 MPa	31.547 MPa
Max Shear (unavg)	58.306 MPa	47.011 MPa	84.947 MPa
Deflection	15.403 μm	12.582 μm	50.572 μm
Vertical bending moment - 1 kNm			
Von Mises (avg)	73.371 MPa	91.249 MPa	115.48 MPa
Von Mises (unavg)	133.89 MPa	166.88 MPa	220.17 MPa
Max Shear (avg)	40.489 MPa	52.683 MPa	61.307 MPa
Max Shear (unavg)	70.7 MPa	90.093 MPa	114.62 MPa
Deflection	51.147 μm	52.298 μm	5.111 μm

When comparing stresses between the assembled state and assembly simulations, most the trends observed for the full-scale MIST V0.0 simulation stay true. The latter outperforms the male and female plates during the tensile and compressive cases, whereas the opposite stays true for lateral shear, as well as moments of twist and vertical bending. The only difference in results is that the vertical shear case shows slightly higher results for the assembly stresses than for the male plate. This could be caused by the mesh sizing which is believed to be the primary cause for the large differences between averaged and unaveraged stresses.

Finally, using the unaveraged stresses computed in the assembly simulation, the maximum loads for each case could be computed, as shown in Table 4-11.

Table 4-11: Maximum load bearing capabilities of MIST V0.0 (120x120)

Load case	Magnitude	Failure mode
Tension	34132 <i>N</i>	Shear
Compression	114826 <i>N</i>	Shear
Shear (vertical)	31684 <i>N</i>	Shear
Shear (lateral)	47362 <i>N</i>	Shear
Lateral bending moment	921.19 <i>N · m</i>	Shear
Moment of twist	1644.358 <i>N · m</i>	Shear
Vertical bending moment	1190.016 <i>N · m</i>	Shear

The failure mode stays consistent with the results of the full-scale interface, as do the relative strengths with respect to load cases. The limit loads again far exceed any load performance of existing interfaces described in [12], [13], [42], [43]. This means that even if the choice in tapering the T-sections results in decreased structural strength there is more than enough margin to still satisfy the structural requirements.

Detailed Interface Design - First Iteration

This chapter covers the first iteration of the MIST design, henceforth referred to as MIST V1.0. Section 5-1 describes the design logic and choices involved in the refinement of the preliminary design, whilst Section 5-2 summarizes the ANSYS simulation results for this iteration of the design.

5-1 First Design Iteration (MIST V1.0)

The first iteration of MIST presents a reasonable solution for the problem of servicing central modules in a structure using this concept, however there are some disadvantages that arise with it. Firstly, using the square plate model as a foundation for the T-sections means that the width of the plate dimension will coincide with the length of actuation motion during assembly. In the case of the full scale, a sliding motion of 400 mm will be required, which presents the chance of snagging when done in space, especially considering the large dimensions of the flanges of the T-sections. The worst case scenario would occur during disassembly when the largest area of contact will have to be considered. One can calculate this maximum surface causing frictional forces using Equation 5-1.

$$A_{friction_{max}} = 4 \cdot H_{plate} \cdot W_{T-flange} \quad (5-1)$$

Where $A_{friction_{max}}$ is the maximum contact area when the interface is assembled, H_{plate} is the height of the plate and $W_{T-flange}$ is the width of the vertical flanges of the T-sections - the x solution of Equation 4-3. Considering the plate is square, the height and width are equal, hence plugging in the values will result in:

$$A_{friction_{max}} = 4 \cdot 400 \cdot 33 = 1600 \cdot 33 = 52800mm^2 = 0.0528m^2$$

Even under the assumption that this surface will not pose any problems from a frictional point of view, a different issue arises - there is no inherent design feature to align the holes in the female and male plates so that the central locking cylinder can pass through. This can be solved mechanically or by adding sensors for guiding, either to the interface itself, or to the assembling element. As sensors can be quite costly, it would be ideal if the problem could be solved through some form of mechanism or a change in design.

In order to solve these two issues, the idea of tapering the T-sections arose. This simplifies assembly actions by not only reducing the contact areas, but also requiring less of a distance in actuation. The larger the taper, the lower the actuation distance, since the module to be assembled no longer needs to be above the fixed module. Furthermore, the tapered T-sections will not only serve the purpose of aligning the male and female plates, thus reducing the need for sensors on the assembler element but also function as a guide during assembly operations.

To maximize the advantages presented by this option, a ratio of 4 to 1 is chosen for the tapering - the consequences of choosing this specific ratio are a decrease in actuation distance by a factor of 6 (or approximately 83.35%) and reduction in contact area of 66.856%, as will be discussed below. This results in the next iteration of the interface, henceforth referred to as MIST V1.0. This new model is still comprised of the same number of elements as V0.0, namely two plates and a locking cylinder, as shown in Figure 5-1.

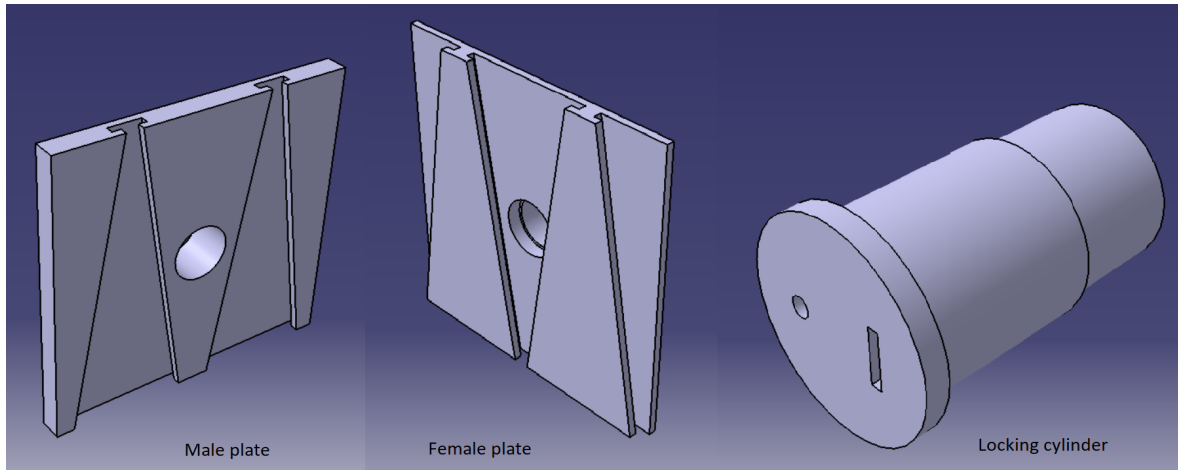


Figure 5-1: Overview of MIST interface components (V1.0)

Using the same idea of equating the smallest T-section with $4x$, as shown previously in Figure 4-3, will lead to $16x$ for the T-section width. In order to minimize the contact area, the lateral sections of the T-sections will be constrained to the same width, irrespective of cross-sectional area of the T-section. Using the top view of the male plate for dimensioning results in the notation shown in Figure 5-2.

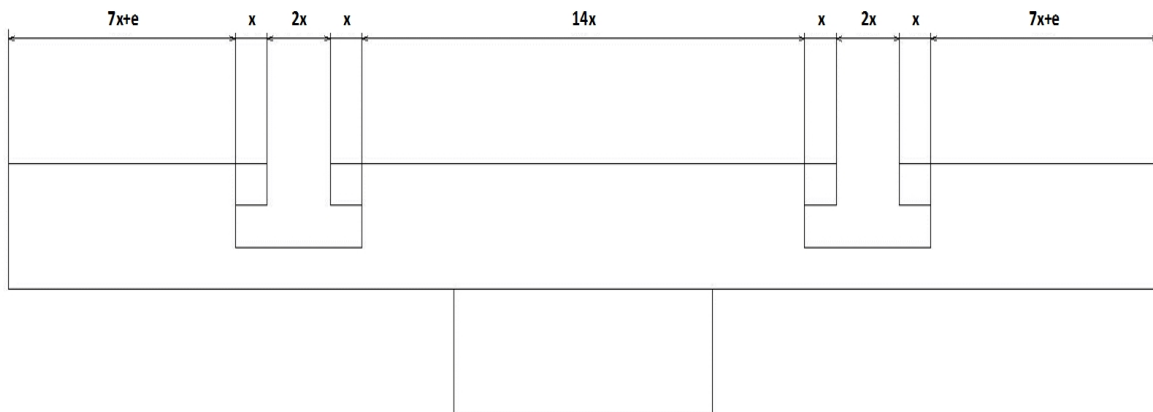


Figure 5-2: MIST V1.0 dimension notation

The e variable is used for the same reason as previously, so as to ensure dimensions remain integers for ease of manufacturing. Based on this notation, Equation 5-2 can be compiled.

$$7 \cdot x + e + 2 \cdot x + x + 14 \cdot x + x + 2 \cdot x + 7 \cdot x + e = W_{plate} \quad (5-2)$$

Re-arranging and substituting 400 mm for the plate width gives Equation 5-3.

$$36 \cdot x + 2 \cdot e = 400mm \quad (5-3)$$

Solving for x and e as integers leads to:

$$x = 11mm \quad e = 2mm$$

The height of the T-sections remains the same, however the diameter of the central connector needs to be adjusted to 75 mm so as to leave sufficient material on the sides of the central T-section. The full technical drawings showing all dimensions of each element are included in Appendix A, Figures A-4, A-5, A-6, corresponding to the male plate, female plate, and locking cylinder, respectively.

The dimensions of the scaled down version for comparison with existing interfaces can be found using Equation 5-4.

$$36 \cdot x + 2 \cdot e = 120mm \quad (5-4)$$

The integer solution, when maximizing x , is:

$$x = 3mm \quad e = 6mm$$

The height of the T-sections is kept the same, however the locking cylinder diameter is changed to 24 mm so as to ensure structural integrity of the sides of the central T-section of the male plate. So as to save space, the technical drawings showing all dimensions of each element can be found in Appendix B, Figures B-4, B-5, B-6, corresponding to the male plate, female plate, and locking cylinder, respectively.

In order to quantify the improvements seen from V0.0 to V1.0 one can consider the difference in actuation distance for assembling them, as well as the maximum surface area in contact for snagging. In order to calculate any of these values, the taper angle needs to be found. This can be done through simple geometry: when considering a front view of the male plate, one can identify two slots in the shape of isosceles trapezoids, with the large base equal to $14x$, small base $2x$ and height equal to the height of the plate, or 400mm. Substituting the results of Equation 5-2 results in:

$$B_{large} = 14 \cdot 11 = 154mm \qquad B_{small} = 2 \cdot 11 = 22mm$$

Where B_{large} is the large base of the isosceles trapezoid, and B_{small} is the corresponding small base. Drawing two perpendiculars from the latter onto the former yields two, equal, right triangles, containing the taper angle. The base of this triangle can be calculated using the half of the difference between bases as shown in Equation 5-5.

$$B_{triangle} = \frac{B_{large} - B_{small}}{2} = \frac{154 - 22}{2} = 66mm \qquad (5-5)$$

The height of this triangle will correspond to the height of the plate, or 400mm. Thus the taper angle can be calculated using an arc tangent function, illustrated in Equation 5-6.

$$\angle taper = \tan^{-1} \frac{B_{triangle}}{400} = \tan^{-1} \frac{66}{400} = 9.36^\circ \qquad (5-6)$$

In order to find out where a trapezoid with base $4x$ would fit into this smaller trapezoidal-shaped hole, one can make use of simple geometrical ratio relations in triangles. If one were to draw any parallel to any of the triangle sides, the ratio between any of the sides of the new small triangle formed, and their corresponding sides in the original triangles stays the same. In this case the dimension of said line forming the new triangle will correspond to half the difference between $4x$ and $2x$, namely:

$$B_{triangle_{small}} = \frac{44 - 22}{2} = 11mm$$

Based on the ratio identity explained above, Equation 5-7 holds.

$$\frac{B_{triangle}}{B_{triangle_{small}}} = \frac{H_{triangle}}{H_{triangle_{small}}} = \frac{66}{11} = 6 \qquad (5-7)$$

This results in the height of the new triangle being:

$$H_{triangle_{small}} = \frac{H_{triangle}}{6} = \frac{400}{6} = 66.66mm$$

This result coincides with the actuation distance necessary for V1.0 while the height of the triangle, or the height of the plate itself is the same as the actuation distance necessary for V0.0. Thus one can conclude that the actuation distance has been reduced by a factor of 6.

Lastly one can easily calculate the largest surface area in contact during the worst case scenario, i.e. when fully assembled, using the areas of the flanges, as dictated by Equation 5-8.

$$A_{friction_{max}} = 4 \cdot H_{plate} \cdot W_{T-flange} = 4 \cdot 400 \cdot 11 = 17600mm^2 = 0.0175m^2 \quad (5-8)$$

The improvement in terms of percentage can be calculated using Equation 5-9.

$$\frac{A_{friction_{V0}} - A_{friction_{V1}}}{A_{friction_{V0}}} \cdot 100 = \frac{0.0528 - 0.0175}{0.0528} \cdot 100 = 66.856\% \quad (5-9)$$

To summarize the change in design results in a reduction in the actuation range required by a factor of 6, and a reduction in frictional area of 66.856%, whilst also solving the issues identified at the beginning of this section regarding MIST V0.0. Based on this reasoning, this iteration can be considered a major improvement.

It is important to note that this iteration does hold a disadvantage in comparison to the previous one, namely that MIST V1.0 can only be assembled from one direction, whereas V0.0 permitted assembly from two. One could assume that this may be an issue when considering multi-layered structures with modules as the base, hence only one direction available for disassembly. This means that, when servicing or replacing a central module, a scenario may arise where this module does not slide out in the desired direction, however if one plans to use this interface correctly, this can be worked around with relatively minor issues by either changing the module shape or by creating a rigorous assembly order.

For the former, one could make use of cube-shaped female and male modules, in other words modules that have solely the male or female side of the interface on all sides. In this scenario, if the any module cannot be slid out in one direction, all the adjacent ones will be able to slide out in the opposite direction. This results in needing to extract a five module cross in order to be able to replace or service the central module in the desired direction. If very large structures containing tens or even hundreds of modules are considered, it is expected that this will have minimal impact on the performance of the whole spacecraft, especially given the fact that power and data can be rerouted through different paths in such a modular network. Furthermore, two major advantages arise from switching to such a concept with respect to manufacturability and serviceability. Firstly, defining male and female modules presents the unique opportunity of creating separate production lines for each and thus profiting off of the advantages of mass production. And secondly, having two types of modules as the building blocks of a structure has the extra advantage of easy replaceability in the case of a module failure. One could even argue that if a critical node in the structure fails, it

could be replaced by an existing non-critical one until a servicing mission is planned to send replacement modules.

If one were to consider the latter option of creating a rigorous assembly order, one can return to the assumption of hexagonal-shaped modules. If one considers even a simple array of seven modules, if the central one is designed with only one type of interface, be it male or female, the immediately adjacent modules will require variations of male and female to account for the sides where they connect with any other module aside from the central one. This results in not being able to capitalize on mass production advantages at a module level but solely at an interface level. Furthermore, planning for the sequencing of the assembly of a structure using such modules would become even more important as many combinations would result in not being able to service centrally placed modules unless the whole structure was disassembled. As this is considered a major disadvantage, it is recommended that cube-shaped modules be used for their advantages in manufacturability and serviceability, in spite of the disadvantages with regards to space optimization when creating the support surface for the mirrors.

It is important to note that changing to a cube-shaped module does come with an increase in number of modules. Based on the size used as a limit for the interface design and the target aperture of 15 meters in diameter discussed in Section 3-3, one would need a height and width spanning 38 modules, and a diagonal spanning 27 modules, as opposed to 15 with the hexagonal option. This can be quantified to approximately 1184 modules in order to have a full base for the given diameter as shown in Figure 5-3, where the red contour represents the mirror size.

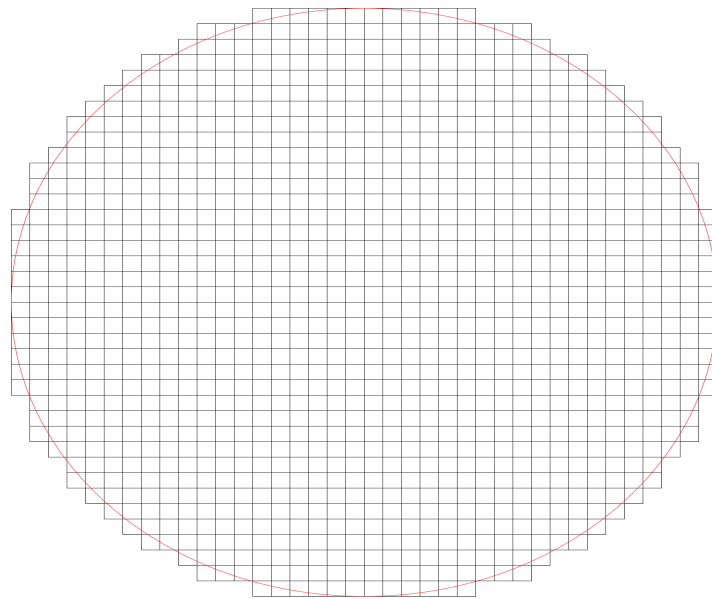


Figure 5-3: Visualization of structure when using cube-shaped modules

This increase from 1101 to 1184 modules is a minimal increase from the first-order estimation in Section 3-3. Furthermore, it is important to keep in mind that the interface itself is designed with flexibility in mind, capable of supporting a range of designs not a single point design. As such, as long as the data, power or load requirements do not exceed the performance of the interface, it can still be used without issue.

5-2 ANSYS Simulation Results for MIST V1.0

The same sequence of simulations was also performed on MIST V1.0, under the assembled state conditions. The stress distributions for the tensile case are illustrated in Figure 5-4, with Subfigures 5-4a, and 5-4b corresponding to the Von Mises and maximum shear stress distribution for the male plate, and Subfigures 5-4c, and 5-4d, for the female plate.

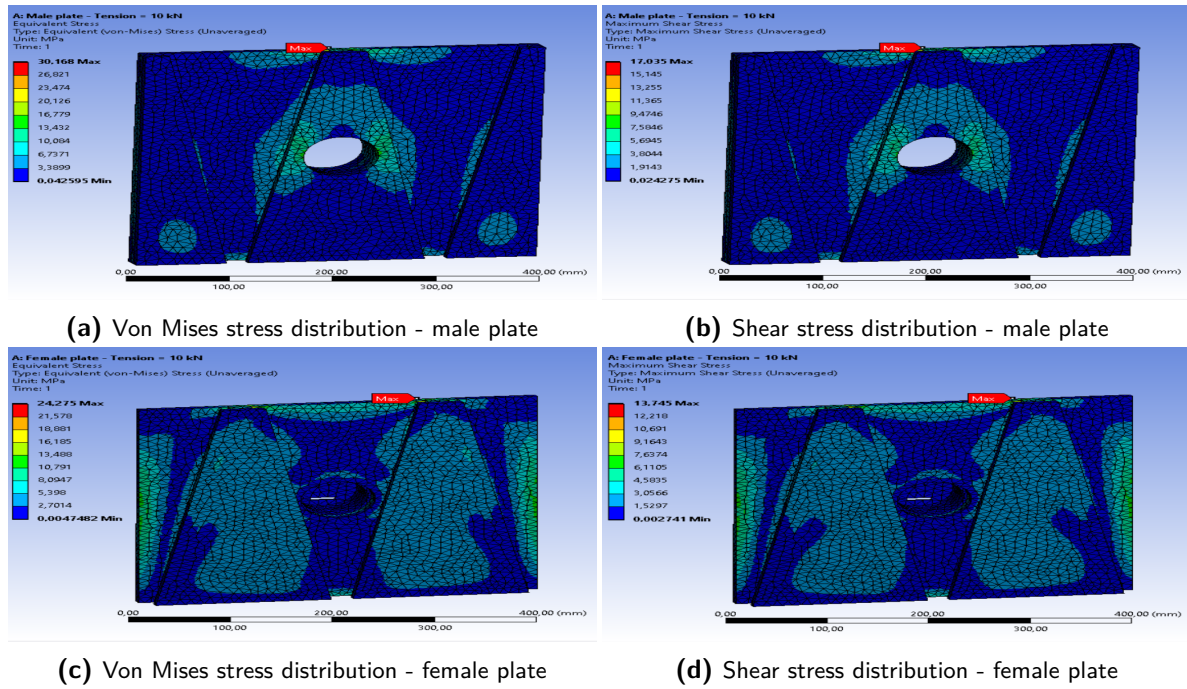


Figure 5-4: Stress distribution under 10 kN tensile load - Assembled state MIST V1.0

The results for MIST V1.0 are very similar to those of the previous version. The main difference is the shift of maximum stress in the direction of taper, in other words, the direction of smaller cross-section. Due to this shift causing lack of symmetry with respect to the lateral central line, the maximum values will only occur at the edges of the tapered parts of the T-sections, two for the male plate, and four for the female. The deformation corresponding to this load case is shown in Figure 5-5.

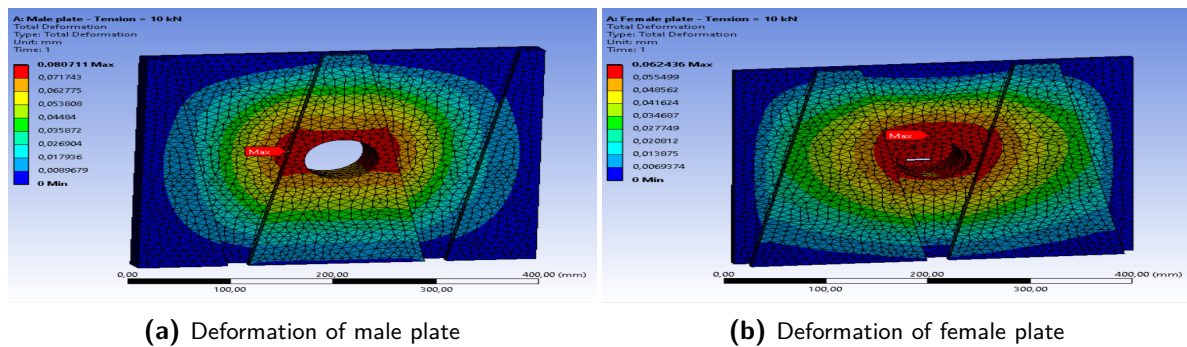


Figure 5-5: Deformation under 10 kN tensile load - Assembled state MIST V1.0

As with the stress distribution, the deformation also shifts in the same direction. In the case of the male plate, two peaks can be discerned on either side of the central hole, on the flanges of the T-section. As for the female plate, there is only one peak occurring above the central cylindrical cutout, as the stress is evenly distributed towards the middle, through the thinnest segment, in this case the plate.

The compressive case stress distributions are shown in Figure 5-6, where Subfigures 5-6a, and 5-6b pertain to the Von Mises and maximum shear stress distribution for the male plate, and Subfigures 5-6c, and 5-6d, for the female plate, respectively.

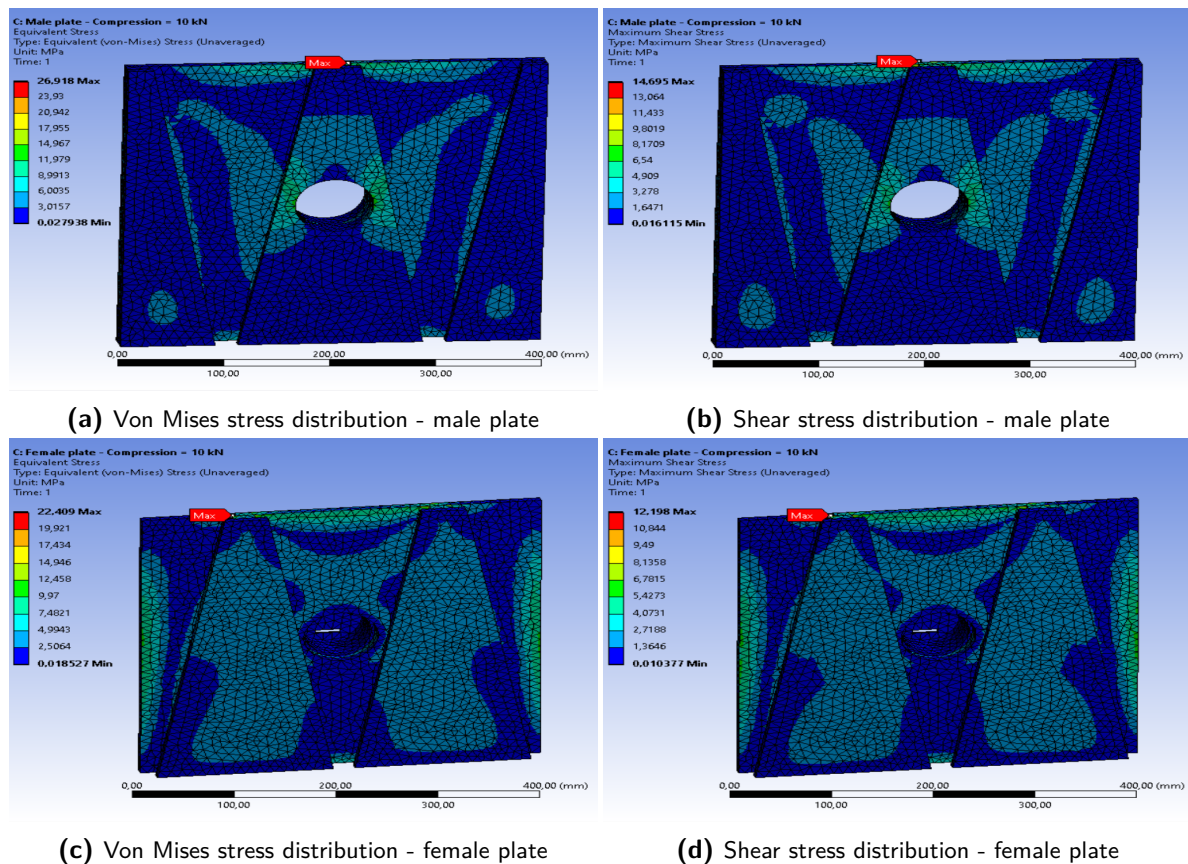
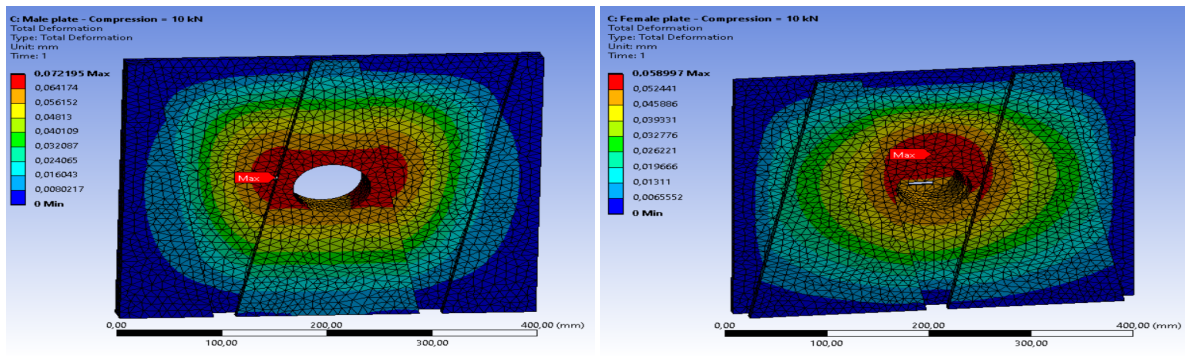


Figure 5-6: Stress distribution under 10 kN compressive load - Assembled state MIST V1.0

The same trend as for tension can also be observed for the compressive one, namely an upwards shift of the stress distributions. Again, as with the previous case the same number and positioning of peaks is seen. Similarly to V0.0, the highest stresses aside from the peaks are concentrated around the middle T-section flanges for the male plate and the outside plate sections for the female. An interesting result is the fact that an upper section of both plates, corresponding to the smallest cross-sections, also exhibit stress distributions whereas the bottom shows almost no contribution. This is mainly due to the increase in plate dimensions due to the tapering. The corresponding deformation is shown in Figure 5-7.

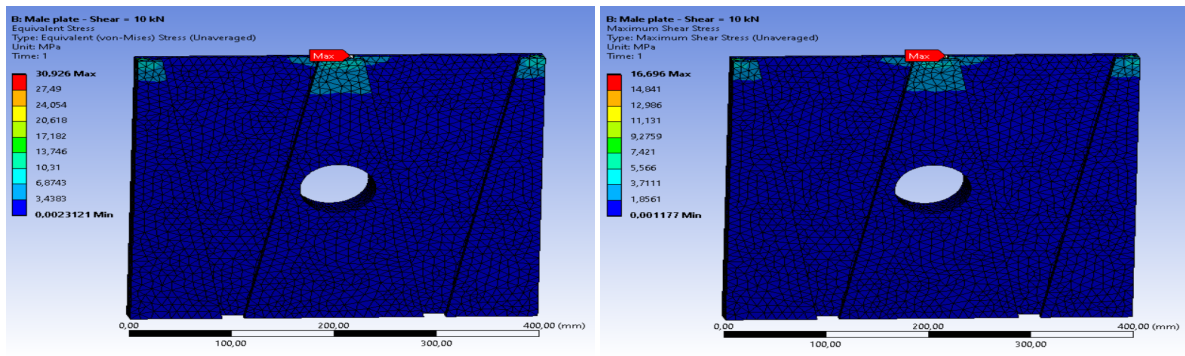


(a) Deformation of male plate (b) Deformation of female plate

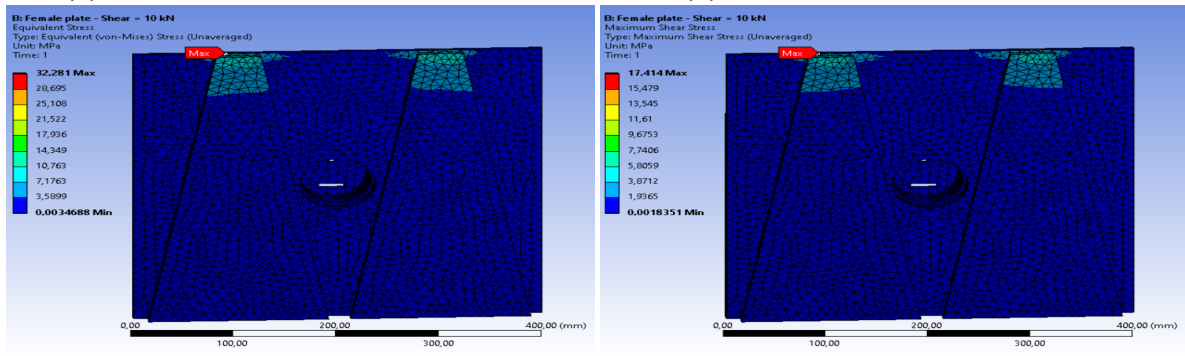
Figure 5-7: Deformation under 10 kN compressive load - Assembled state MIST V1.0

The deformation distribution is exactly the same as for the tensile case, with two peaks on the lateral flanges of the central T-section for the male plate, and a single peak above the cylindrical cut-out for the female plate.

The vertical shear load causes the stress distributions shown in Figure 5-8, where Subfigures 5-8a, and 5-8b correspond to the Von Mises and maximum shear stress distribution for the male plate, and Subfigures 5-8c, and 5-8d, for the female plate.



(a) Von Mises stress distribution - male plate (b) Shear stress distribution - male plate



(c) Von Mises stress distribution - female plate (d) Shear stress distribution - female plate

Figure 5-8: Stress distribution under 10 kN vertical shear load - Assembled state MIST V1.0

The vertical shear case exhibits stress concentrations towards the smallest cross-sections of

the T-sections. This is mainly due to the fact that this surface was chosen for load application, so as to register the highest stress concentrations for the given load, as explained previously. There is slight stress transfer around the T-sections, however this does not result in any peaks. Similarly to MIST V0.0, the male plate exhibits a single peak on the central section, whereas the female element shows two peaks, one on each T-flange. The associated deformation is shown in Figure 5-9.

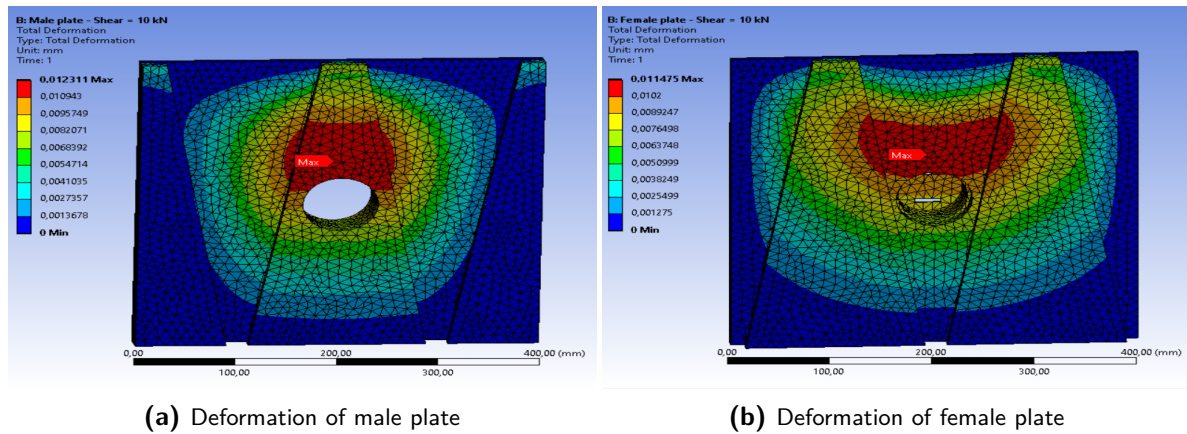


Figure 5-9: Deformation under 10 kN vertical shear load - Assembled state MIST V1.0

The deformation for this load case exhibits two peaks for the male plate, at the points where the lateral flanges of the T-section connect with the vertical one. As for the female plate, a single peak occurs above the cylindrical cut-out. This makes sense as the stresses are distributed more towards the top sections, in other words the areas of minimal cross-section.

Under lateral shear loading, the ensuing stress distributions are shown in Figures 5-10 and 5-11, where Subfigures 5-10a, and 5-10b correspond to the Von Mises and maximum shear stress distribution for the male plate, and Subfigures 5-11a, and 5-11b, for the female plate, respectively.

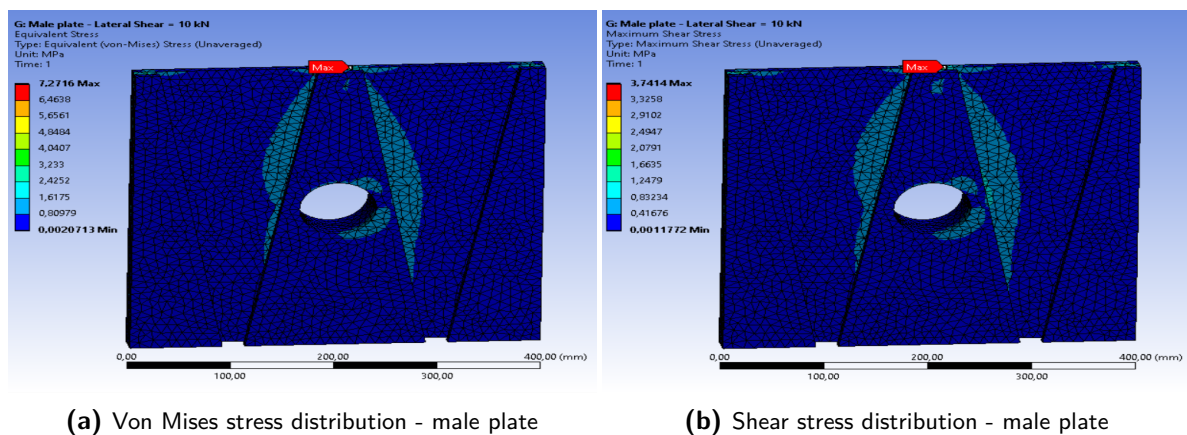
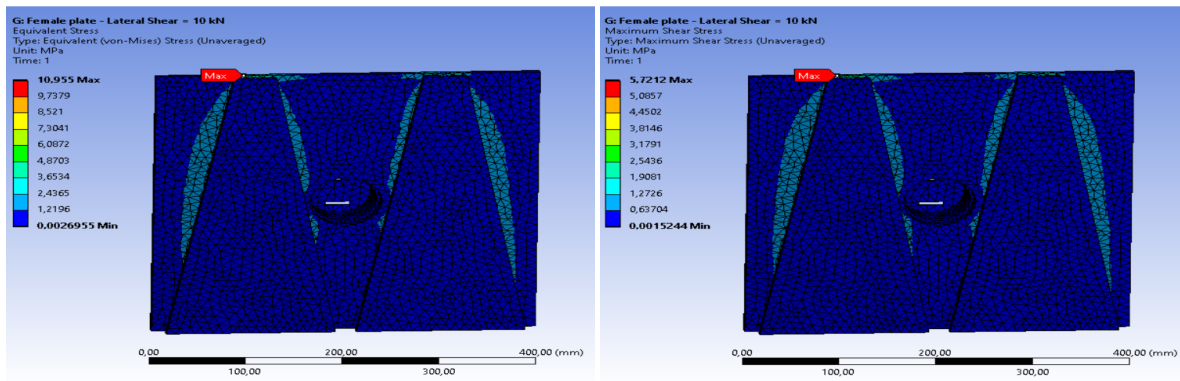


Figure 5-10: Stress distribution under 10 kN lateral shear load - Assembled state MIST V1.0 male

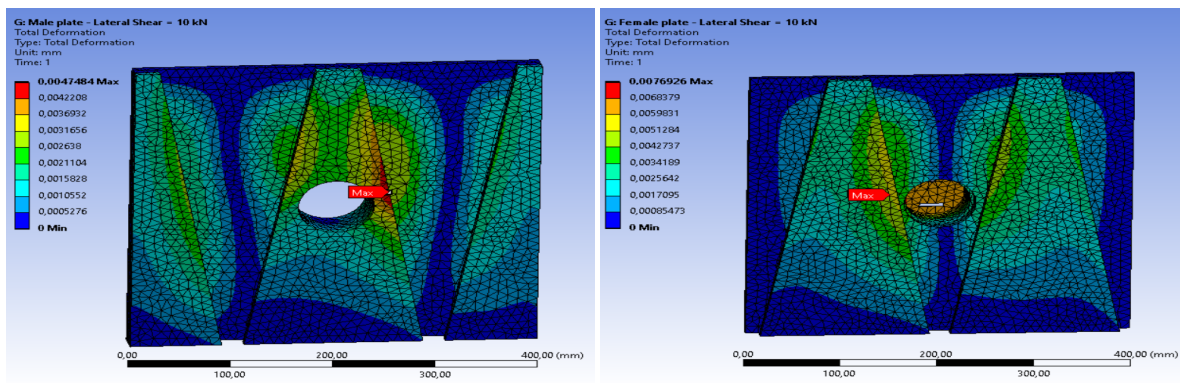


(a) Von Mises stress distribution - female plate

(b) Shear stress distribution - female plate

Figure 5-11: Stress distribution under 10 kN lateral shear load - Assembled state MIST V1.0 female

As for the previous version, the stress is more concentrated in the direction of load application. This is exceedingly obvious for the male plate, however it is not as clear for the female plate. However, when one considers the assembly logic, it becomes clearer that in the case of MIST V1.0 the loading is complementary, i.e. from left to right on the male plate, opposite direction in the case of the female plate. There is a single peak present for both plates, on the central T-section, and on the T-element in the opposite side of the load direction. The resulting deformation is shown in Figure 5-12.



(a) Deformation of male plate

(b) Deformation of female plate

Figure 5-12: Deformation under 10 kN lateral shear load - Assembled state MIST V1.0

The deformation peak for the male plate occurs on a single side of the central section. This makes sense, as the surfaces in that direction are the ones on which the load is applied. A similar situation occurs with the female plate, however the peak only occurs on one T-section. This is due to the fact that this face is closer to the cylindrical cutout which, as mentioned time and again, reduces the structural integrity of the model.

The stress distributions caused by the vertical bending moment case are shown in Figure 5-13, where Subfigures 5-13a, and 5-13b pertain to the Von Mises and shear stress distribution for the male plate, and Subfigures 5-13c, and 5-13d, for the female plate.

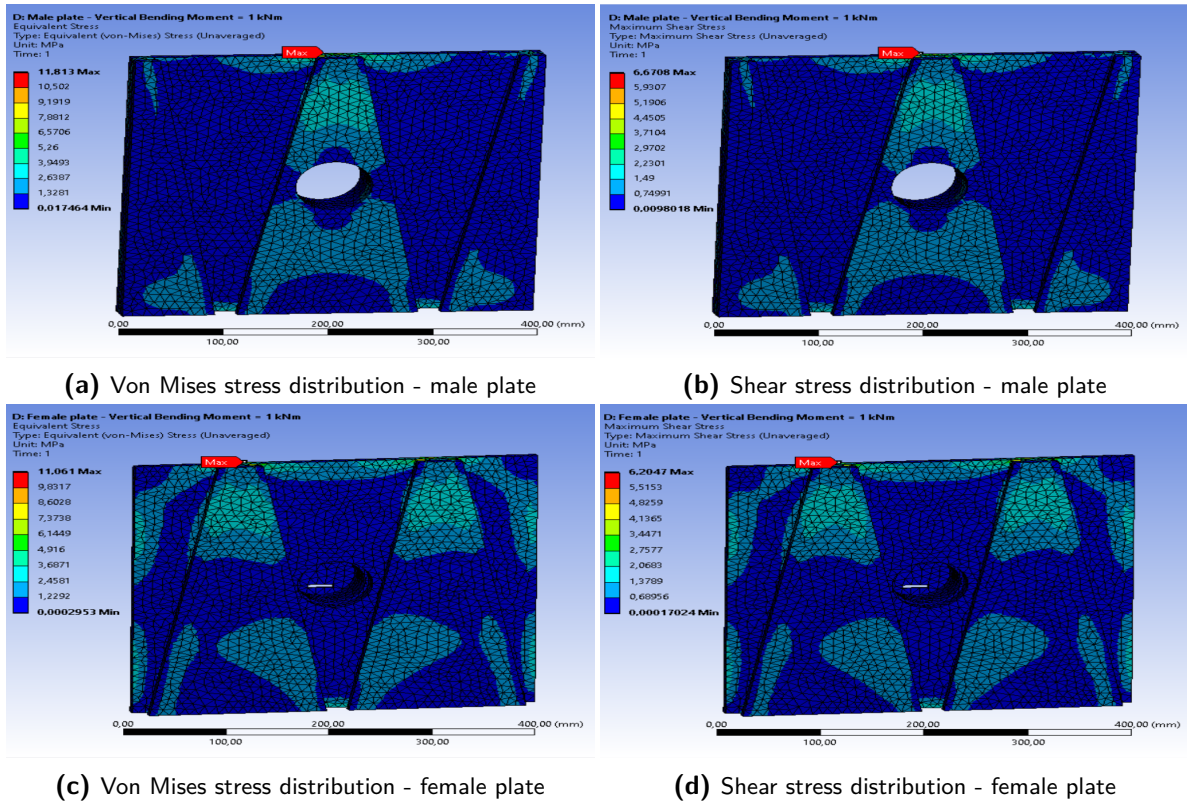


Figure 5-13: Stress distribution under 1 kNm vertical bending moment - Assembled state MIST V1.0

The highest stresses occur towards the sides with smallest cross-sections. This is due to the fact that the thickness of the vertical section (of the T-sections) is lowest here, thus reducing the strength of the elements in that direction. Two symmetric peaks occur on the central T-section of the male plate, whilst the female plate exhibits four. The resulting deformation is shown in Figure 5-14.

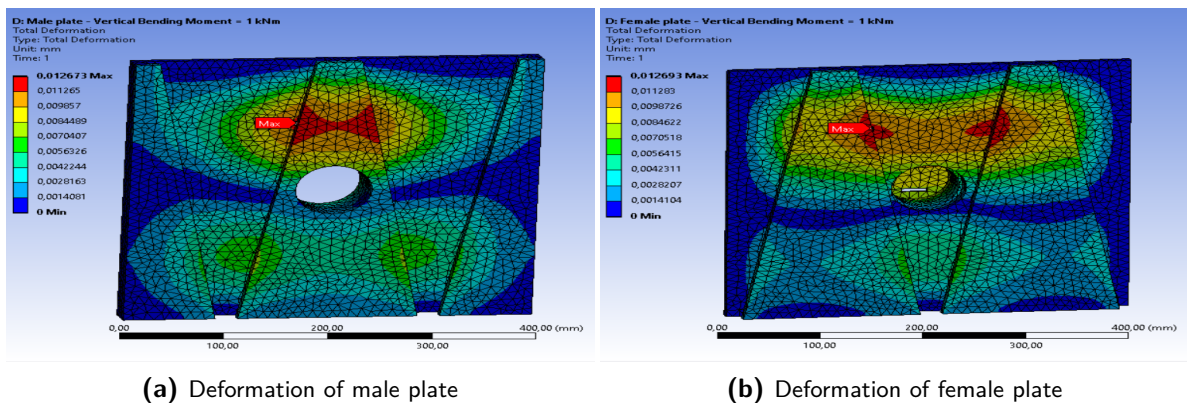


Figure 5-14: Deformation under 1 kNm vertical bending moment - Assembled state MIST V1.0

The difference in deformation distribution as opposed to the previous interface version is

again a shift towards the tapered side. This makes sense as a smaller cross-section cannot support as high a load as a larger one. Both the male and female plates have two peaks in deformation. In the case of the former, this is where the central T-section vertical and lateral flanges meet. For the latter, a similar location is observed on each T-section, in the direction of the cylindrical cutout.

The results of the lateral bending moment case with respect to stress distributions are shown in Figure 5-15, where Subfigures 5-15a, and 5-15b correspond to the Von Mises and Shear stress distribution for the male plate, and Subfigures 5-15c, and 5-15d, for the female plate, respectively.

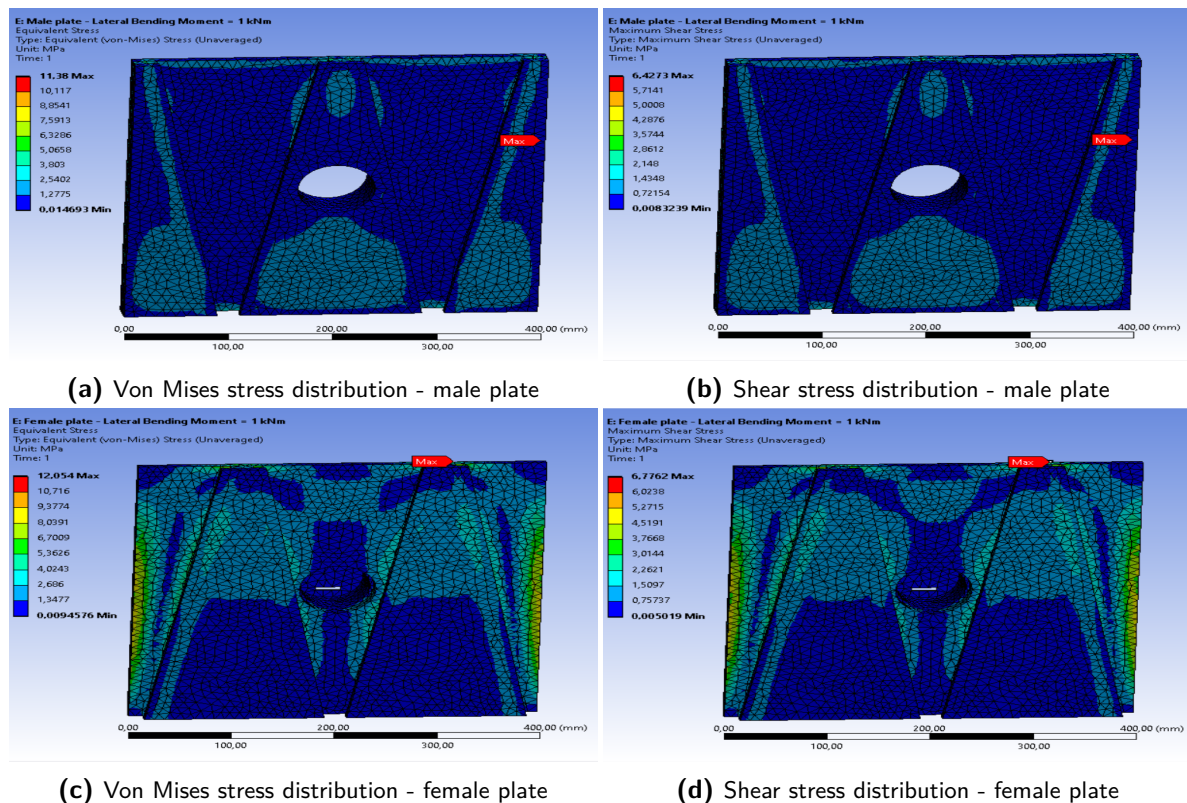


Figure 5-15: Stress distribution under 1 kNm lateral bending moment - Assembled state MIST V1.0

This load case presents some very surprising results. Although the female plate follows the trend up until now of a shift in stress distribution towards the tapered side of the element, this is not the case for the male plate. The latter shows a shift towards the highest cross-sectional area which is quite surprising. In spite of this, the peaks correspond to edges, but they are also shifted off-center in the direction of taper. While the direction makes sense, the location seems to indicate stress concentrations instead of actual peaks. More tests should be performed to confirm this fact, as the results for the male plate raise a number of questions on the validity of the results. On the other hand, the female plate shows two peaks, one on each T-section, towards the right-hand side. This is due to the definition of the load case and the surfaces it was applied on. The associated deformation is shown in Figure 5-16.

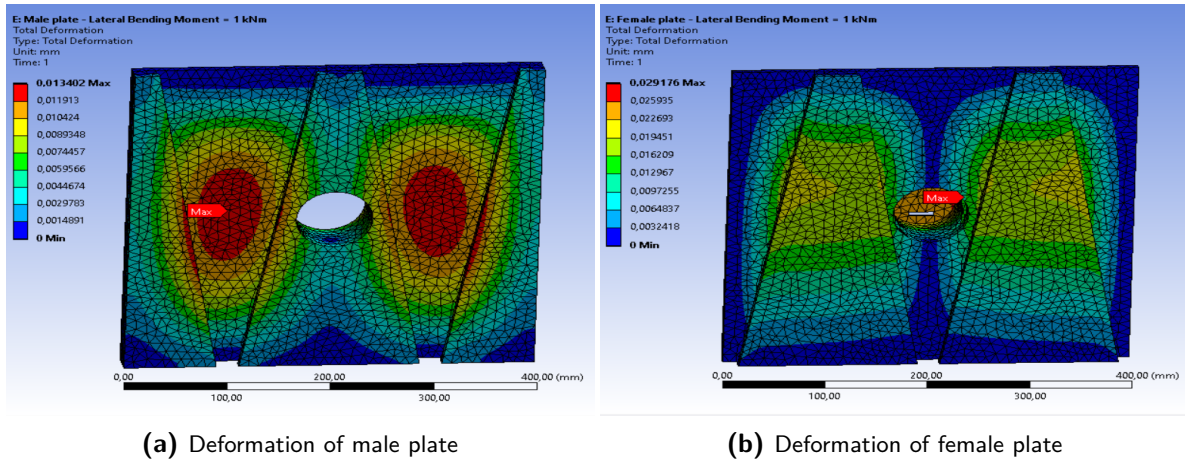


Figure 5-16: Deformation under 1 kNm lateral bending moment - Assembled state MIST V1.0

In spite of the stress distribution results, the deformation patterns exhibited by both the male and female plates make logical sense. Although the red sectors are almost symmetrical with respect to the lateral axis, they are slightly moved towards the side with lowest cross-sectional area. With respect to peaks, two (based on symmetry with respect to the vertical axis) occur in both cases. For the male plate they are located on the plate section, where the thickness is lowest, whereas for the female section they occur on the edge of the cylindrical cutout, which makes sense when considering thicknesses.

In the case of applying a moment of twist, the ensuing stress distributions are shown in Figures 5-17 and 5-18, where Subfigures 5-17a, and 5-17b pertain to the Von Mises and Shear stress distribution for the male plate, and Subfigures 5-18a, and 5-18b, for the female plate.

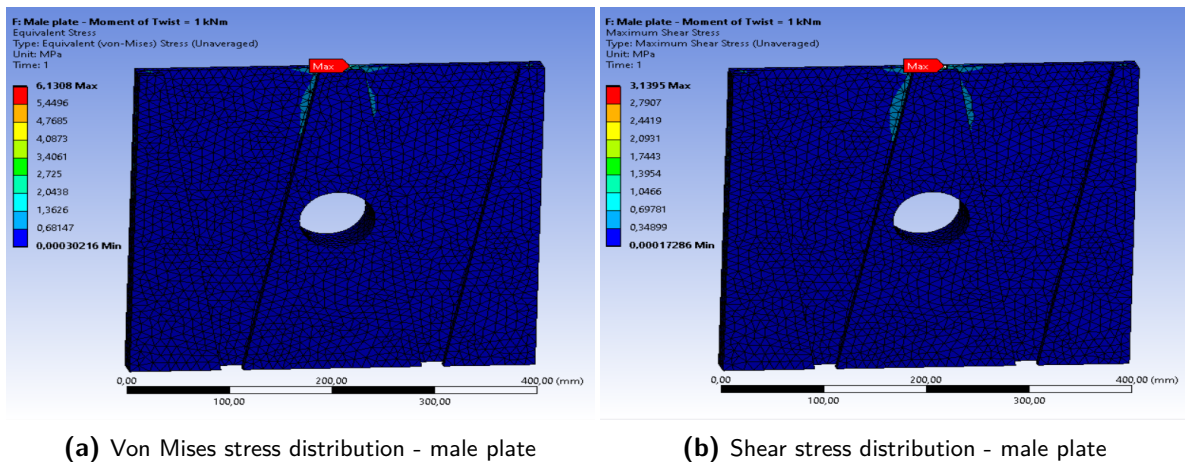
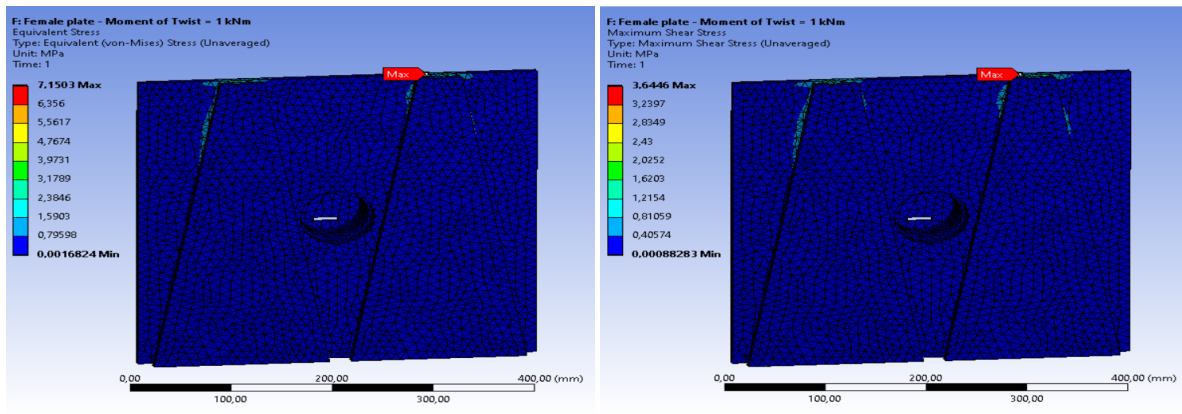


Figure 5-17: Stress distribution under 1 kNm moment of twist - Assembled state MIST V1.0 male

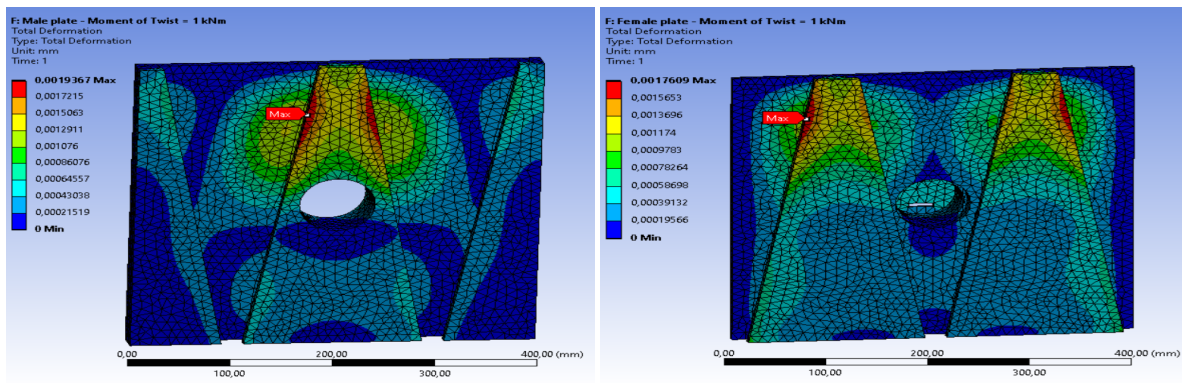


(a) Von Mises stress distribution - female plate

(b) Shear stress distribution - female plate

Figure 5-18: Stress distribution under 1 kNm moment of twist - Assembled state MIST V1.0 female

This load case presents very low stresses, mostly concentrated around the top edges of the T-sections (in the direction of taper). There is a single peak for the male plate and two symmetrical ones on the female one. This was expected due to the fact that those locations coincide to the smallest thickness of the vertical flanges of the T-sections. The corresponding deformation is shown in Figure 5-19.



(a) Deformation of male plate

(b) Deformation of female plate

Figure 5-19: Deformation under 1 kNm moment of twist - Assembled state MIST V1.0

With respect to deformation, the aforementioned trend of shift towards the tapered side stays true. Two maximums occur for both the male and female plate, on the sides of the central section, for the former, and on the exterior-facing sides of the two T-sections, for the latter. This distribution can be mainly attributed to the combination of the sides being fixed as well as load application surface definition.

In order to make a comparison between the assembled state simulation and fully assembled simulation, the results of each load case were compiled and summarized in Table 5-1. Both the averaged and non-averaged values for the stresses are included so that a better understanding may be gained about the accuracy of the simulation process as well.

Table 5-1: Part and assembly load simulation results MIST V1.0 (ANSYS)

Loading case	Female Plate	Male Plate	Assembly
Tension - 10 kN			
Von Mises (avg)	18.963 MPa	22.485 MPa	13.02 MPa
Von Mises (unavg)	24.275 MPa	30.168 MPa	16.311 MPa
Max Shear (avg)	10.294 MPa	12.291 MPa	7.0815 MPa
Max Shear (unavg)	13.745 MPa	17.035 MPa	9.1685 MPa
Deflection	62.436 μm	80.711 μm	32.503 μm
Compression - 10 kN			
Von Mises (avg)	15.622 MPa	19.347 MPa	4.4998 MPa
Von Mises (unavg)	22.409 MPa	26.918 MPa	6.8278 MPa
Max Shear (avg)	8.4757 MPa	10.57 MPa	2.484 MPa
Max Shear (unavg)	12.198 MPa	14.695 MPa	3.9087 MPa
Deflection	58.997 μm	72.195 μm	12.369 μm
Shear (vertical) - 10 kN			
Von Mises (avg)	12.975 MPa	12.381 MPa	10.33 MPa
Von Mises (unavg)	32.281 MPa	30.926 MPa	12.148 MPa
Max Shear (avg)	6.9479 MPa	6.6499 MPa	5.2546 MPa
Max Shear (unavg)	17.414 MPa	16.696 MPa	6.237 MPa
Deflection	11.475 μm	12.311 μm	24.329 μm
Shear (lateral) - 10 kN			
Von Mises (avg)	5.5656 MPa	3.7437 MPa	6.8685 MPa
Von Mises (unavg)	10.955 MPa	7.2716 MPa	12.158 MPa
Max Shear (avg)	3.039 MPa	2.067 MPa	3.9141 MPa
Max Shear (unavg)	5.7212 MPa	3.7414 MPa	6.4331 MPa
Deflection	7.6926 μm	4.7484 μm	17.536 μm
Lateral bending moment - 1 kNm			
Von Mises (avg)	9.1968 MPa	8.3008 MPa	7.4849 MPa
Von Mises (unavg)	12.054 MPa	11.38 MPa	11.929 MPa
Max Shear (avg)	5.0483 MPa	4.6037 MPa	4.1704 MPa
Max Shear (unavg)	6.7762 MPa	6.4273 MPa	6.5441 MPa
Deflection	29.176 μm	13.402 μm	48.051 μm
Moment of twist - 1 kNm			
Von Mises (avg)	3.0715 MPa	3.0519 MPa	4.1076 MPa
Von Mises (unavg)	7.1503 MPa	6.1308 MPa	7.9771 MPa
Max Shear (avg)	1.661 MPa	1.6943 MPa	2.3482 MPa
Max Shear (unavg)	3.6446 MPa	3.1395 MPa	4.2341 MPa
Deflection	1.7609 μm	1.9367 μm	7.2258 μm
Vertical bending moment - 1 kNm			
Von Mises (avg)	8.7215 MPa	9.0112 MPa	7.9712 MPa
Von Mises (unavg)	11.061 MPa	11.813 MPa	11.609 MPa
Max Shear (avg)	4.7515 MPa	4.9544 MPa	4.4311 MPa
Max Shear (unavg)	6.2047 MPa	6.6708 MPa	6.3497 MPa
Deflection	12.693 μm	12.673 μm	41.348 μm

In comparison to the previous iteration of the interface, slightly lower stresses are observed in the case of tension and vertical bending moment, and significantly lower maximum stresses result under compression and moment of twist. However, in the case of both types of shear and lateral bending moment loading higher stress peaks are found for V1.0 in comparison to MIST V0.0.

As was the case for the previous set of results, there is a significant difference between the averaged and unaveraged stresses for all cases. These are summarized as percentages in Tables 5-2 and 5-3.

Table 5-2: Percentile difference between averaged and unaveraged stress values - MIST V1.0 Part 1

Stress type	Sim type	Tension	Compression	Vertical Shear	Lateral Shear
Von Mises	Female	28.01 %	43.45 %	148.79 %	96.83 %
	Male	34.17 %	39.13 %	149.79 %	94.24 %
	Assembly	25.28 %	51.74 %	17.6 %	77.01 %
Shear	Female	33.52 %	43.92 %	150.64 %	88.26 %
	Male	38.6 %	39.03 %	151.07 %	81.01 %
	Assembly	29.47 %	57.36 %	18.7 %	64.36 %

Table 5-3: Percentile difference between averaged and unaveraged stress values - MIST V1.0 Part 2

Stress type	Sim type	Lateral Bending	Twist	Vertical Bending
Von Mises	Female	31.07 %	132.8 %	26.82 %
	Male	37.1 %	100.88 %	31.09 %
	Assembly	59.37 %	94.2 %	45.64 %
Shear	Female	34.23 %	119.42 %	30.58 %
	Male	39.61 %	85.3 %	34.64 %
	Assembly	56.92 %	80.31 %	43.3 %

The highest differences found for both shear and Von Mises stress peaks are observed under vertical shear, and vertical bending moment loading. It is interesting to note that, while the latter shows large differences between averaged and unaveraged values for all iterations of the simulations, the former shows very small differences for the assembly itself. This could be due to the fact that in the assembled state simulations the force is solely applied to the plates themselves, on a surface that is tapered, hence stress transfer is not resolved efficiently by the solver. Another possibility is the fact that for the assembly itself the load is mainly transferred to the central locking mechanism, which is of a very simple shape, thus the combination of meshing and solver can achieve better results. In the case of vertical bending, most of the load is translated to the tapered T-sections, thus the first possibility for the large differences seems to be more plausible. A second observation that can be made is the fact that the assembly simulation has less variation in stresses compared to the assembled state for most of the load cases, such as tension, both types of shear, as well as moment of twist. This leaves

three cases where the stress difference is larger for the assembly, namely compression, and lateral and vertical bending moments.

With regards to the results presented in Table 5-1, the assembly outperforms both plates with respect to stress for the tensile, compressive and vertical shear load cases. On the other hand, the opposite is true for lateral shear, moment of twist and vertical bending. For lateral bending, the assembly outperforms the female plate performance with respect to stress, but fails to show improvements in comparison to the male plate. This is a relatively unexpected result since the way the bending moment load cases were defined for the assembly should result in an effective increase in moment arm due to distance from the application surface to the area of contact (which coincides with the application surface in the case of the male and female plates). By this logic there are two possible explanations for these results - either the size of the mesh and its positioning caused sufficient variation in the stress calculation to make the assembly results outperform the female plate, or there are some stress concentrations present in the female plate assembled state case that make it have higher peak stresses. For the lateral shear case, the surface area on which the load is applied is larger in the case of the assembly simulation in comparison to the assembled state one. This leads to higher stress distribution in the former case as opposed to the latter. A clearer image of how big these differences are can be obtained by consulting Table 5-4, which compares the male, female and assembly simulation with each other with respect to both unaveraged stresses and deformation. For more clarity, the data is presented as percentages.

Table 5-4: Percentile comparison between assembled state and assembly simulation - unaveraged stress results

Load case	Value	Male vs Female	Male vs Assembly	Female vs Assembly
Tension	Von Mises	+24.28 %	-45.93 %	-32.81 %
	Shear	+23.94 %	-46.18 %	-33.3 %
	Deformation	+20.12 %	-59.73 %	-47.94 %
Compression	Von Mises	-4.2 %	-74.63 %	-69.53 %
	Shear	-4.12 %	-73.4 %	-67.96 %
	Deformation	+7.29 %	-82.87 %	-79.03 %
Vertical Shear	Von Mises	-33.62 %	-60.72 %	-62.37 %
	Shear	-34.6 %	-62.64 %	-64.18 %
	Deformation	-38.27 %	+97.62 %	+112.02 %
Lateral Shear	Von Mises	-5.59 %	+67.2 %	+10.98 %
	Shear	-5.15 %	+71.94 %	+12.44 %
	Deformation	-54.06 %	+269.3 %	+127.96 %
Lateral Bending	Von Mises	-14.26 %	+4.82 %	-1.04 %
	Shear	-13.86 %	+1.82 %	-3.43 %
	Deformation	+9.98 %	+258.54 %	+64.69 %
Moment of twist	Von Mises	-14.26 %	+30.12 %	+11.56 %
	Shear	-13.86 %	+34.87 %	+16.17 %
	Deformation	+9.98 %	+273.1 %	+310.35 %
Vertical Bending	Von Mises	+6.8 %	-1.73 %	+4.95 %
	Shear	+7.51 %	-4.81 %	+2.34 %
	Deformation	-0.16 %	+226.27 %	+225.75 %

With respect to stress, the female plate outperforms the male one in tension and vertical bending, while the opposite is true for the rest of the load cases. This makes sense when considering the lateral T-sections on the male plate which add significant structural strength for most loads. Furthermore one can notice that in the load cases where the assembly outperforms both male and female plates it does so by a significant amount (over 30 %). Another interesting aspect that is made apparent by the data above is that the deformation of the male plate is higher in comparison to the female one for all cases except for tension, compression and moment of twist. Additionally, there is a very large difference in deformation (over 100%) between assembly and assembled state in the case of vertical and lateral shear, as well as all moment cases.

Including a safety factor coefficient function for both Von Mises and maximum shear stress, the limit loads for each case can be simulated. Using the unaveraged stresses from the assembly simulation leads to the results summarized in Table 5-5. It is important to note that the right-hand side column represents the failure mode under each load, based on either Von Mises or maximum shear failure criteria.

Table 5-5: Maximum load bearing capabilities of MIST V1.0

Load case	Magnitude	Failure mode
Tension	152707 N	Shear
Compression	358416 N	Shear
Shear (vertical)	222734 N	Shear
Shear (lateral)	217698 N	Shear
Lateral bending moment	20633.589 $N \cdot m$	Shear
Moment of twist	32856.527 $N \cdot m$	Shear
Vertical bending moment	22030.646 $N \cdot m$	Shear

In comparison to MIST V0.0, this iteration outperforms it slightly in the case of maximum tensile force and vertical bending moment. It is significantly more resistant in compression and moment of twist, whilst being weaker than V0.0 in all other cases. The magnitude of the limit loads confirm what was mentioned previously, namely that even with the decrease in performance under certain load cases, the interface is more than sufficient for a much larger telescope structure than the 15 m diameter aperture considered for preliminary sizing.

A similar comparison is made between the assembled state simulations of the male and female plates, and the assembly simulation for MIST V1.0, scaled down to 120 mm by 120 mm. This is done so as to be able to compare with existing interfaces [12], [13], [42], [43], which have similar dimensions. A summary of the simulation results is presented in Table 5-6.

Table 5-6: Part and assembly load simulation results MIST V1.0 120x120 version (ANSYS)

Loading case	Female Plate	Male Plate	Assembly
Tension - 10 kN			
Von Mises (avg)	61.154 MPa	72.256 MPa	53.407 MPa
Von Mises (unavg)	84.267 MPa	102.74 MPa	62.632 MPa
Max Shear (avg)	33.222 MPa	39.783 MPa	29.024 MPa
Max Shear (unavg)	47.503 MPa	58.028 MPa	35.682 MPa
Deflection	60.071 μm	65.956 μm	39.339 μm
Compression - 10 kN			
Von Mises (avg)	50.405 MPa	63.523 MPa	19.068 MPa
Von Mises (unavg)	68.619 MPa	88.739 MPa	22.636 MPa
Max Shear (avg)	27.421 MPa	34.276 MPa	10.244 MPa
Max Shear (unavg)	38.696 MPa	50.118 MPa	12.798 MPa
Deflection	59.214 μm	57.168 μm	11.085 μm
Shear (vertical) - 10 kN			
Von Mises (avg)	79.383 MPa	53.071 MPa	70.158 MPa
Von Mises (unavg)	164.42 MPa	110.29 MPa	86.092 MPa
Max Shear (avg)	42.84 MPa	30.5 MPa	36.933 MPa
Max Shear (unavg)	93.713 MPa	62.372 MPa	44.124 MPa
Deflection	20.234 μm	15.879 μm	65.928 μm
Shear (lateral) - 10 kN			
Von Mises (avg)	32.2 MPa	16.864 MPa	28.336 MPa
Von Mises (unavg)	62.136 MPa	31.439 MPa	55.312 MPa
Max Shear (avg)	17.729 MPa	9.4203 MPa	15.877 MPa
Max Shear (unavg)	31.889 MPa	16.643 MPa	29.81 MPa
Deflection	13.08 μm	7.4196 μm	13.49 μm
Lateral bending moment - 1 kNm			
Von Mises (avg)	117.33 MPa	111.89 MPa	148.5 MPa
Von Mises (unavg)	159.95 MPa	147.44 MPa	176.43 MPa
Max Shear (avg)	64.414 MPa	61.041 MPa	84.803 MPa
Max Shear (unavg)	90.075 MPa	82.732 MPa	93.115 MPa
Deflection	90.882 μm	55.952 μm	236.53 μm
Moment of twist - 1 kNm			
Von Mises (avg)	72.408 MPa	46.66 MPa	82.445 MPa
Von Mises (unavg)	144.23 MPa	90.804 MPa	170.59 MPa
Max Shear (avg)	38.677 MPa	26.082 MPa	46.587 MPa
Max Shear (unavg)	75.133 MPa	46.111 MPa	93.265 MPa
Deflection	18.705 μm	10.854 μm	60.807 μm
Vertical bending moment - 1 kNm			
Von Mises (avg)	115.04 MPa	92.191 MPa	133.78 MPa
Von Mises (unavg)	153.29 MPa	134.26 MPa	214.83 MPa
Max Shear (avg)	66.301 MPa	51.204 MPa	74.266 MPa
Max Shear (unavg)	88.501 MPa	74.653 MPa	117.36 MPa
Deflection	40.192 μm	34.738 μm	110.21 μm

All the trends from the full-scale MIST V1.0 results stay true for the scaled down version. The assembly outperforms the plates in the tensile, compressive and vertical shear cases, whereas the opposite holds true under all other load cases. This makes the assumption that the trend deviation seen in V0.0 is an error caused by result inaccuracy even more likely.

In the same manner as for the full-scale interface model, the unaveraged stress values for the assembly coupled with a safety factor function leads to the limit loads summarized in Table 5-7.

Table 5-7: Maximum load bearing capabilities of MIST V1.0 (120x120)

Load case	Magnitude	Failure mode
Tension	39186 N	Shear
Compression	109174 N	Shear
Shear (vertical)	34041 N	Shear
Shear (lateral)	46823 N	Shear
Lateral bending moment	1460.275 $N \cdot m$	Shear
Moment of twist	1399.944 $N \cdot m$	Shear
Vertical bending moment	1241.851 $N \cdot m$	Shear

These limit loads outperform all the existing interfaces ([12], [13], [42], [43]) in all load cases by a significant margin. Additionally, even at this scale, a 15 m diameter primary aperture telescope is easily achievable, however it would take many more modules to create such a structure. A numerical comparison between the load bearing capabilities of MIST and those of existing state-of-the-art interfaces is given in Table 5-8.

Load case	MIST	Other Interfaces	Performance Increase (%)
Tension	39186 N	6000 N (iBoss)	553.1%
Compression	109174 N	6000 N (iBoss)	1719.57%
Shear (vertical)	34041 N	5000 (SIROM)	580.82%
Shear (lateral)	46823 N	5000 (SIROM)	836.46%
Lateral bending moment	1460.275 $N \cdot m$	400 $N \cdot m$ (iBoss)	265.07%
Moment of twist	1399.944 $N \cdot m$	420 $N \cdot m$ (SIROM)	233.32%
Vertical bending moment	1241.851 $N \cdot m$	400 $N \cdot m$ (iBoss)	210.46%

Table 5-8: Performance Comparison Between MIST and Existing Interfaces

Chapter 6

Detailed Interface Design - Final Iterations

This chapter covers the final iterations of the MIST concept as well as the design considerations that were not included in previous iterations. Section 6-1 describes the logic and choices that drove the iterations from V1.0 to V2.2, whilst Section 6-2 summarizes the simulation results involving vibrations and natural frequency identification. Finally, Section 6-3 describes the final adjustments to the MIST design, namely the clearance necessary so that assembly can be smoothly performed, as well as the impact of environmental temperature on this design choice.

6-1 Interface Final Design (MIST V2.0-V2.2)

Although the first iteration of MIST presents many advantages, there are still potential issues that can be addressed. The biggest one is that the locking cylinder is both a load-bearing structure (in the case of shear loads) whilst also doubling as the channel through which data and electrical connectors run through. This is problematic as any damage to this system may interfere with or even sever these connections completely. In order to avoid such problems, it is decided to decouple these two roles by splitting the central part into two, resulting in a new iteration of the interface, henceforth referred to as MIST V2.0. This version will comprise of four elements, two plates, a central locking cylinder that is hollowed out, and a connector cylinder which has the role of passing both current and data when assembled, as illustrated in Figure 6-1.

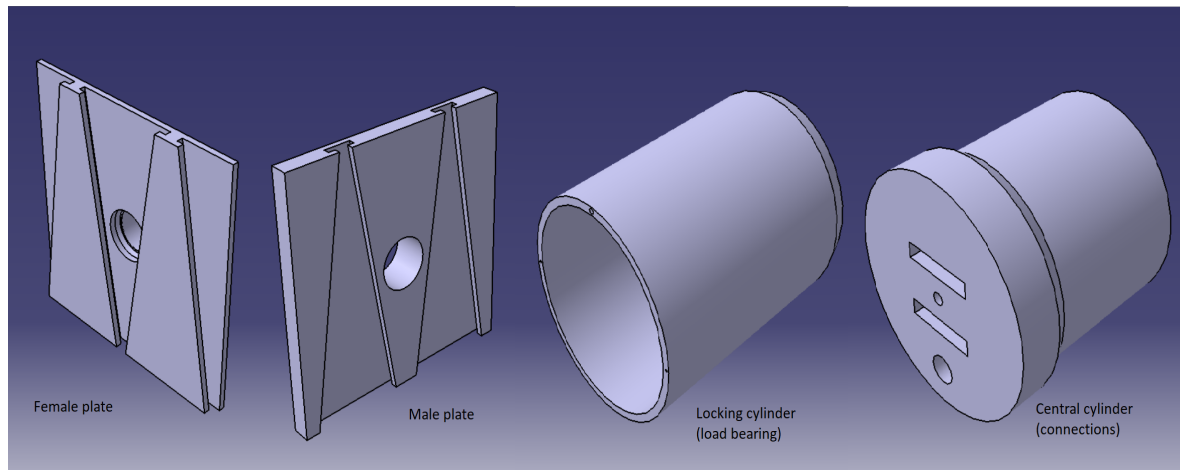


Figure 6-1: Overview of MIST interface components (V2.0)

This design decision will result in the previously single moving part now being separated into two, requiring separate actuation. This would again raise some issues of alignment similar to the assembly of the two plates, hence the choice of tapering for the end of the locking cylinder and the beginning of the central connector. This leads to minor modifications required for the central channel of the female plate, whilst all dimensions pertaining to the plate as well as T-sections remain unchanged. For completeness, all technical drawings for MIST V2.0 at full scale were added in Appendix A, Figures A-7, A-8, A-9, A-10, corresponding to the male plate, female plate, locking cylinder, and end connector, respectively. Similarly, the scaled down version is included in Appendix B, Figures B-7, B-8, B-9, B-10, with consistency being retained with respect to interface element order.

In spite of this being the last version of the MIST interface, a few slight iterations were performed in order to promote ease of assembly and design flexibility. When considering the central mechanism, due to the separation between the locking cylinder and the end connector, a choice must be made with respect to actuation. Either one can use a single linear actuator to drive the entirety of the mechanism or two separate actuators can be used. Due to the nature of the dimensions and the ready availability of lower stroke length actuators, it is decided that separate actuation will be used for the end-connector and the central locking cylinder. This results in the need for interfacing elements between the target parts for the actuators and the actuators themselves, as can be seen in the Appendices containing the technical drawings. Additionally this decision is also guided partly by a consideration for redundancy, as given a sufficiently long stroke length for the latter, the mechanism can still be actuated fully even if the secondary actuator were to fail, provided said failure locked it in fully extended mode. Following this decision the question of flexibility with respect to choice of actuator comes into play. The most common linear actuators use rotation in their actuation, and considering they also represent the cheapest option, it would not be recommended to discount these options from the design space. As such, an easy solution would be to design guides for both locking cylinder and end-connector elements so that, provided the linear actuator torque does not exceed the limit load tolerances of said guides, both rotating and non-rotating linear actuators can be used. This leads to the modifications illustrated in Figure 6-2. This iteration of the interface will henceforth be referred to as MIST V2.1.

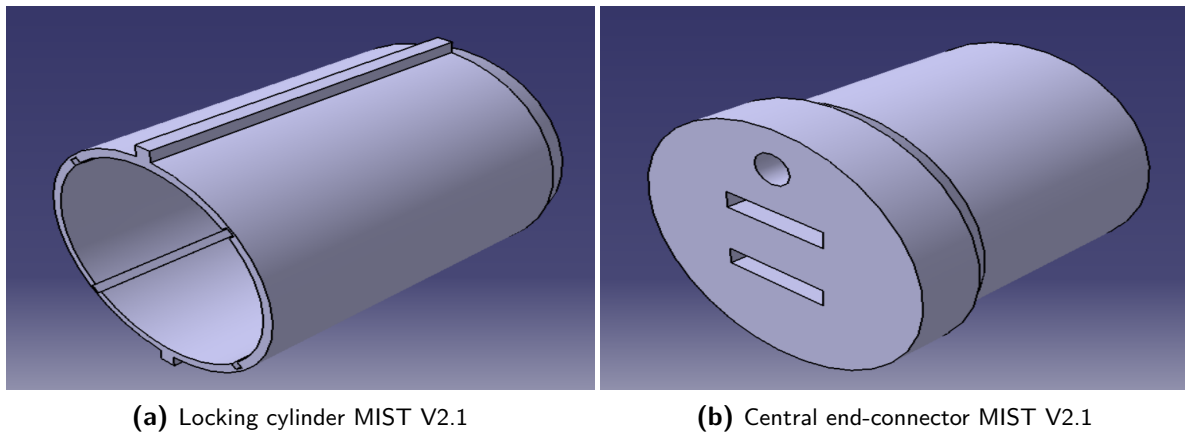


Figure 6-2: Main parts modified with guide elements for MIST V2.1

Due to space constraints the full technical drawings for this interface version will not be included here, but added in Appendix A (for the full-scale model), Figures A-11, A-12, A-13, A-14, A-15. As for the scaled down version for comparison with existing interfaces, the technical drawings are included in Appendix B, Figures B-11, B-12, B-13, B-14, B-15.

It is important to note that although a preliminary choice of linear actuators will be discussed in the following subsection, the guides discussed permit a change in actuator selection with minimal design changes. This ensures that the design can be used for various missions with different budgets and design philosophies.

The final modification leading to MIST 2.2 mainly concern ease of assembly and redundancy, specifically in the case of the end-connector. Multiple data and electrical end-connector slots have been added and the end has been tapered so that the linear actuator has an easier time of guiding said element along its stroke length, effectively producing the desired data and electrical connection. This is illustrated in Figure 6-3.

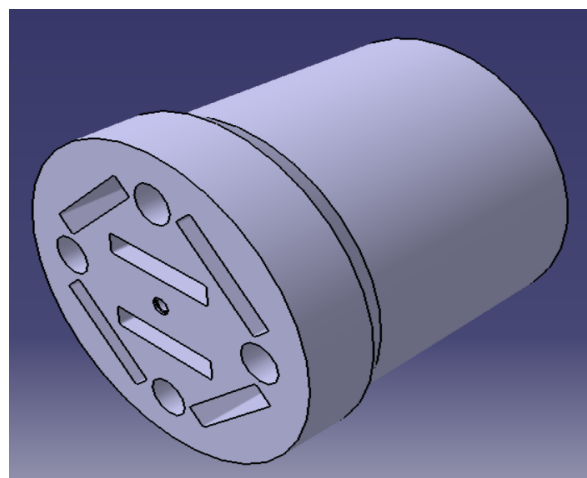


Figure 6-3: Modified end-connector element with redundancy and tapered end

The full mechanism including all part technical drawings is included in Appendix A, Figures A-16,A-17,A-18,A-19,A-20,A-21. Due to dimensional constraints, it was impossible to add redundancy to the scaled-down version, as such the only design modification would be the taper being added to a single part. As such, it is considered a sufficiently insignificant change so as to not warrant the inclusion of the full specifications for this scaled-down version.

6-2 ANSYS simulation results - Natural Frequency

In order to satisfy the frequency requirements (MIST-S-1.1 and MIST-S-1.2), a modal analysis was performed in ANSYS in order to identify the first six resonance frequencies of not only individual components of the interface but also cubic modules using the interface described in this work. This was done so as to ensure that not only modules can be launched in any type of launcher but spare parts of the smallest scale can also be sent if necessary (although this is not recommended). For the female and male plate, the same surfaces were used as fixed support for the simulation. In the case of the central elements, the male-facing end was constrained as fixed. Finally for the modules, one of the two surfaces not containing interfaces was defined as fixed support. Table 6-1 summarizes the results of these simulations.

Table 6-1: First six natural frequencies of MIST V2.2 elements and modules using MIST V2.2

Element	f_1	f_2	f_3	f_4	f_5	f_6
Male plate	798.55 Hz	1633.2 Hz	1847.3 Hz	2531 Hz	2605.2 Hz	3140.3 Hz
Female plate	890.5 Hz	1242.4 Hz	1964.8 Hz	2436.7 Hz	2498.5 Hz	3013.8 Hz
Locking cylinder	2075.1 Hz	2138.8 Hz	3173.9 Hz	3283.6 Hz	4173.4 Hz	4189.4 Hz
End-connector	6522.2 Hz	6994.6 Hz	11337 Hz	16861 Hz	17822 Hz	1827 Hz
Male module	441.56 Hz	582.19 Hz	582.21 Hz	613.08 Hz	694.91 Hz	933.96 Hz
Female module	439.45 Hz	598.07 Hz	598.13 Hz	641.26 Hz	758.1 Hz	894.55 Hz

All natural frequencies for all test cases are significantly above 60 Hertz, thus both requirements are easily satisfied. For the plate elements, the first natural frequency corresponds to lateral motion along the locking axis, as illustrated in Figure 6-4.

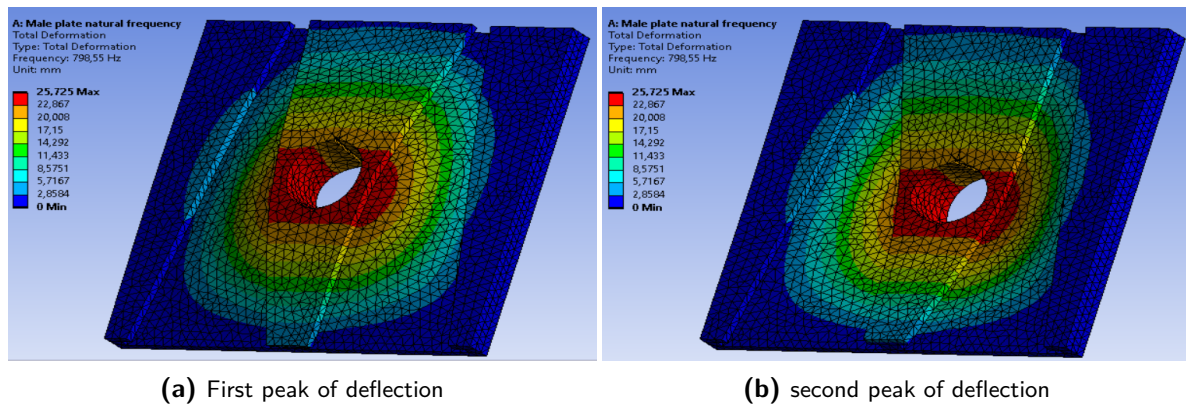


Figure 6-4: Male plate - deflection at f_1

The deformation is similar to the tensile and compressive cases, with the highest values being registered around the central hole through which the locking cylinder is fitted. The maximum deformation pattern is also shifted downward from the center of the hole due to the tapered T-section. The second natural frequency corresponds to lateral motion in-plane, as shown in Figure 6-5.

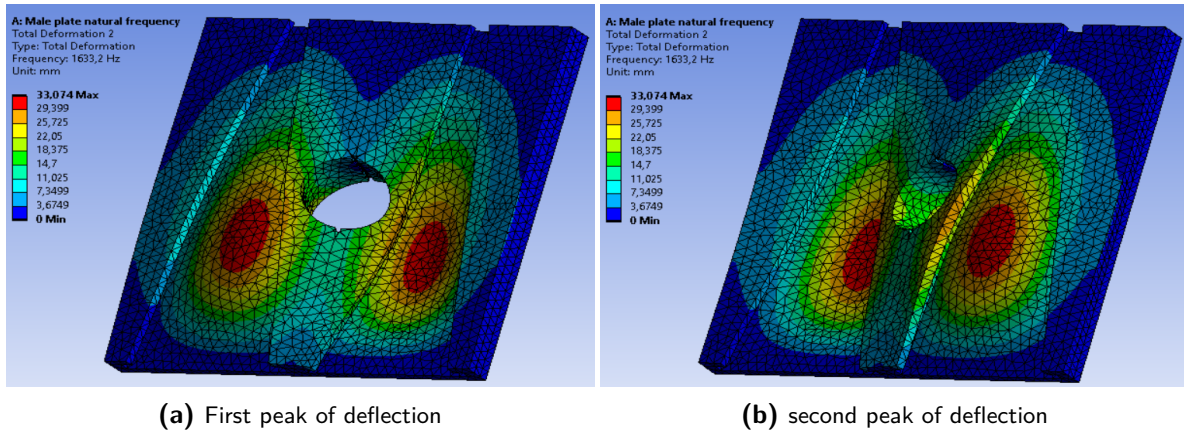


Figure 6-5: Male plate - deflection at f_2

In this case, the maximum deflection is registered between the T-sections, in the middle of the plate elements. The peaks are shifted even farther downwards due to the fact that the larger the distance between the tapered T-sections, the lower the resistance of the plate elements, especially for buckling failure modes. For the third natural frequency, motion is registered along the vertical axis, in other words longitudinal natural frequency, as illustrated in Figure 6-6.

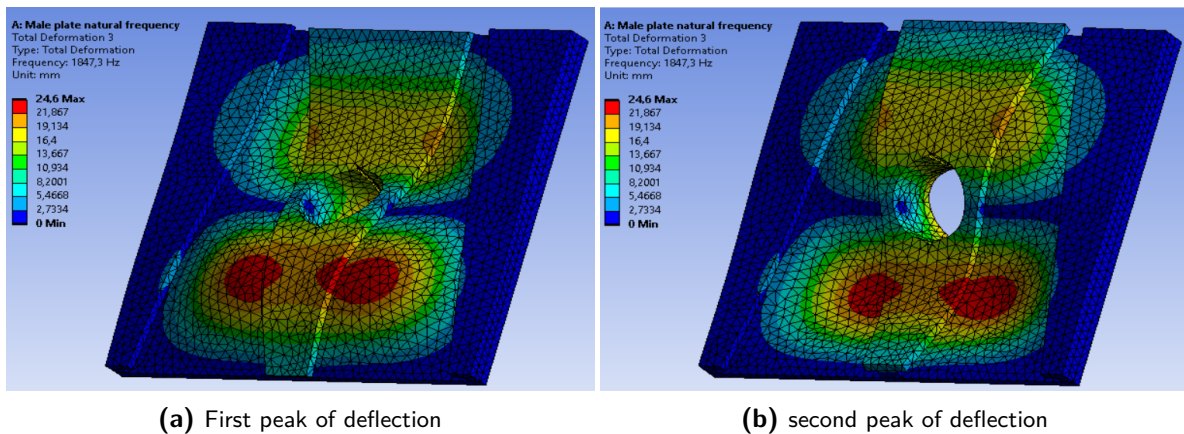


Figure 6-6: Male plate - deflection at f_3

It is important to note that the peaks of deflection are again shifted downwards from the central horizontal axis, due to the same reasoning as for the previous natural frequency case. Furthermore, due to the nature of the buckling mode, they are more concentrated towards the vertical symmetry axis. The peaks do not meet at the middle however, mainly due to

the extra structural resistance conferred by the central T-section. Slightly lower values of deformation can be seen above the central horizontal line, at the edges of the lateral sides of the central T-shaped element. Whereas all the other natural frequencies found for the plates can be categorized as either lateral or longitudinal, the fourth natural frequency is a special case that can most accurately be described as twist, or a combination of both lateral and longitudinal motion, as shown in Figure 6-7.

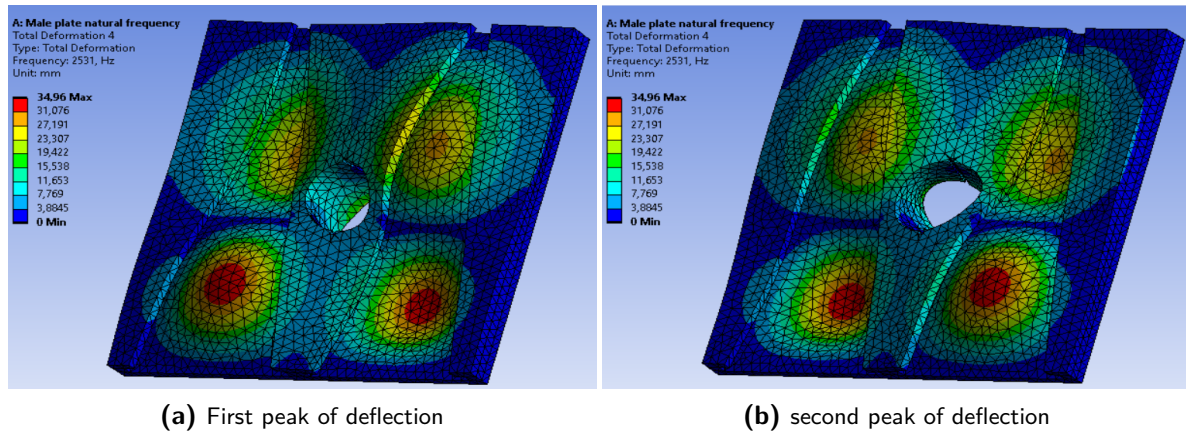


Figure 6-7: Male plate - deflection at f_4

Similarly to the fourth natural frequency, the main peaks in deflection for this mode is registered towards the bottom of the plate sections, with slightly lower deflection peaks in the top plate sections. These two different peaks are almost symmetrical with respect to the horizontal middle axis, however they are slightly shifted downwards due to tapering. The fifth natural frequency corresponds to the second mode along the locking direction, as illustrated in Figure 6-8.

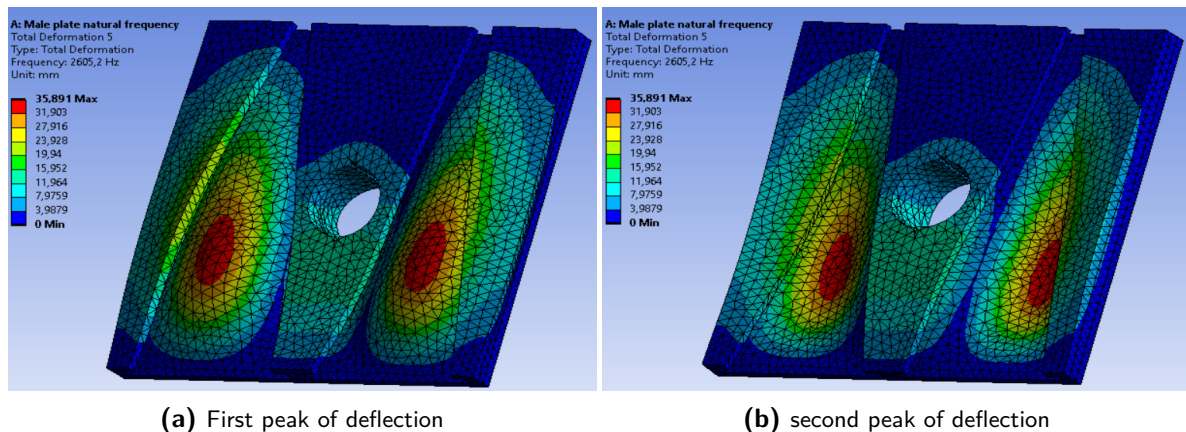


Figure 6-8: Male plate - deflection at f_5

The peaks for this natural frequency case are very similar to the second natural frequency, however deflection is slightly higher (approximately 10%). The last natural frequency for the plates corresponds to the second mode for lateral in-plane motion, as shown in Figure 6-9.

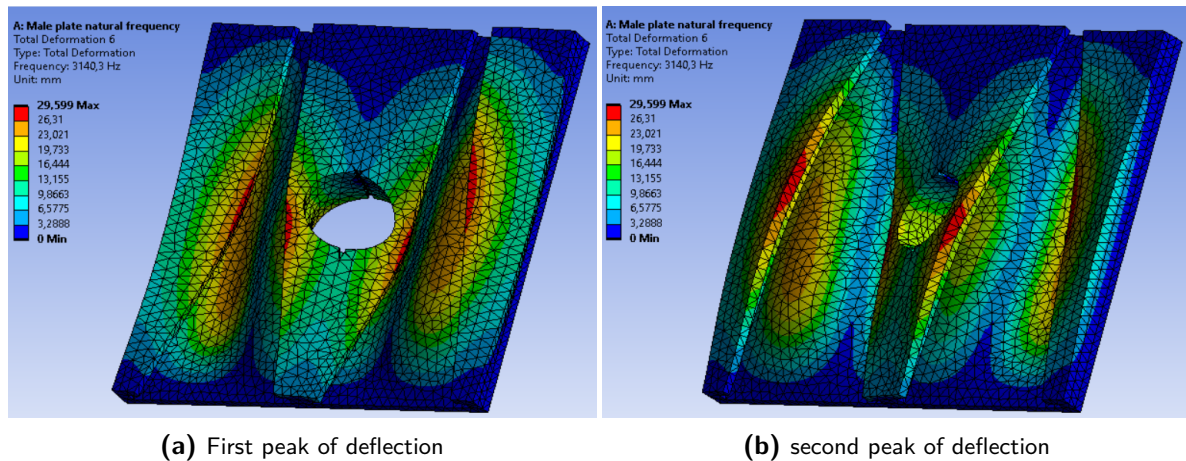


Figure 6-9: Male plate - deflection at f_6

The distribution of peaks for deflection for this last natural frequency case is mainly concentrated around the edges of the T-sections. This is mainly attributed to a combination between where buckling occurs (closer to the lateral T-sections rather than the middle of the plate), coupled with the edges having the same thickness as the plate elements. For both locking cylinder and end-connector parts, the order of the natural frequencies corresponds to different cases than for the plates. The first one corresponds to the first longitudinal mode, as illustrated in Figure 6-10.

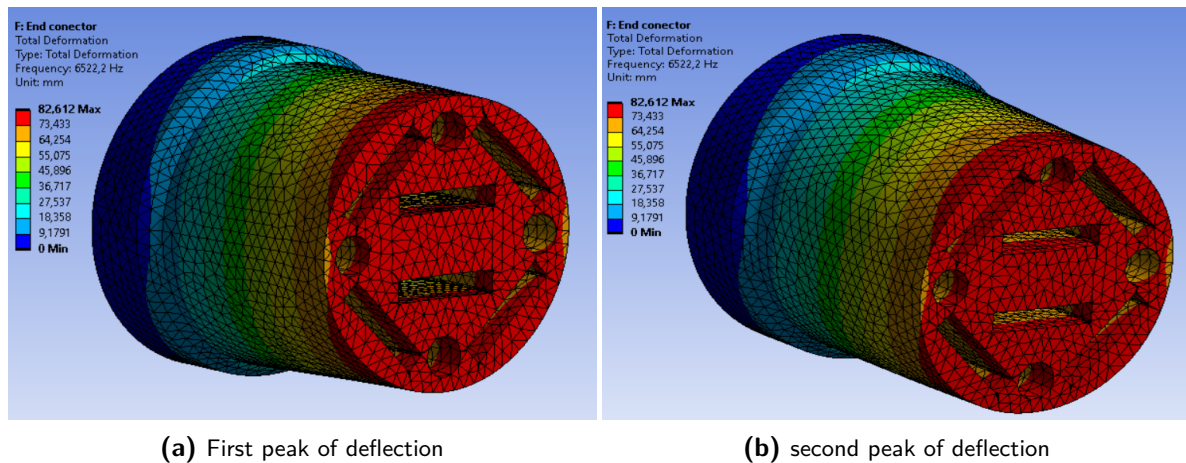


Figure 6-10: End-connector - deflection at f_1

As expected given the buckling mode above, the deformation is almost evenly distributed throughout the piece, with the peaks occurring at the end where the connectors come out. The second frequency leads to motion in the lateral direction, as shown in Figure 6-11.

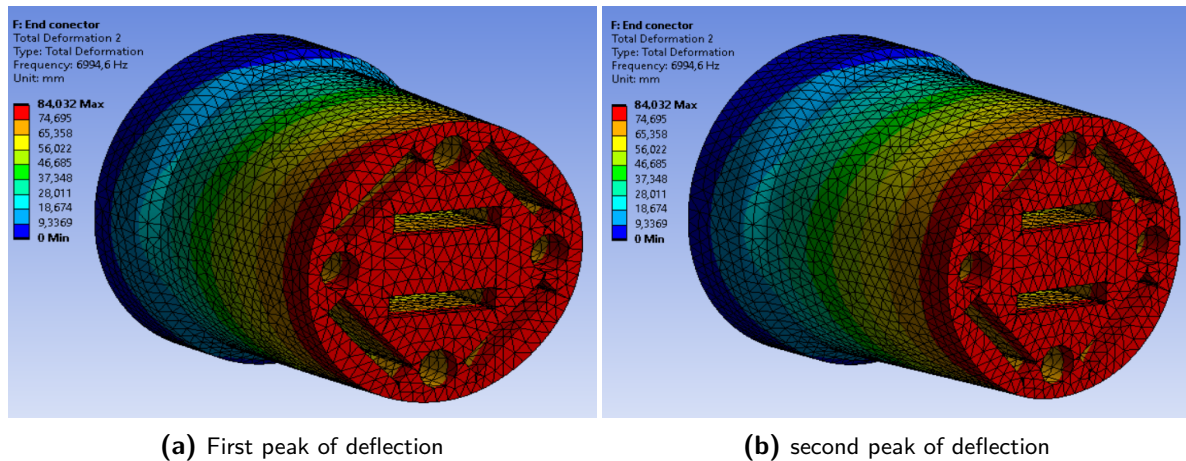


Figure 6-11: End-connector - deflection at f_2

Similarly to the previous natural frequency case, the maximum deformation is mainly distributed around the front-end of the piece. It is important to note however, that due to the lateral motion caused by the vibration there is higher deformation around the horizontal edges, rather than the vertical ones. Whereas all the other natural frequencies found for the plates can be categorized as either lateral or longitudinal, the third frequency case is a combination of the two, most accurately described as twist or radial, as illustrated in Figure 6-12.

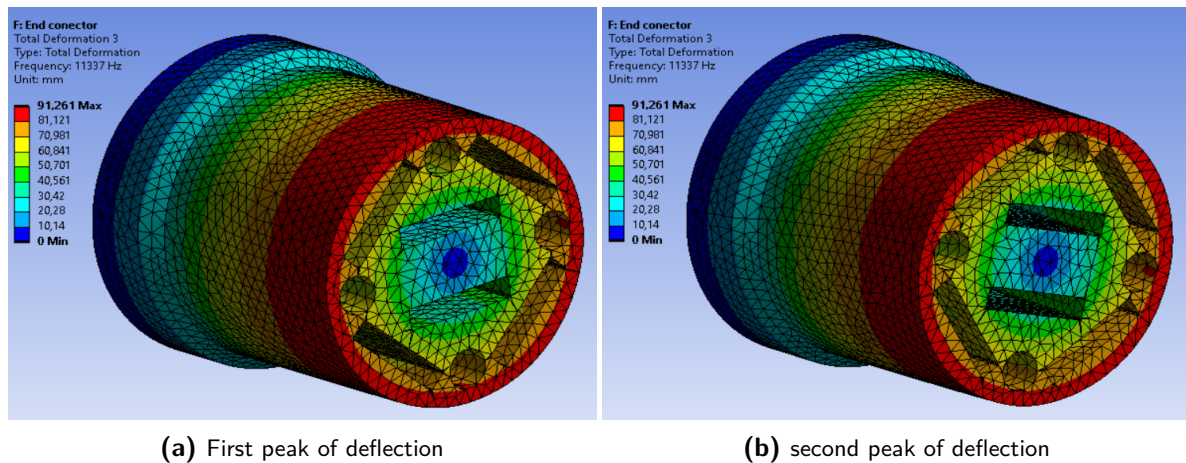


Figure 6-12: End-connector - deflection at f_3

Due to the nature of the twisting motion, one can notice the deformation lowering both from front to back, as well as from the edges to the central part of the piece. The fourth natural frequency is the second mode for radial motion, as shown in Figure 6-7.

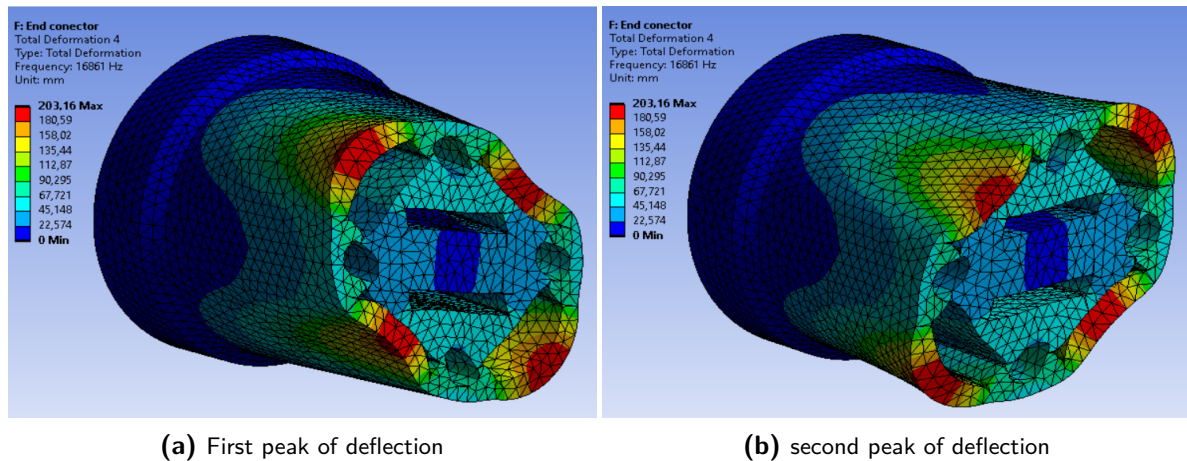


Figure 6-13: End-connector - deflection at f_4

This fourth case shows some very interesting results, as the peaks in deformation are registered on the diagonal parts. This is attributed to not only the buckling mode, but the fact that the holes where the data connectors run through create a weakness in the structural integrity of the piece in comparison to a filled out cylinder. The fifth natural frequency corresponds to the second longitudinal mode, as illustrated in Figure 6-14.

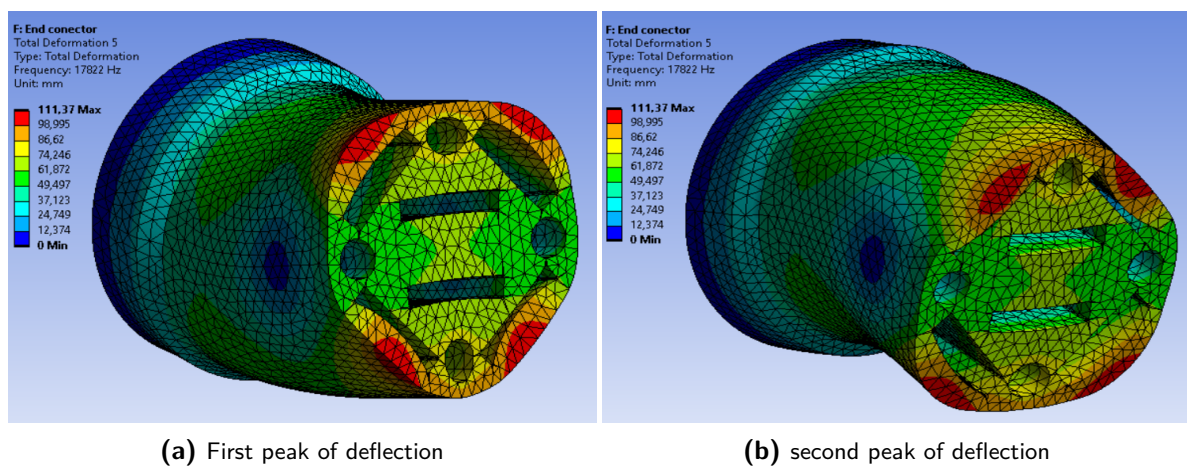


Figure 6-14: End-connector - deflection at f_5

Although very similar results are registered for the deflection peaks as for the previous case, the secondary peaks are not distributed symmetrically around the main peaks, instead they are spread around the top and bottom of the cylinder. The last natural frequency for the plates corresponds to motion along the locking axis, as shown in Figure 6-15.

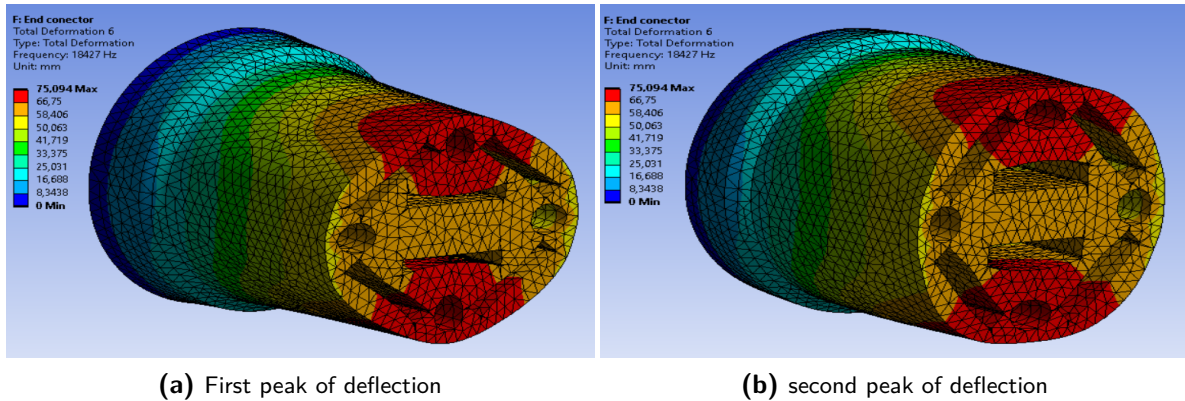


Figure 6-15: End-connector - deflection at f_6

The last natural frequency shown for the central cylinder shows what can be explained as a combination of the first and fifth natural frequency. To be more specific, the highest peaks in deformation are registered towards the top and bottom of the front end of the piece, lowering towards the back end. Finally, the male and female modules also present different directions of deflection from the two classes of elements previously discussed. The first natural frequency represents the longitudinal mode, as illustrated in Figure 6-16.

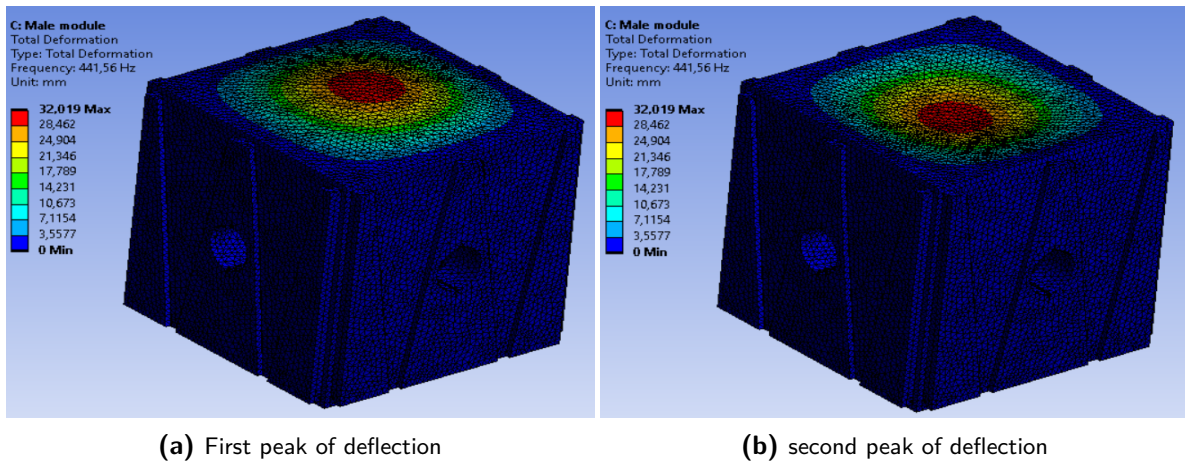


Figure 6-16: Male/Female module - deflection at f_1

For the modules themselves, the first natural frequency causes symmetrical deflection peaks in both the top and the bottom plates, slowly decreasing from the center towards the interface walls. The second frequency leads to motion in the two lateral directions, as shown in Figure 6-17.

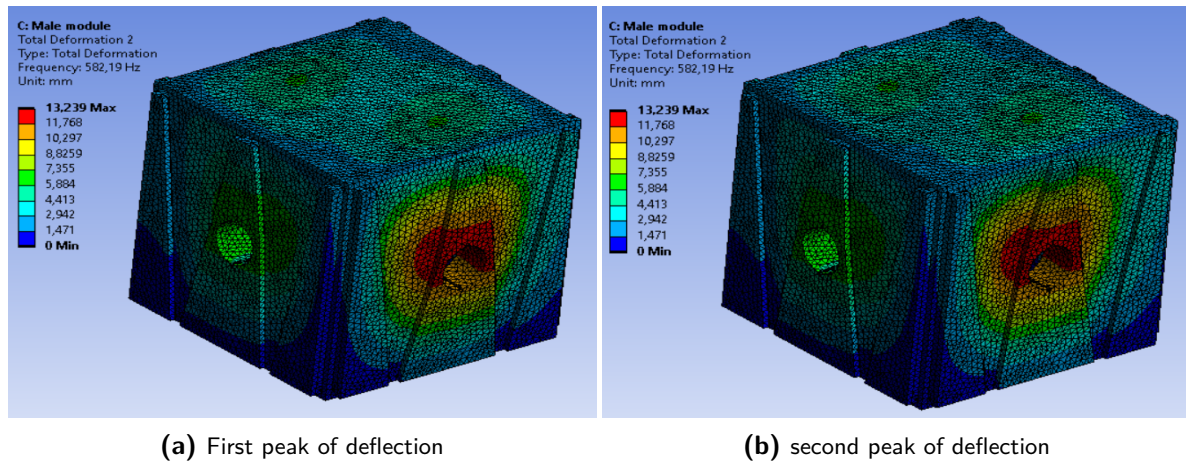


Figure 6-17: Male/Female module - deflection at f_2

Due to the nature of the buckling mode, the main deflection peaks are registered symmetrically on two of the interface walls, whilst the rest of the walls only register about 40% or less deflection. The third natural frequency leads to movement in the other lateral axis as compared to the previous one, as illustrated in Figure 6-18.

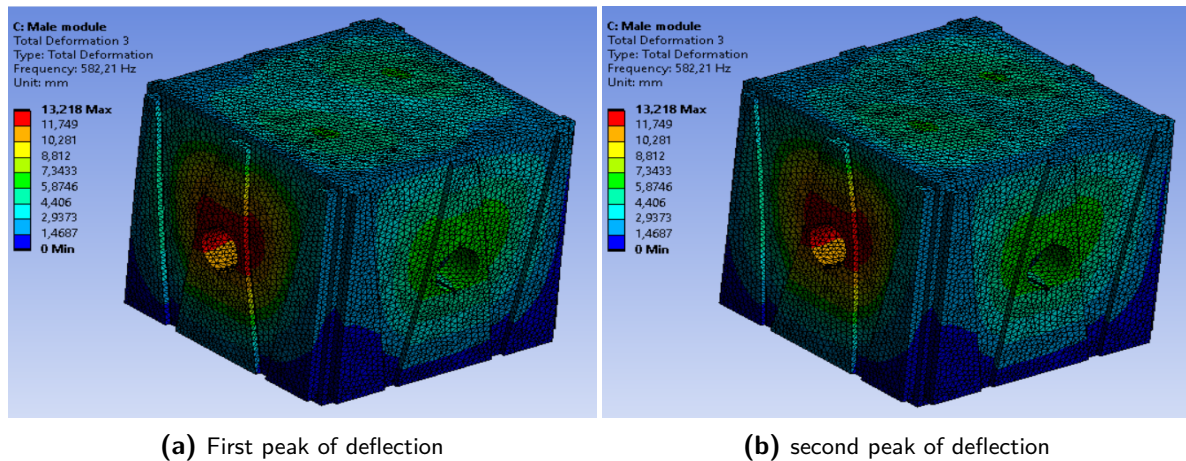


Figure 6-18: Male/Female module - deflection at f_3

The third natural frequency shows a very similar trend in comparison to the second natural frequency. The only difference is that the direction of buckling is perpendicular to the previous case. In that regard, the deflection is the same, but in the direction just explained. The fourth natural frequency seems to be a combination of motion in both lateral directions, as shown in Figure 6-19.

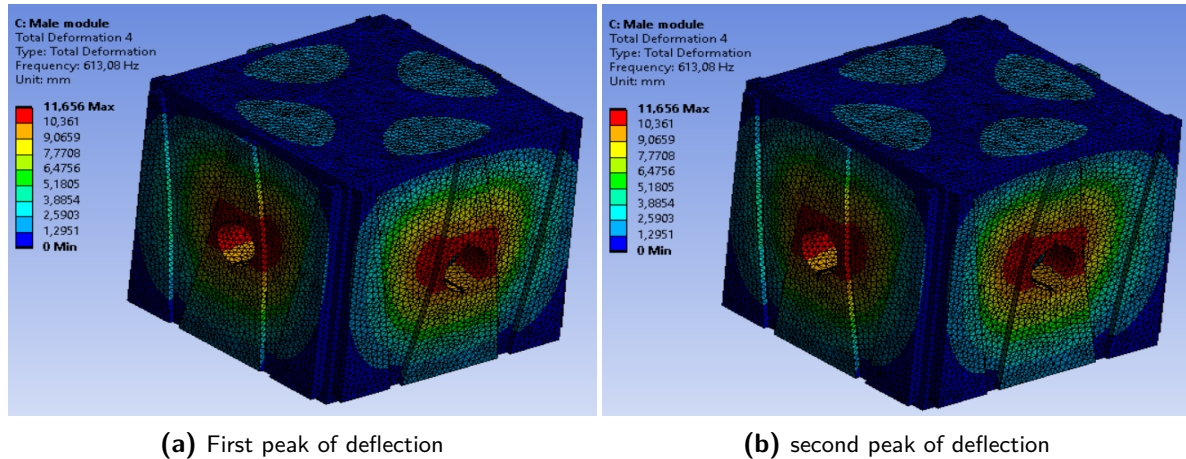


Figure 6-19: Male/Female module - deflection at f_4

It can be noted that this case seems like a perfect superposition of the second and third natural frequencies however, due to the interaction between the two motions the deflection on the top and bottom plates are much lower. It is important to notice that whilst the movement in one of the two perpendicular (lateral) directions is inwards, the other one is outwards. This makes for a very interesting buckling case that is generally not seen in a lot of structures. The fifth natural frequency shows a combination of both lateral modes and the longitudinal one, as illustrated in Figure 6-20.

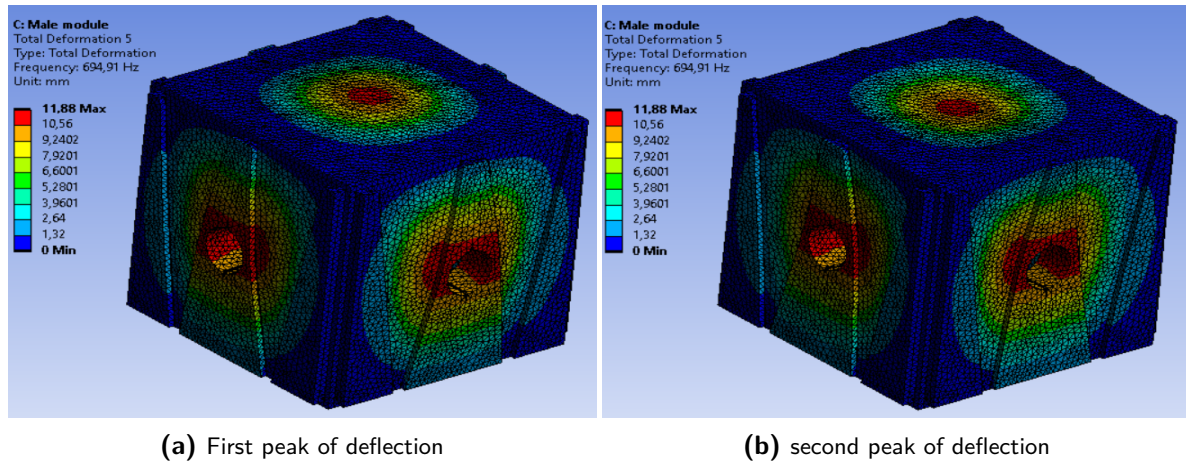


Figure 6-20: Male/Female module - deflection at f_5

The fifth natural frequency mode shows similarities to the fourth one, however all walls are either deflecting outwards or inwards at the same time. This also makes it so that the top and bottom plates have much higher deflection values, with the peaks slowly decreasing from the middle towards the edges. The final natural frequency for the modules corresponds to the second mode along the lateral axis that the second frequency also caused movement in, as shown in Figure 6-21.

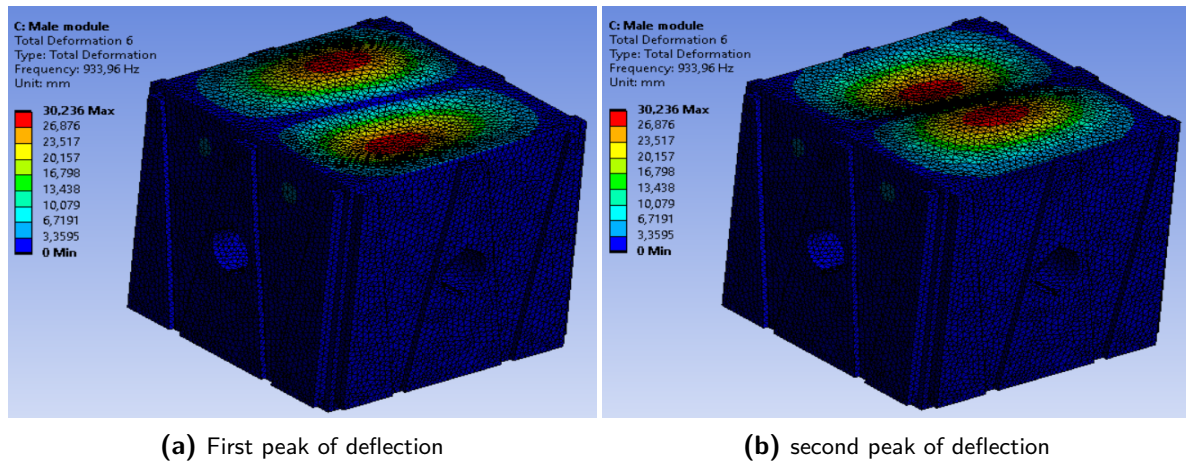


Figure 6-21: Male/Female module - deflection at f_6

The final natural frequency mode shows symmetrical deflection in both the top and bottom plate, with very low influence on any of the lateral interface walls. There are two main peaks on each plate, mainly attributed to the buckling mode involved. This concludes the evaluation of the natural frequency failure modes for not only the interface elements (plates and central cylinder) but for the modules envisioned in the MIST design as well.

6-3 Clearance and Thermal Considerations

The first thing that will be considered in this section is the clearance necessary so that all parts can be smoothly assembled. In order to do so, one must first consider what sort of fit is needed for each part of the system. As this is necessary solely for the dimensions that lead to direct contact between the various components, a notation was established for each of the key dimensions, as illustrated in Figures 6-22, 6-23, 6-24.

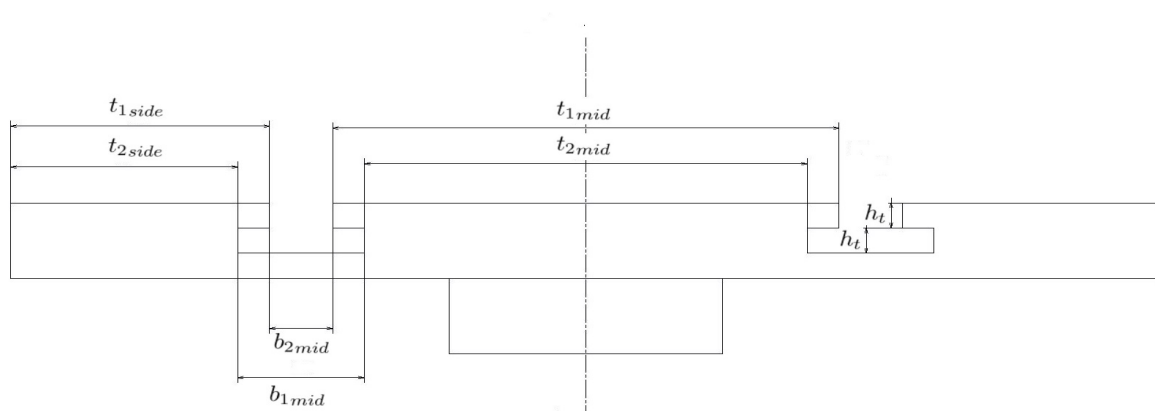


Figure 6-22: Contact dimensions notation for top of the male plate

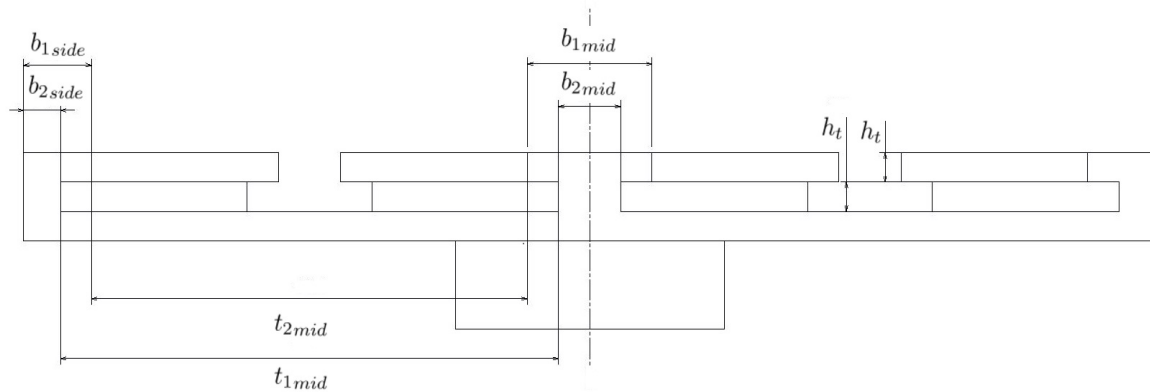
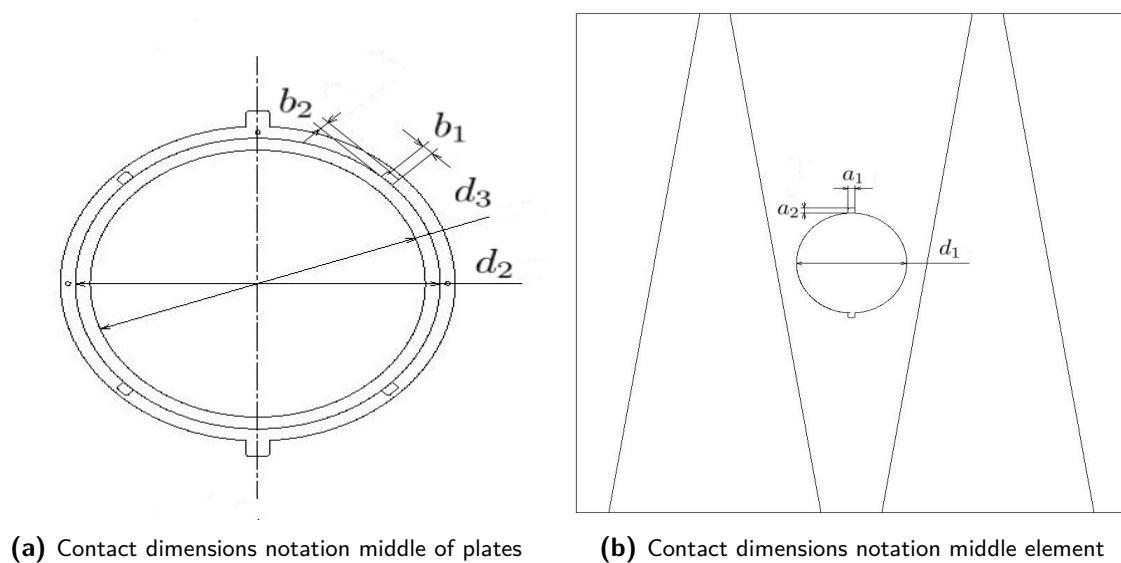


Figure 6-23: Contact dimensions notation for bottom of the male plate



(a) Contact dimensions notation middle of plates

(b) Contact dimensions notation middle element

Figure 6-24: Central contact dimensions notation

The ISO 286-1 standard provides a coherent system of categorizing fits, from clearance, to transitional and interference fits [17]. Table 6-2 provides an overview of this standard and what each type of fit means. In the case of MIST, the only class that is of interest is the clearance fit, however all classes are included for completeness.

Table 6-2: ISO 286-1 standard fits explained, courtesy of [17]

Fit type	Hole Basis	Shaft Basis	Description
Clearance fit	H11/c11	C11/h11	Loose running fit for wide commercial tolerances or allowances on external members.
	H9/d9	D9/h9	Free running fit not for use where accuracy is essential, but good for large temperature variations, high running speeds, or heavy journal pressures.
	H8/f7	F8/h7	Close running fit for running on accurate machines and for accurate location at moderate speeds and journal pressures.
	H7/g6	G7/h6	Sliding fit not intended to run freely, but to move and turn freely and locate accurately.
	H7/h6	H7/h6	Locational clearance fit provides snug fit for locating stationary parts; but can be freely assembled and disassembled.
Transition fit	H7/k6	K7/h6	Locational transition fit for accurate location, a compromise between clearance and interference.
	H7/n6	N7/h6	Locational transition fit for more accurate location where greater interference is permissible.
Interference fit	H7/p6	P7/h6	Locational interference fit for parts requiring rigidity and alignment with prime accuracy of location but without special bore pressure requirements.
	H7/s6	S7/h6	Medium drive fit for ordinary steel parts or shrink fits on light sections, the tightest fit usable with cast iron.
	H7/u6	U7/h6	Force fit suitable for parts which can be highly stressed or for shrink fits where the heavy pressing forces required are impractical.

One of the most important things to be considered is that providing too much clearance for the T-sections would lead to loss of rigidity of the overall system. As such, the tightest clearance fit is selected for the dimensions corresponding to the T-sections, namely H7/h6. As for the central sections, a looser fit would not be a problem considering the added taper in the MIST V2.2 iteration. As such H7/g6 is chosen so that sufficient sliding space is allowed. Using a freely available tolerance calculator [112] results in the dimensions and corresponding clearances shown in Table 6-3.

Table 6-3: Initial and final values for dimensions requiring clearance

Dimension notation	Initial size	Fit type	Clearance dimension	Final size
t_{1mid}	176 mm	H7/h6	(2x) 0.065 mm	175.87 mm
t_{2mid}	154 mm	H7/h6	(2x) 0.065 mm	153.87 mm
t_{1side}	90 mm	H7/h6	0.057 mm	89.943 mm
t_{2side}	79 mm	H7/h6	0.049 mm	78.951 mm
b_{1mid}	44 mm	H7/h6	(2x) 0.041 mm	43.918 mm
b_{2mid}	22 mm	H7/h6	(2x) 0.034 mm	21.932 mm
b_{1side}	24 mm	H7/h6	0.034 mm	23.966 mm
b_{2side}	13 mm	H7/h6	0.024 mm	12.976 mm
h_t	10 mm	H7/g6	(2x) 0.029 mm	9.942 mm
d_1	80 mm	H7/g6	(2x) 0.059 mm	79.882 mm
d_2	73.6 mm	H7/g6	(2x) 0.059 mm	73.482 mm
d_3	67.6 mm	H7/g6	(2x) 0.059 mm	67.482 mm
a_1	5 mm	H7/g6	(2x) 0.024 mm	4.952 mm
a_2	4 mm	H7/g6	0.024 mm	3.976 mm
b_1	3 mm	H7/g6	(2x) 0.018 mm	2.964 mm
b_2	2 mm	H7/g6	0.018 mm	1.982 mm

The final step when considering assembly clearance is to account for thermal contraction since the manufacturing will not be done at the temperatures a space telescope will operate in. Thermal expansion is governed by Equation 6-1, where α is the coefficient of thermal expansion corresponding to the selected material, L is the dimension under consideration, ΔT is the difference in temperature between the original (ground in this case) and operational temperature, and ΔL is the amount by which the dimension contracted or expanded.

$$\Delta L = \alpha \cdot L \cdot \Delta T \quad (6-1)$$

In this case, the operational temperature is 246.2 K, corresponding to $-26.95\text{ }^{\circ}\text{C}$, and the initial temperature is assumed to be sea-level temperature, or $15\text{ }^{\circ}\text{C}$. Furthermore, the coefficient of thermal expansion for Al 7075-T6 corresponds to $23.6\frac{\mu\text{m}}{\text{m}\cdot^{\circ}\text{C}}$. Substituting into the above equation yields:

$$\Delta L = L \cdot 23.6\frac{\mu\text{m}}{\text{m}\cdot^{\circ}\text{C}} \cdot (-26.95^{\circ}\text{C} - 15^{\circ}\text{C}) = -990.02\frac{\mu\text{m}}{\text{m}} \cdot L = -0.99002\frac{\text{mm}}{\text{m}} \cdot L \quad (6-2)$$

Substituting the dimensions evaluated for clearance in Table 6-3 into the above equation leads to the results presented in Table 6-4.

Table 6-4: Thermal expansion of critical clearance dimensions both before and after applying clearance

Dimension notation	Initial size	Corresponding thermal contraction	Dimensions with clearance	Corresponding thermal contraction
t_{1mid}	176 mm	0.17424352 mm	175.87 mm	0.174114817 mm
t_{2mid}	154 mm	0.15246308 mm	153.87 mm	0.152334377 mm
t_{1side}	90 mm	0.0891018 mm	89.943 mm	0.089045368 mm
t_{2side}	79 mm	0.07821158 mm	78.951 mm	0.07817728 mm
b_{1mid}	44 mm	0.04356088 mm	43.918 mm	0.043479698 mm
b_{2mid}	22 mm	0.02178044 mm	21.932 mm	0.021713118 mm
b_{1side}	24 mm	0.02376048 mm	23.966 mm	0.023726819 mm
b_{2side}	13 mm	0.01287026 mm	12.976 mm	0.012846499 mm
h_t	10 mm	0.009902 mm	9.942 mm	0.00984277884 mm
d_1	80 mm	0.0792016 mm	79.882 mm	0.079084777 mm
d_2	73.6 mm	0.072865472 mm	73.482 mm	0.072748649 mm
d_3	67.6 mm	0.066925352 mm	67.482 mm	0.066808529 mm
a_1	5 mm	0.004951 mm	4.952 mm	0.00490257904 mm
a_2	4 mm	0.0039608 mm	3.976 mm	0.00393631952 mm
b_1	3 mm	0.0029706 mm	2.964 mm	0.00293441928 mm
b_2	2 mm	0.0019804 mm	1.982 mm	0.00196221964 mm

Both original dimensions and those after clearance is implemented are considered since there could be a choice made to achieve the original imposed clearance at the operational temperature. However, based on these results one could easily observe that thermal contraction accounts for differences in dimensions in the order of a couple of tenths of a millimeter at most. Considering no stringent requirements for rigidity are considered for the design of this interface it is considered that simply applying the original clearance should prove sufficient

for the purposes of this design. As such, the most right-hand column shows the expected thermal contraction for the critical contact dimensions of MIST V2.2. It is important to mention that, since contraction instead of expansion occurs, it only serves to widen the clearance fits already established, hence simplifying assembly, which is desirable.

Experimental Setup and Results

This chapter summarizes the physical experiments performed on the interface. It is structured as follows: Section 7-1 talks about the two different implementations of the interface, and the logic behind this choice, whilst Section 7-2 details the results of the aforementioned experiments, as well as the limitations thereof.

7-1 Experimental Setup

In order to validate some of the design decisions one would first need to create a proof of concept (PoC) of the MIST design. Since the thesis budget is limited, making sure no problems occur because of design choices before actually manufacturing it from expensive materials is a must. With this in mind, one of the main concerns with the interface iterations, starting from V1.0 onwards, is how smoothly the tapered T-sections can be assembled with each other and if this causes snagging during assembly operations. Since creating both the male and female plate from Aluminium would be somewhat expensive, as will be seen later on in this chapter, it was decided to first create a simplified version that could be 3D printed in-house at the TU Delft facilities.

Upon contacting the staff it was found that the MakerBot Replicator 5th Generation 3D printer, shown in Figure 7-1, was available and also easy to use. Furthermore, the material used by this machine was readily available at the faculty, so no extra costs were involved in purchasing it.



Figure 7-1: MakerBot Replicator 3D printer used for PoC production, courtesy of [16]

The main specifications of this printer can be summarized as follows: it uses a single extruder, with a filament diameter of 1.75 mm, and a print speed of 150 mm/s, can be connected either through USB or WiFi, and supports polylactide (PLA) as material [16]. The maximum build volume it can print is 9.92 x 9.92 x 5.9 inches or, in SI, 251.968 x 251.968 x 148.96 millimeters. Due to this restriction, it was decided to print the scaled down version of the interface, simplified so that the whole locking cylinder system did not exist. In essence this meant the male and female plates, minus the central slots.

Furthermore, due to the filament diameter affecting the dimensions of the 3D printed object, it was recommended that the clearances for the plates be increased to at least 0.2 mm, resulting in the prototypes illustrated in Figures 7-2 and 7-3, for the male and female plates, respectively. The observant reader will notice that the plate dimensions have been further reduced from the small scale model to 104 by 104 mm so as to reduce print time.

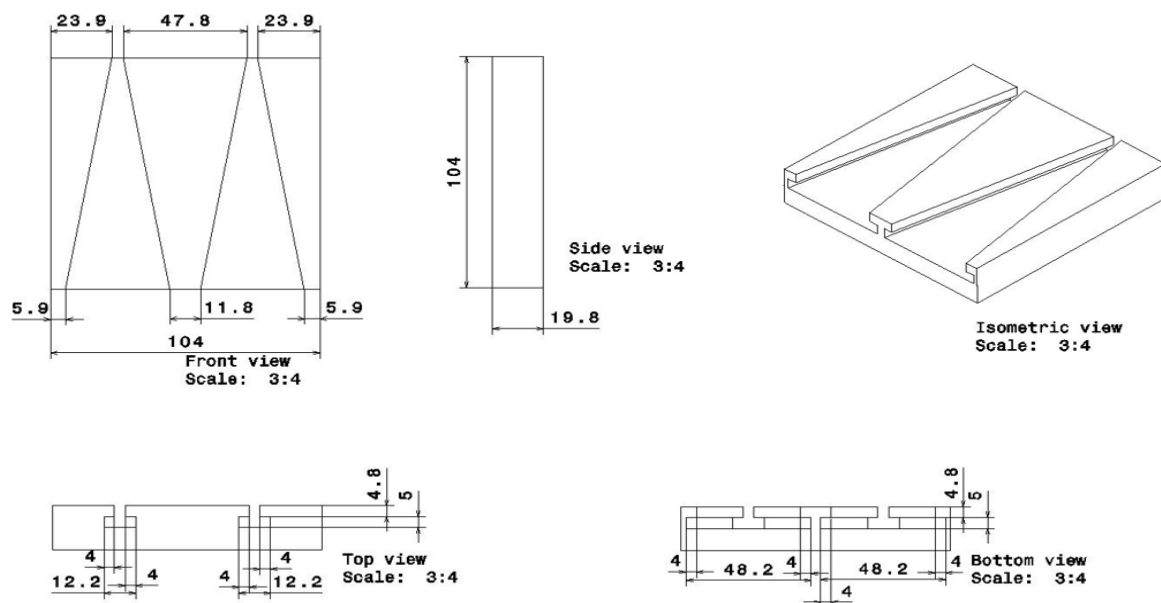


Figure 7-2: Technical drawing of 3D printed male plate

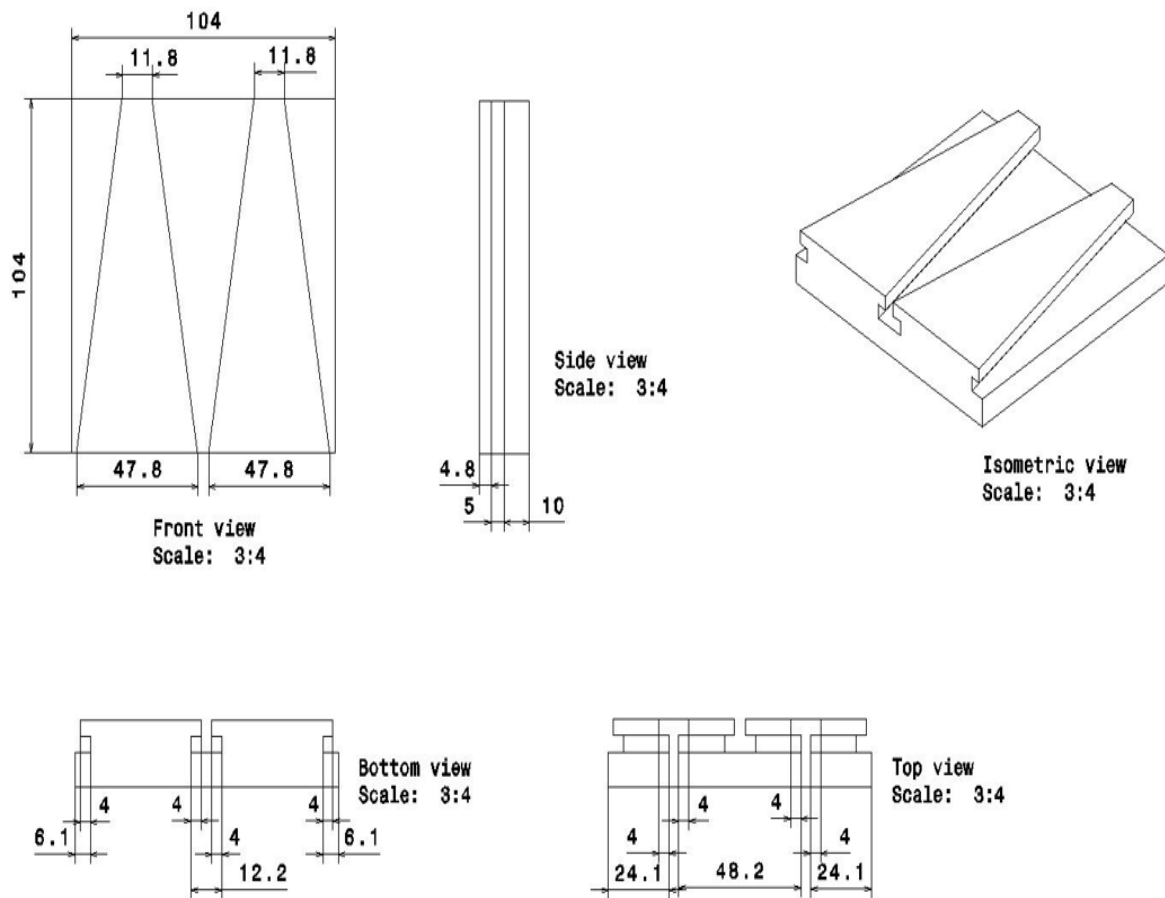


Figure 7-3: Technical drawing of 3D printed female plate

In order to use this printer more easily, the MakerBot Print application was installed. The main advantage of this is that STL files can directly be imported and the printer settings can be controlled. In the case of the MIST PoC, it was recommended to change the default settings for the Base Layer to a Raft type, with a Model offset (or base layer height) of 1 mm. Once these settings have been selected, the model can be checked as an animation and sent to the 3D printer through USB connection or via WiFi.

The estimated duration for printing the male and female plates was around 4 hours per piece. Although the printing progress was checked regularly at half hour intervals, the first attempt at printing was unsuccessful due to the extruder head snagging on a printed segment and moving the full piece by a certain distance. Although this was unexpected, this did not occur again on the second try, the printing of both pieces ending in a success. The finished product is shown in Figure 7-4.



Figure 7-4: 3D Printed Components for Assembly Testing

When testing the assembly operations with these versions of the PoC, a slight issue was observed - due to the lack of smoothness created by the print the slide in mechanism did not perform as planned. However, after a bit of manual labour, mainly involving filing and smoothing out of the surfaces the desired connection was achieved and the prototype fulfilled its function smoothly, as illustrated in Figure 7-5. It is also important to note that slight curvature caused by thermal effects is present in both pieces, on the bottom for the left-hand side one, on the top for the right-hand side element. Although this was not a specification of the design, it is not considered to be a problem per se, as during manufacturing from Aluminium or other materials, this would not occur, especially if machining is used as a production technique.



Figure 7-5: Assembly Test of 3D Printed Model

After consulting the staff that worked with this 3D printer it was revealed that a higher clearance than 2 mm and a sturdier/thicker base for printing could have been good solutions to avoid the problems encountered with the print. As such, it is recommended for further such prints to make use of a Raft layer of at least 2 mm - to avoid curvature -, and use a minimum clearance of 3 mm (at least for sliding mechanisms with large contact surfaces).

With the tapered sections being validated as a working concept through the use of the 3D printed model, the next step was to produce a prototype from the materials selected in Subsection 4-1-2 or as close of a material as possible if the costs were too high. The chosen manufacturing method was Computer Numerical Control (CNC) machining, as the parts were relatively complicated in nature and even small deviations in the model could compromise the assembly operations. Luckily, when perusing online offers for CNC machining, it was found that the selected material for the simulation (Aluminium alloy T60) was a common material for use in this manufacturing process. The test setup selected was initially envisioned as a combination of the following components:

1. Interface assembly
2. Support plates (which could essentially be thought of as the bottom of a module)
3. Simple fixture elements (so that the interface could be mounted on the support plates)
4. Actuator for the central cylinder section of the interface
5. Actuator mount
6. Actuator driver circuit
7. Electrical and data connector components

In order to design the actuator mount, one first needed to select the actuator itself. For the purposes of testing, a low power, low cost actuator that was readily available would be sufficient. As such the Portescap Miniature Linear Electric Actuator (26DBM20B2U-L) [113] was chosen. The technical specifications of this actuator are summarized in Table 7-1, courtesy of [114].

Table 7-1: Portescap 26DBM20B2U-L Technical specifications

Performance parameter	Value
Operating voltage	12 <i>V</i>
Rated current per phase	0.2 <i>A</i>
Minimum holding force	17.8 <i>N</i>
Stroke length	48 <i>mm</i>
Linear travel accuracy	± 1 step
Steps per revolution	48
Ambient temperature range	-20 to +70 $^{\circ}C$
Weight	34 <i>g</i>

After contacting manufacturing companies all around the world that provided machining services that could produce the proof of concept, the plates and central locking mechanisms were produced out of Al 7075-T6 for €500. Figure 7-7 shows the plates and assembled central structure, whilst Figure 7-8 illustrates how the assembly itself works.

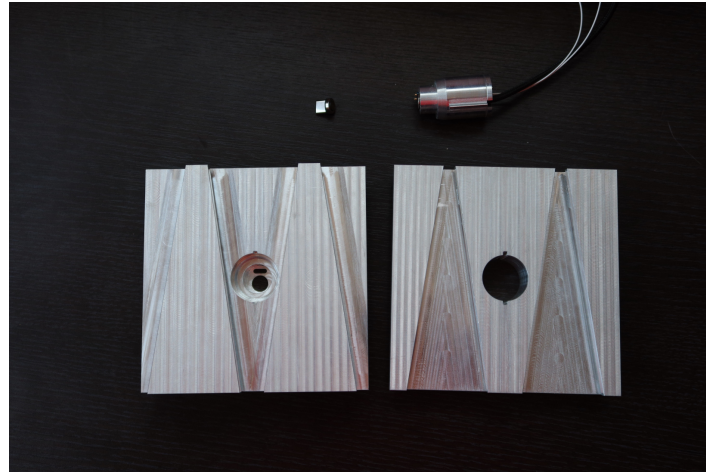
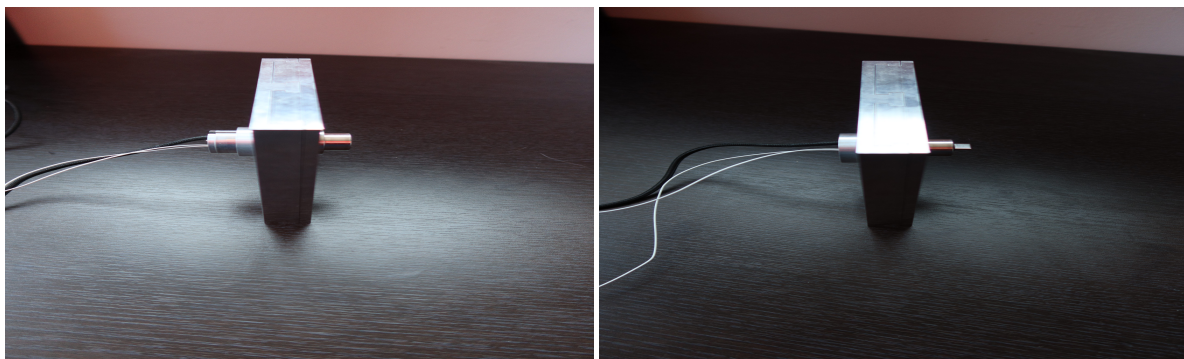


Figure 7-7: Plates and Assembled Central Locking Mechanism - PoC MIST V2.0



(a) Stage 1 - Only Plates Locked

(b) Stage 2 - Interface Fully Locked

Figure 7-8: Example of Assembly

It is worth mentioning that during the discussions with the manufacturer it was further mentioned that the clearance tolerances should be increased to a minimum of 0.1mm, as higher precision would further raise the costs. This was found to be acceptable and manufacturing was started on the PoC. All components were produced and delivered within a month.

Upon receiving both the interface mechanism and the actuator it was necessary to create a circuit that could drive the 26DBM20B2U-L linear actuator. This will be affected by the type of motor included, in this case a unipolar stepper motor. At the recommendation of the distributor (RS), the driver circuit was based off the baseline illustrated in Figure 7-9, courtesy of [115].

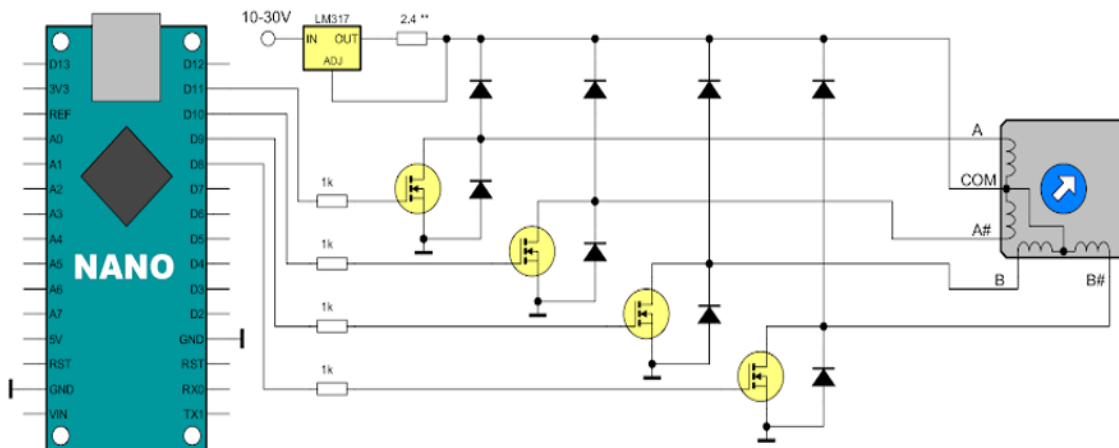


Figure 7-9: Suggested driver circuit for linear actuator

In this circuit, the Arduino Nano board serves as the controller for the whole actuation process, the LM317 circuit works as a limiter for the intensity of the current, whilst the simple circuits leading to each wire of the actuator serve as voltage controllers. Although this is a good start for a circuit, upon speaking with the staff at the TU Delft university, it was discovered that a source with controllable intensity as well as voltage could be used. As such, the top left LM317 circuit could be eliminated altogether since the operating voltage and intensity are known for the actuator [114]. A summary of the components purchased for the purpose of creating this circuit can be found below:

- Arduino Nano micro-controller (x1) [116]
- N-MOSFETs (x5) [117]
- 1 kOhm Resistors (x4) [118]
- Voltage Regulator Diodes (x10) [119]

The observant reader will notice that extra diodes and N-MOSFETs were ordered. This is due to packaging conditions on the Farnell website.

Once the soldering of the circuit was done, the only thing left was to upload an actuation code to the Arduino micro-controller. The inputs necessary for the stepper motor the linear actuator is equipped with can be summarized by Figure 7-10.

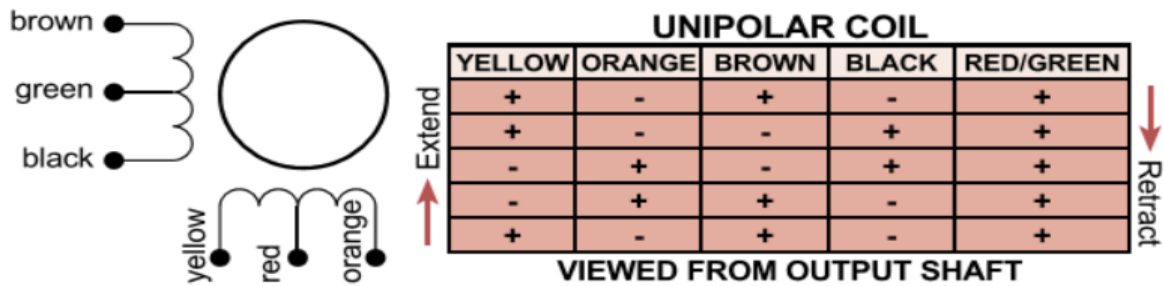


Figure 7-10: Inputs required for driving the linear actuator

Once this was done, the experimental setup was completed, as shown in Figure 7-11.

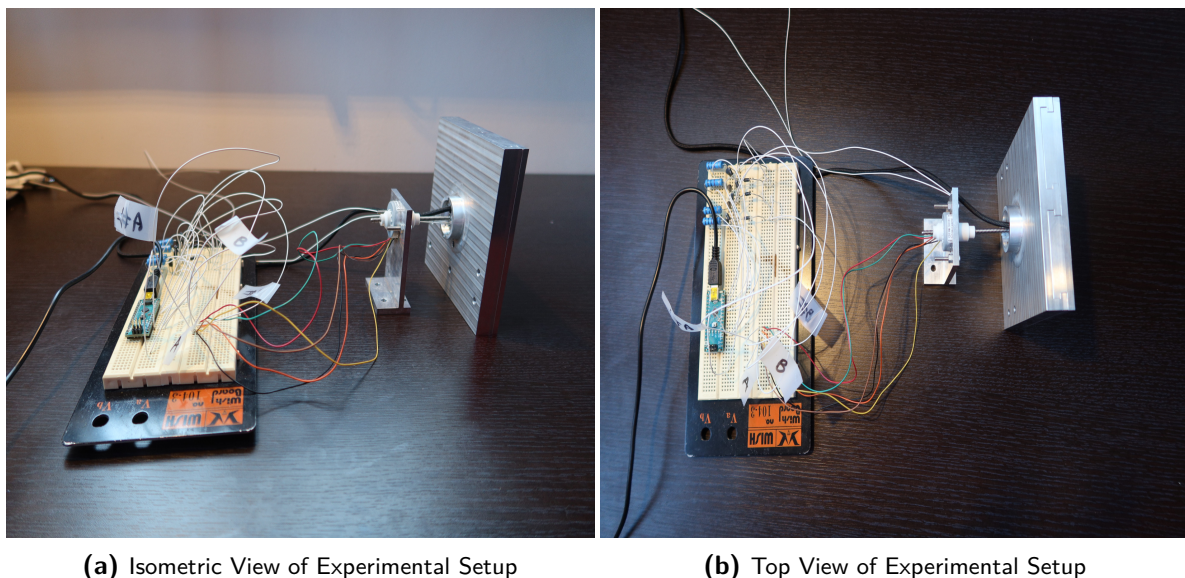


Figure 7-11: Complete Experimental Setup

7-2 Experimental Results

The first tests conducted for the interface were subsystem tests, namely checking the proper functioning of both the data and the electric connector. The USB-C magnetic connector chosen for data transfer was tested with multiple devices, including laptops, different phones and PCs, as well as different file types - ranging from a large number of very small files (e.g. txt or small images), to very large files (i.e. high resolution images or even movies). The detected rate ranged between 18 and 53 MBps for all of them, achieving the theoretical maximum of 53 MBps declared for USB 2.0 standards. As expected, the data transfer rates did not change even when included in the assembly. A graph of the data rate variation registered during testing is illustrated in Figures 7-12a and 7-12b for transfer from and to a HP ZBook G5 laptop, respectively.

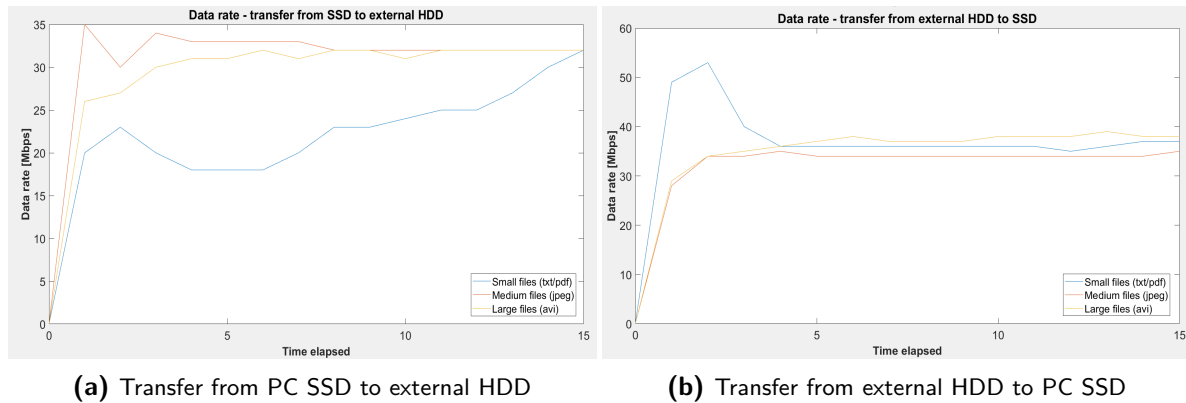


Figure 7-12: Results of data transfer testing

When considering the testing of the three different file sizes, one can note that the transfers have the lowest data rate when sending a large number of very small files, whereas medium to large files show a similar performance. This confirms that transfers have lower data rates when the target object is made up of a significant number of very small files - this aspect should be taken into account when deciding on data encoding as it can potentially halve expected performance as seen above. On the other hand, when comparing the two directions of transfer, it seems that transferring data from an external HDD to the laptop SSD has a higher performance than the other way around. This can be attributed to the writing speed of the memory device used, as SSD has a higher writing speed than HDD. Finally, it is necessary to mention that a combination of small file size and low writing speed resulted in the minimum data rate registered (18 Mbps), which only accounts for approximately 34% of the stated maximum rate of USB 2.0. This is not considered to be a problem under the assumption that both these aspects will be taken into account when designing the Command and Data Handling subsystem of a spacecraft making use of MIST V2.2.

The electric connectors chosen were tested both independently and once assembled using the controllable voltage and intensity source available at the university. Ampere meter and voltmeters were used to check the current and voltage both before and after the connector location. Both tests showed the voltage up to 100 V and current intensity up to 4 A (2 A per contact) passing through the electric connection, as per specifications. Since the source used had controllable voltage and current settings, the readings did not change over time, hence a graph of their evolution at various settings was not included.

On the mechanical side, the manufactured parts were first assembled with no actuator involved, so that any problems with clearance could be observed before any other tests would be performed. No problems were detected during this test, as expected given the larger clearance required by the manufacturing company. Once this was complete, the system testing began, as all the components were assembled including wiring and connectors. During the system test however, an issue was observed with the linear actuator selected. When driven with no load, a significant amount of rotation due to looseness was observed. The manufacturer was contacted and it was stated that this was normal, as the target load to be pushed should be guided for the actuator to work. However, even upon being loaded with the target central elements that it was required to drive, the actuator did not perform to standards. Due to the looseness, the fillet would sometimes skip while turning, causing no motion along the desired

axis. Sadly this could not be remedied by buying a new/different actuator as the budget had already been used. In spite of the problems with actuation, using manual methods (forces ranging between approximately 19.62 and 29.43 Newtons) to push the central locking cylinder showed that the interface concept was sound and all connectors worked as intended once assembly was complete.

Once assembly was complete, each load case was tested manually, and with weights, with forces ranging between 10 and 12 kilograms (98.1-117.72 N). Due to the small size of the interface prototype, larger loads were not tested as at the time of testing it was not possible to use laboratory testing any more. Due to this fact, the validation process was limited to very low load scenarios, which were assured to be successful based on the simulation results. It is important to note that the aforementioned results still need to be validated, especially the limit loads, however that would require destructive testing for each load case, thus seven prototypes would need to be manufactured for full validation of MIST V2.2. Whilst the malfunctioning of the linear actuator did not prevent the validation of the assembly mechanism, it did, in combination with the lack of testing under high loads, prevent the testing of two scenarios. The first one was validating that the nominal force of the linear actuator was sufficient to keep the central mechanism locked under high loads, for all cases simulated. The second test that could not be performed was to validate that the structural resistance of the central mechanism would dissipate loads sufficiently so that the structural integrity of the linear actuator was preserved even under very high loads approaching the failure limit. These two scenarios are very important if the decision is made to use the scaled down version of the interface, however one can assume that a system employing modules of 0.12x0.12x0.12 meters will not be large enough to require loads anywhere close to the limits resulting from simulations. As such it can be argued that in order to truly validate MIST V2.2 for the limit loads, one should not only limit test the full-scale interface under all load cases considered, but also validate the two scenarios arising from the linear actuator not functioning correctly with the actual actuator chosen for the interface designed for modules of 0.4x0.4x0.4 meters.

To summarize, mechanically the interface functioned as intended, both the data and electrical connectors had nominal performance on both individual tests and full assembly tests. The only element that did not work as specified was the actuator, however this is deemed to not be a problem that affects the interface itself. As such, it can be said that the interface design was a success with regards to the tests performed. It is important to note that due to the fact that the thesis scope was already quite broad, coupled with time constraints, multiple other tests could not be performed. It is recommended that in the future, before using this interface concept, the following tests be performed:

- Destructive testing - meant to validate maximum loads.
- Vibration testing - meant to validate the expected natural frequencies, thus affecting choice of launch vehicle.
- Thermal testing - in other words validation of the clearance dimensions chosen for the interface concept.
- Structural testing under thermal load - checking the maximum loads for thermal conditions that the interface would be subjected to during its operational lifetime.

- All testing scenarios above should also be performed on the scaled-up model of MIST V2.2 - this is meant to ensure that performance is validated for the planned scale of the interface and no unforeseen issues arise.

Conclusions and Future Recommendations

The purpose of this thesis was to design an interface to be used in the on-orbit assembly of space telescopes, offering sufficient flexibility so as to be reused as much as possible across multiple platforms and missions. The main advantages of such a system are the ability to bypass launcher constraints and the potential for cost reduction given mass production capabilities entailed with adopting this interface for widespread usage in space telescopes missions. This resulted in the Modular Interface for Space Telescopes (MIST), iterated up until version 2.2. A summary of the technical specifications of MIST V2.2 is given in Table 8-1. It should be noted that a safety factor of 10% is added to the limit loads of the design computed through simulation so as to account for the lack of their validation through destructive testing.

Table 8-1: Dimensions and performance parameters of MIST V2.2

Performance parameters	MIST V2.2
Tension (max)	137436.3 <i>N</i>
Compression (max)	322574.4 <i>N</i>
Shear Vertical (max)	200460.6 <i>N</i>
Shear Lateral (max)	195928.2 <i>N</i>
Bending (X-axis moment)	18570.2301 <i>Nm</i>
Torque (Y-axis moment)	29570.8743 <i>Nm</i>
Bending (Z-axis moment)	19827.5814 <i>Nm</i>
Data rate	1 Gbps
Current intensity	100 <i>A</i>
Voltage rating	100 <i>V</i>
Dimensions:	
Diameter	0.4 <i>m</i>
Height	0.4 <i>m</i>

In order to evaluate if all requirements were met during the design, one must first compare

the MIST interface with existing state-of-the-art interfaces. In a similar way to the full scale version, a safety factor of 10 % is added to the limit loads. The dimensions as well as performance limitations of all interfaces considered are presented in Table 8-2.

Table 8-2: Dimensions and performance comparison between existing SoA interfaces and the down-scaled version of MIST

SoA Interfaces	SWARM	iBoss	SIROM	MIST V2.2	Performance Increase (%)
Tension (max)	N/A	6000 <i>N</i>	1300 <i>N</i>	35267.4 <i>N</i>	487.79%
Compression (max)	N/A	6000 <i>N</i>	5000 <i>N</i>	98256.6 <i>N</i>	1537.61%
Shear/Radial (max)	N/A	400 <i>N</i>	5000 <i>N</i>	30636.9 <i>N</i>	512.738%
Bending (X-axis moment)	N/A	400 <i>Nm</i>	150 <i>Nm</i>	1314.2475 <i>Nm</i>	228.56%
Torque (Y-axis moment)	N/A	400 <i>Nm</i>	420 <i>Nm</i>	1259.9496 <i>Nm</i>	199.99%
Bending (Z-axis moment)	N/A	400 <i>Nm</i>	150 <i>Nm</i>	1176.666 <i>Nm</i>	194.17%
Dimensions:				0.12x0.12 <i>m</i>	N/A
Diameter	0.076 <i>m</i>	0.119 <i>m</i>	0.132 <i>m</i>		N/A
Thickness	0.038 <i>m</i>	0.048 <i>m</i>	0.1265 <i>m</i>	0.015	N/A

The simulation results above show that at similar dimensions, the MIST concept far outperforms all existing interfaces, in all load cases (from a minimum of 194.17% increase in performance for the bending moment in the Z-axis, to a 1537.61% increase under compressive loads), hence even at these scaled down dimensions it can constitute a viable option for use in missions designed around very large structures. This more than satisfies requirement MIST-S-1.6.

With respect to the totality of the requirements, all structural requirements are satisfied, including the natural frequency ones. As for the data and electrical requirements, it was initially specified that two different configurations would be investigated, one with low and one with high power and data throughput, respectively. However, this idea was abandoned in favor of the latter configuration as a successful design for higher requirements would naturally entail that a lower performance is easily achievable by either eliminating some connectors or switching to less expensive ones which can achieve lower throughput. Although most of the requirements were either verified through analysis, inspection or even testing, as shown in Tables 8-3 and 8-4, it is worth mentioning that the electrical requirements can only be verified based on the assumption that the selected system performs as advertised.

Identifier	Requirement details	Verification mode
MIST-E-1.0	Interface design shall consider two options - a lower, and a higher power implementation corresponding to ≤ 1.5 kW, and ≤ 8 kW, respectively.	Decided against
MIST-E-1.1	Interface shall be able to pass 8 kW of electrical power from module to module.	Inspection

Table 8-3: Requirements Verification Matrix - Part 1

Identifier	Requirement details	Verification mode
MIST-E-1.2	Interface shall be able to pass voltages of 28 ± 1.4 V in the case of the low power implementation.	Decided against
MIST-E-1.3	Interface shall be able to pass voltages of 50 ± 2.5 V in the case of high power version.	Testing
MIST-D-1.0	Interface design shall consider two options - a lower data link version for bus and housekeeping, and a higher data link version for scientific instruments.	Decided against
MIST-D-1.1	The high data rate version shall be able to transfer data at speeds up to 0.9 Gbps.	Testing
MIST-D-1.2	The version in charge of housekeeping shall be able to transfer data at speeds up to 2.742 Mbps.	Testing
MIST-S-1.0	The interface shall have a lateral natural frequency of at least 15 Hz.	Simulation
MIST-S-1.1	The interface shall have a longitudinal natural frequency above 60 Hz.	Simulation
MIST-S-1.2	The interface shall be able to withstand lateral launch loads of ± 3.0 g.	Simulation
MIST-S-1.3	The interface shall be able to withstand longitudinal launch loads of 8.5g in compression and 4.0 g in tension.	Simulation
MIST-S-1.4	The interface shall be able to withstand orbital perturbations up to $1.3464 \cdot 10^{-3} Nm$ on fully assembled system.	Simulation
MIST-S-1.5	The load bearing capabilities of the interface shall be comparable to current state-of-the-art options.	Simulation
MIST-S-1.6	The interface design shall allow for easy assembly and disassembly in order to facilitate servicing.	Testing
MIST-S-1.7	The interface dimensions shall not exceed 0.4 by 0.4 m.	Inspection
MIST-S-1.8	The interfacing dimension shall not exceed 0.02 m.	Inspection

Table 8-4: Requirements Verification Matrix - Part 2

Due to budget and scope limitations, the chosen electrical connector for the full scale interface could not be bought, hence could not be physically tested. This should technically not be a problem, but it is advised to proceed with such tests if MIST technology is to be incorporated into any space mission as is, without any further refining iterations.

In order for MIST to be ready for space usage and classify as a standardized interface that can be used across multiple platforms and missions, a list of recommendations for future work is given. This can be classified into two types: work that would be necessary to make the current MIST design space-qualified, and work that could be done to further iterate and improve MIST for better performance:

1. Future work meant to qualify MIST V2.2 for space use:

- **Use higher performance simulations on MIST V2.2** - as specified previously, the simulation environment used had numerical limits that prevented mesh refinement to the extent where only small differences could be registered between averaged and unaveraged stresses. This could be solved by employing more powerful tools that could be used to better verify the limit loads MIST is capable of supporting.
- **Testing of chosen electrical connector** - as mentioned previously the electrical connector selected for the full-scale design was not purchased due to budget constraints, hence not validated through experimental testing. As such, purchasing and validating that this performs as advertised should be considered before making use of MIST V2.2.
- **Rigorous structural testing** - this is meant to validate the limit loads found through simulation.
- **In-depth thermal testing** - should validate two critical aspects: the clearances expected due to thermal contraction at operational temperatures, and the influence of thermal stresses on limit loads.
- **Vacuum testing** - preliminary testing meant to validate the assembly concept in vacuum conditions. This can be achieved with or without the selected robotic assembler selected for a specific mission.
- **Optimization of robotic arm(s) best suited for space missions employing MIST technology** - this includes optimization of number of DOF, joints, as well as motion planning algorithms, number and type of sensors equipped on the robotic manipulator, and material selection.
- **Assembly demonstration in vacuum conditions** - testing meant for the final stages of mission planning, where the selected robotic arm for a specific mission is used in vacuum conditions to validate that assembly works.
- **Planning and execution of a (scaled-down) space demonstration mission** - to validate the interface concept fully and raise its TRL to 9, there is a need to conceptualize and execute a demonstration mission that uses this technology in orbit, with all aspects of assembly and disassembly being accounted for.

2. Future work that could create improved iterations of MIST:

- **Simulation of trapezoidal shape as a different option from the T-sections** - improved simulations that can simulate not only limit loads, but also forces required during assembly could be used as a better comparison for the choice between these two options, hence verifying the design choice in this thesis.
- **Optimization of interface dimensions for specific (point) designs** - if desired by the shareholders, the interface could be made lighter provided that the target structure to be created using this technology does not need such high structural performance. As such, depending on the point design an optimization algorithm could be designed and employed to generate the most suitable dimensions for the mission at hand. This would imply an initial development investment in both time and cost, however in the long run, given the extensive use of this solution, it would create savings in both the temporal and economical sectors.

- **Explore the need and benefits of in-built sensors for the interface** - one of the design choices in this work was to avoid sensors altogether at the interface level, and fully depend on the assembler spacecraft for such things. However, one could argue that equipping some degree of sensing in the interface itself could simplify the assembler, thus reducing overall cost. This of course results in added fragility of the interface, hence the decision to avoid it in this thesis. It would be recommended to thoroughly investigate if there is no middle ground solution that uses some degree of resilient in-built sensing technology at the interface level.
- **Rigidity concerns and extra fastening mechanisms** - one of the limitations for the interface design explored in this thesis is that given a sufficiently large structure, the addition of multiple modules with set clearances will result in a structure that has some degree of looseness. This could be addressed at the level of the next layer (the mirror supporting layer) which could be used to fasten all modules as well as support the mirrors, or it could be enhanced through locking mechanisms that are built into the interface or modules. A study of these two cases based on value added and cost entailed for each option is thus necessary if very high rigidity requirements are expected for the mission using MIST.

Taking all of this into account, it is clear that the MIST concept developed in this thesis is at the intermediate stage, where there is still a significant amount of work to be done to make it space-worthy. However, given that all of the above recommendations are satisfied, it is expected that this interface design can become a worthy choice for the development of next-generation space missions that are no longer constrained by launcher size and carrying capabilities, but are instead assembled on orbit. This unlocks incredible potential in the space sector, potentially paving the way towards improving humanity's knowledge and understanding of the universe, if not even enhancing mankind's capabilities of harnessing the resources that our solar system offers.

Appendix A

Appendix A - Interface Technical Drawings (Full Scale)

A-1 Interface V0.0

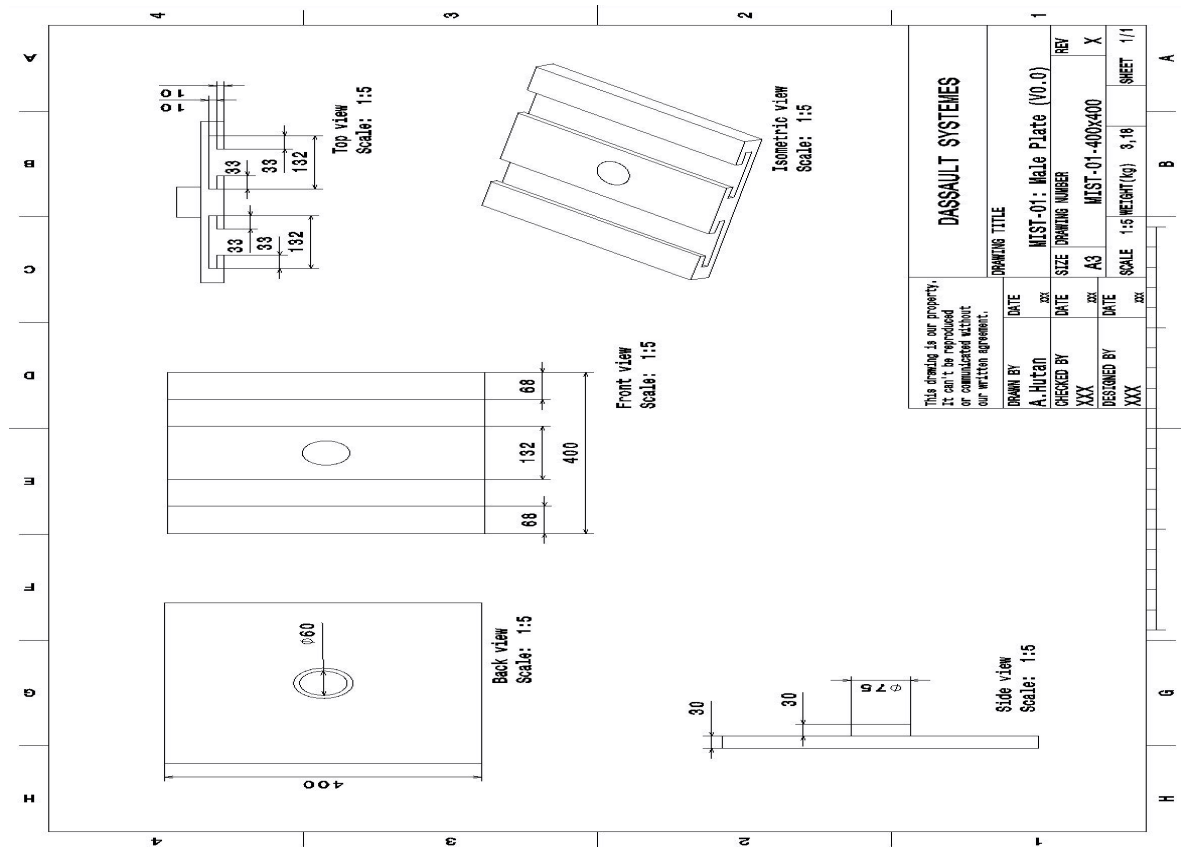


Figure A-1: Technical drawing of MIST-01 part, Interface V0.0 (400x400 Scale)

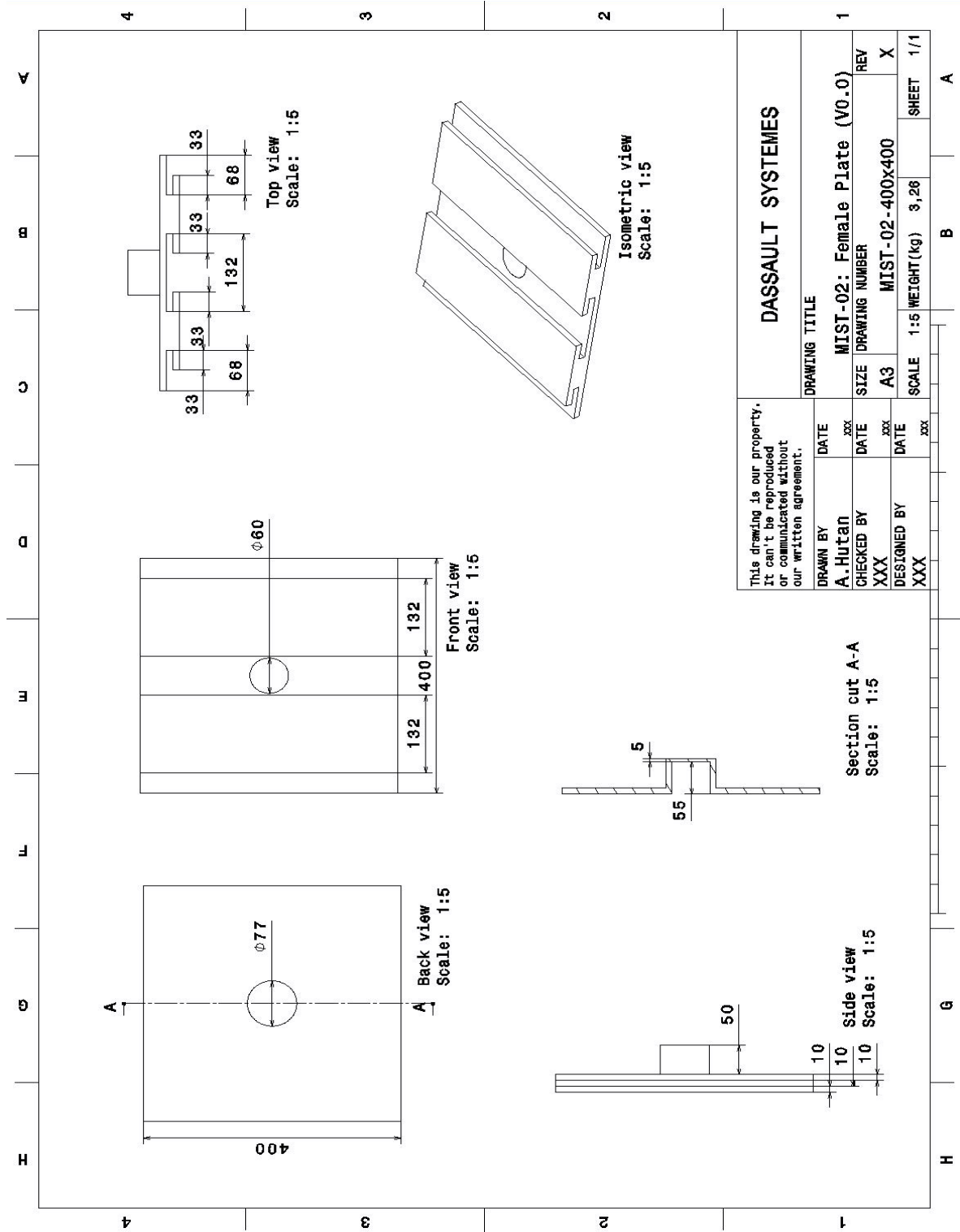


Figure A-2: Technical drawing of MIST-02 part, Interface V0.0 (400x400 Scale)

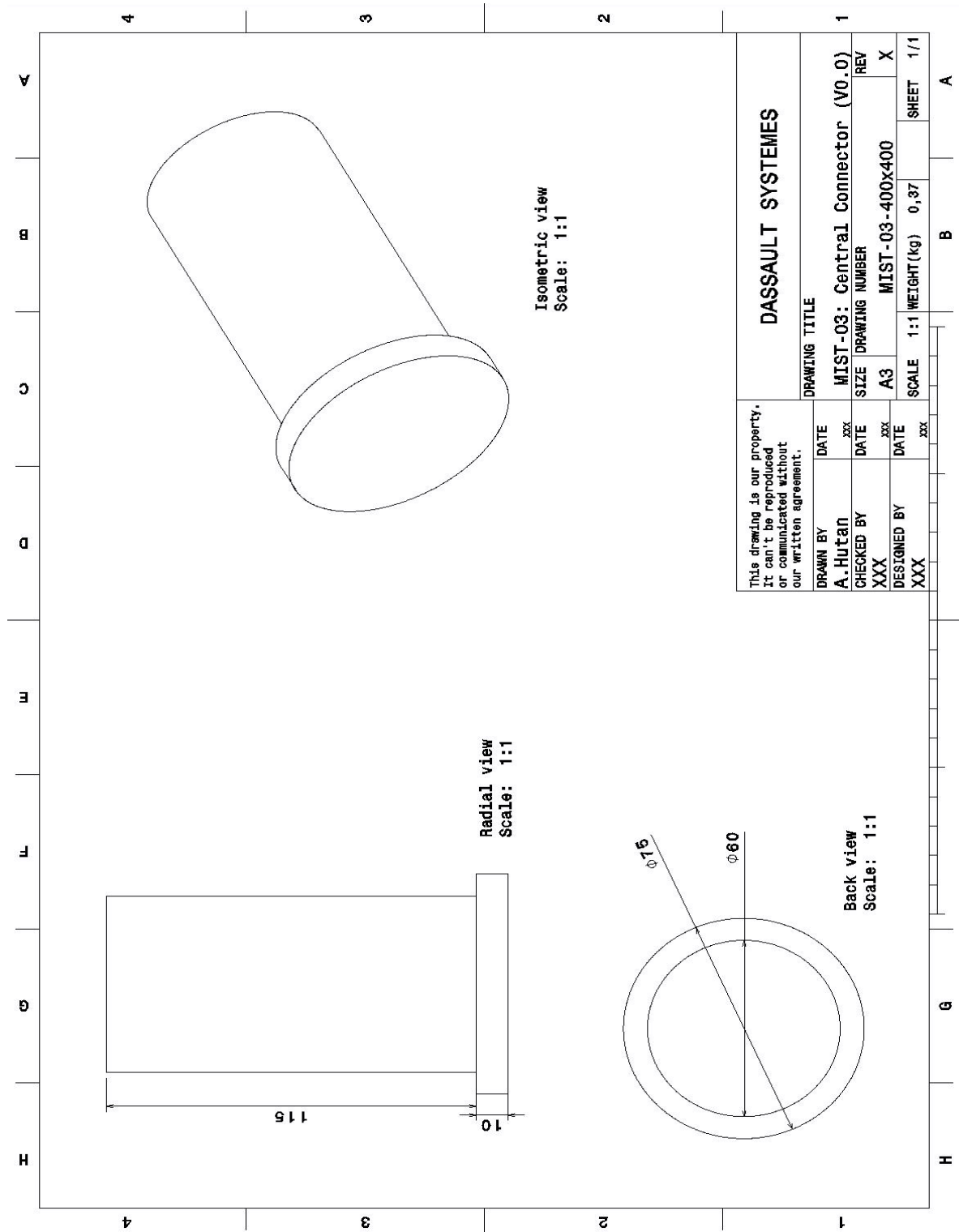


Figure A-3: Technical drawing of MIST-03 part, Interface V0.0 (400x400 Scale)

A-2 Interface V1.0

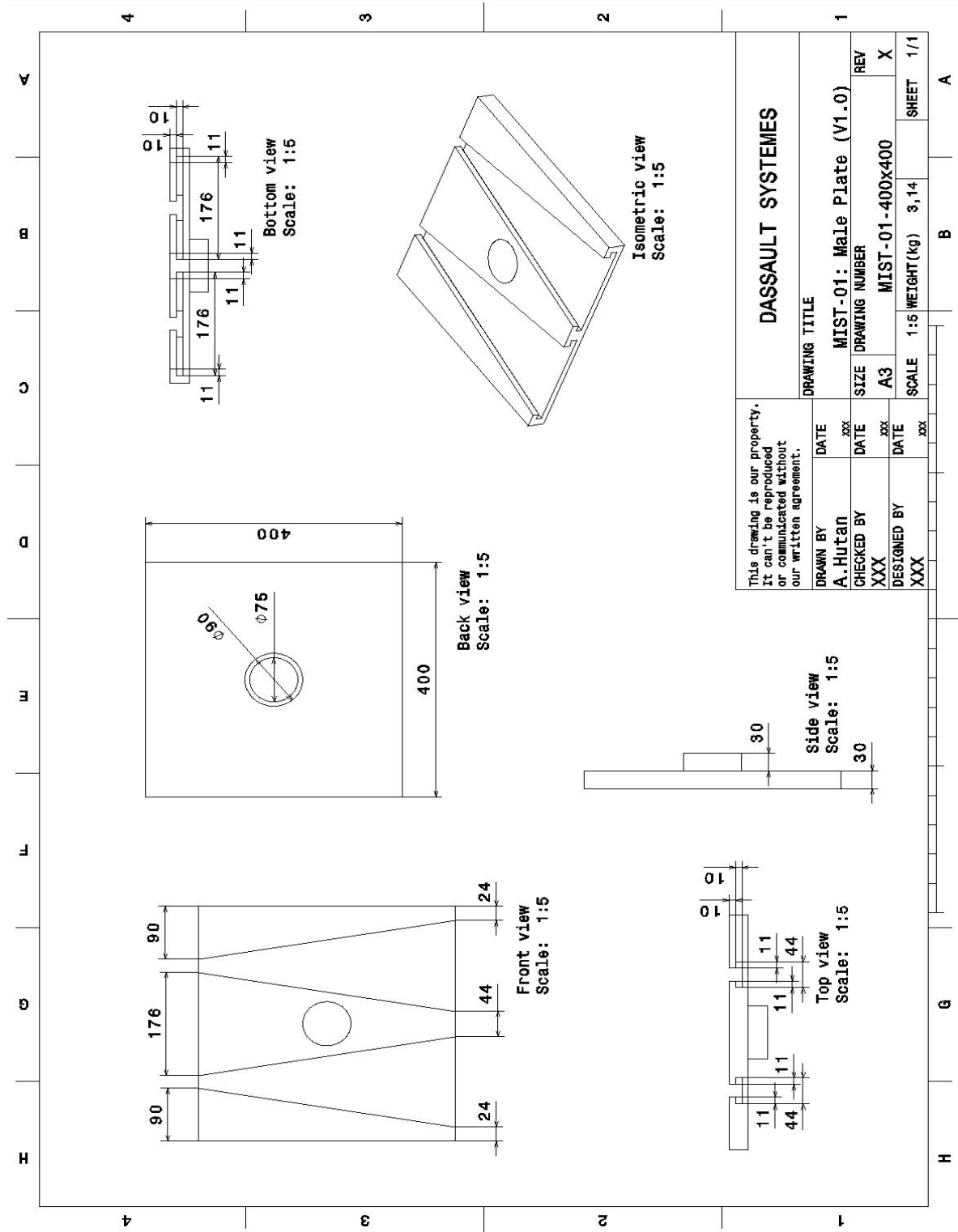


Figure A-4: Technical drawing of MIST-01 part, Interface V1.0 (400x400 Scale)

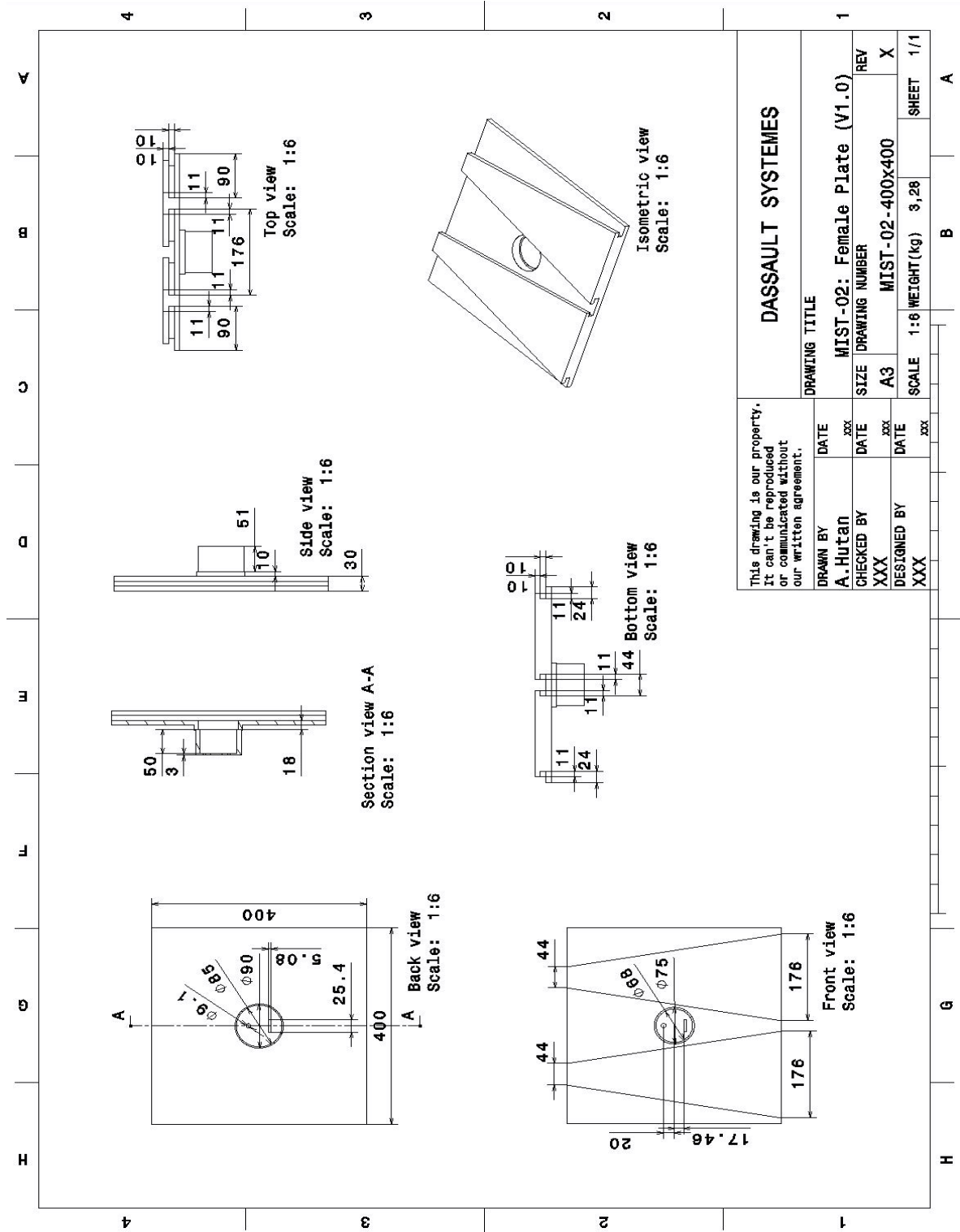


Figure A-5: Technical drawing of MIST-02 part, Interface V1.0 (400x400 Scale)

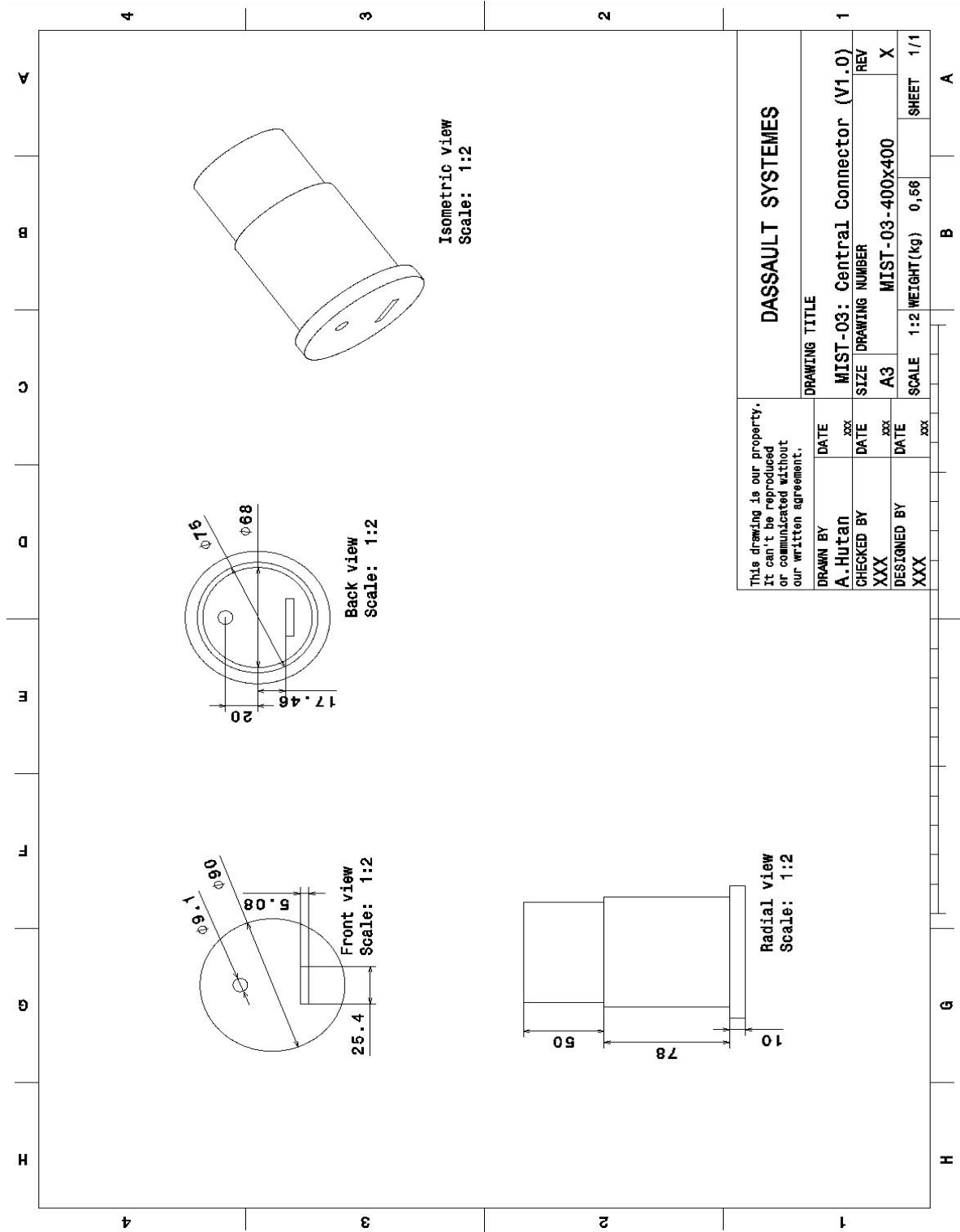


Figure A-6: Technical drawing of MIST-03 part, Interface V1.0 (400x400 Scale)

A-3 Interface V2.0

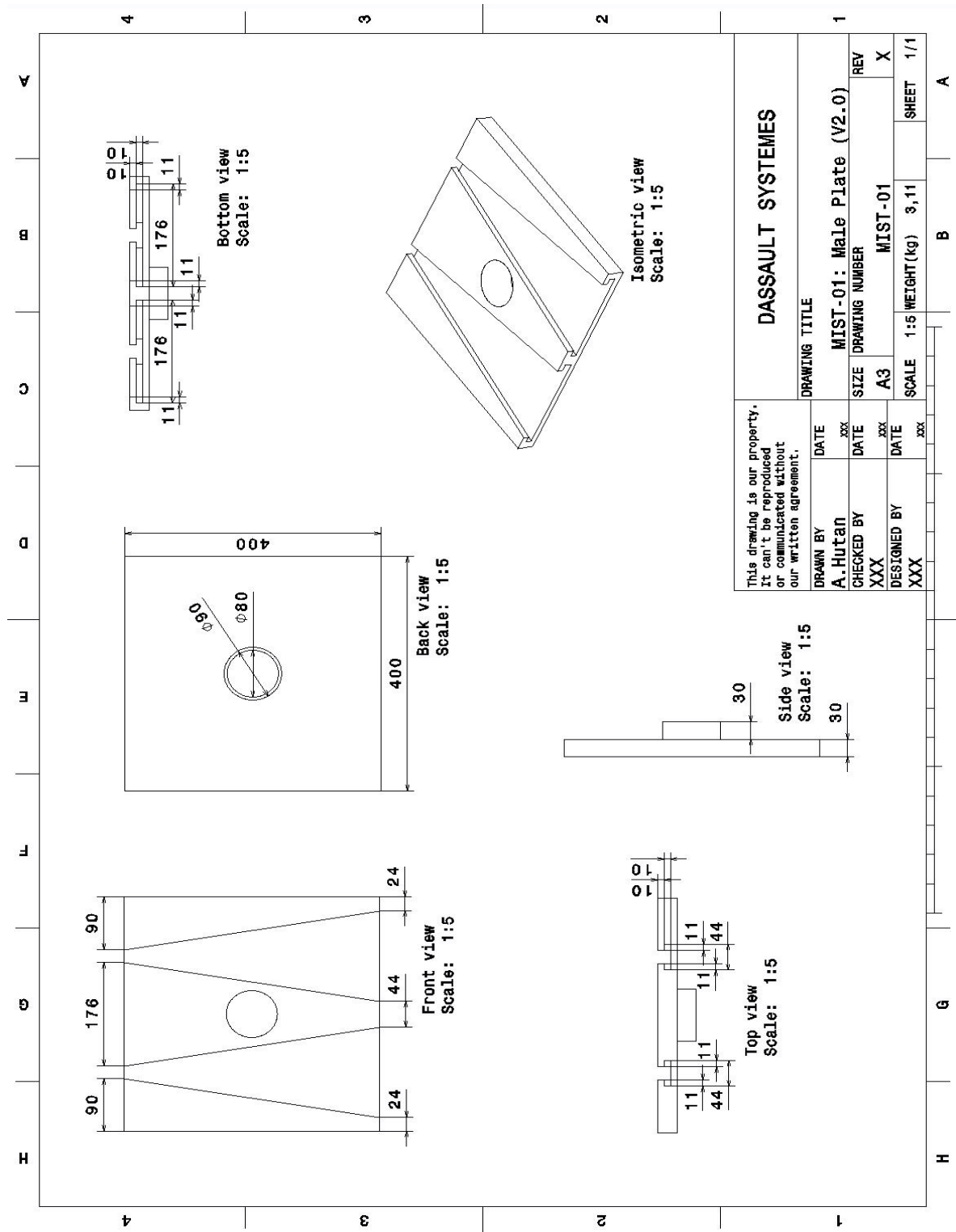


Figure A-7: Technical drawing of MIST-01 part, Interface V2.0 (400x400 Scale)

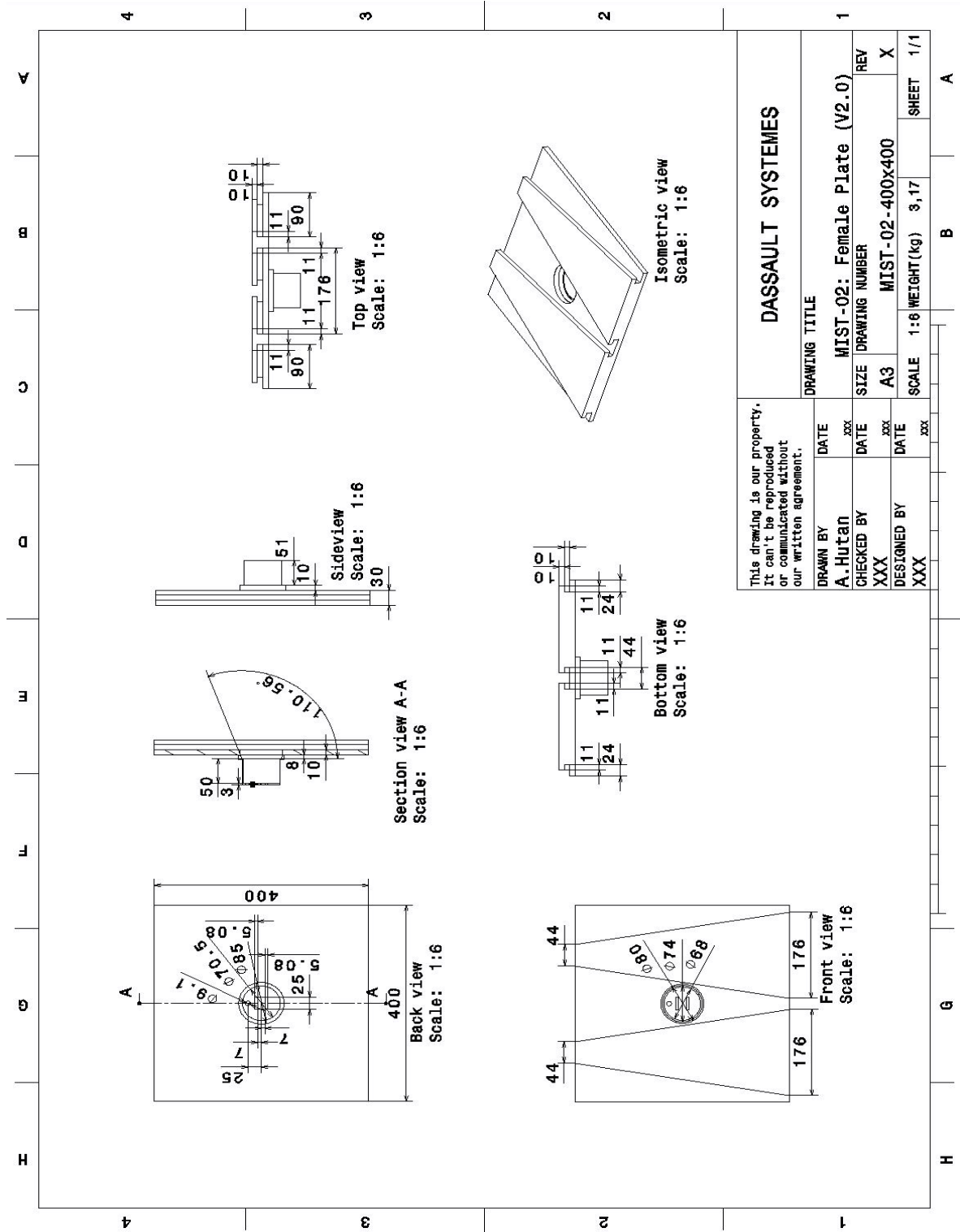


Figure A-8: Technical drawing of MIST-02 part, Interface V2.0 (400x400 Scale)

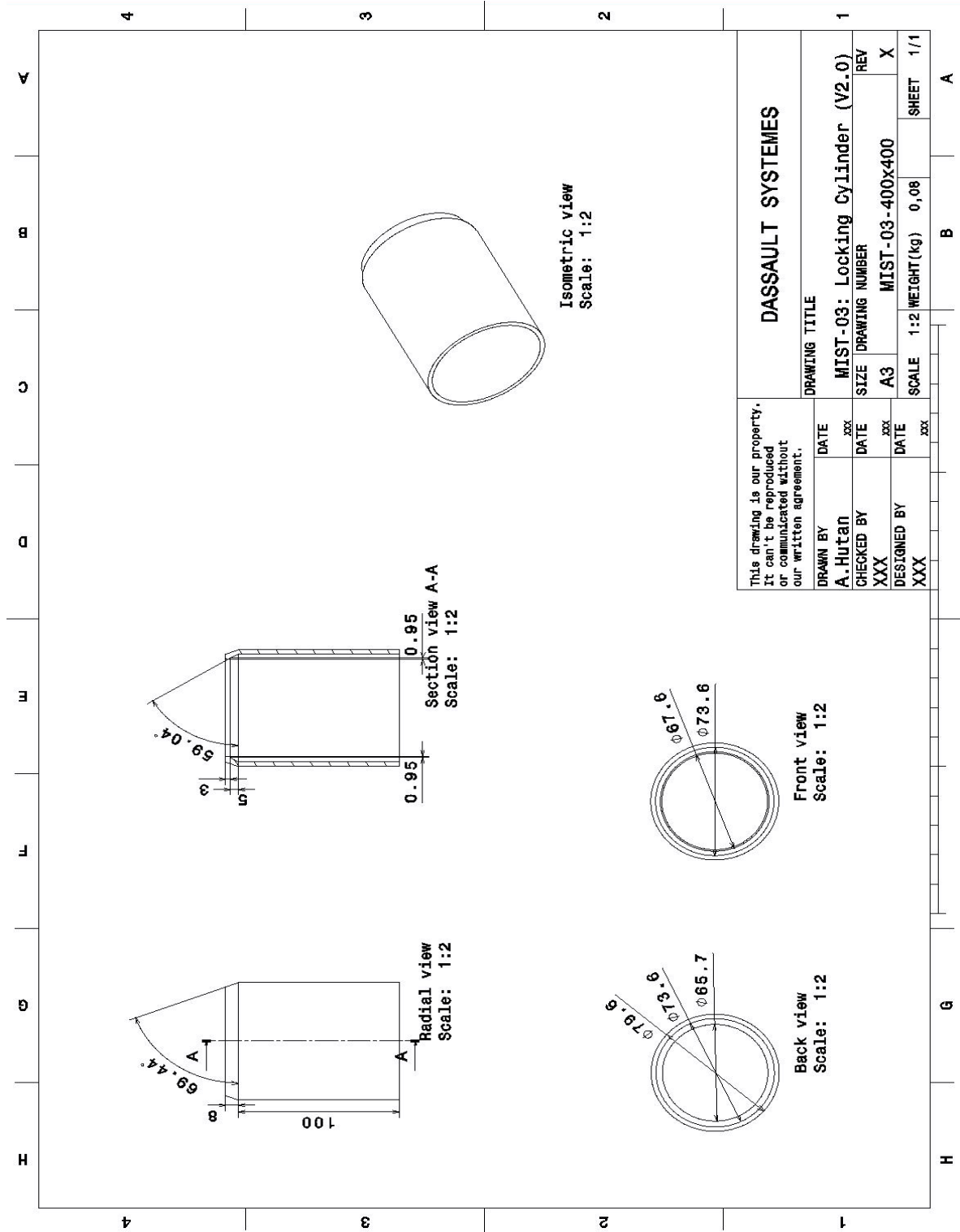


Figure A-9: Technical drawing of MIST-03 part, Interface V2.0 (400x400 Scale)

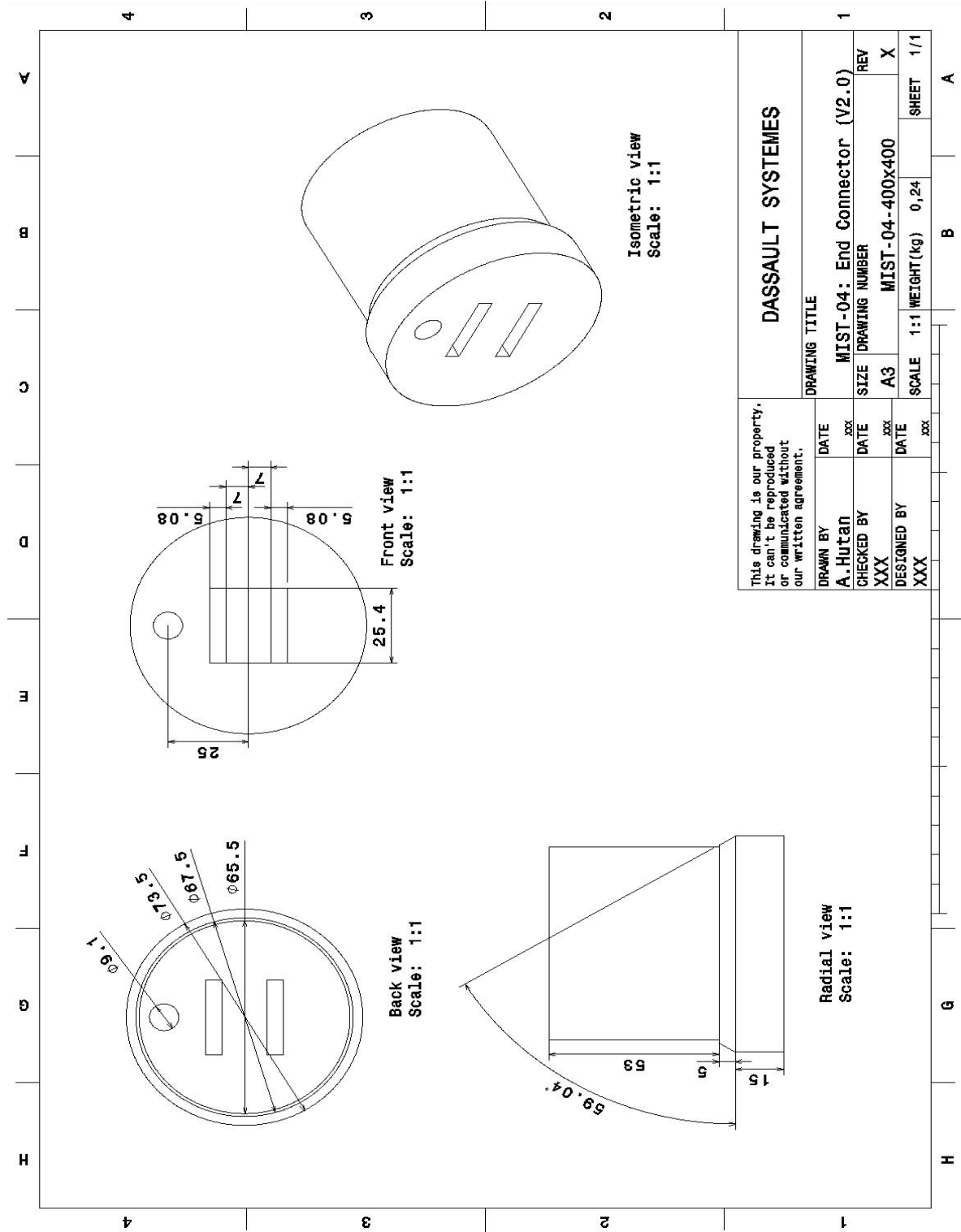


Figure A-10: Technical drawing of MIST-04 part, Interface V2.0 (400x400 Scale)

A-4 Interface V2.1

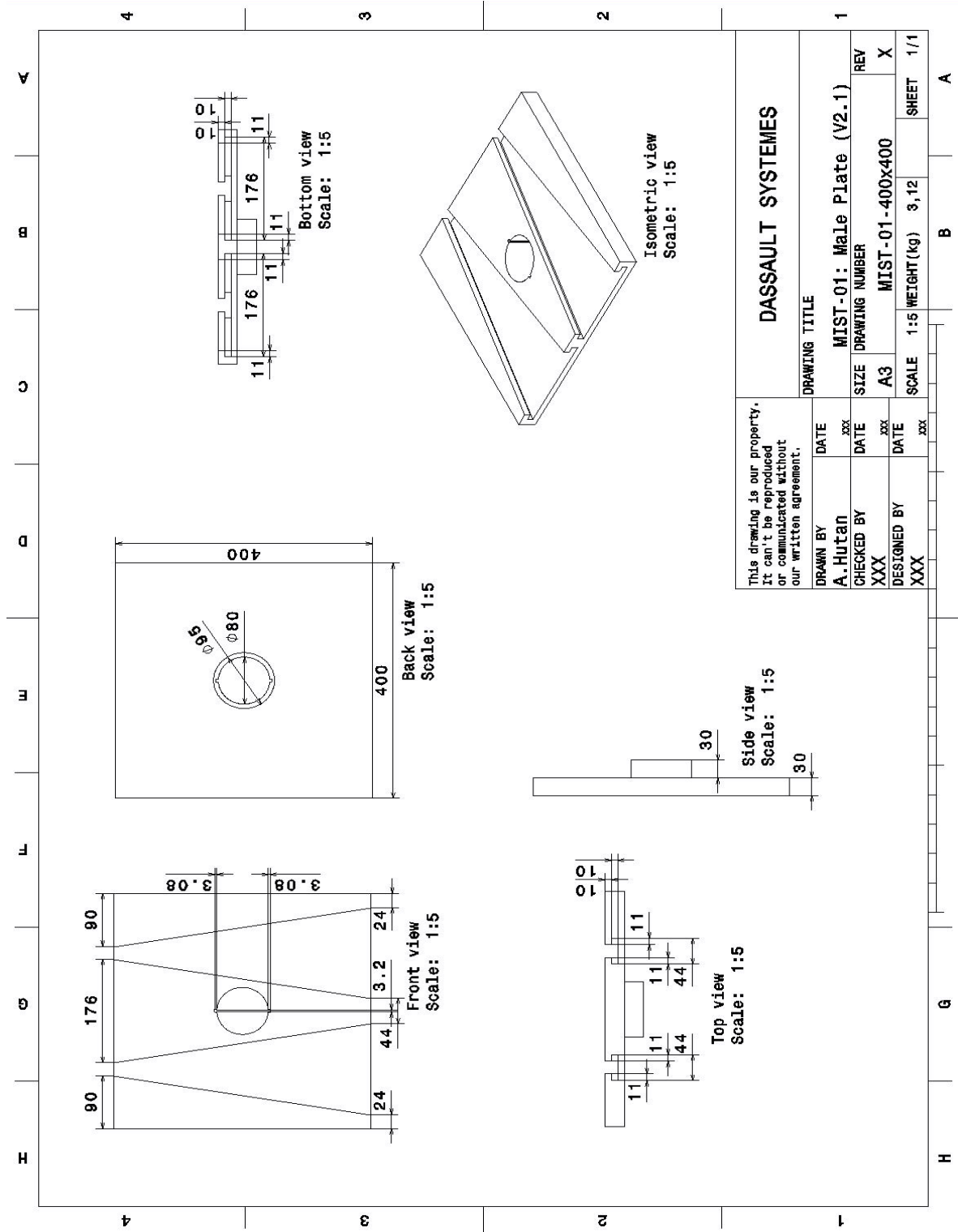


Figure A-11: Technical drawing of MIST-01 part, Interface V2.1 (400x400 Scale)

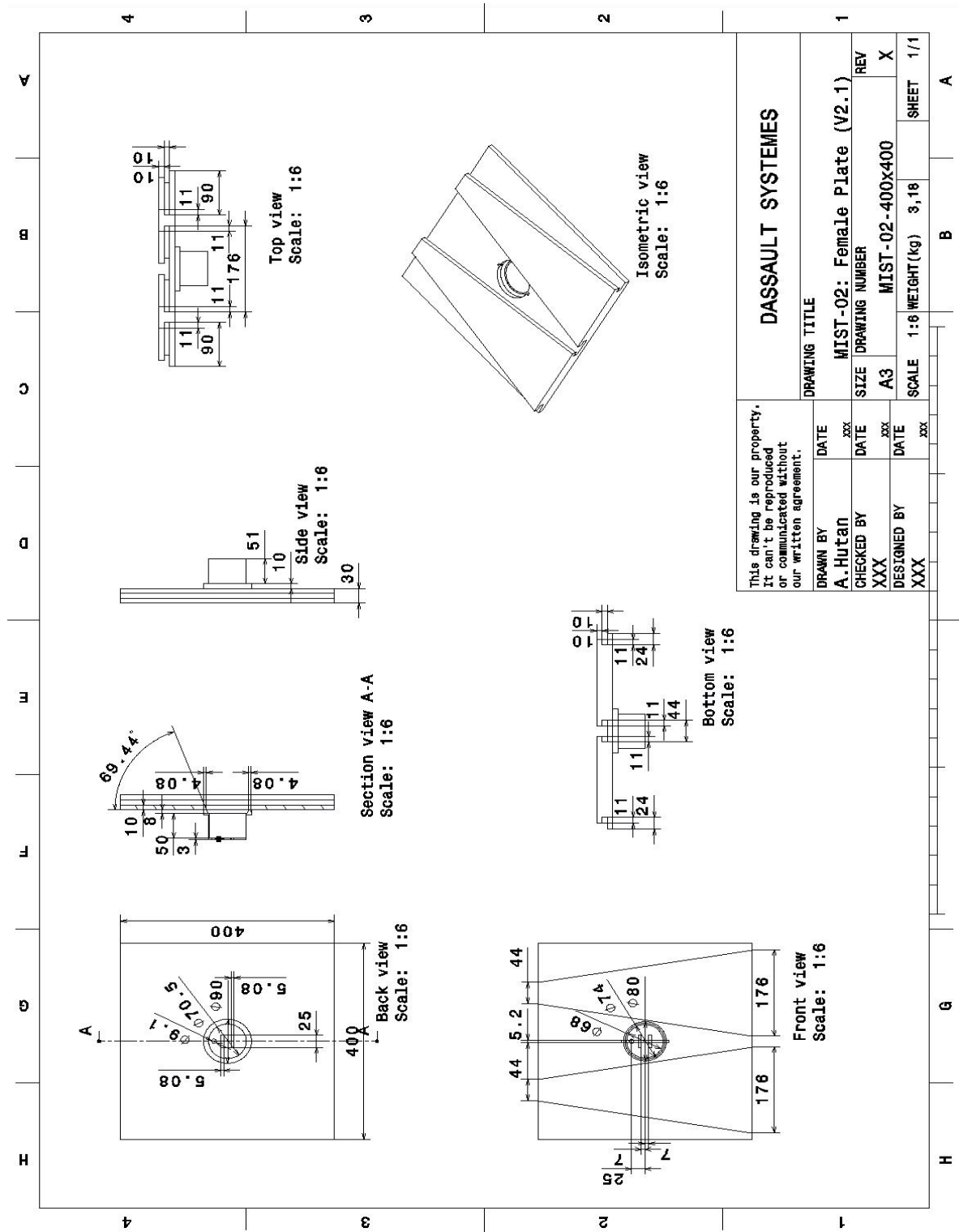


Figure A-12: Technical drawing of MIST-02 part, Interface V2.1 (400x400 Scale)

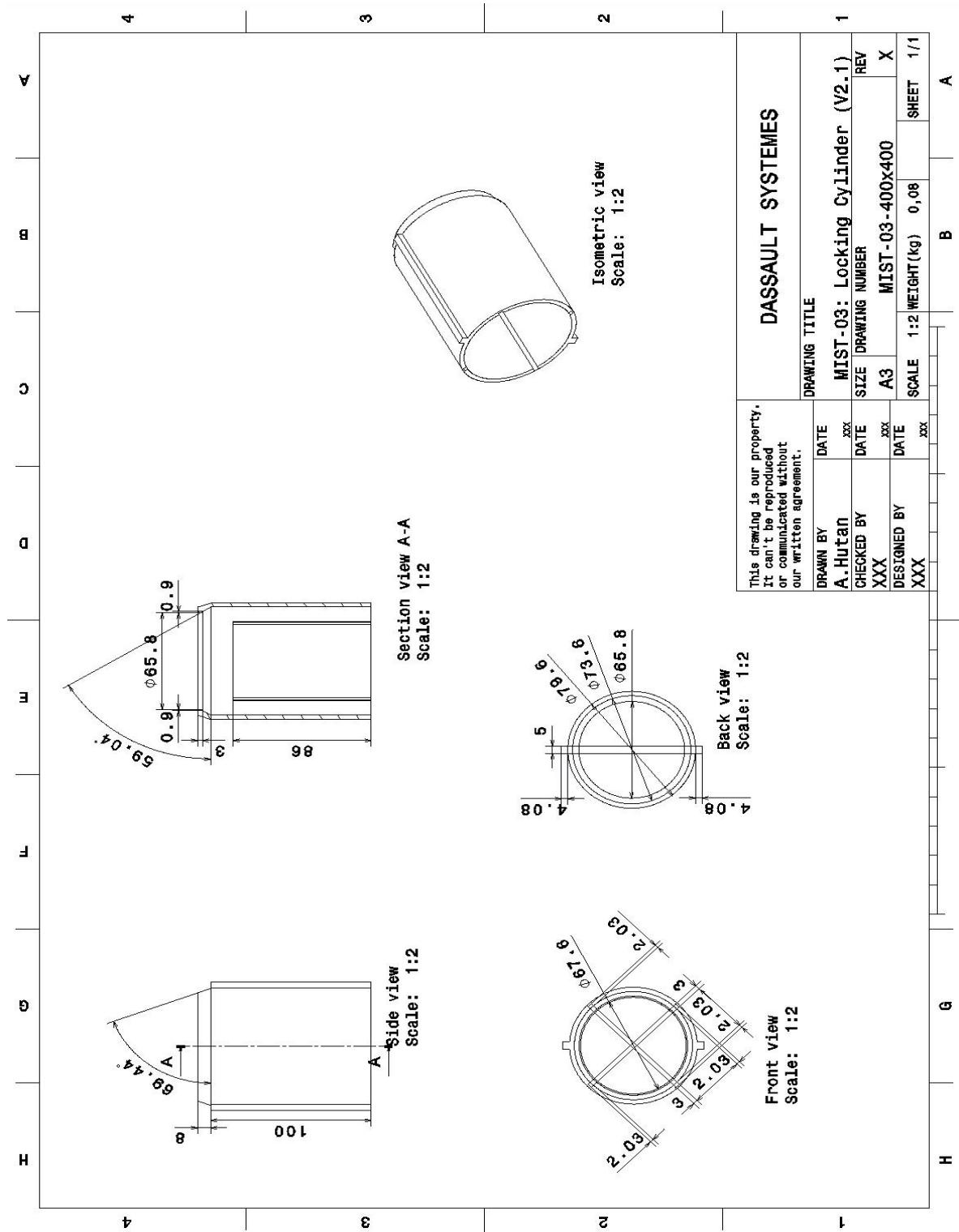


Figure A-13: Technical drawing of MIST-03 part, Interface V2.1 (400x400 Scale)

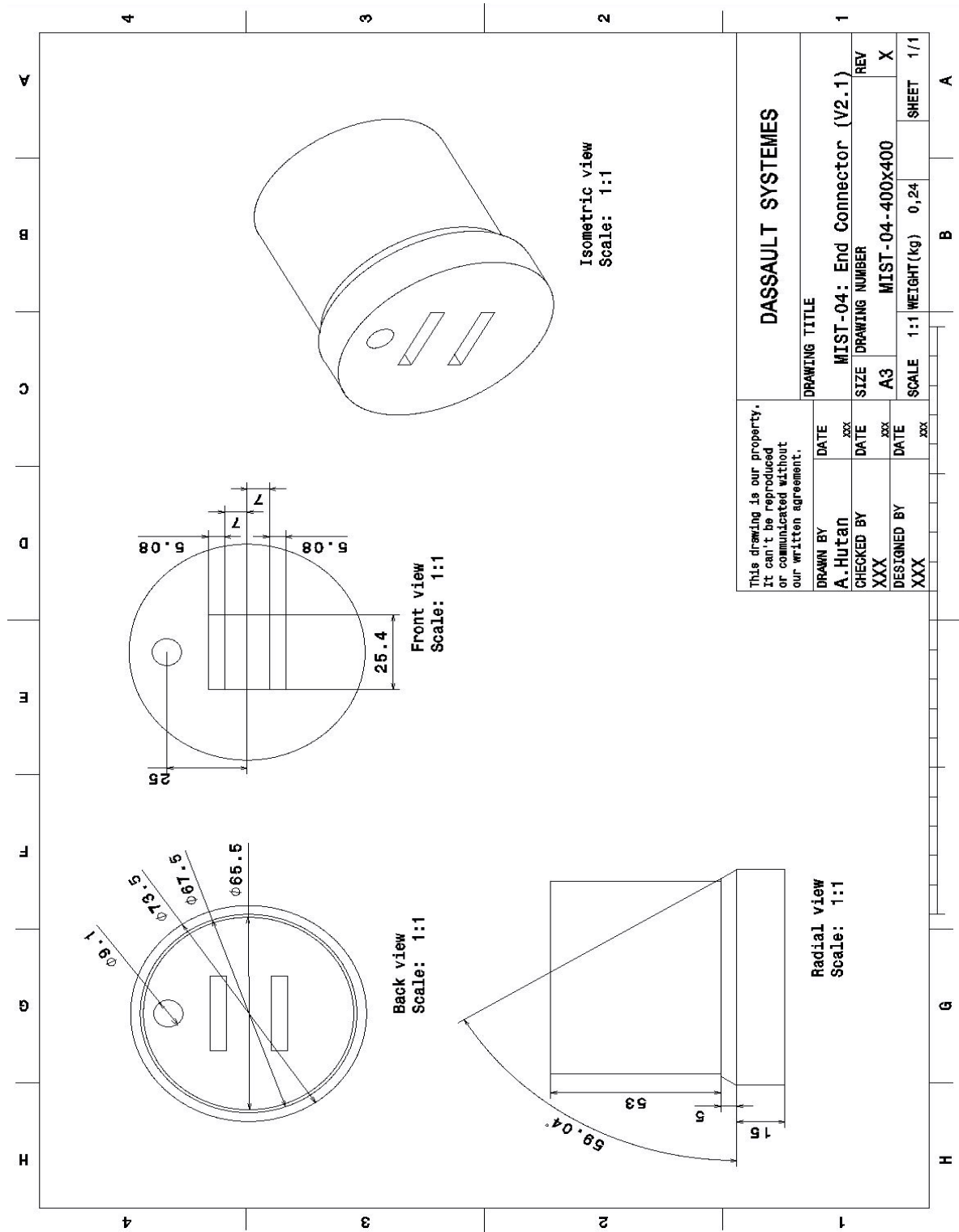


Figure A-14: Technical drawing of MIST-04 part, Interface V2.1 (400x400 Scale)

A-5 Interface V2.2

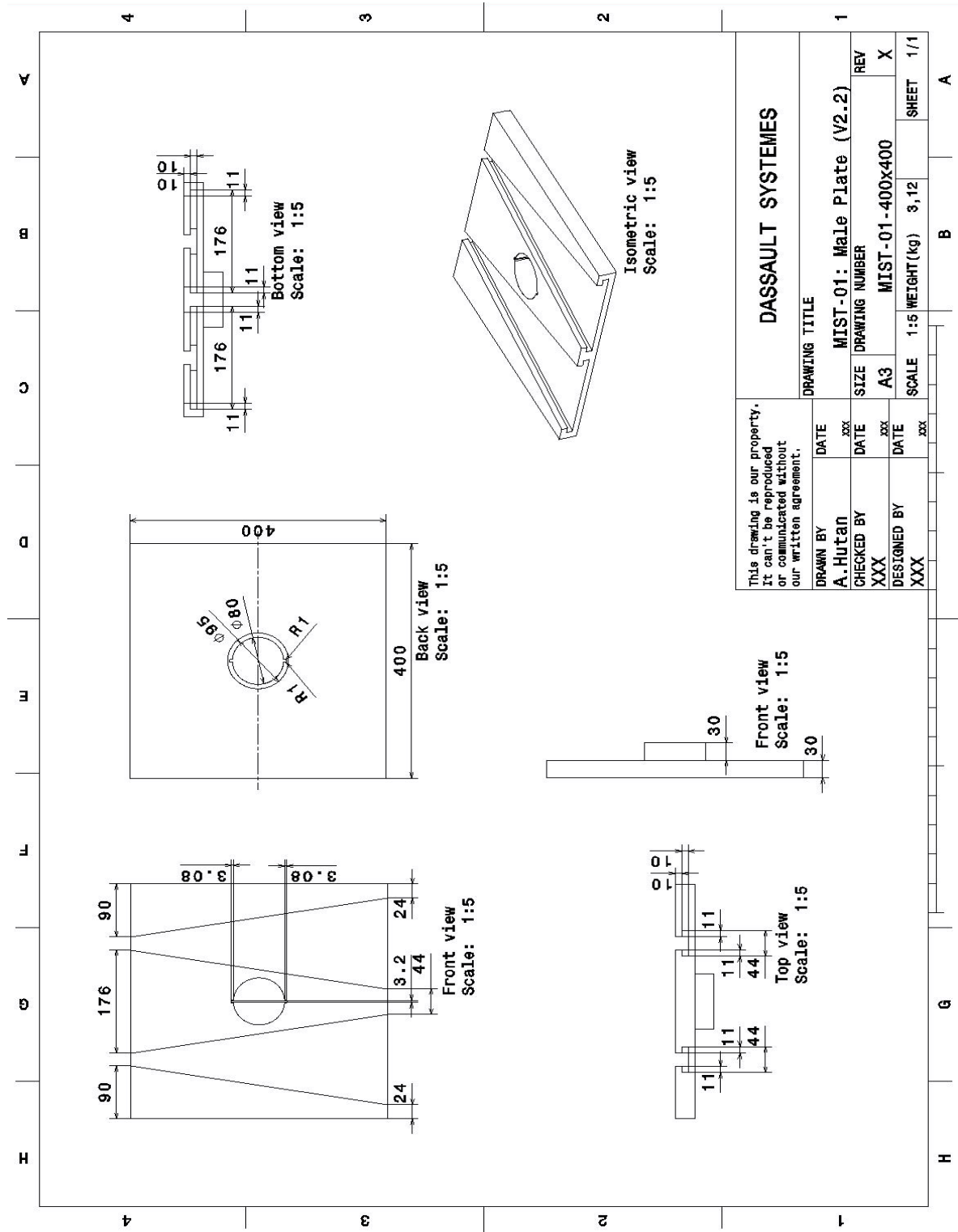


Figure A-16: Technical drawing of MIST-01 part, Interface V2.2 (400x400 Scale)

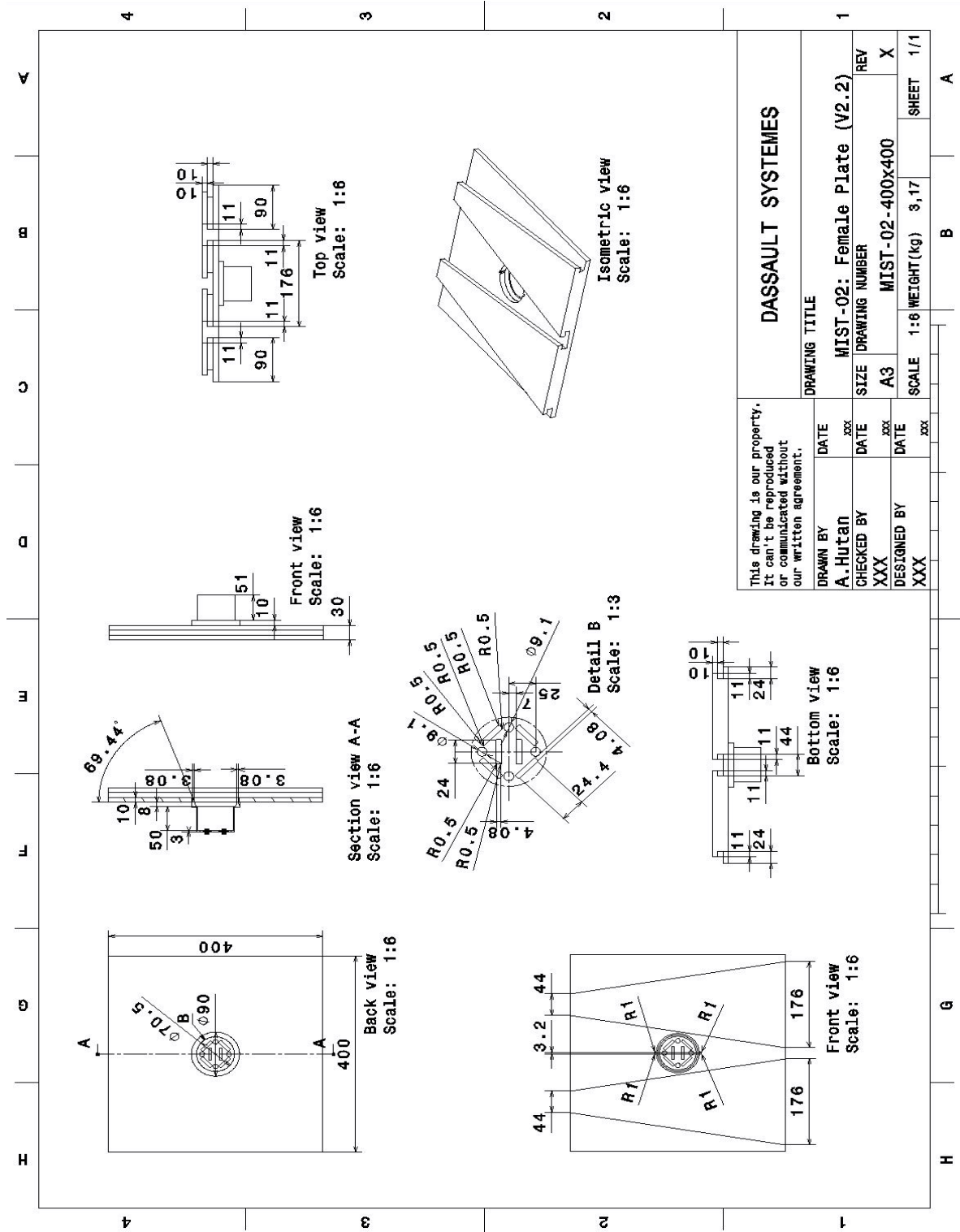


Figure A-17: Technical drawing of MIST-02 part, Interface V2.2 (400x400 Scale)

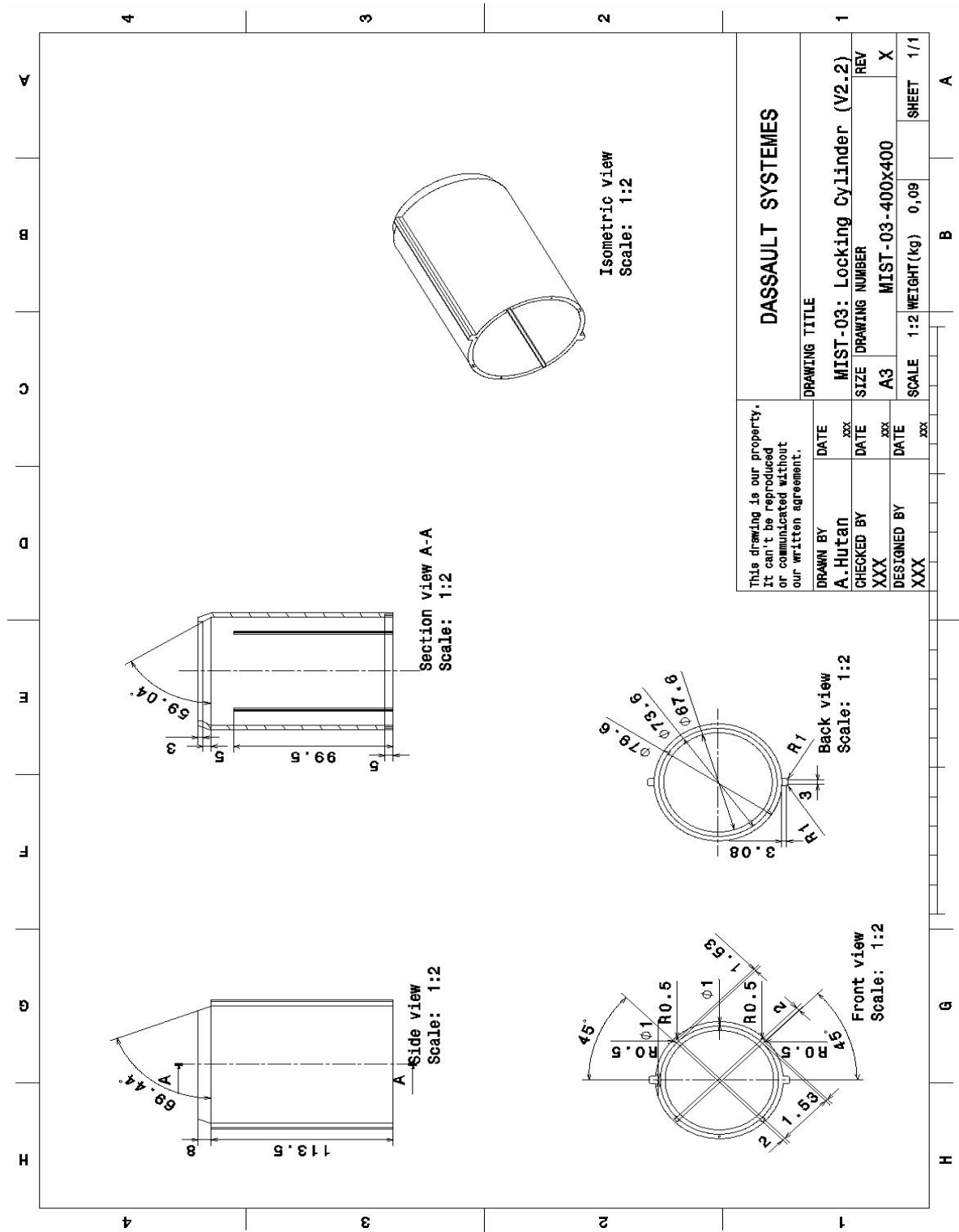


Figure A-18: Technical drawing of MIST-03 part, Interface V2.2 (400x400 Scale)

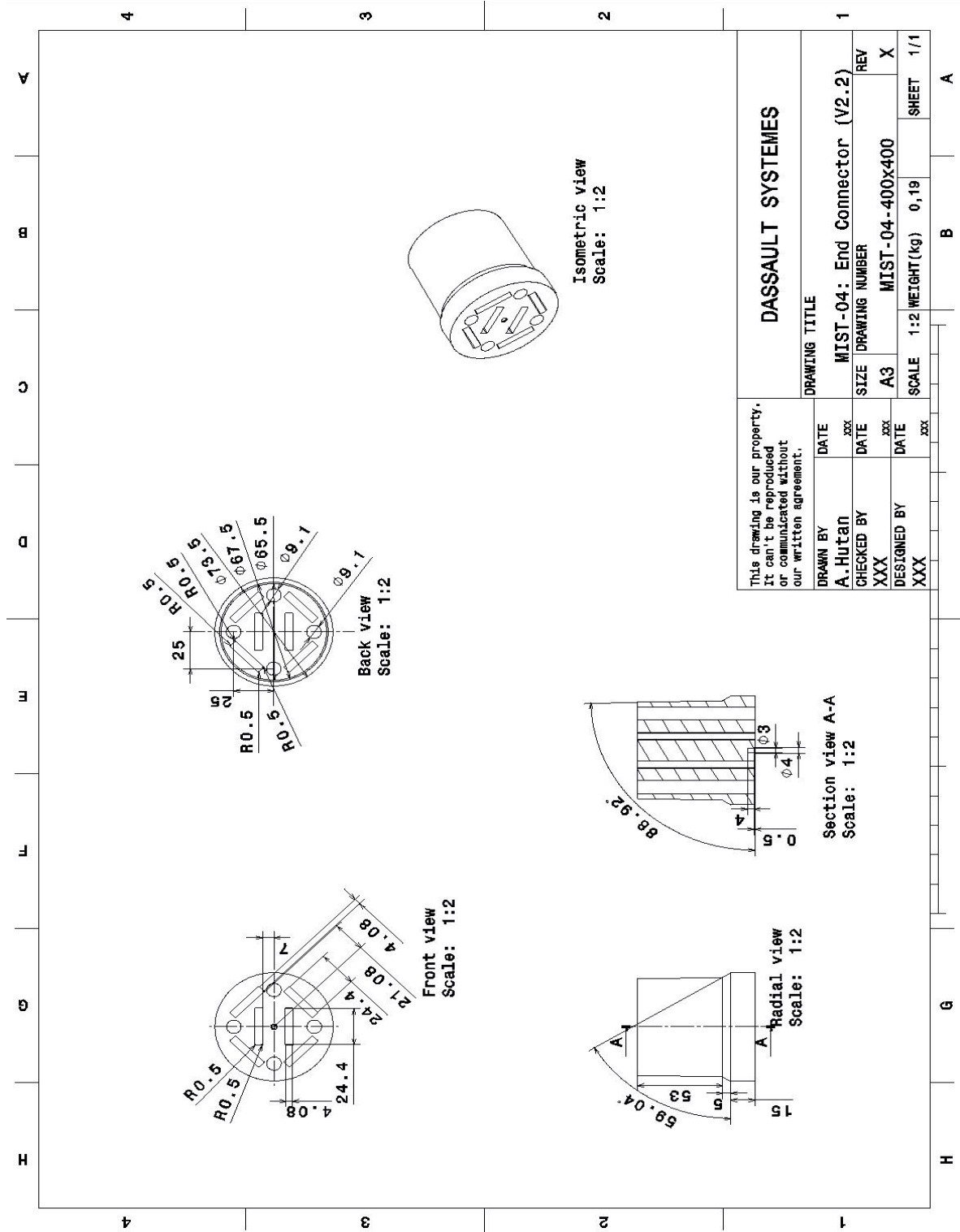


Figure A-19: Technical drawing of MIST-04 part, Interface V2.2 (400x400 Scale)

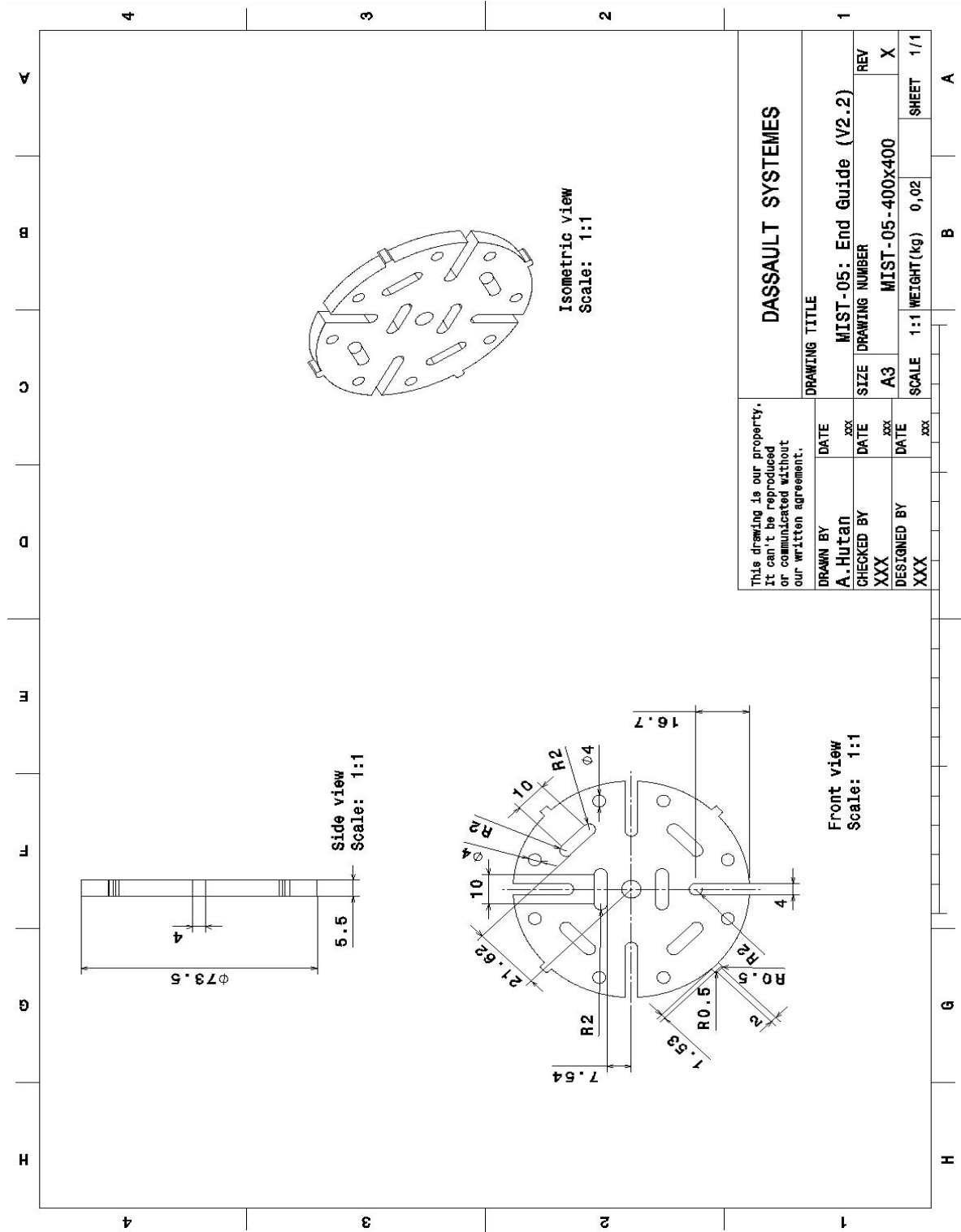


Figure A-20: Technical drawing of MIST-05 part, Interface V2.2 (400x400 Scale)

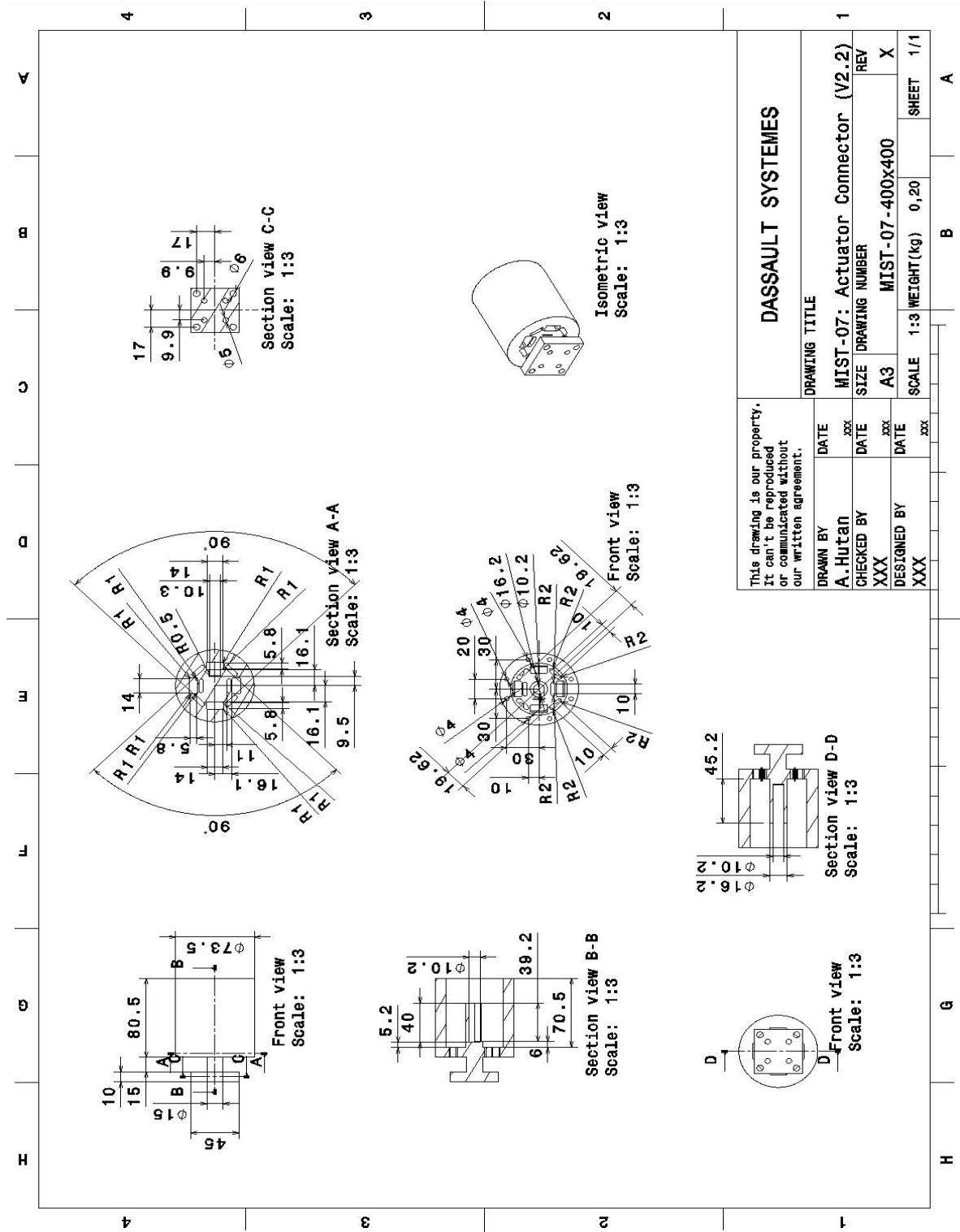


Figure A-21: Technical drawing of MIST-07 part, Interface V2.2 (400x400 Scale)

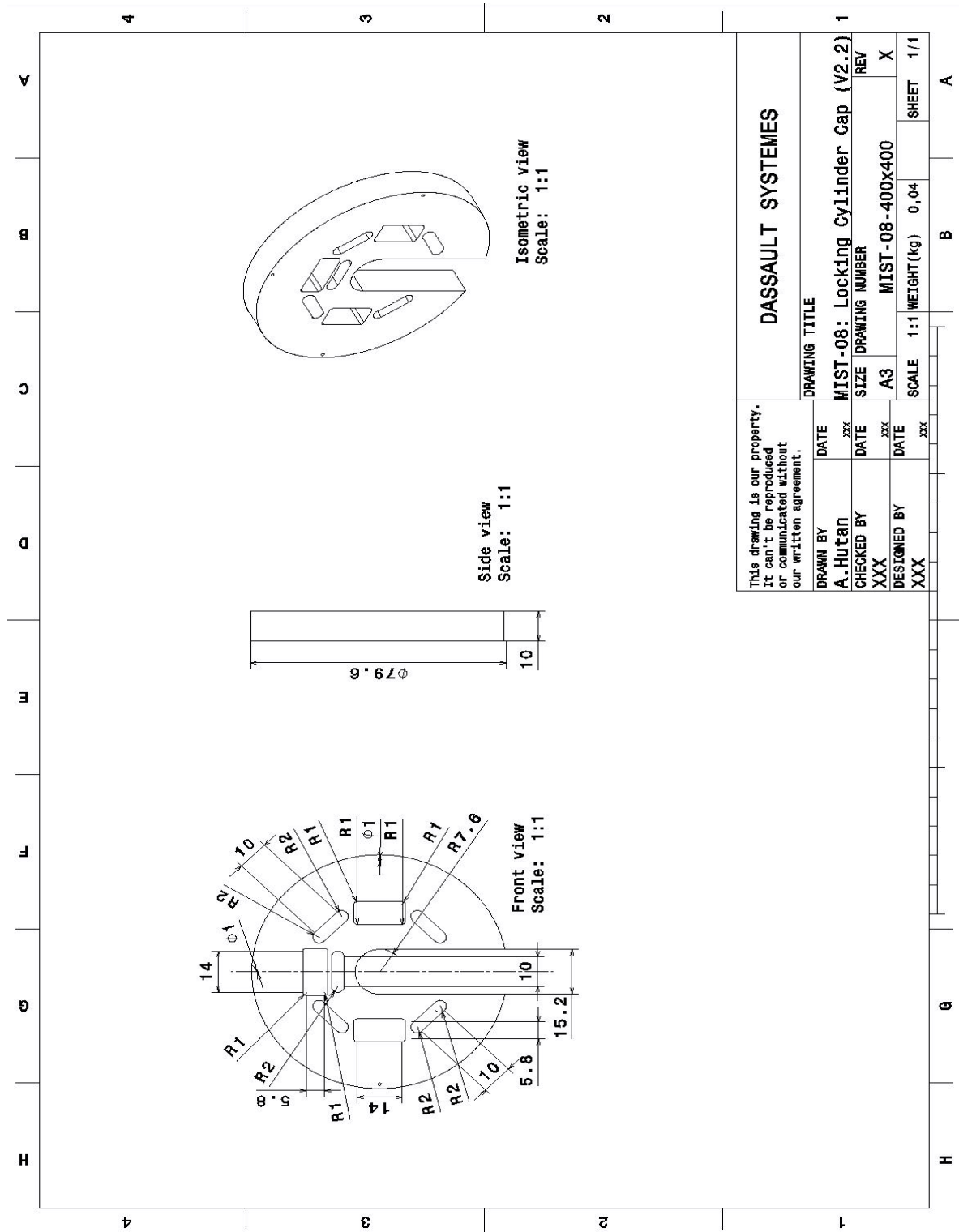


Figure A-22: Technical drawing of MIST-08 part, Interface V2.2 (400x400 Scale)

Appendix B

Appendix B - Interface Technical Drawings (120x120 Scale)

B-1 Interface V0.0

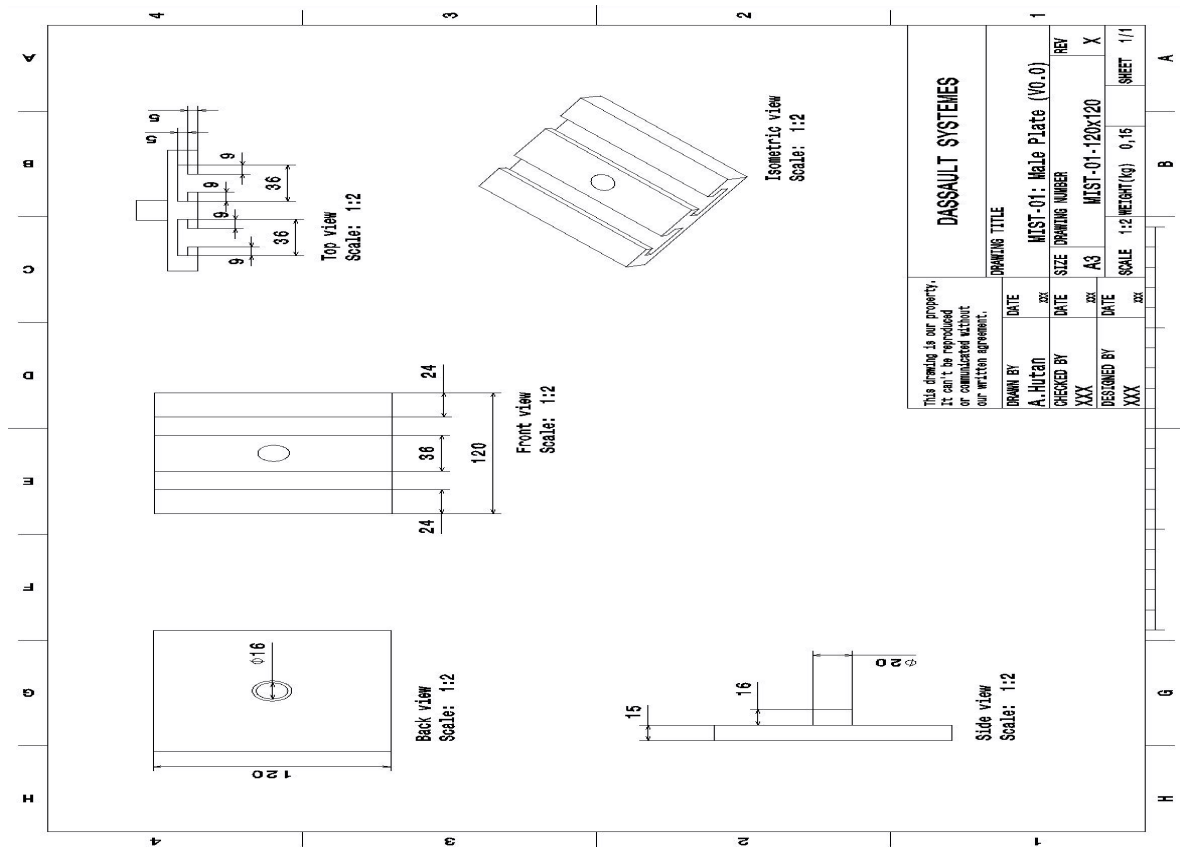


Figure B-1: Technical drawing of MIST-01 part, Interface V0.0 (120x120 Scale)

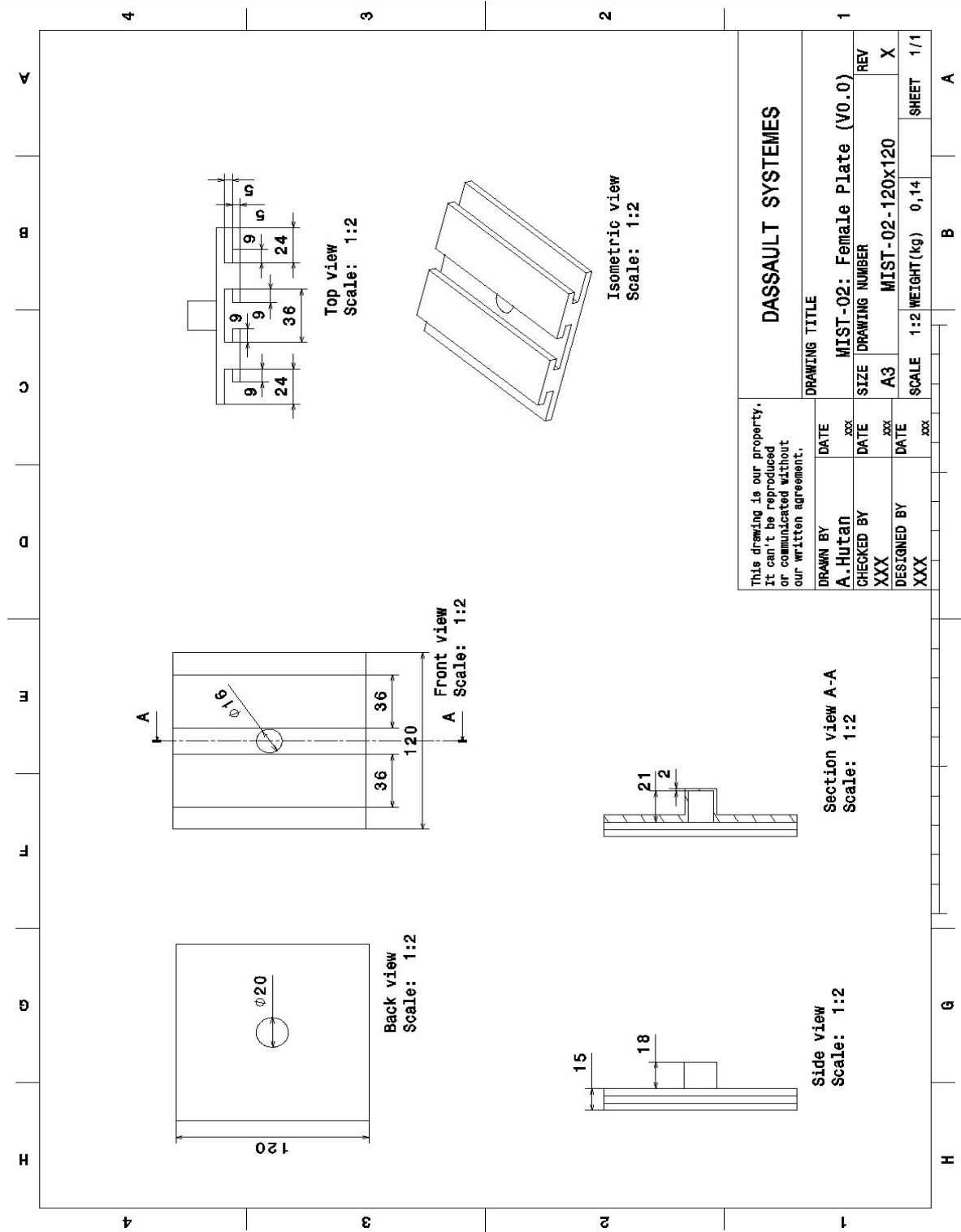


Figure B-2: Technical drawing of MIST-02 part, Interface V0.0 (120x120 Scale)

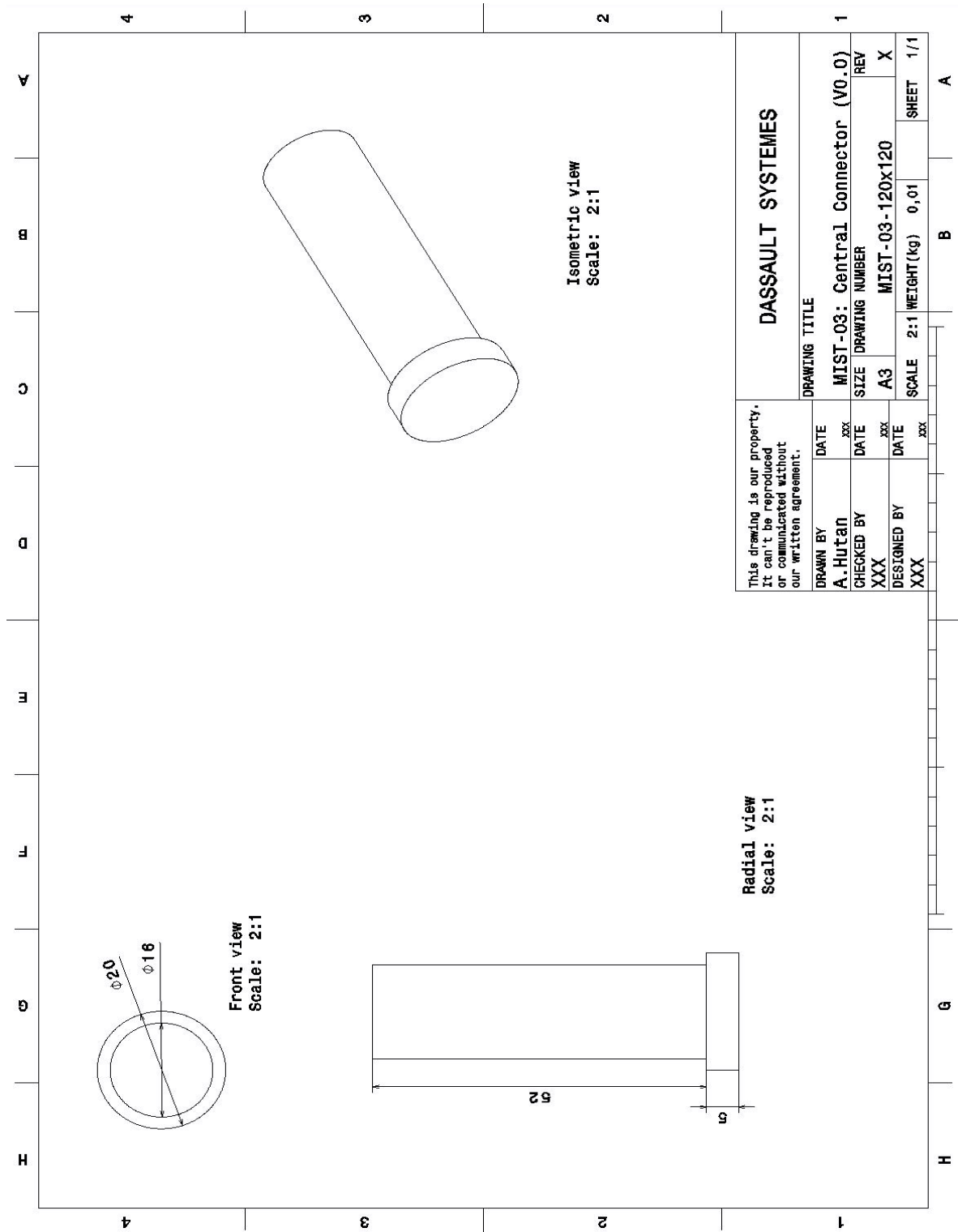


Figure B-3: Technical drawing of MIST-03 part, Interface V0.0 (120x120 Scale)

B-2 Interface V1.0

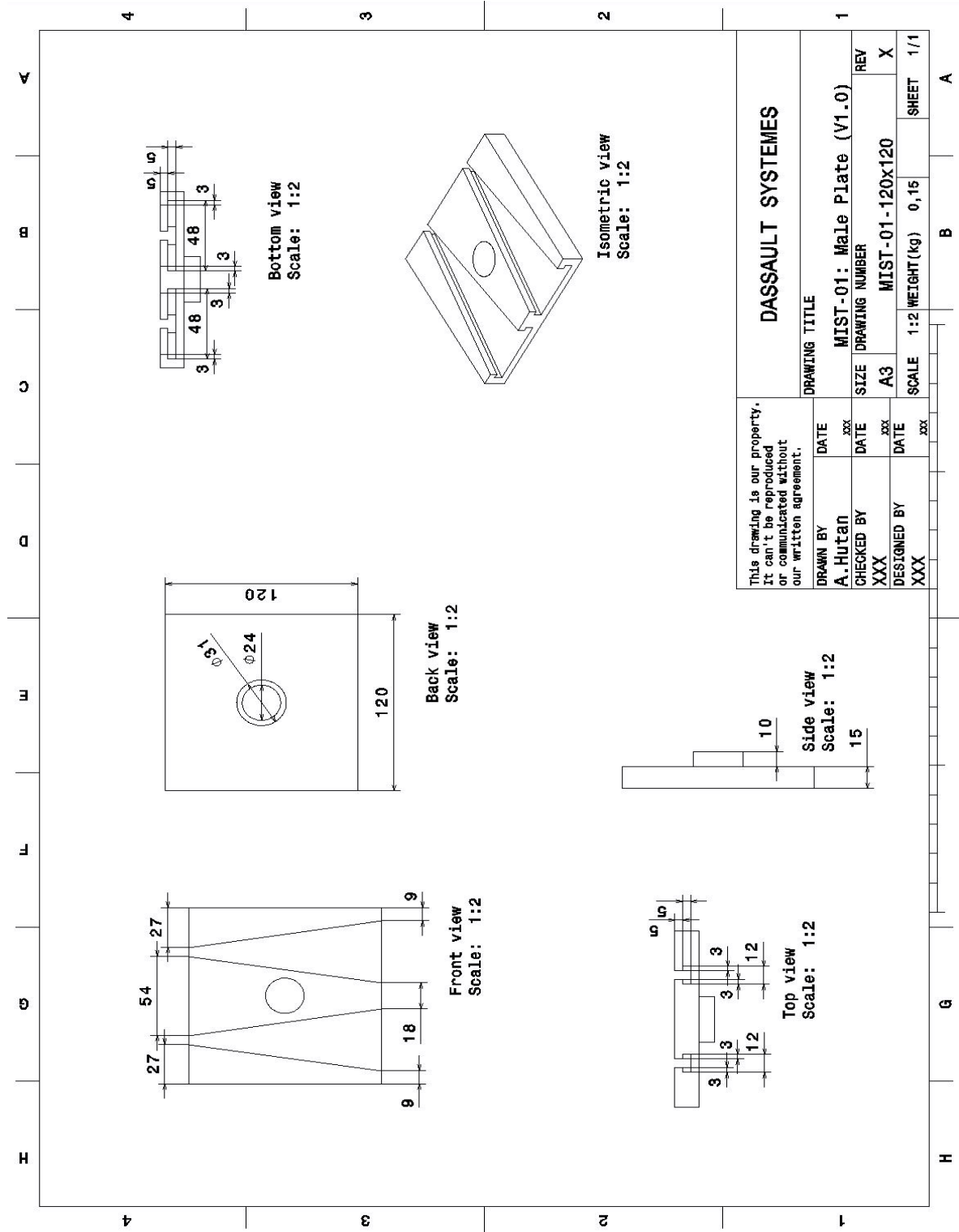


Figure B-4: Technical drawing of MIST-01 part, Interface V1.0 (120x120 Scale)

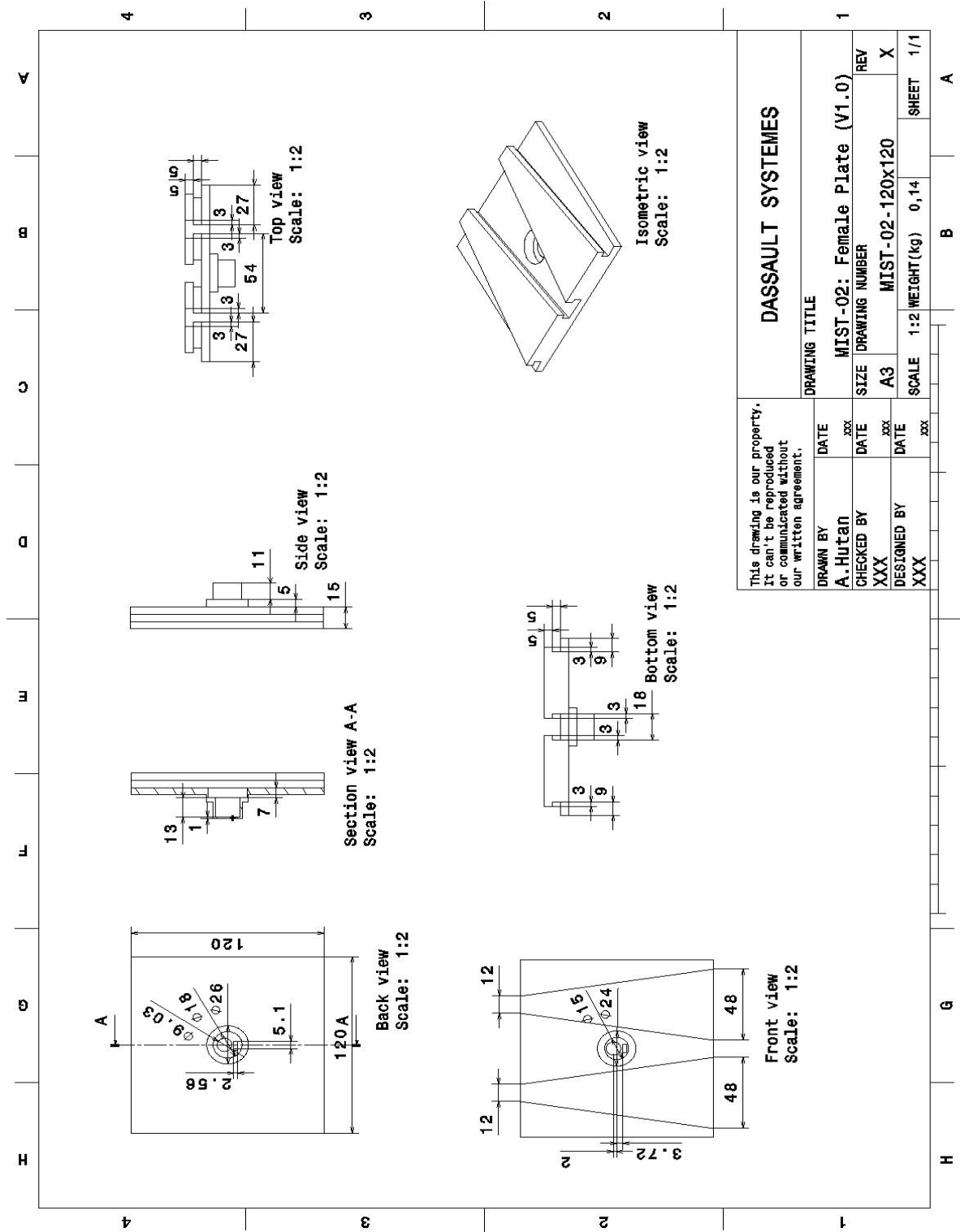


Figure B-5: Technical drawing of MIST-02 part, Interface V1.0 (120x120 Scale)

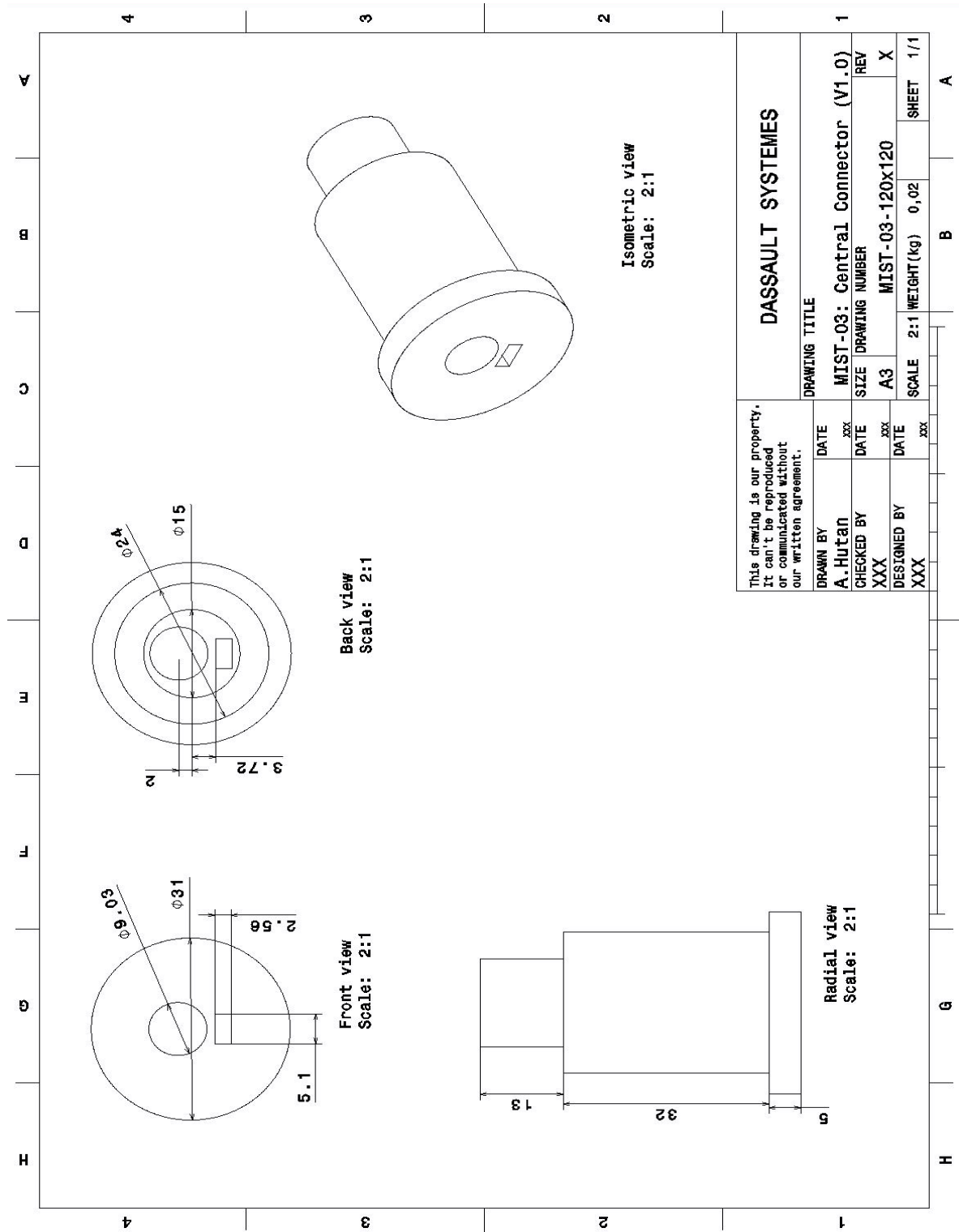


Figure B-6: Technical drawing of MIST-03 part, Interface V1.0 (120x120 Scale)

B-3 Interface V2.0

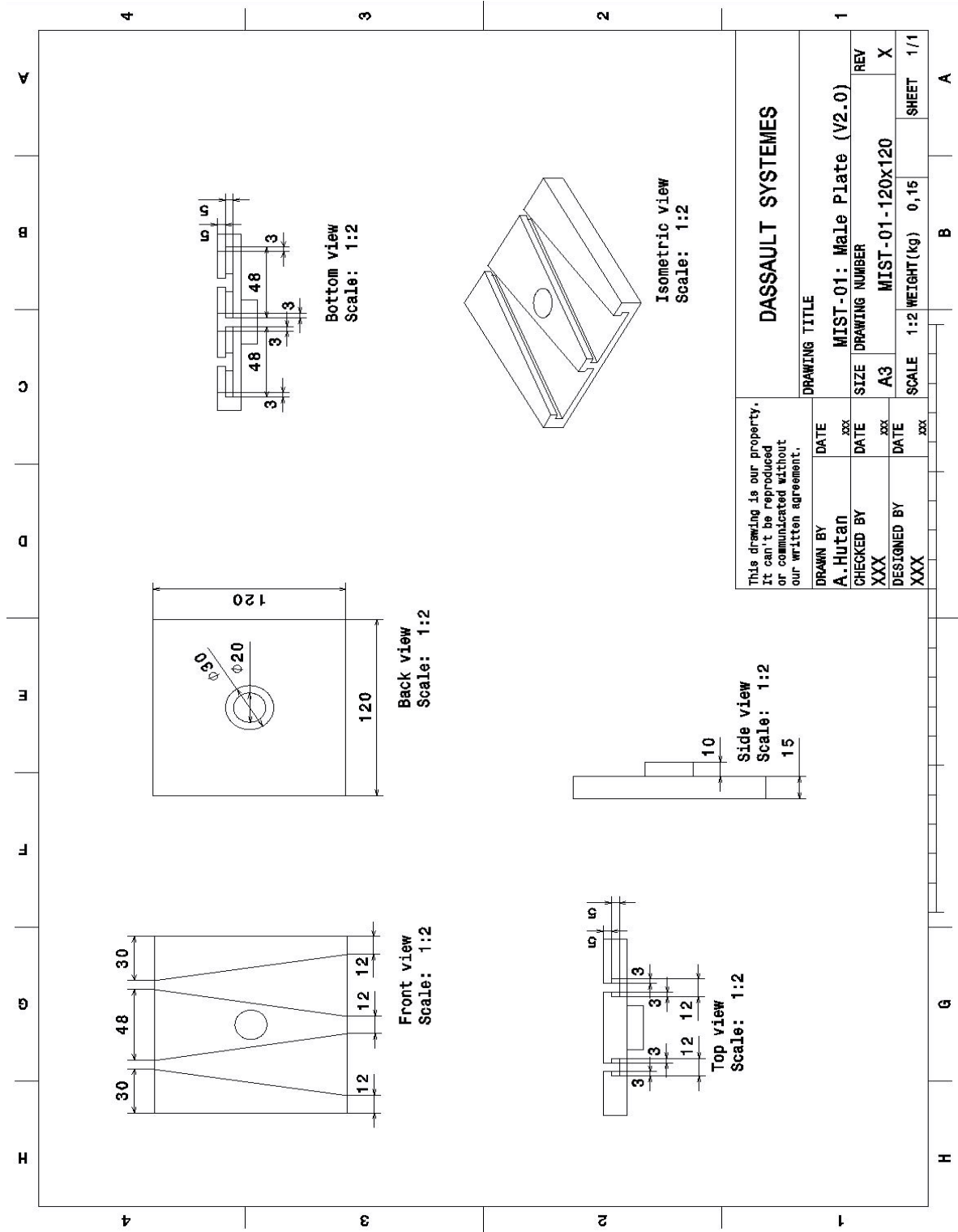


Figure B-7: Technical drawing of MIST-01 part, Interface V2.0 (120x120 Scale)

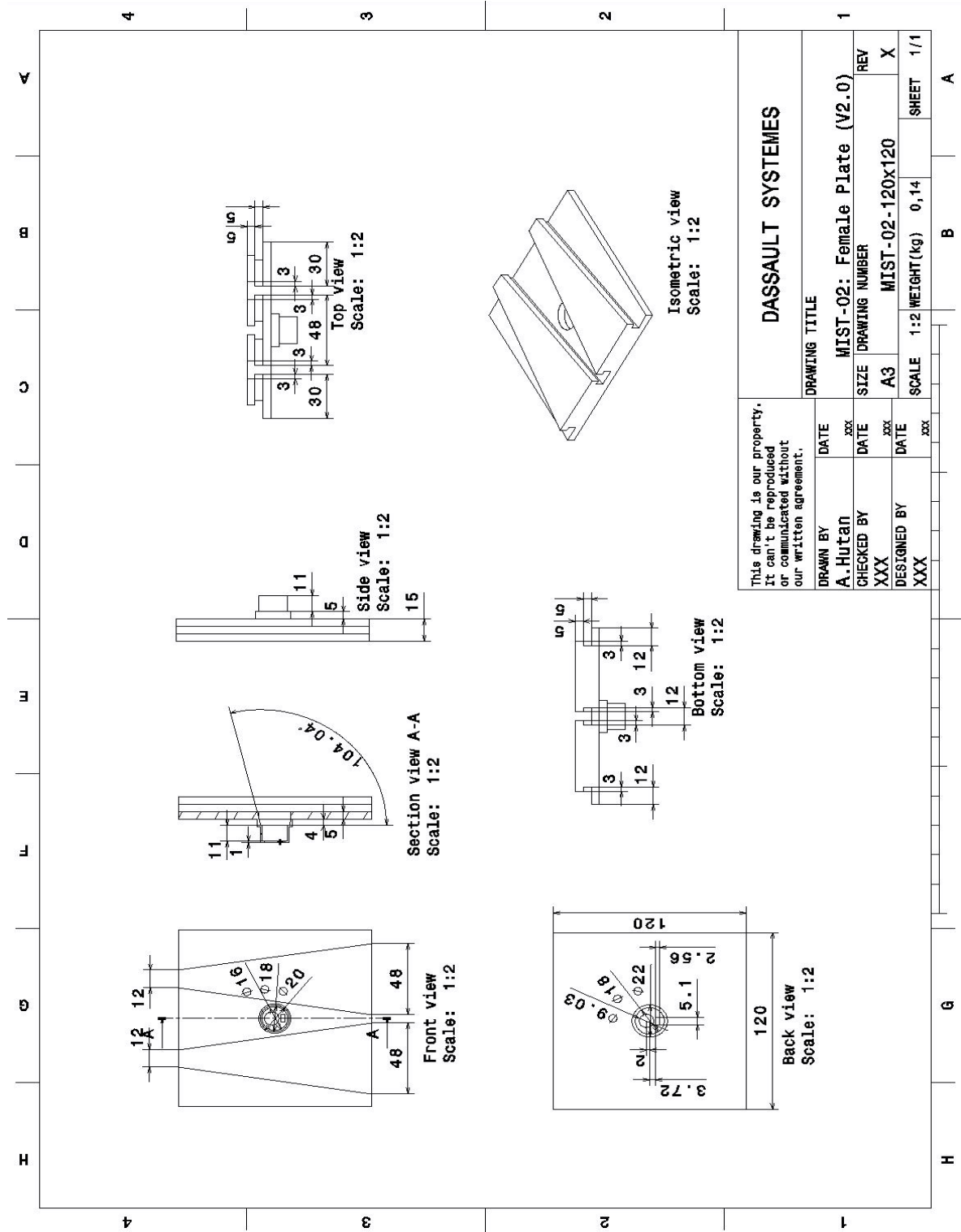


Figure B-8: Technical drawing of MIST-02 part, Interface V2.0 (120x120 Scale)

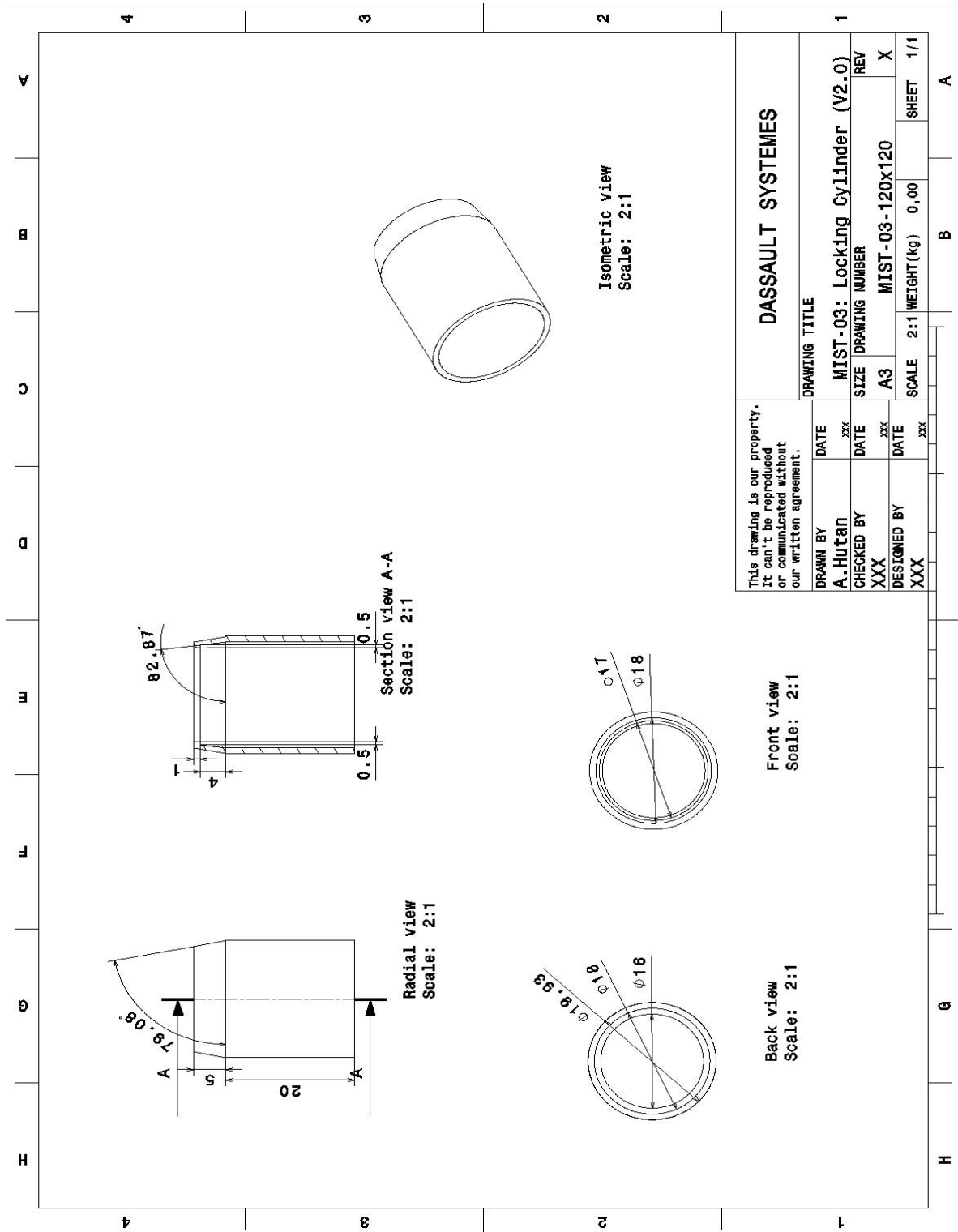


Figure B-9: Technical drawing of MIST-03 part, Interface V2.0 (120x120 Scale)

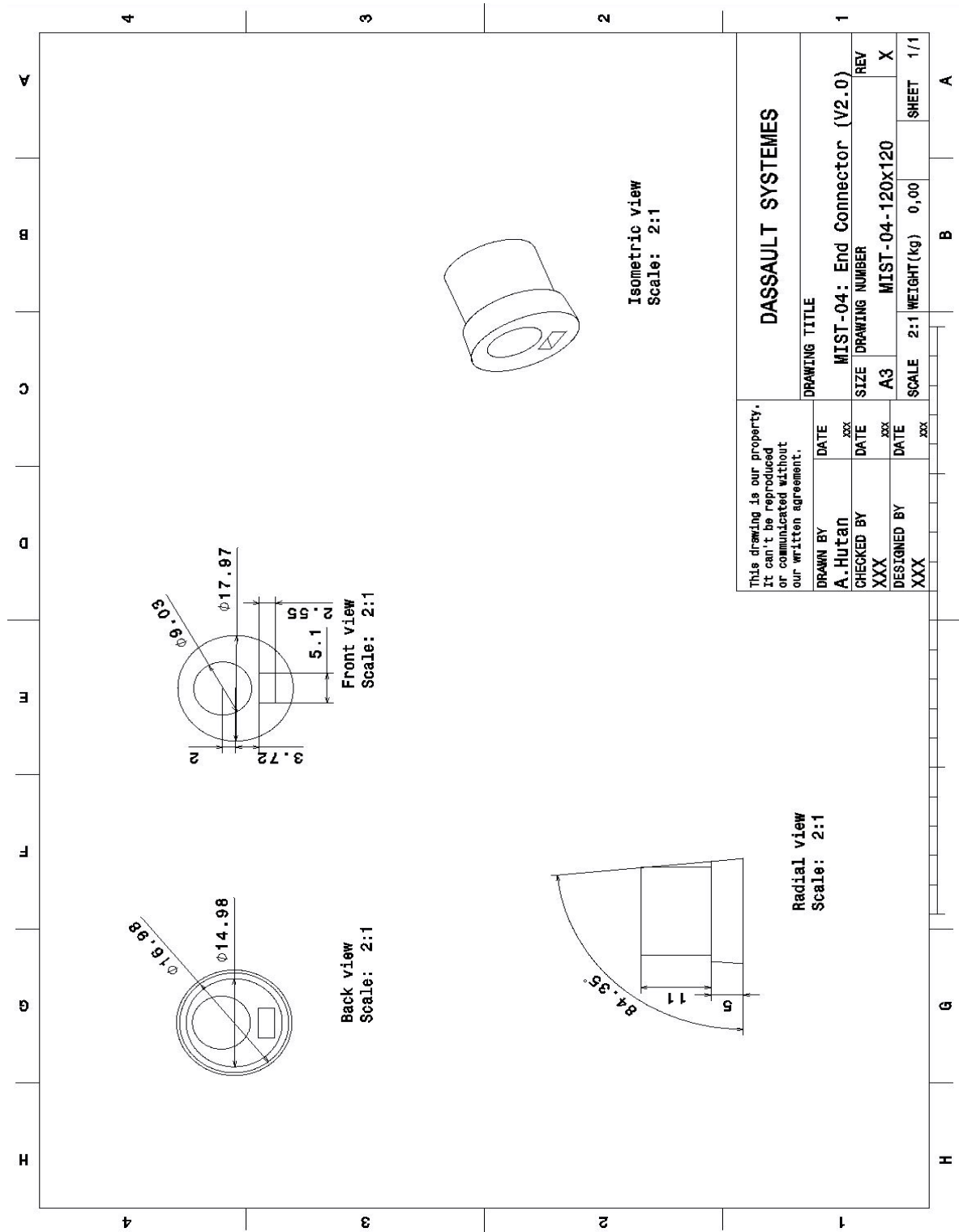


Figure B-10: Technical drawing of MIST-04 part, Interface V2.0 (120x120 Scale)

B-4 Interface V2.1

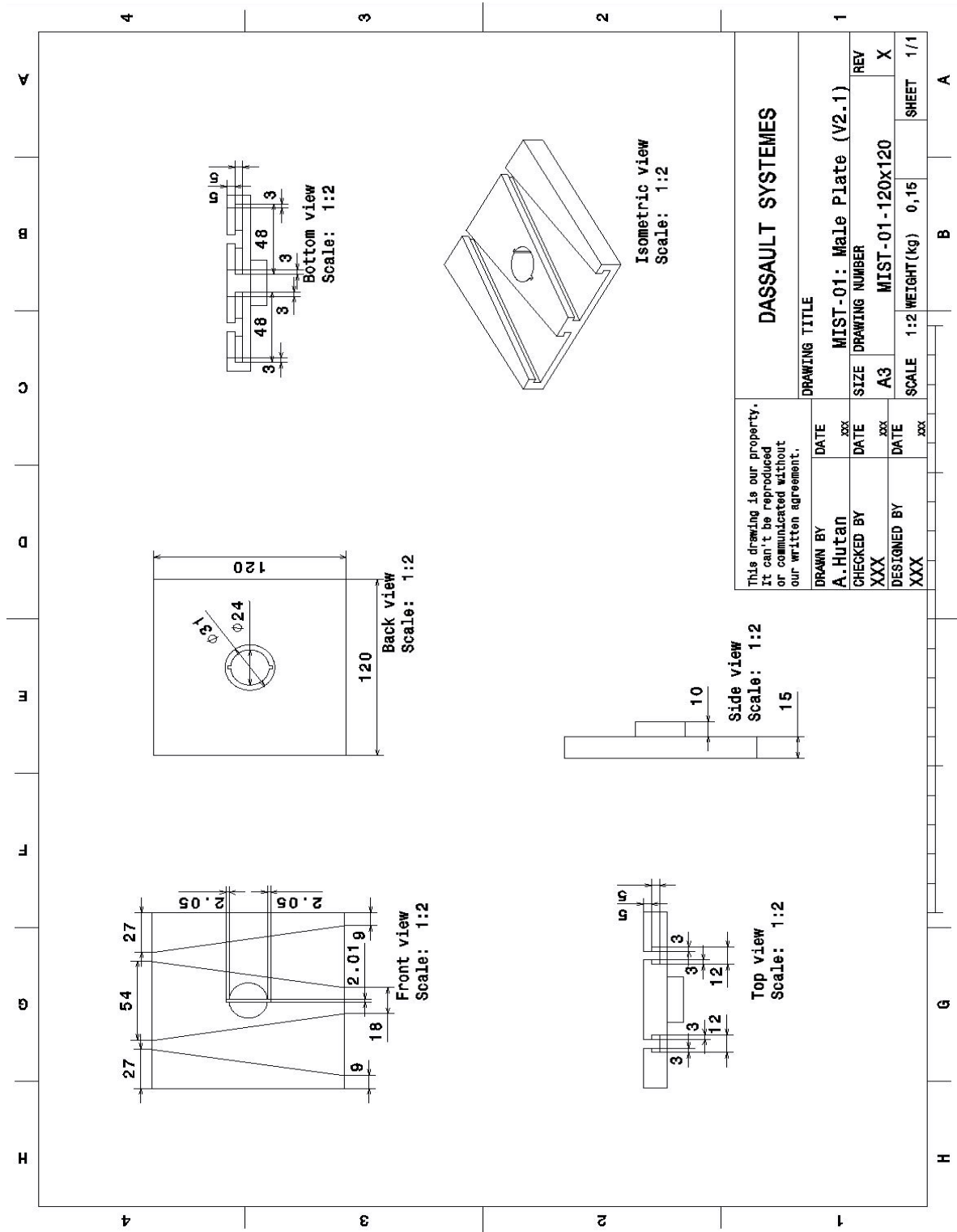


Figure B-11: Technical drawing of MIST-01 part, Interface V2.1 (120x120 Scale)

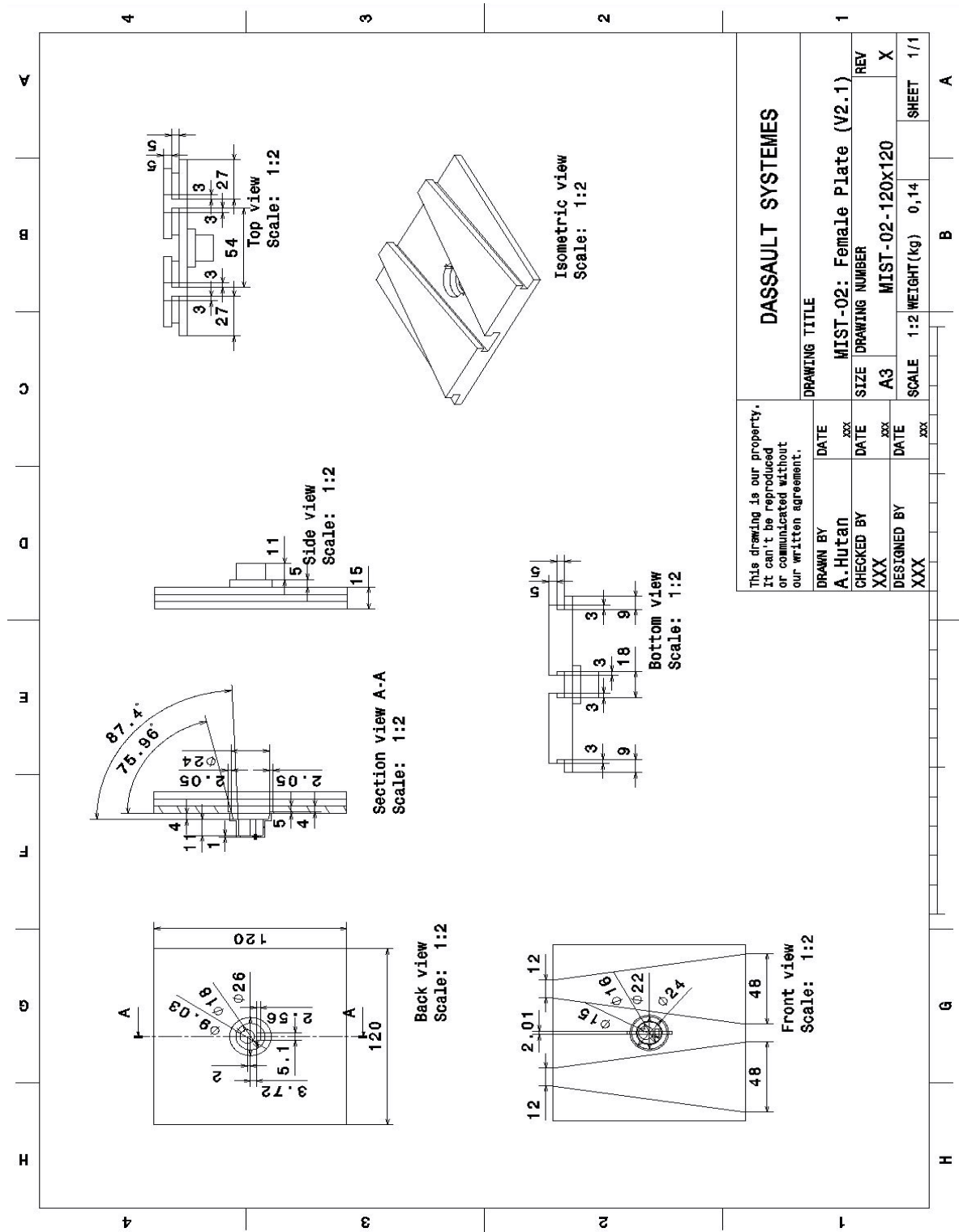


Figure B-12: Technical drawing of MIST-02 part, Interface V2.1 (120x120 Scale)

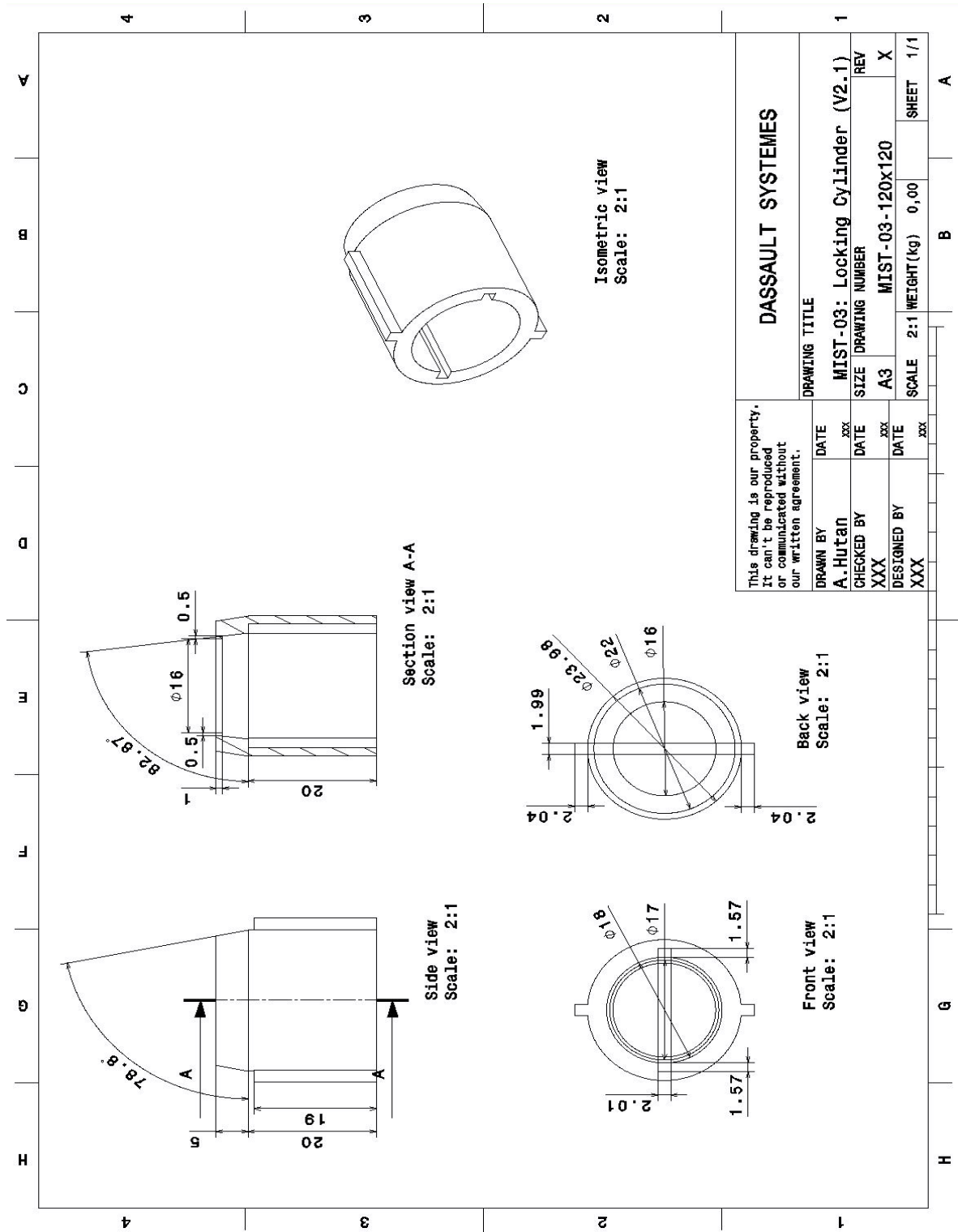


Figure B-13: Technical drawing of MIST-03 part, Interface V2.1 (120x120 Scale)

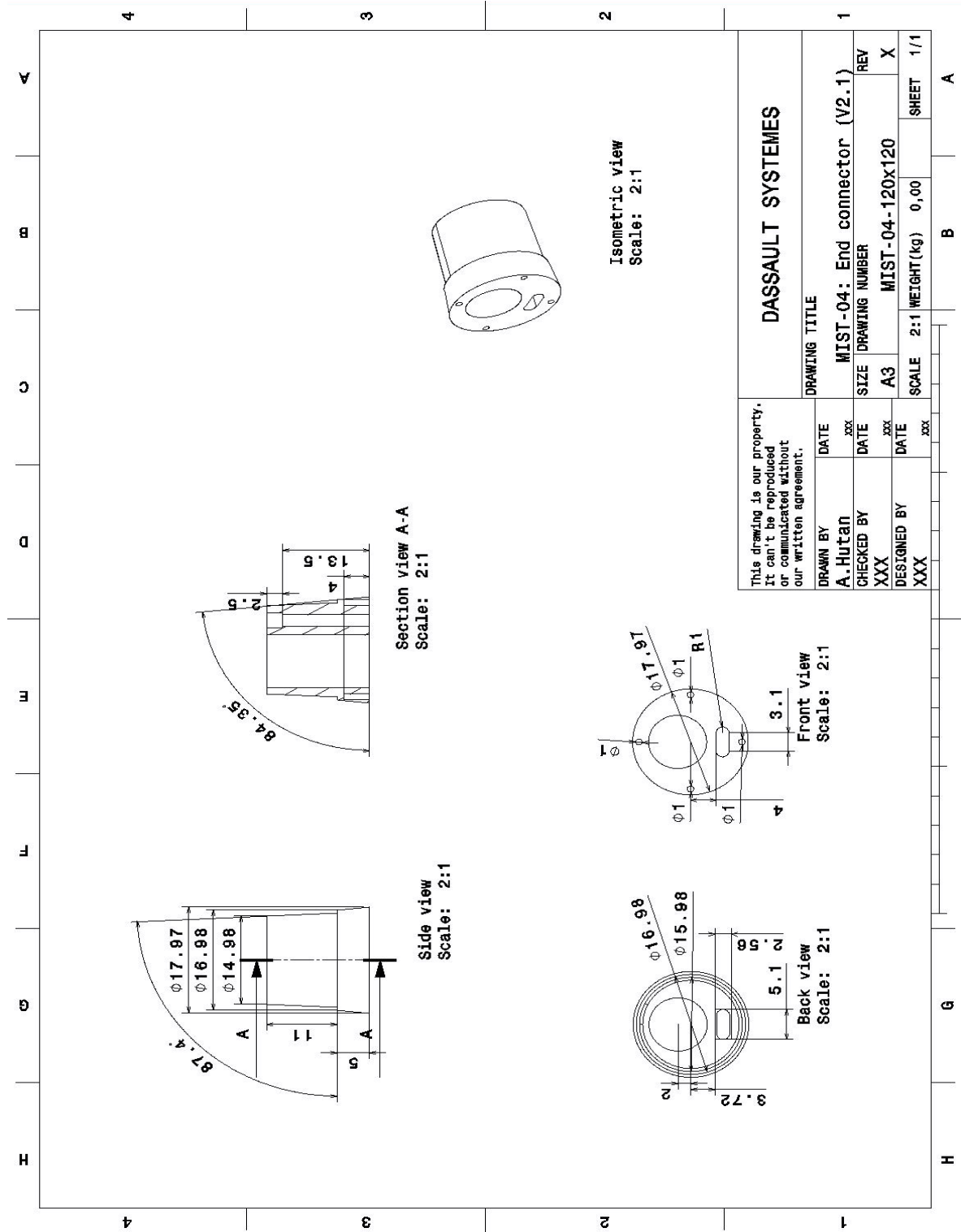


Figure B-14: Technical drawing of MIST-04 part, Interface V2.1 (120x120 Scale)

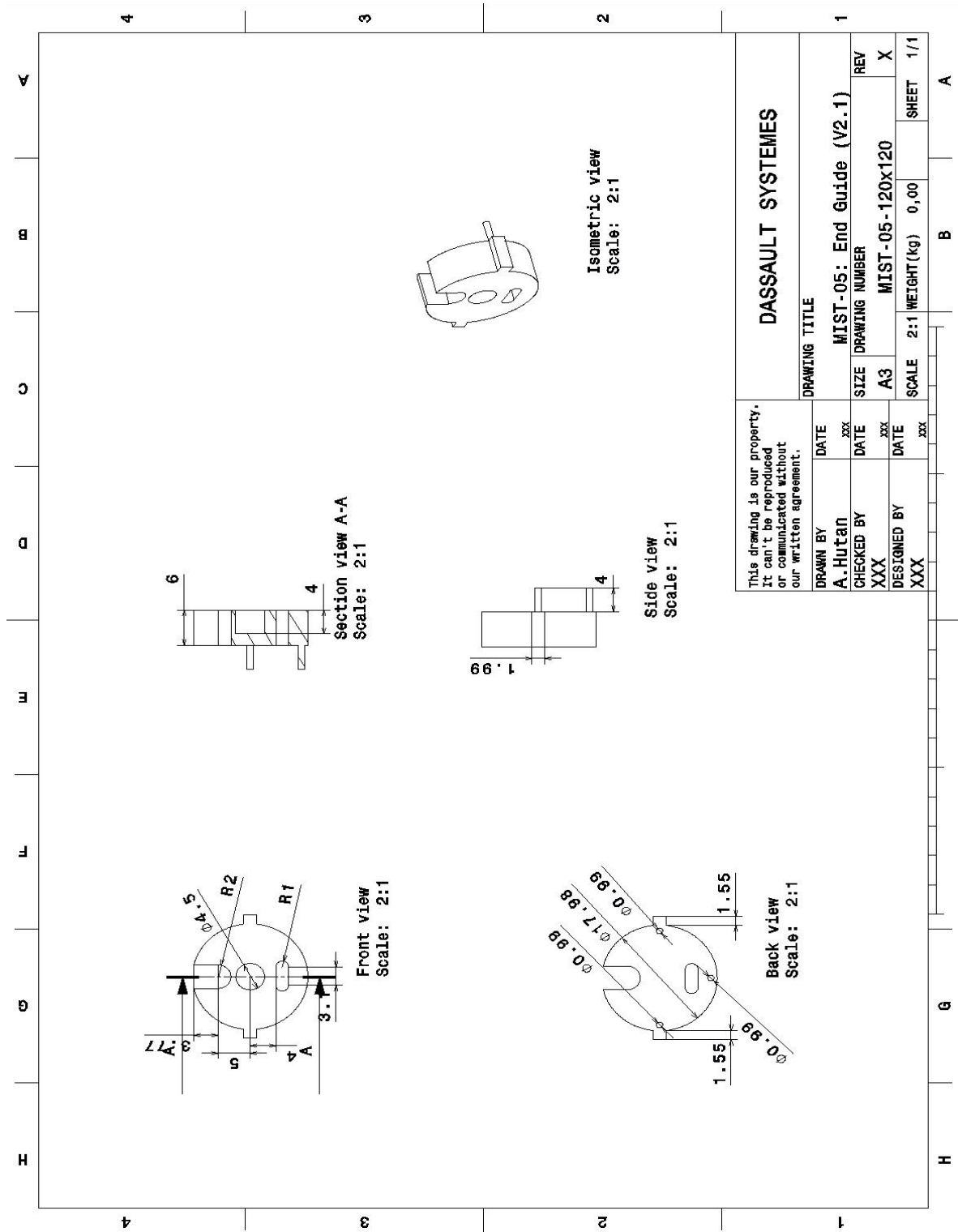


Figure B-15: Technical drawing of MIST-05 part, Interface V2.1 (120x120 Scale)

Appendix C

Appendix C - Interface Proof of Concept (PoC)

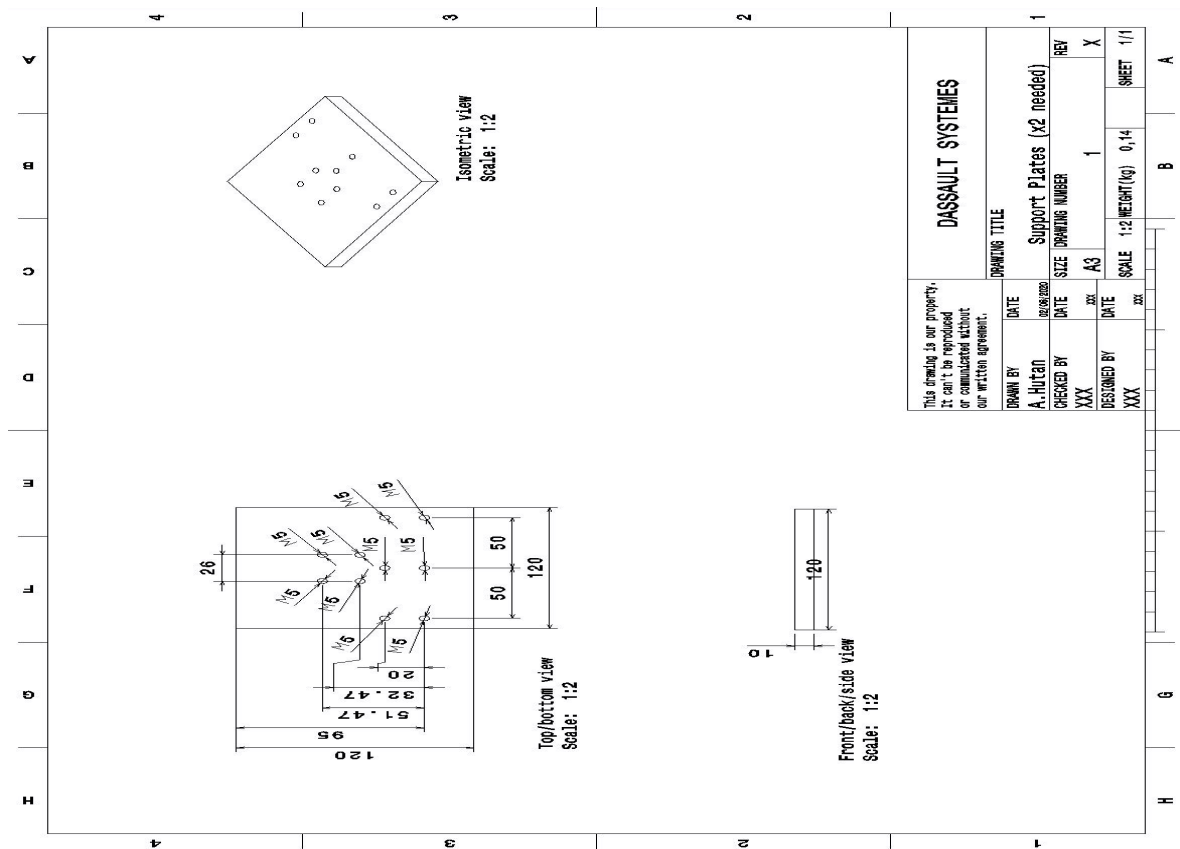


Figure C-1: Technical drawing POC: support plates (X2)

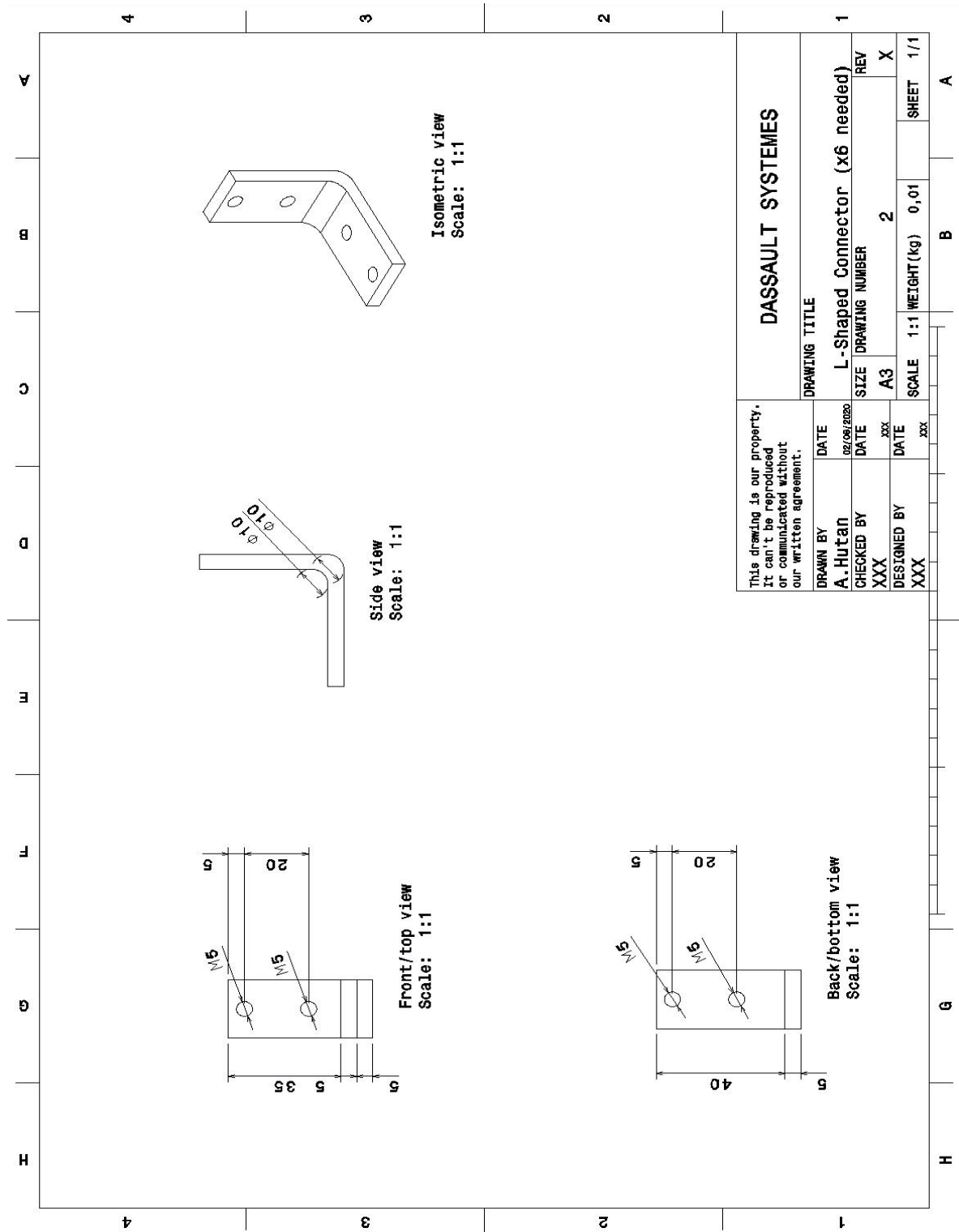


Figure C-2: Technical drawing POC: interface - support plate connectors (X6)

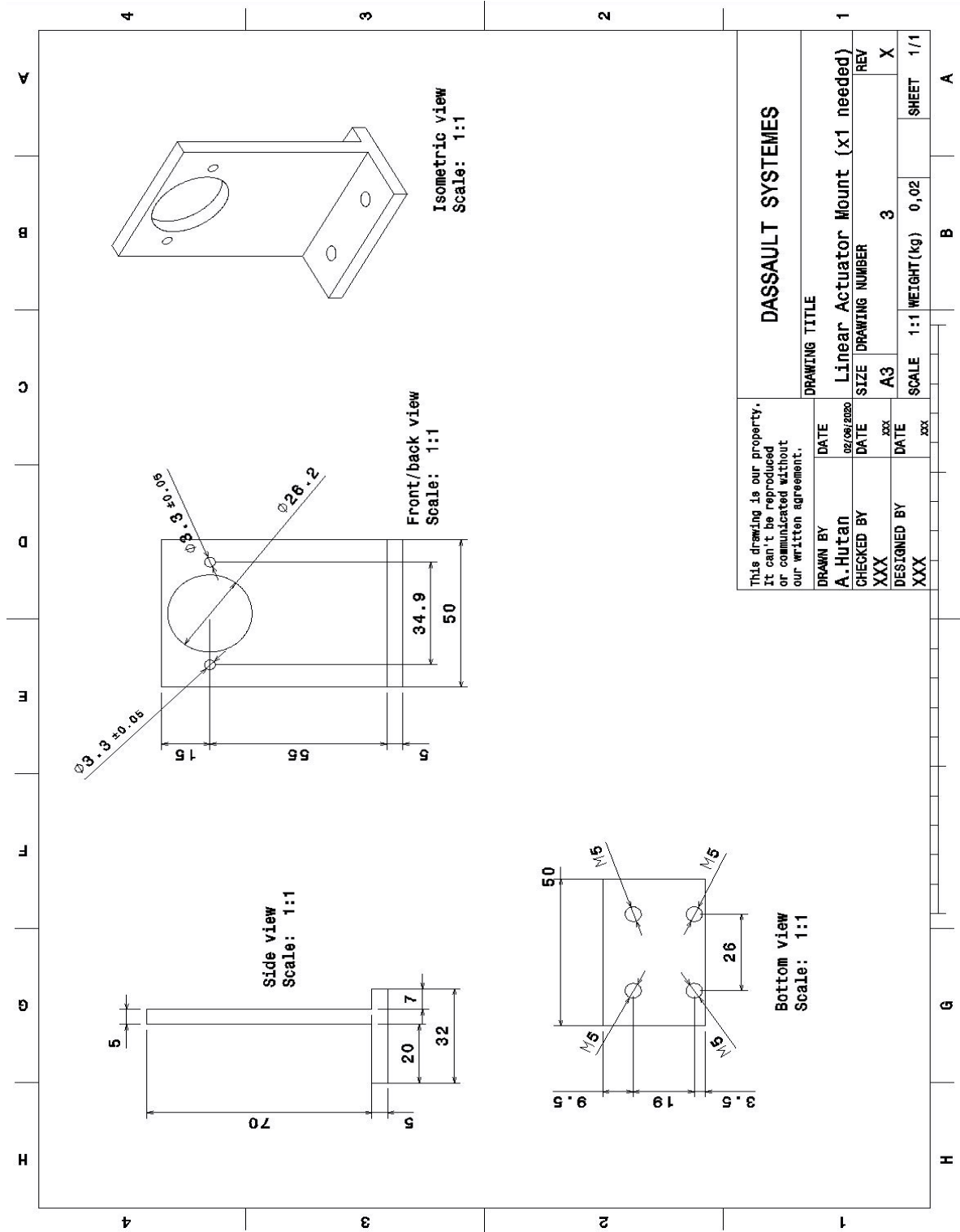


Figure C-3: Technical drawing POC: linear actuator mount (X1)

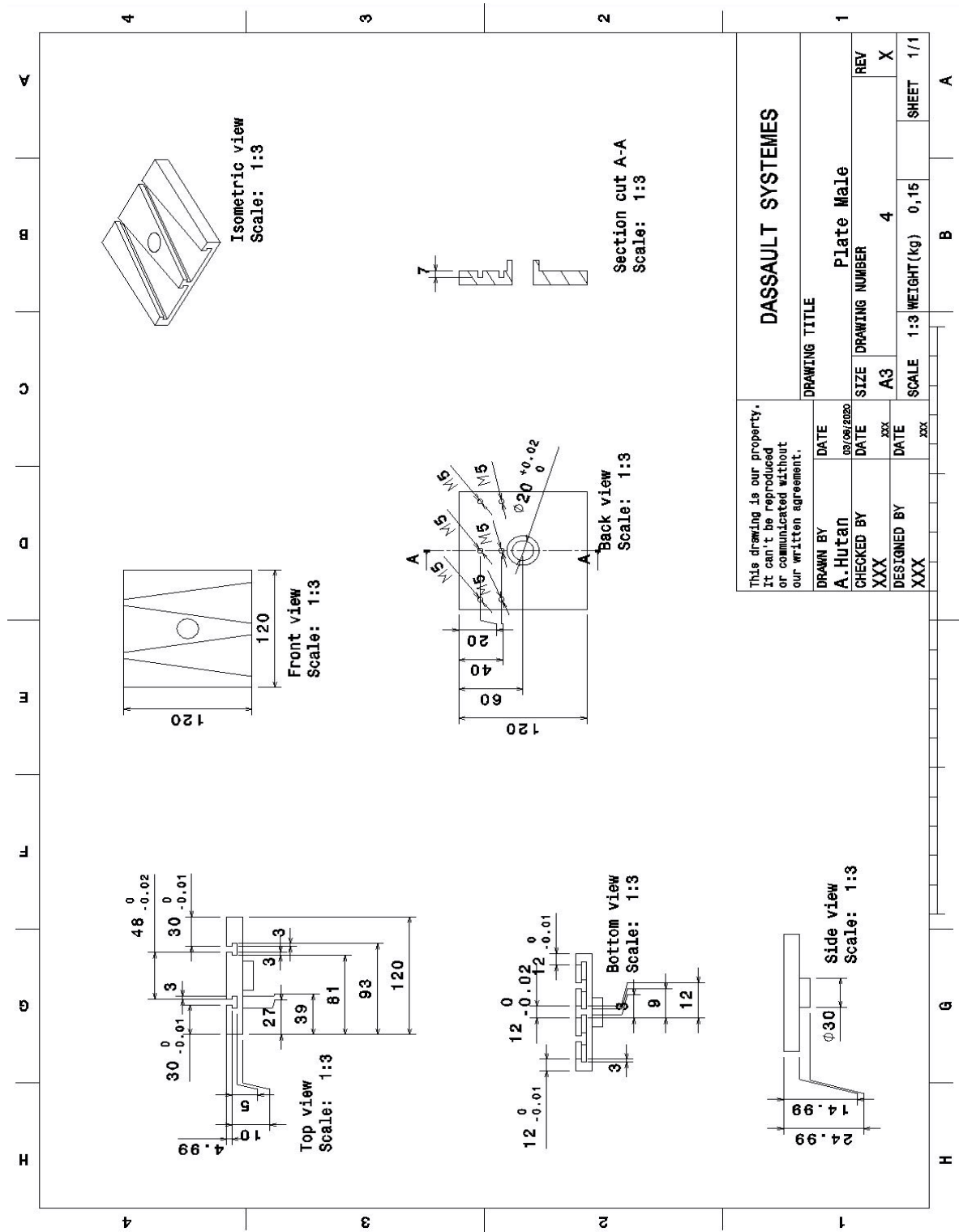


Figure C-4: Technical drawing POC: interface - male plate (X1)

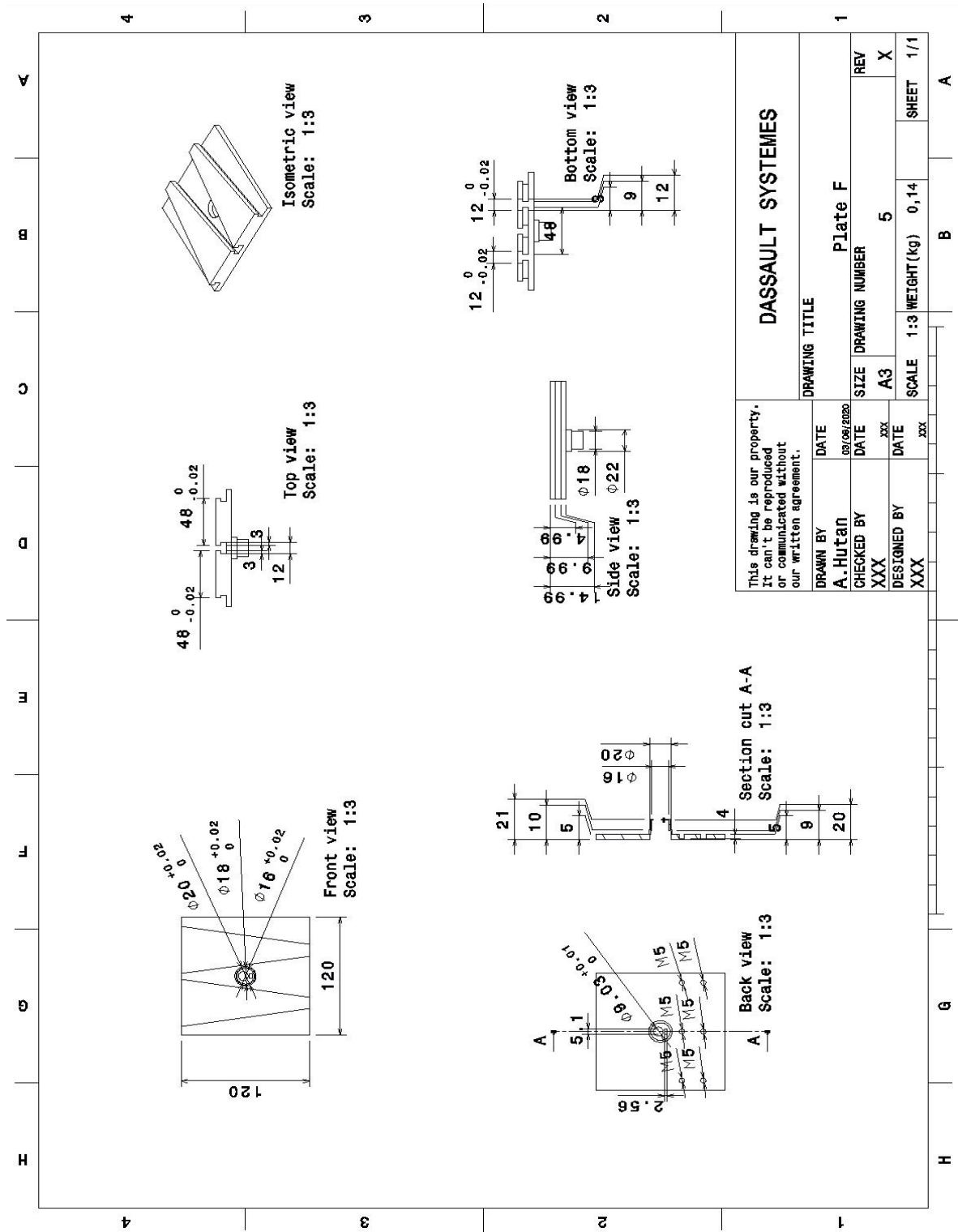


Figure C-5: Technical drawing POC: interface - female plate (X1)

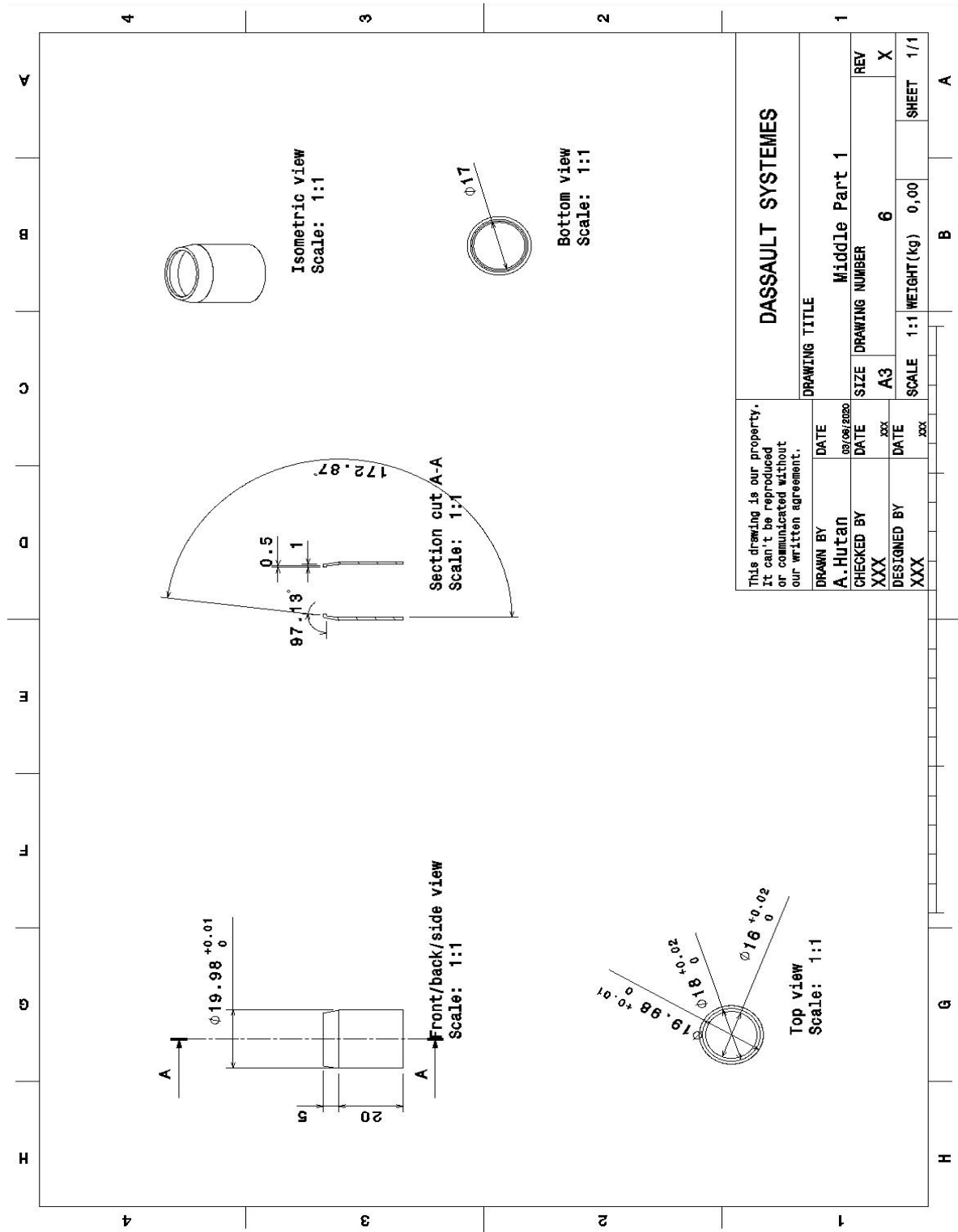


Figure C-6: Technical drawing POC: interface - central locking cylinder (x1)

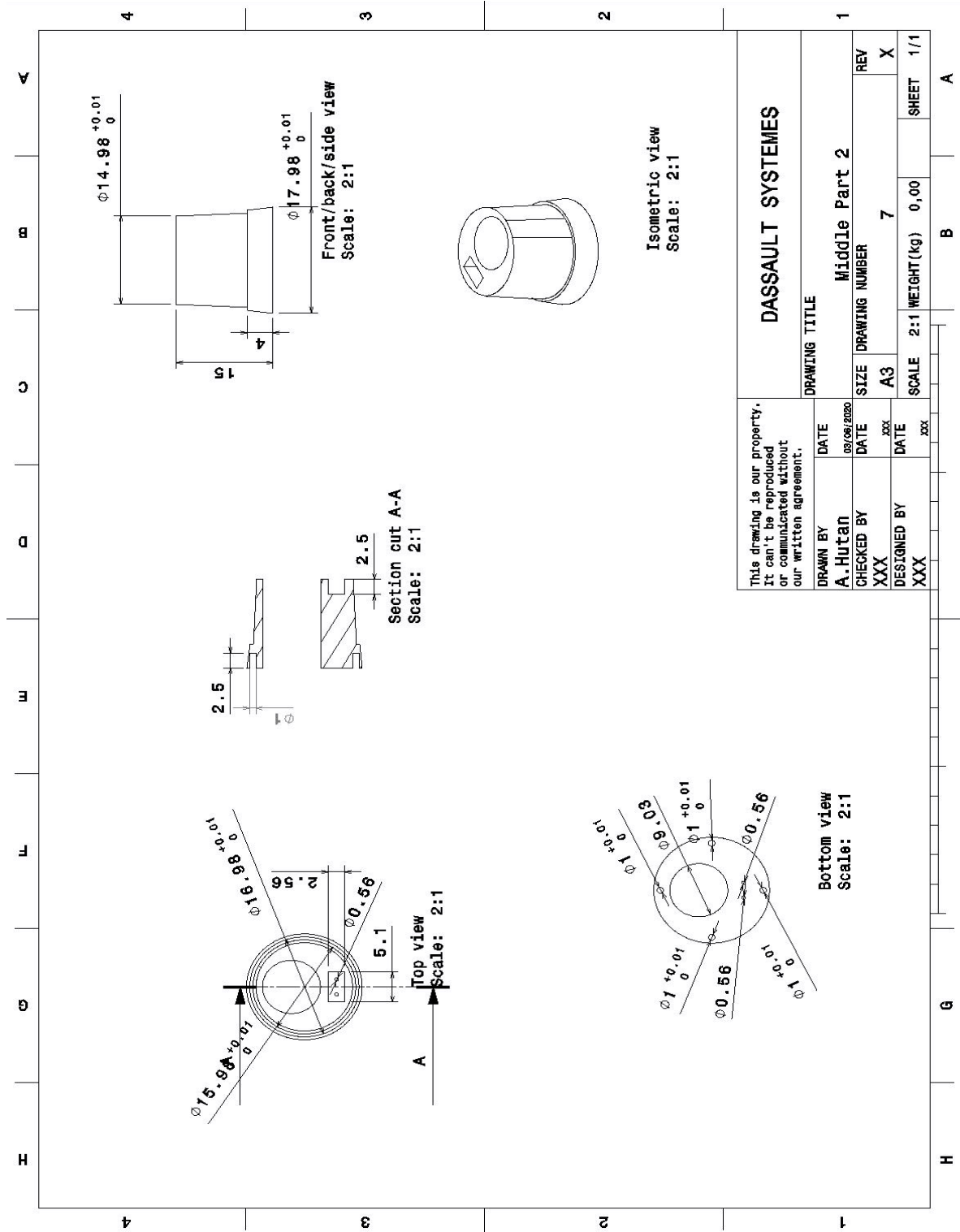


Figure C-7: Technical drawing POC: interface - central end connector (X1)

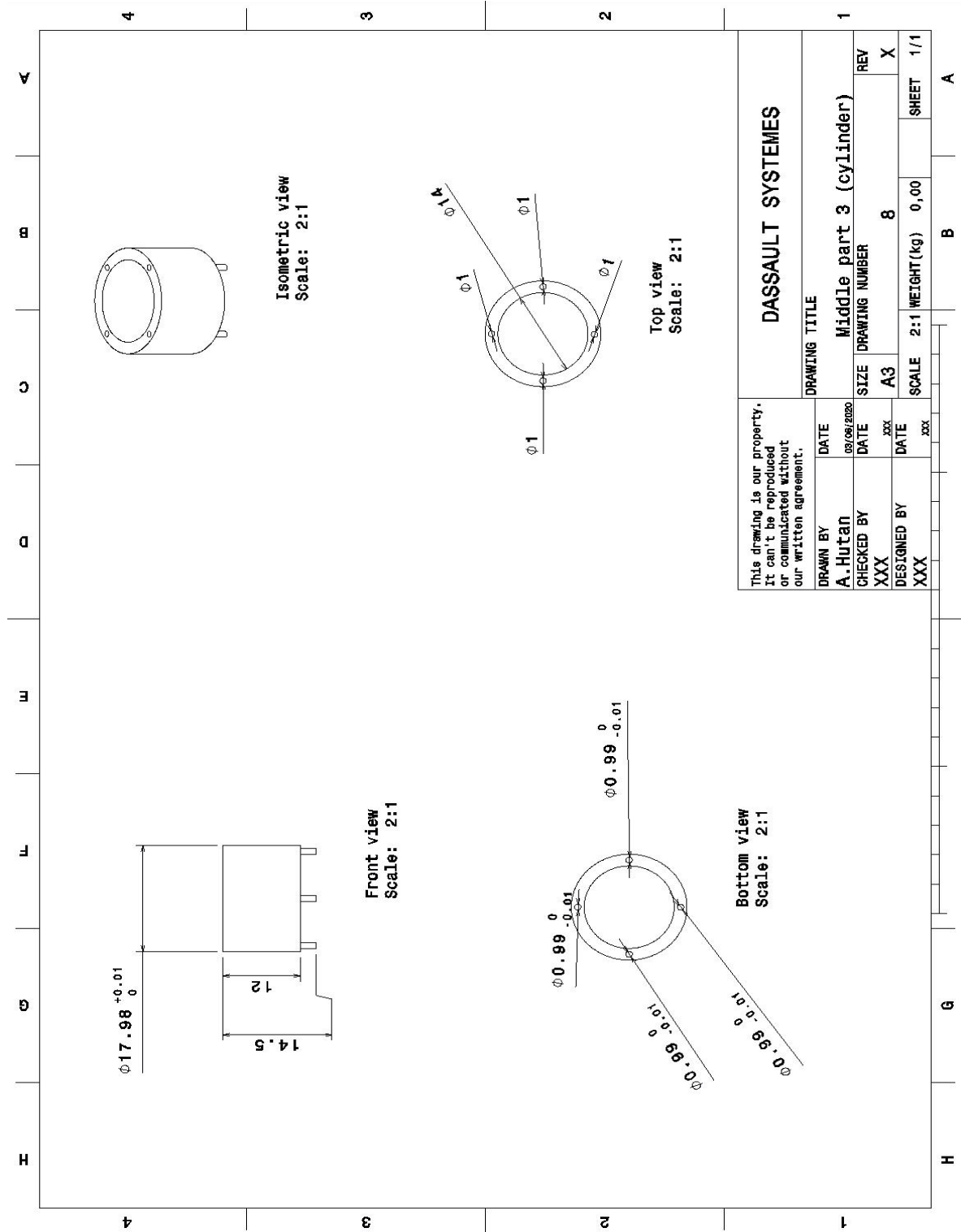


Figure C-8: Technical drawing POC: interface- central inter-connector (X1)

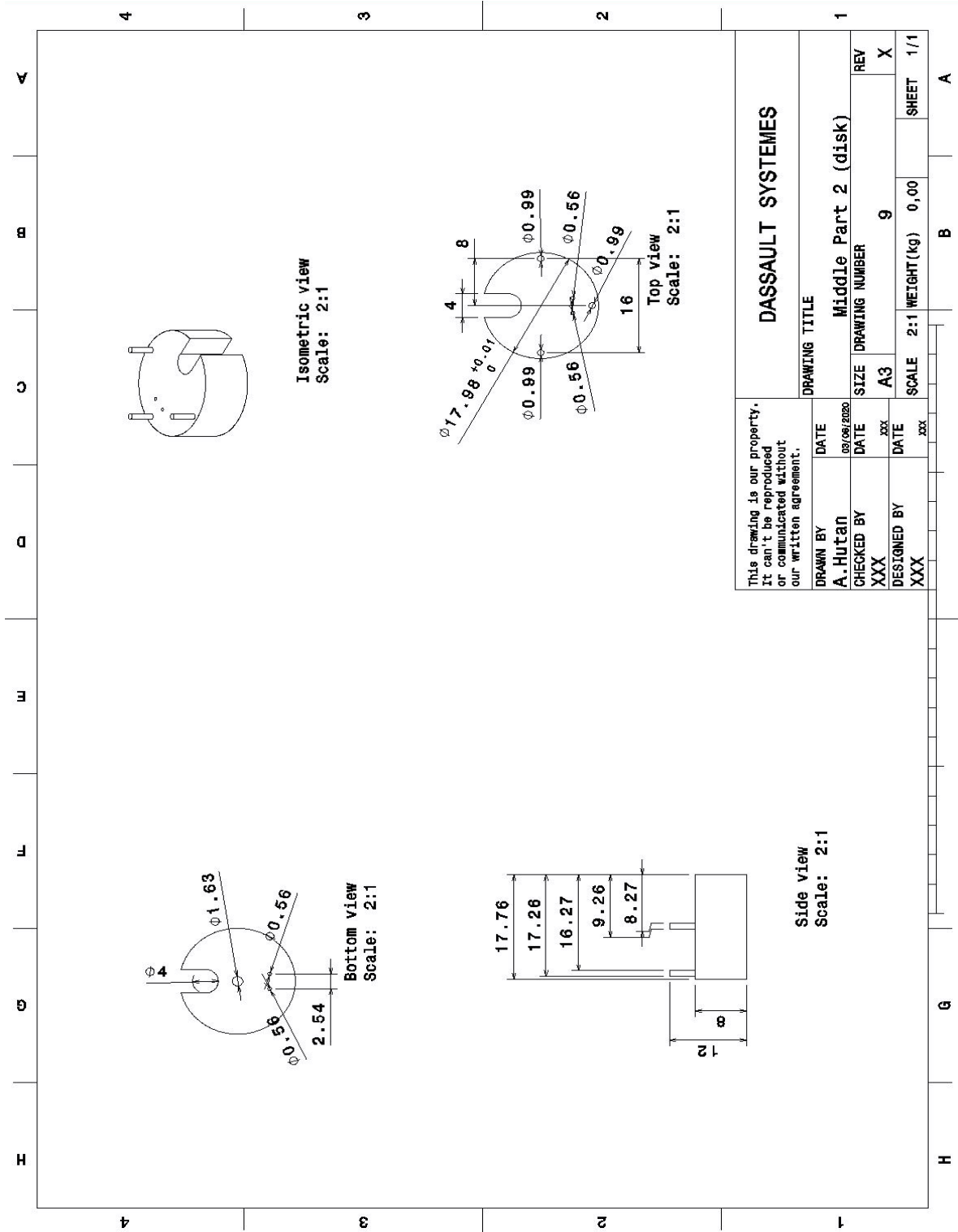


Figure C-9: Technical drawing POC: interface - interface between end-connector and actuator head (X1)

Bibliography

- [1] D. Piskorz and K. L. Jones, “On-Orbit Assembly of Space Assets: A Path to Affordable and Adaptable Space Infrastructure,” tech. rep., 2018.
- [2] M. A. Faget, C. C. Johnson, and D. J. Bergeron III, “Modular Spacecraft System,” May 30 1989. US Patent 4,834,325 A.
- [3] K. H. Rourke and R. J. Hart, “Multipurpose Modular Spacecraft,” Nov. 14 1989. US Patent 4,880,187 A.
- [4] H. S. Eller, R. Coronel, L. E. Elliott, A. Barrett, and D. W. Y. Lee, “Modular Spacecraft Architecture,” Nov. 9 1999. US Patent 5,979,833 A.
- [5] A. B. Bosse, W. J. Barnds, M. A. Brown, N. G. Creamer, A. Feerst, C. G. Henshaw, A. S. Hope, B. E. Kelm, P. A. Klein, F. Pipitone, B. E. Plourde, and B. P. Whalen, “SUMO: spacecraft for the universal modification of orbits,” 2004.
- [6] R. Wolff, C. Preusche, and A. Gerndt, “A Modular Architecture for an Interactive Real-Time Simulation and Training Environment for Satellite On-Orbit Servicing,” in *15th IEEE/ACM International Symposium on Distributed Simulation and Real Time Applications*, 2011.
- [7] D. L. Wenberg, C. B. Wellins, B. B. Rubio Castaneda, J. Kang, and T. Lai, “Miniaturizing the Robotic Assembly of Spacecraft: ISAR Development and On-Orbit Demonstration,” 2018.
- [8] D. Barnhart, B. Sullivan, R. Hunter, J. Bruhn, E. Fowler, L. Hoag, S. Chappie, G. Henshaw, B. Kelm, T. Kennedy, M. Mook, and K. Vincent, “Phoenix Project Status 2013,” in *AIAA SPACE 2013 Conference and Exposition*, 2013.
- [9] P. Melroy, L. Hill, E. Fowler, T. Jaeger, and J. Palmer, “DARPA Phoenix Satlets: Progress towards Satellite Cellularization,” in *AIAA SPACE 2015 Conference and Exposition*, 2015.

- [10] J. Pei, "Ground Demonstration on the Autonomous Docking of Two 3U CubeSats Using a Novel Permanent Magnet Docking Mechanism," 2017.
- [11] N. Miller, "The Rapid Response Radiation Survey (R3S) mission using the HISat Conformal Satellite Architecture," tech. rep.
- [12] L. Rodgers, N. Hoff, E. Jordan, M. Heiman, and D. W. Miller, "A Universal Interface for Modular Spacecraft," tech. rep.
- [13] M. Kortmann, S. Rühl, J. Weise, J. Kreisel, T. A. Schervan, H. Schmidt, and A. Dafnis, "Building Block-based "iBOSS" Approach: Fully Modular Systems with Standard Interface to Enhance Future Satellites," tech. rep., 2015.
- [14] S. Aerospacial, "Standard Interface for Robotic Manipulation (SIROM) - brochure." <https://www.aerospacial.sener/en/>.
- [15] G. S. Aglietti, M. Bandecchi, F. Chatel, G. E. Dorrington, J. B. Farrow, N. P. Fillery, C. R. Francis, G. Hall, J. M. Houghton, J. B. Moss, T. Ransome, K. M. Redford, C. J. Savage, R. E. Sheriff, D. Stanton, M. N. Sweting, A. R. L. Tatnall, and C. I. Underwood, *Spacecraft Systems Engineering Fourth Edition*. Wiley, 2011.
- [16] J. Evans, "MakerBot 5th Generation Review." <https://www.3dbeginners.com/makerbot-replicator-5th-generation-review/>.
- [17] AmesWeb, "Preferred Fits and Tolerances Charts (ISO & ANSI Metric Standards)." <https://amesweb.info/fits-tolerances/>.
- [18] C. Mullins, S. A. Jefferies, R. W. Moses, F. Stillwagen, D. Hamill, and E. Gresham, "Space Science and Technology Partnership Forum: Analysis for a Joint Demonstration of High Priority, In-Space Assembly Technology," 2018.
- [19] E. S. Agency, "Building the International Space Station." <http://www.esa.int/>, 2019.
- [20] H. Frommert, "International Space Station: Assembly Flight Sequence." <http://spider.seds.org/>, 2018.
- [21] "Hubble Space Telescope - Servicing Mission 4 Media Reference Guide." <https://www.nasa.gov/pdf>.
- [22] N. Aeronautics and S. A. . E. S. Agency, "Enabling Science Through New Technologies." <http://www.hubblesite.org/>.
- [23] C. Reynerson, "Spacecraft Modular Architecture Design for on-orbit servicing," in *Space Technology Conference and Exposition*, 1999.
- [24] D. D. Scott, "Apparatus and Methods for In-space Satellite Operations," Jan. 18 2005. US Patent 6,843,446 B2.
- [25] C. Guariniello and D. A. DeLaurentis, "Maintenance and Recycling in Space: Functional Dependency Analysis of On-Orbit Servicing Satellites Team for Modular Spacecraft," in *AIAA SPACE 2013 Conference and Exposition*, 2013.

-
- [26] A. Flores-Abad, O. Ma, K. Pham, and S. Ulrich, "A review of space robotics technologies for on-orbit servicing," 2014.
- [27] D. Wenberg, A. Hardy, T. Lai, C. Wellins, and J. Kang, "Advancing On-Orbit Assembly With ISAR," tech. rep., 2018.
- [28] B. Rubiocastaneda, D. L. Wenberg, J. Kang, T. Lai, and E. A. Hanlon, "Intelligent Space Assembly Robot: Design and Ground Testing," 2017.
- [29] D. A. Whelan, E. A. Adler, S. B. Wilson, and G. M. Roesler, "DARPA Orbital Express program: effecting a revolution in space-based systems," in *International Symposium on Optical Science and Technology - Proceedings of SPIE*, 2000.
- [30] R. B. Friend, "Orbital Express program summary and mission overview," in *SPIE Defense and Security Symposium Proceedings*, 2008.
- [31] A. Ogilvie, J. Allport, M. Hannah, and J. Lymer, "Autonomous Satellite Servicing Using the Orbital Express Demonstration Manipulator System," tech. rep.
- [32] L. Gunn, J. Palmer, J. Leung, A. Ogilvie, A. Tadros, L. Chappell, K. Weldy, E. Fowler, J. Eagan, and B. Sullivan, "DARPA Phoenix Payload Orbital Delivery System: Progress towards Small Satellite Access to GEO," in *29th Annual AIAA/USU Conference on Small Satellites*, 2013.
- [33] B. Sullivan, D. Barnhart, P. Oppenheimer, B. Benedict, G. van Ommering, L. Chappell, J. Ratti, and P. Will, "DARPA Phoenix Payload Orbital Delivery (POD) System: "FedEx to GEO","
- [34] L. Bowman, E. E. Komendera, B. R. Doggett, J. T. Dorsey, and W. K. Belvin, "In-space assembly application and technology for NASA's future science observatory and platform missions," 2018.
- [35] K. Damadeo, "Robotic Arm Gets a Workout." <https://www.nasa.gov/>, 2018.
- [36] E. E. Komendera and J. Dorsey, "Initial Validation of Robotic Operations for In-Space Assembly of a Large Solar Electric Propulsion Transport Vehicle," 2017.
- [37] NASA, "Orbital ATK Supports Ground Testing on CIRAS at NASA's Langley Research Center." <https://www.nasa.gov/>, 2017.
- [38] S. Patane, E. R. Joyce, M. P. Snyder, and P. Shestople, "Archinaut: In-Space Manufacturing and Assembly for Next-Generation Space Habitats," 2017.
- [39] J. Dorsey, J. Boccio, L. Bowman, B. Hollenstein, M. Hanson, J. Lymer, A. Tadros, K. Emerick, W. R. Doggett, and B. King, "Commercial Application of In-Space Assembly," 2016.
- [40] S. Ridinger, "NASA's Dragonfly Project Demonstrates Robotic Satellite Assembly Critical to Future Space Infrastructure Development." <https://www.nasa.gov/>, 2017.
- [41] D. Sellers, R. Elandt, A. K. Weber, A. BenShabat, J. Rosenthal, J. Pei, V. Stewart, L. Murchison, M. Banchy, and D. Elliott, "Autonomous Rendezvous and Docking of Two 3U Cubesats Using a Novel Permanent-Magnet Docking Mechanism," 2016.

- [42] M. A. Lakshmanan, M. A. Adomeit, P. Seefeldt, and V. Reimer, "Androgynous Coupling Device for Connecting Modules, and Corresponding Modules," Jan. 19 2017. US Patent Application Publication US 2017/0015443 A1.
- [43] J. Vinals, J. Gala, and G. Guerra, "Standard Interface for Robotic Manipulation (SIROM): SRC H2020 OG5 Final Results - Future Upgrades and Applications." <https://www.hou.usra.edu/meetings/>.
- [44] E. Commission, "Periodic Reporting for period 1 - SIROM (Standard Interface for Robotic Manipulation of Payloads in Future Space Missions)." <https://cordis.europa.eu/project/>, 2019.
- [45] M. Jankovic, W. Brinkmann, S. Bartsch, R. Palazzetti, and X. Yan, "Concepts of Active Payload Modules and End-Effectors Suitable for Standard Interface for Robotic Manipulation of Payloads in Future Space Missions (SIROM) Interface," 2018.
- [46] C. Mathieu and A. L. Weigel, "Assessing the Flexibility Provided by Fractionated Spacecraft," 2005.
- [47] A. T., M. J., H. D., S. Lloyd, L. J., M. D., M. C., M. F., N. D., R. D., and W. D., "ESD Terms and Definitions," in *Version 12, Working Paper Series, Engineering Systems Division*, 2001.
- [48] H. D.E. and M. H.L., "A Framework for Understanding Uncertainty and its Mitigation and Exploitation in Complex Systems," in *INCOSE International Symposium*, 2005.
- [49] P. Eremenko and O. Brown, "Fractionated space architectures: A vision for responsive space," tech. rep.
- [50] W. J. Larson, J. R. Wertz, and J. J. Puschell, *Space Mission Engineering: The New SMAD*. Microcosm Press, Hawthorne, CA, United States of America, 2011.
- [51] O. Brown and P. Eremenko, "The Value Proposition for Fractionated Space Architectures," in *AIAA SPACE 2006 Conference*, 2006.
- [52] O. C. Brown, P. Eremenko, and P. D. Collopy, "Value-Centric Design Methodologies for Fractionated Spacecraft: Progress Summary from Phase I of the DARPA System F6 Program," in *AIAA SPACE 2009 Conference & Exposition*, 2009.
- [53] O. Brown, P. Eremenko, and M. Bille, "Fractionated Space Architectures: Tracing the Path to Reality," in *23rd Annual AIAA/USU Conference on Small Satellites*, 2009.
- [54] M. Mosleh, K. Dalili, and B. Heydari, "Optimal Modularity for Fractionated Spacecraft: The Case of System F6 a," in *Procedia Computer Science 28*, 2014.
- [55] S. Hur-Diaz and B. O'Connor, "Cluster Flight Application on System F6," tech. rep.
- [56] R. M. Ewart, "Transitioning DARPA Science and Technology Results into Space Capabilities III," in *2018 AIAA SPACE and Astronautics Forum and Exposition*, 2018.
- [57] A. Meiyang, W. Zhaokui, and Z. Yulin, "A Hardware-in-Loop Simulation System for Fractionated Spacecraft Cluster," *Journal of Aerospace Science and Technology*, vol. 1, pp. 1–8, 2015.

-
- [58] C. Araguz, E. Bou-Balust, and E. Alarcón, “Applying autonomy to distributed satellite systems: Trends, challenges, and future prospects,” *Systems Engineering*, 2018.
- [59] S. Downs, J. A. Dempsey, D. Hamill, E. Rodgers, C. Mullins, P. A. Williams, and E. Gresham, “Space Science and Technology Partnership Forum: Value Proposition, Strategic Framework, and Capability Needs for In-Space Assembly,” 2018.
- [60] R. S. Skomorohov, A. M. Hein, and C. Welch, “In-orbit Spacecraft Manufacturing: Near-term Business Cases,” tech. rep.
- [61] M. R. Bolcar, K. Balasubramanian, M. Clampin, J. Crooke, L. Feinberg, M. Postman, M. Quijada, B. Rauscher, D. Redding, N. Rioux, S. Shaklan, H. P. Stahl, C. Stahle, and H. Thronson, “Technology development for the Advanced Technology Large Aperture Space Telescope (ATLAST) as a candidate large UV-Optical-Infrared (LUVOIR) surveyor,” in *UV/Optical/IR Space Telescopes and Instruments: Innovative Technologies and Concepts VII*, vol. 9602, p. 960209, SPIE, 9 2015.
- [62] M. Postman, V. Argabright, B. Arnold, D. Aronstein, P. Atcheson, M. Blouke, M. Bolcar, T. Brown, D. Calzetti, W. Cash, M. Clampin, D. Content, D. Dailey, R. Danner, R. Doxsey, D. Ebbets, P. Eisenhardt, L. Feinberg, E. Freymiller, A. Fruchter, M. Givalisco, T. Glassman, Q. Gong, J. Green, J. Grunsfeld, T. Gull, G. Hickey, R. Hopkins, J. Hraba, T. Hyde, I. Jordan, J. Kasdin, S. Kendrick, S. Kilston, A. Koekemoer, B. Korechhoff, J. Krist, J. Mather, C. Lillie, A. Lo, R. Lyon, S. McArthur, P. McCullough, G. Mosier, M. Mountain, B. Oegerle, B. Pasquale, L. Purves, C. Pendera, R. Polidan, D. Redding, K. Sahu, B. Saif, K. Sembach, M. Shull, S. Smith, G. Sonneborn, D. Spergel, P. Stahl, K. Stapelfeldt, H. Thronson, G. Thronton, J. Townsend, W. Traub, S. Unwin, J. Valenti, R. Vanderbei, P. Warren, M. Werner, R. Wesenberg, J. Wiseman, and B. Woodgate, “Response to the Second RFI from the Astro2010 Committee - The Advanced Technology Large-Aperture Space Telescope (ATLAST),” 8 2009.
- [63] M. Postman, V. Argabright, B. Arnold, D. Aronstein, P. Atcheson, M. Blouke, M. Bolcar, T. Brown, D. Calzetti, W. Cash, M. Clampin, D. Content, D. Dailey, R. Danner, R. Doxsey, D. Ebbets, P. Eisenhardt, L. Feinberg, E. Freymiller, A. Fruchter, M. Givalisco, T. Glassman, Q. Gong, J. Green, J. Grunsfeld, T. Gull, G. Hickey, R. Hopkins, J. Hraba, T. Hyde, I. Jordan, J. Kasdin, S. Kendrick, S. Kilston, A. Koekemoer, B. Korechhoff, J. Krist, J. Mather, C. Lillie, A. Lo, R. Lyon, S. McArthur, P. McCullough, G. Mosier, M. Mountain, B. Oegerle, B. Pasquale, L. Purves, C. Pendera, R. Polidan, D. Redding, K. Sahu, B. Saif, K. Sembach, M. Shull, S. Smith, G. Sonneborn, D. Spergel, P. Stahl, K. Stapelfeldt, H. Thronson, G. Thronton, J. Townsend, W. Traub, S. Unwin, J. Valenti, R. Vanderbei, P. Warren, M. Werner, R. Wesenberg, J. Wiseman, and B. Woodgate, “Advanced Technology Large-Aperture Space Telescope (ATLAST): A Technology Roadmap for the Next Decade,” 5 2009.
- [64] C. Saunders, D. Lobb, M. Sweeting, and Y. Gao, “Building large telescopes in orbit using small satellites,” *Acta Astronautica*, vol. 141, pp. 183–195, 12 2017.
- [65] W. R. Oegerle, L. R. Purves, J. G. Budinoff, R. V. Moe, T. M. Carnahan, D. C. Evans, and C. K. Kim, “Concept for a large scalable space telescope: in-space assembly,” in *Space Telescopes and Instrumentation I: Optical, Infrared, and Millimeter*, vol. 6265, p. 62652C, SPIE, 6 2006.

- [66] N. Lee, P. Backes, J. Burdick, S. Pellegrino, C. Fuller, K. Hogstrom, B. Kennedy, J. Kim, R. Mukherjee, C. Seubert, and Y.-H. Wu, "Architecture for in-space robotic assembly of a modular space telescope," *Journal of Astronomical Telescopes, Instruments, and Systems*, vol. 2, p. 041207, 7 2016.
- [67] NASA, "James Webb Space Telescope." <https://webb.nasa.gov/content>.
- [68] M. T. Menzel', M. Bussman', M. Davis', G. Golnik', S. Irish', J. Lawrence', R. Lynch', P. Maghami', L. Markley', K. Mehalick', G. Mosier', D. Muheim', K. Parrish', S. Thomson', P. Geithner', J. Pitman, J. Wehnerc, J. Arenberg, B. Costanza°, S. Anandakrishnan, B. Burt, and R. Hejal', "Systems Engineering on the James Webb Space Telescope," tech. rep.
- [69] J. Gal-Edd Greenbelt, "James Webb Space Telescope Ka-Band Trade," tech. rep.
- [70] P. A. Lightsey, "James Webb Space Telescope: large deployable cryogenic telescope in space," *Optical Engineering*, vol. 51, p. 011003, 2 2012.
- [71] N. Siegler, R. Mukherjee, H. Thronson, and S. Scientist, "NASA-Chartered In-Space Assembled Telescope Study: Final Report," tech. rep., 2019.
- [72] M. Rudranarayan, N. Siegler, H. Thronson, K. Aaron, J. Arenberg, P. Backers, A. Barto, K. Belvin, L. Bowman, D. Calero, W. Doggett, J. Dorsey, M. East, D. Folta, M. Fuller, S. Glassner, J. Grunsfeld, K. Havey, R. Hellekson, G. Henshaw, J. Hoffman, S. Jeffries, J. Knight, P. Lightsey, J. Lymer, E. Mamajek, D. McGuffey, D. Miller, K. Mehalick, B. Naasz, A. Nordt, K. Patton, C. Peters, M. Perrin, B. Peterson, J. Pitman, R. Polidan, A. Qureshi, D. Redding, K. Ruta, H. Stahl, G. Roesler, R. Shishko, A. Tadros, A. Van Otten, W. Vincent, K. Warfield, S. Wiens, and J. Wood, "When is it worth assembling observatories in space," 2019.
- [73] R. Mukherjeea, N. Sieglerb, H. Thronsonc, and C. Author, "The Future of Space Astronomy will be Built: Results from the In-Space Astronomical Telescope (iSAT) Assembly Design Study," tech. rep., 2019.
- [74] B. Naasz, "Notional ISAT Concept of Operations 10m 20m," tech. rep., 2019.
- [75] N. Siegler, "Building the Future: In-Space Assembled Telescopes (iSAT) Study - Overview and Status," tech. rep., 2019.
- [76] R. Sterritt, G. Wilkie, G. Brady, C. Saunders, and M. Doran, "Autonomic Robotics for Future Space Missions," tech. rep.
- [77] M. W. Werner, T. L. Roellig, F. J. Low, G. H. Rieke, M. Rieke, W. F. Hoffmann, E. Young, J. R. Houck, B. Brandl, G. G. Fazio, J. L. Hora, R. D. Gehrz, G. Helou, B. T. Soifer, J. Stauffer, J. Keene, P. Eisenhardt, D. Gallagher, T. N. Gautier, W. Irace, C. R. Lawrence, L. Simmons, J. E. V. Cleve, M. Jura, E. L. Wright, and D. P. Cruikshank, "THE SPITZER SPACE TELESCOPE MISSION," tech. rep.
- [78] D. G. Koch, W. Borucki, E. Dunham, J. Geary, R. Gilliland, J. Jenkins, D. Latham, E. Bachtell, D. Berry, W. Deininger, R. Duren, T. N. Gautier, L. Gillis, D. Mayer, C. D. Miller, D. Shafer, C. K. Sobeck, C. Stewart, and M. Weiss, "Overview and status of

- the Kepler Mission,” in *Optical, Infrared, and Millimeter Space Telescopes*, vol. 5487, p. 1491, SPIE, 10 2004.
- [79] G. L. Pilbratt, J. R. Riedinger, T. Passvogel, G. Crone, D. Doyle, U. Gageur, A. M. Heras, C. Jewell, L. Metcalfe, S. Ott, and M. Schmidt, “Herschel Space Observatory,” *Astronomy and Astrophysics*, vol. 518, 7 2010.
- [80] G. R. Ricker, J. N. Winn, R. Vanderspek, D. W. Latham, G. Bakos, J. L. Bean, Z. K. Berta-Thompson, T. M. Brown, L. Buchhave, N. R. Butler, R. P. Butler, W. J. Chaplin, D. Charbonneau, J. Christensen-Dalsgaard, M. Clampin, D. Deming, J. Doty, N. De Lee, C. Dressing, E. W. Dunham, M. Endl, F. Fressin, J. Ge, T. Henning, M. J. Holman, A. W. Howard, S. Ida, J. M. Jenkins, G. Jernigan, J. A. Johnson, L. Kaltenegger, N. Kawai, H. Kjeldsen, G. Laughlin, A. M. Levine, D. Lin, J. J. Lissauer, P. MacQueen, G. Marcy, P. R. McCullough, T. D. Morton, N. Narita, M. Paegert, E. Pallé, F. Pepe, J. Pepper, A. Quirrenbach, S. A. Rinehart, D. Sasselov, B. Sato, S. Seager, A. Sozzetti, K. G. Stassun, P. Sullivan, A. Szentgyorgyi, G. Torres, S. Udry, and J. Villaseñor, “Transiting Exoplanet Survey Satellite,” *Journal of Astronomical Telescopes, Instruments, and Systems*, vol. 1, p. 014003, 10 2014.
- [81] D. Spergel, N. Gehrels, C. Baltay, D. Bennett, J. Breckinridge, M. Donahue, A. Dressler, B. S. Gaudi, T. Greene, O. Guyon, C. Hirata, J. Kalirai, N. J. Kasdin, B. Macintosh, W. Moos, S. Perlmutter, M. Postman, B. Rauscher, J. Rhodes, Y. Wang, D. Weinberg, O. D. Benford, M. Hudson, W. S. Jeong, Y. Mellier, W. Traub, T. Yamada, C. P. Capak, J. Colbert, D. Masters, M. Penny, D. Savransky, D. Stern, N. Zimmerman, S. Team, R. Barry, L. Bartusek, K. Carpenter, E. Cheng, D. Content, F. Dekens, R. Demers, K. Grady, C. Jackson, G. Kuan, J. Kruk, M. Melton, B. Nemati, B. Parvin, I. Poberezhskiy, C. Peddie, J. Ruffa, J. K. Wallace, A. Whipple, E. Wollack, and F. Zhao, “Wide-Field InfraRed Survey Telescope-Astrophysics Focused Telescope Assets WFIRST-AFTA 2015 Report by the Science Definition Team (SDT) and WFIRST Study Office Wide-Field InfraRed Survey Telescope-Astrophysics Focused Telescope Assets WFIRST-AFTA 2015 Report Science Definition Team (SDT) and WFIRST Study Office,” tech. rep., 2015.
- [82] I. Jordan, “Electric propulsion: Which one for my spacecraft?,” 03 2001.
- [83] D. Walker, “Faster production of high-quality telescope mirrors.” <https://spie.org/news/>.
- [84] T. Armstrong, A. Bonardi, G. Bonnoli, P. Brun, G. Pareschi, H. Baba, J. Bahr, R. Canestari, P. Chadwick, M. Chikawa, P. H. Carton, V. de Souza, J. Dipold, M. Doro, D. Durand, M. Dyrda, A. Foster, M. Garczarczyk, E. Giro, J. F. Glicenstein, Y. Hanabata, M. Hayashida, M. Hrabovski, C. Jeanney, M. Kagaya, H. Katagiri, L. Lessio, D. Mandat, M. Mariotti, C. Medina, J. Michalowski, P. Micolon, D. Nakajima, J. Niemee, A. Nozato, M. Palatka, M. Pech, B. Peyaud, G. Puhlhofer, M. Rataj, G. Rodeghiero, G. Rojas, J. Rousselle, R. Sakonaka, P. Schovanek, K. Seweryn, K. Schultz, S. Shu, F. Stinzinger, M. Stodulski, M. Teshima, P. Travnicek, C. van Eldik, V. Vassiliev, L. Wisniewski, A. Wornlein, and T. Yoshida, “Status of the technologies for the production of the Cherenkov Telescope Array (CTA) mirrors,” tech. rep., 2013.

- [85] C. Underwood, S. Pellegrino, H. Priyadarshan, V. Lappas, C. Bridges, B. Taylor, S. Chhaniyara, T. Theodorou, P. Shaw, M. Arya, J. Breckinridge, K. Hogstrom, K. Patterson, J. Steeves, L. Wilson, and N. Horri, "Autonomous Assembly of a Reconfigurable Space Telescope (AAReST) - A CubeSat/Microsatellite Based Technology Demonstrator," 2013.
- [86] C. Underwood, S. Pellegrino, H. Priyadarshan, H. Simha, C. Bridges, A. Goel, T. Talon, A. Pedivellano, C. Leclerc, Y. Wei, F. Royer, S. Ferraro, M. Sakovsky, M. Marshall, K. Jackson, C. Sommer, A. Vaidhyanathan, S. Vijayakumari, S. Nair, and J. Baker, "AAReST Autonomous Assembly Reconfigurable Space Telescope Flight Demonstrator," tech. rep., 2018.
- [87] K. Hogstrom, "Robotically Assembled Space Telescopes With Deployable Modules - Concepts and Design Methodologies," 2017.
- [88] "VEGA C USER'S MANUAL ISSUE 0 REVISION 0," tech. rep., 2018.
- [89] "Soyuz at the Guiana Space Centre User's Manual Issue 2-Revision 0," tech. rep., 2012.
- [90] "Ariane 5 User's Manual Issue 5 Revision 2 Issued and approved by Arianespace Roland LAGIER Senior Vice president Chief technical officer," tech. rep.
- [91] "Atlas V Launch Services User's Guide," tech. rep., 2010.
- [92] U. Launch Alliance, "Delta IV Launch Services User's Guide," tech. rep., 2013.
- [93] S. E. T. C. S. X), "Falcon_Users_Guide_082020," tech. rep., 2020.
- [94] D. D. C. (DDC), "REVIEW AND RATIONALE OF MIL-STD-1553 A AND B II. REVIEW AND RATIONALE OF MIL-STD-1553A AND MIL-STD-1553B," tech. rep.
- [95] R. E. A. I. (REA), "Using CAN Bus Serial Communications in Space Flight Applications," tech. rep., 2018.
- [96] D. Slide, "Introduction to Industrial Linear Slides." <https://www.durabondslide.com/introduction-to-industrial-linear-slides/>.
- [97] L. M. Tips, "What are boxway slides and where are they used?." <https://www.linearmotiontips.com/what-are-boxway-slides-and-where-are-they-used/>.
- [98] E. M. Afify, T. Altan, W. F. Ames, D. C. Anderson, V. W. Antonetti, N. K. Arakere, A. F. Armor, R. E. A. Arndt, B. Atkinson, R. Bajura, W. W. Bathie, K. J. Bell, D. E. Berg, S. A. Berger, A. K. Bergles, D. Bharanthan, B. Bhushan, S. M. Birn, K. B. Black, C. J. Bliem, R. F. Boehm, E. R. Booser, M. L. Brown, M. Buczek, G. Cain, M. Capobianchi, V. P. Carey, T.-C. Chang, J. C. Chen, L.-Y. Chen, S. W. Churchill, W. Clark, R. Clear, H. W. Coleman, H. E. Cook, N. E. J. Cook, J. R. Crandall, M. J. Crocker, P. C. Crouse, P. S. Curtiss, M. R. Cutkosky, A. Denver, K. R. Diller, J. Fildes, J. Firor, W. F. I. Fischer, J. M. Fitzgerald, J.-P. Fleurial, D. M. Frangopol, S. I. Freedman, M. Gad-el Hak, S. Ghosh, B. C. Goswami, D. Y. Goswami, H. Grant, V. A. Greenhut, G. W. Hall, R. R. Hewitt Cohen, K. G. T. Hollands, T. D. Howes, S.-H. Huang, I. Husain, J. D. Idol, T. Illangasekare, H. A. Ingley, T. R. J. Irvine, B. J.

Ivarsson, W. D. Jackson, C. K. Jotshi, R. L. Kautz, C. J. Kempf, F. E. Kennedy, J. Kern, J. Kim, N. H. Kim, D. E. Klett, Y. Koren, S. H. Kosmatka, J. F. Kreider, F. Kreith, A. Kumar, A. V. Kumar, K. Lau, Z. Lavan, A. C. Lee, K.-M. Lee, R. L. Lehman, J. I. Leonard, F. L. Lewis, A. Lezuo, S. Y. Liang, N. Lior, K. Liu, T.-I. Liu, S. E. Lyshevski, M. J. Madou, R. L. Mahajan, I. Marinescu, A. T. McDonald, J. E. McMahon, M. Mehregany, M. Merker, M. D. Meyer, A. F. Mills, G. L. Mines, M. F. Modest, R. J. Moffat, M. J. Moran, T. Nakagawa, R. M. Nelson, P. Norton, A. D. Oliver, R. P. Overend, R. Pagano, C. S. Park, J. A. Pearce, I. Pence, G. A. Peters, W. D. Pilkey, D. W. Plummer, J. W. Priest, A. Rabl, G. Raithby, S. Rajgopal, K. P. Rajurkar, M. L. Ramalingam, M. J. Reed, K. C. Reinhardt, R. D. Reitz, J. L. Renner, R. Reuther, A. Ridilla, G. Rizzoni, R. Roloff, B. L. Sandor, R. E. Schafrik, P. Schonfeld, R. K. Shah, T. E. Shannon, T. B. Sheridan, S. A. Sherif, P. W. Shuldiner, S. Smith, W. G. J. Steele, G. T. J. Stevens, W. B. Stine, D. J. Strange, N. P. Suh, N. V. Suryanarayana, L. W. Swanson, Y. Taketomi, J. M. A. Tanchoco, D. D. Tippet, J. Todd, M. Tomizuka, Y. L. Tong, J. S. Tulenko, B. P. Tullis, J. P. Tullis, J. W. Valvano, I. D. Walker, C. Wang, S. K. Wang, W. M. Wang, W. Wang, J. Webster, W. T. Welford, F. M. White, D. F. Wilcock, R. Winston, C. C. Wong, S. Wood, L. L. Wright, T. Yamaguchi, S.-H. Yang, D. J. Young, T. H. Young, F. Zangrando, P. Zannetti, C. Zhou, H. Zhou, C. A. Zorman, and P. J. Zulueta, *The CRC Handbook of Mechanical Engineering*. CRC Press, 2005.

- [99] A. A. S. M. Inc., “Aluminium 7075-T6; 7075-T651.” <http://asm.matweb.com/>.
- [100] A. A. S. M. Inc., “Titanium Ti-6Al-4V (Grade 5), Annealed.” <http://asm.matweb.com/>.
- [101] A. Materials, “Sintered Silicon Carbide (SiC) Properties and Applications.” <https://www.azom.com/>.
- [102] M. Kutz, *Mechanical Engineer’s Handbook Volume 1: Materials and Engineering Mechanics*. John Wiley & Sons, 2015.
- [103] I. Toray Composite Materials America, “M55J High Modulus Carbon Fiber.” <https://www.toraycma.com/>.
- [104] I. Toray Composite Materials America, “T800S Intermediate Modulus Carbon Fiber.” <https://www.toraycma.com/>.
- [105] A. A. I. Solutions, “High Data Rate Links up to 40Gb/s: Faster Transmission.” <https://www.axon-cable.com/en/>.
- [106] GORE, “Catalog: GORE Space Cables for Traditional Space Applications.” <https://www.gore.com/products/>.
- [107] A. A. I. Solutions, “High Speed Links.” <https://www.axon-cable.com/publications/>.
- [108] “NetDot 12th Generation 3 in 1 Magnetic Charging Cable Fast Charge and Data Transfer for Micro USB/USB-C.” <https://www.amazon.de/>.
- [109] S. Interconnect, “LSH Power Rack and Panel Connector.” <https://www.smithsinterconnect.com/products/>.
- [110] M. Max, “821 Spring-Loaded Pogo Pin Header Strip.” <https://www.mill-max.com/products/>.

-
- [111] E. Toolbox, “Friction - Friction Coefficients and Calculator.” <https://www.engineeringtoolbox.com/>, 2004.
- [112] AmesWeb, “ISO Preferred Fits Calculator.” <https://amesweb.info/fits-tolerances/>.
- [113] RS, “26DBM20B2U-L | Portescap Miniature Electric Linear Actuator -, 12 V dc, 8.9 N, 48 mm | RS Components.” <https://nl.rs-online.com/web/>.
- [114] Portescap, “Portescap Product Catalog.” <https://pdf.directindustry.com/pdf/>.
- [115] Cornelius, “Driver and Arduino code for unipolar stepper motors.” <https://www.onetransistor.eu/>.
- [116] Farnell, “Arduino Nano A000005 Micro-controller.” <https://nl.farnell.com/arduino/>.
- [117] Farnell, “N-MOSFET 2N7000.” <https://nl.farnell.com/on-semiconductor/>.
- [118] Farnell, “Metal film resistor MCMF03WJJ0102AA9.” <https://nl.farnell.com/multicomp/>.
- [119] Farnell, “Fast/Ultra-fast Diode MUR160RLG.” <https://nl.farnell.com/on-semiconductor/>.

Glossary

List of Acronyms

AAReST	Autonomous Assembly of a Reconfigurable Space Telescope
ADCS	Attitude Determination and Control Subsystem
ASDA	Adaptable System Design and Analysis
ASTRO	Autonomous Space Transporter and Robotic Orbiter
ATLAS	Advanced Telerobotic Actuation System
ATLAST	Advanced Technology Large-Aperture Space Telescope
CIRAS	Commercial Infrastructure for Robotic Assembly and Services
CDGPS	Carrier-Phase Differential Global Position Systems
CFA	Cluster Flight Application
CSA	Canadian Space Agency
CNDH	Command and Data Handling
DARPA	Defense Advanced Research Projects Agency
DART	Demonstration for Autonomous Rendezvous Technology
DLR	German Aerospace Center (Deutsches Zentrum für Luft- und Raumfahrt)
DOF	Degree Of Freedom
DTM	Deployable Truss Module
EEL	Engineering Evaluation Laboratory
ETS-VII	Experimental Test Satellite VII
EVA	Extra Vehicular Activities
eXCITe	eXperiment for Cellular Integration Technology
FDNA	Functional Dependency Network Analysis
FREND	Front-end Robotics Enabling Near-Term Demonstration
F6	Future, Fast, Flexible, Fractionated, Free-Flying (Spacecraft)
GEO	Geosynchronous Earth Orbit

GOAT	Giant Orbiting Astronomical Telescope
HISat	Hyper-Integrated Satlet
HPA	Hosted Payload Assembly
HST	Hubble Space Telescope
iBoss	intelligent Building Blocks for On-Orbit Satellite Servicing
IPJR	Intelligent Precision Jigging Robot
ISAR	Intelligent Space Assembly Robot
ISS	International Space Station
JAXA	Japan Aerospace Exploration Agency
JWST	James Webb Space Telescope
LEO	Low Earth Orbit
LVLH	Local Vertical Local Horizontal
MIST	Modular Interface for Space Telescopes
MIT	Massachusetts Institute of Technology
MLI	Multi-Layer Insulation
NASA	National Aeronautics and Space Administration
NextSat	Next Generation Serviceable Satellite
NGHDM	Next Generation Hyper-Dextrous Manipulator
NINJAR	NASA Intelligent Jigging Assembly Robot
NRL	Naval Research Laboratory
OOA	On-Orbit Assembly
OEDMS	Orbital Express Demonstration Manipulator System
OOM	On-Orbit Manufacturing
OOS	On-Orbit Servicing
PAC	Package of Aggregate Cells
PODs	Payload Orbital Delivery system
RAMST	Robotically Assembled Modular Space Telescope
RCA	Retired Cooperative/Candidate Asset
RCS	Reaction Control System
RKA	Russian Space Agency (Roscosmos)
ROKVISS	Robotics Component Verification on the International Space Station
ROTEX	Robot Technology Experiment
RWA	Reaction Wheel Assembly
R1	Robonaut 1
R2	Robonaut 2
R/D	Rendezvous/Docking

SAMEE	Scanning and Additive Manufacturing End-Effector
SAMURAI	Strut Assembly, Manufacturing, Utility & Robotic Aid
SEP	Solar Electric Propulsion
SE-L2	Sun-Earth Lagrange 2
SIRE	Satellite Inspection Recovery and Extension
SIROM	Standard Interface for Robotic Manipulation
SMAD	Spacecraft Modular Architecture Design
SoS	System-of-Systems
SRMS	Shuttle Remote Manipulator System
SSRMS	Space Station Remote Manipulator System
SSL	Space System Loral
SUMO	Spacecraft for the Universal Modification of Orbits
SWARM	Self-assembling Wireless Autonomous and Reconfigurable Modules
TALISMAN	Tendon Actuated Lightweight In-Space Manipulator
TECSAS	Technology Satellites for Demonstration and Verification of Space Systems
TESS	Transiting Exoplanet Surveillance Satellite
TMST	Thirty Meter Space Telescope
TRL	Technological Readiness Level
UDA	User Defined Adapter
USNA	United States Naval Academy
WFIRST	Wide-Field InfraRed Survey Telescope

